BULLETIN OF THE MINERAL RESEARCH AND EXPLORATION

2023 171 ISSN : 0026-4563
E-ISSN : 2651-3048

CONTENTS

Research Articles

Review Article

LOCATION OF MANAGEMENT
Bilimsel Dokümantasyon ve Tanıtma Dairesi Başkanlığı
Maden Tetkik ve Arama Genel Müdürlüğü
Çukurambar Mahallesi
Dumlupınar Bulvarı No: 11 06530
Çankaya/ANKARA
e-mail: bilimsel_dairesi@mta.gov.tr

Bull. Min. Res. Exp. is indexed and abstracted in TR Dizin, Emerging Source Citation Index (ESCI), Scopus, The ICI Journals Master List (Copernicus), Directory of Open Access Journals (DOAJ), Open Academic Journals Index (OAJI), Georef, MIAR, EBSCO and Zoological Record.

The Bulletin of the Mineral Research and Exploration is published in three issues in a year. Each volume is published in Turkish and English in pdf format on the website of Bulletin of the Mineral Research and Exploration and English issue published in print. The English volüme of the "Bulletin of the Mineral Research and Exploration" can be obtained from "BDT Department" free of charge, either directly or ordered by adding postage fee from the correspondence address. Typesetting and printing operations are carried out and followed by the Publication Service of the Scientific Documentation and Publicity Department. e-mail: bilimsel_dairesi@mta.gov.tr

The section of "notes to the authors", format, copyright and other information can be obtained from www.mta.gov.tr as PDF files.

Printed Date: .....
Printing House: Neyir Matbaacılık-Matbaacılar Sitesi 1341 cd. No: 62 İvedik OSB-Yenimahalle/Ankara
Phone: 0312 395 53 00 • Fax: 0312 395 84 20 • www.neyir.com
Periodical
ISSN: 0026-4563
E-ISSN: 2651-3048

Bulletin of the Mineral Research and Exploration

http://bulletin.mta.gov.tr

Integration of structural, hydrogeological and thermal remote sensing data for the determination of geothermal capacity: Edremit (Balıkesir) Basin as a case study

Önder KAYADİBİ[a], Şule GÜRBOĞA[a], Hafize AKILLI[a], Serap ARIKAN[a], Sevilay TAN[a], Zehra DEVECİ ARAL[a] and Halim MUTLU[b]

[a]*General Directorate of Mineral Research and Exploration, Ankara, Türkiye*
[b]*Ankara University, Department of Geological Engineering, Ankara, Türkiye*

Research Article

Keywords:
Geothermal, Remote Sensing and GIS, Tectonic, Hydrogeology, Edremit (Balıkesir) Basin.

ABSTRACT

Basins formed on active strike-slip faults are important prospect areas for geothermal energy exploration since the crust gets thinner in these areas and tectonic structures provide favorable conditions for heat-fluid circulation and transportation. The objective of the recent study is to evaluate the geothermal capacity of the Edremit Basin utilizing tectonic, geological, and hydrogeological studies, combining remote sensing (land surface temperature-LST, hydrothermal alteration, and multi-temporal InSAR (MT-InSAR) assessments). We present structural literature data and the results of field mapping, which revealed the geometry, kinematics, and dynamics of structural features, geological units as geothermal system components, thermal and cold water chemistry, and thermal infrared remote sensing analysis. For the purpose of assessing new targets and recent geothermal capacity, these data are combined and evaluated. According to the outcomes of the study, the fault pattern in the Edremit Basin is generated by N-S extension, which produced E-W dominant striking normal faults with a heritage of paleostructures oriented in various directions. According to remote sensing analyses, the primary LST regions in the basin are defined by the active faults. Therefore, a high sodium sulfate ratio recorded in the chemical analyses of the water samples indicates a deep circulation and high possibility for the presence of thermal water. Consequently, our findings are consistent with the work to include thorough field geology surveys, structural patterns, LST, and water chemistry to refined exploration process. All these results indicated that Edremit (Balıkesir) Basin holds a great promise for the discovery of new geothermal energy sources.

Received Date: 23.05.2022
Accepted Date: 02.05.2023

1. Introduction

As a result of technological developments, increasing population, industrialization, and rapid urbanization, energy requirements rise, requiring greater exploration of alternative energy resources such as wind, solar, wave, geothermal, and biomass. Geothermal energy is regarded as one of the most prominent renewable and clean energy resources in this context. Furthermore, geothermal energy has a wide range of applications despite its low environmental impact (CO_2 emissions are the lowest). The energy (heat) is transferred naturally between a heat source and a heat sink in a constrained area of the Earth's crust using a geothermal system. Accordingly, there are various specialties relating to geothermal energy, including geological engineering and geotechnologies (Zannina et al., 2020).

Citation Info: Kayadibi, Ö., Gürboğa, Ş., Akıllı, H., Arıkan, S., Tan, S., Deveci Aral, Z., Mutlu, H. 2023. Integration of structural, hydrogeological and thermal remote sensing data for the determination of geothermal capacity: Edremit (Balıkesir) Basin as a case study. Bulletin of the Mineral Research and Exploration 171, 1-32. https://doi.org/10.19111/bulletinofmre.1291349

**Corresponding author: Önder KAYADİBİ; onder.kayadibi@mta.gov.tr*

During the last two decades, a number of studies has utilized the satellite imagery (Gutiérrez et al., 2012; Hulley et al., 2012; Vaughan et al., 2012*a* and *b*; Littlefield and Calvin, 2014; Song and Park, 2014; Van der Meer et al., 2014; Hewson et al., 2017; Parastatidis et al., 2017; Sheng et al., 2009; Ramírez-González et al., 2019) to determine the fault-controlled geothermal anomalies which enable better estimation of underground temperatures (Pieri and Adams, 2004 and 2005; Faulds et al., 2006; Srivastava et al., 2009; Giordano et al., 2013; Nukman and Moeck, 2013; Norini et al., 2015; Calderón-Chaparro and Vargas-Cuervo, 2019) and volcanic systems (Braddock et al., 2017; Waswa, 2017). For this reason, attention is currently being given to the deeper zones that lie under the geothermal reservoirs in order to better understand the comparatively near-surface regions. Accordingly, near-surface and surface data, such as surface temperature values (Land Surface Temperature-LST), geothermal heat flux (GHF) values, hydrothermal alteration zones, and alteration minerals linked to geothermal resources define fault directions and types, as well as geophysical and drilling outputs, and have a direct impact on the geothermal capacity. Surface data are collected prior to the application of high-cost field applications such as geophysical and drilling studies, which significantly contribute to the exploration of suitable areas for geothermal sources (Waswa, 2017; Chan et al., 2018; Mia et al., 2014; 2018; Calderón-Chaparro et al., 2019; Ramírez-González et al., 2019). Remote sensing and geographic information system (GIS) are widely used in various stages of geothermal energy exploration and evaluation studies, such as the identification and monitoring of potential target areas (Vaughan et al., 2003, 2012*a* and *b*; Gutiérrez et al., 2012; Kruse, 2012; Giordano et al., 2013; Van der Meer et al., 2014; Wang et al., 2014; Calvin and Pace, 2016; Mia et al., 2018; Reinisch et al., 2020).

The Edremit Basin in the Biga Peninsula is a known geothermal field, and in this work, we used a multi-approach technique to analyze the surface evidence of the field (Figure 1a). The Edremit Basin and its surroundings covering an area of about 5000 km^2 are the subject of this investigation. In the research, we combined various methods that deal with geology, tectonic, hydrogeochemical, and remote sensing data. Geometric and kinematic analyses of structural characteristics are all included in the tectonic research. Remote sensing analyses comprise determination of anomalies of land surface temperature (LST) and hydrothermal alteration by using multispectral satellite images and multispectral satellite images as well as investigation of surface deformation pattern by using InSAR data.

Additionally, spatial data layers are combined, analyzed, and evaluated using GIS in order to determine the best location for geothermal potential. Hydrogeological studies consist of geochemistry of thermal and cold waters in the Edremit-Derman geothermal field. Utilizing a variety of chemical geothermometers and mineral-fluid equilibrium models, hydrogeological research aims to identify the characteristics of hydrogeochemical facies and calculate the fluid reservoir temperatures. In addition, evaluation of the stable isotope compositions (oxygen-O, hydrogen-H) of the waters revealed the origins of the compounds dissolved in the waters and to provide insight about the chemistry of the fluids in the potential geothermal areas. Tritium (T) is the radioactive isotope of hydrogen with a half-life of 12.32 years. The subsurface circulation time of the water was estimated using data from tritium isotopes. The relationship between the hydrogeochemical data and geological and remote sensing studies is examined.

The aim of this study is to investigate the geothermal energy potential of the Edremit (Balıkesir) Basin with geological, tectonic and hydrogeological studies based on remote sensing data, and to analyze and evaluate the available data in GIS application for the reconnaissance of possible geothermal target areas.

2. Geological and Hydrogeological Settings

2.1. Geological Setting

The Biga Peninsula (NW Türkiye) is located at the north of the İzmir-Ankara Suture Zone, which separates the Sakarya Zone in the north from the Anatolide-Tauride Block in the south. The region witnessed two main events: Closure of Paleo- and Neo-Tethys Oceans and it was formed as a tectonic mosaic by different continental units, representing the Sakarya Continent and oceanic assemblages of different origin and ages (Şengör and Yılmaz, 1981; Okay and Tüysüz, 1999; Bozkurt and Mittwede, 2001; Okay et al., 2008).

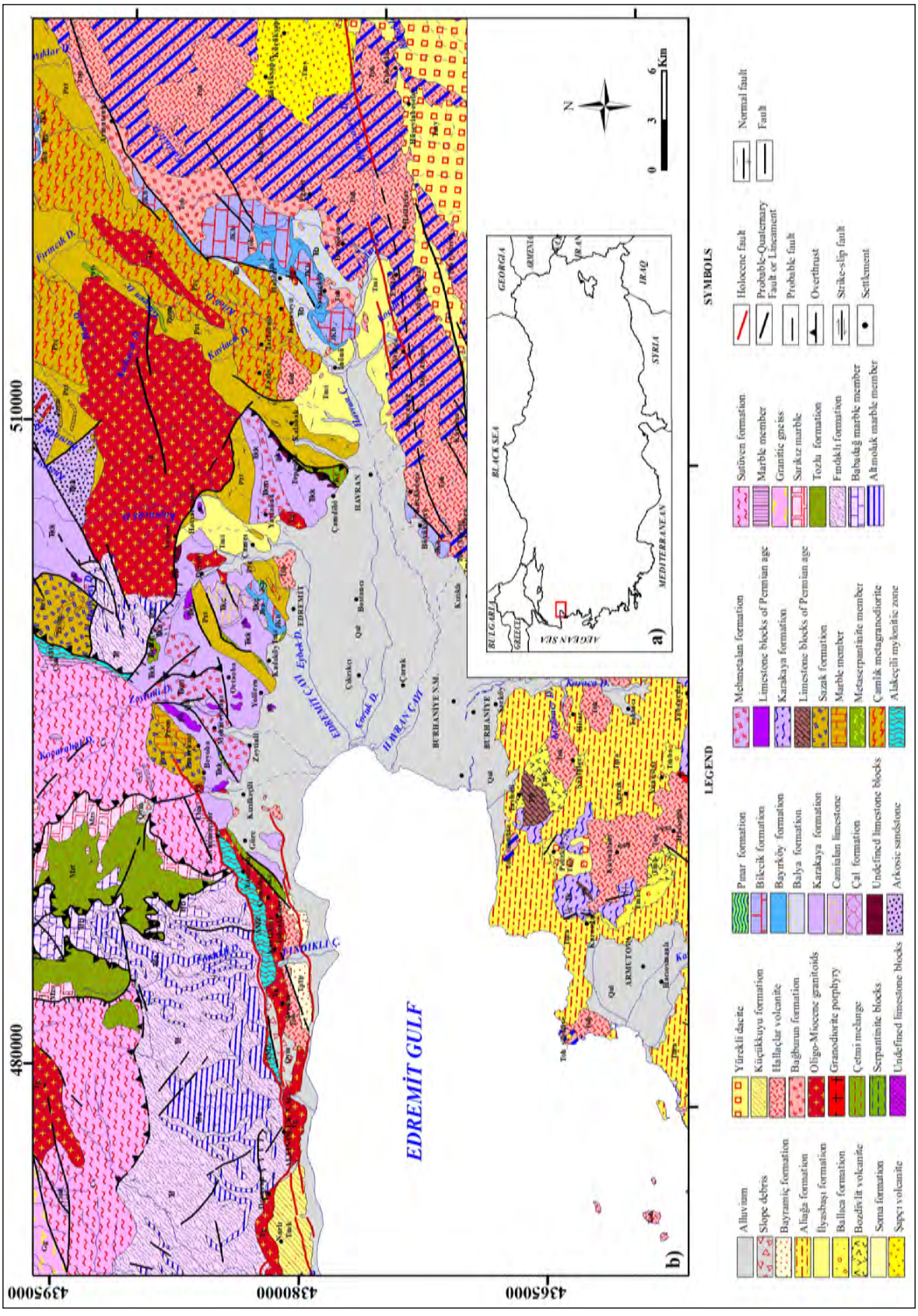

Figure 1- a. Location of Edremit Basin in Türkiye; b. Geological map of study area (Duru et al., 2004; Duru et al., 2007*a*, *b*; Dönmez, 2013; Emre et al., 2011).

The basement rocks in the region are quartz micaschist and minor calc-schist, metaquartzite, marble and eclogite, called as 'Çamlıca Metamorphics' and 'Kazdağı Massif' (Okay et al., 1991). The age of metamorphism is suggested as the Late Cretaceous–Early Paleocene (70–64 Ma) (Okay and Satır, 2000; Aygül et al., 2012). The Kazdağ Massif forms a structural and topographic dome of high-grade metamorphic rocks (Okay and Satır, 2000). It crops out as a tectonic window under the Karakaya Complex that includes the remnants of Paleotethys Ocean. The Complex consists of metabasic and metasedimentary rocks with Permian limestone blocks (Okay and Göncüoğlu, 2004). The cover units consist of widespread Eocene to Pleistocene volcanic and plutonic rocks, continental and shallow to deep marine sedimentary rocks (Siyako et al., 1989; Dönmez et al., 2005; Altunkaynak and Genç, 2008; Genç et al., 2012; Ilgar et al., 2012). Cenozoic magmatism is the result of northward subduction of continental slab during the closure of Neotethys Ocean (references and discussion in Okay and Satır, 2000). The subduction-related volcanic activity started in the Eocene and lasted until the Miocene producing volcanic suites ranging in composition from basalt to dacite (Bingöl et al., 1982 and 1992; Altunkaynak and Genç, 2008). Considering the literature data (Duru et al., 2007*a, b*; Emre et al., 2011; Dönmez, 2013; TJVT database) and field observations, a simplified geological map of the Edremit area was prepared (Figure 1b).

The geology of the region is basically dominated by two main features: (1) the widespread occurrence of Cenozoic magmatism, and (2) NE-SW striking of all geological features as a result of dextral strike-slip faulting (Beccaletto, 2003). This resulted in the development of a more complex stratigraphic succession. From bottom to top, the stratigraphic succession is briefly explained as follows: Metamorphites so called Çetmi mélange and Kazdağ metamorphites form the basement rocks (Figure 2). The Cretaceous Çetmi mélange consists of ophiolitic units and various rocks. It is composed of tectonic slices and/or olistostromes. The stratigraphic position and fossil content of the unit indicate that the mélange was emplaced in the region before the Maastrichtian (Okay et al., 1990 and 1991; Duru et al., 2007*a*). The Kazdağ metamorphics are composed of the Altınoluk marble member, Fındıklı formation (alternations of amphibolite gneiss, marble and amphibolite), Babadağ marble member, the Tozlu formation (ophiolitic rocks), Sarıkız marble and the Sutüven formation (gneiss, migmatite, marble and granitic gneisses). These metamorphics are cut by Oligo-Miocene granitoids. Dating by $^{207}Pb/^{206}Pb$ method indicates that the Kazdağ metamorphites are Late Carboniferous in age (Okay et al., 1996). However, 233±24 Ma age obtained from K/Ar method shows that the age of the unit is late Early Triassic-early Late Triassic (Bingöl, 1969 and 1971). The Carboniferous-Devonian Kalabak group overlying the Kazdağ metamorphics with a tectonic contact consists of low-grade metamorphics (Duru et al., 2007*b*). It contains the Torasan formation represented by phyllites, schists, metavolcanites and marbles. The Sazak formation (metatuff, metavolcanite, phyllite, schist, metabasite, marble and recrystallized limestone) and the Çamlık metagranodiorite (Devonian-Carboniferous) cut by several young granites and aplitic dykes. The Karakaya complex unconformably overlies the Kalabak group with a tectonic relation (Duru et al., 2007*a*, 2007*b*). The basal contact of the complex, which is considered to be Triassic in age, is mostly defined as tectonic.

The Balya formation, Late Triassic sandstone and Halobian shales, forming the cover units of the Sakarya Zone, unconformably overlie the units of the Kalabak group. The Bayırköy formation, Early Jurassic conglomerate, sandstone, siltstone, claystone and clayey limestone set above the Balya formation. Bilecik formation (Callovian-Hautrivian limestones) is widely seen in the Sakarya Zone. The Pınar formation of Hautrivian-Albian age is made up of hemipelagic, micritic limestone and claystone alternation. Most of basin deposits are found on top of the Sakarya Zone. They start with andesitic lava, ignimbrite, agglomerate and volcanoclastics of the Bağburun formation which is the product of volcanism that continued until the Late Oligocene-Early Miocene (Dönmez et al., 2005). Altered volcanic rocks of the Hallaçlar volcanite are observed at the upper part of the Bağburun formation. Shallow intrusions generally of granodioritic composition emplaced in the region in the Oligocene-Late Miocene interval. The Küçükkuyu formation, which is composed of Miocene bituminous shale, tuff, mudstone, sandstone, conglomerate and limestones, unconformably overlies the Hallaçlar volcanics. The

Early Miocene dacite, rhyolite and rhyodacites cut the Hallaçlar volcanite. They are also unconformably overlain by the Late Miocene Aliağa formation consisting of conglomerate, sandstone, claystone, tuff, tuffite, claystone and lacustrine limestone. The Early Miocene Şapçı volcanite, which is composed of andesite and pyroclastics unconformably overlies the Yürekli dacite. The conglomerate and sandstone of Middle Miocene Ballıca formation unconformably overlie the Middle Miocene Bozdivlit volcanite, which consists of lavas of basalt-andesite composition. The unit is transitional to the lacustrine sandstone, claystone, tuff, tuffite and limestones of the Aliağa formation. The Late Miocene İlyasbaşı formation, which is composed of marl, limestone, mudstone, tuff, sandstone and conglomerate, covers the Early Miocene units. The Bayramiç formation that comprises the Plio-Quaternary fluvial deposits and Quaternary alluvial deposits unconformably sets above all these units.

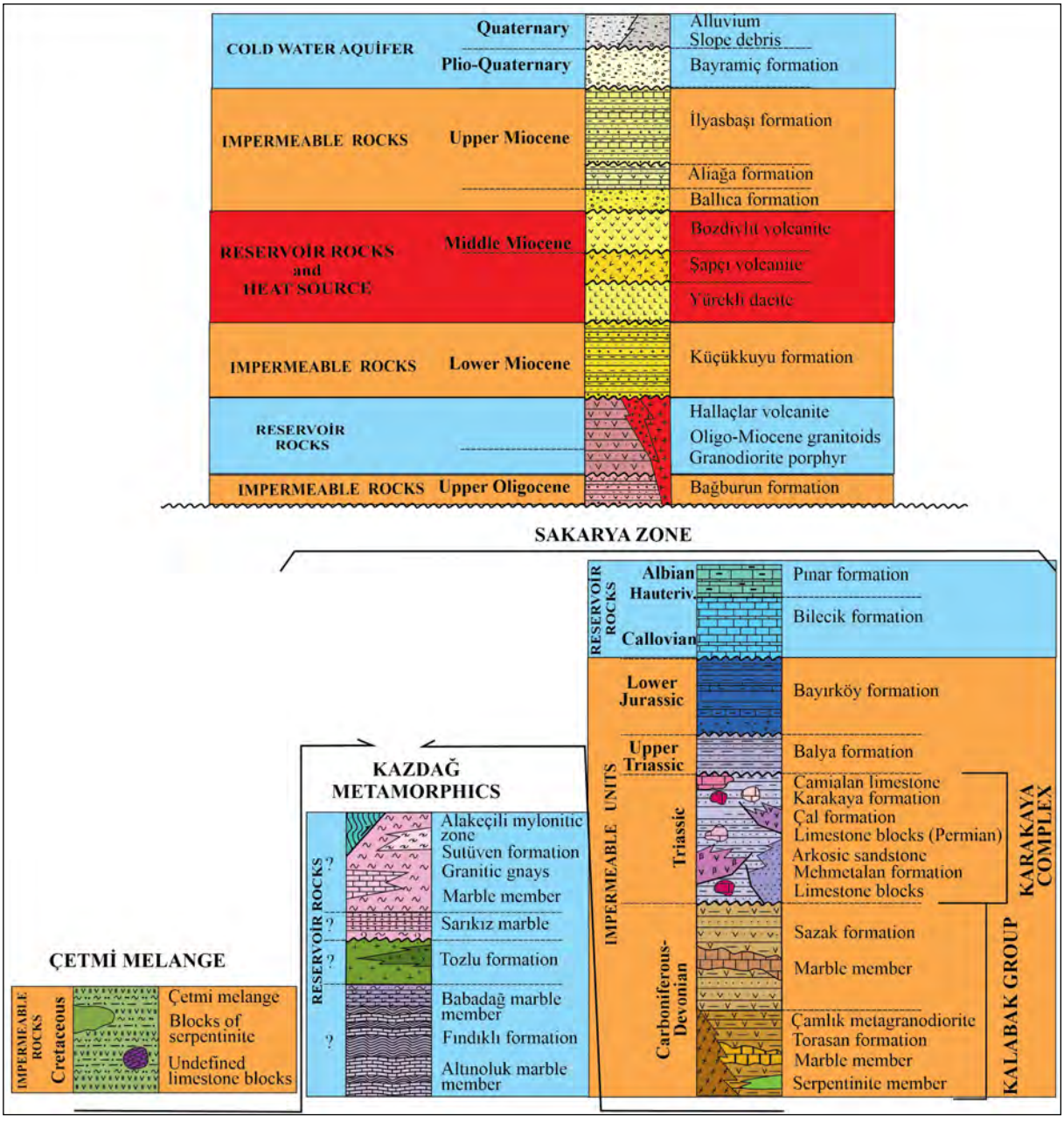

Figure 2- Stratigraphic section of the Edremit Basin (modified from Duru et al., 2004, 2007*a, b;* Dönmez, 2013).

2.2. Hydrogeological Setting

Reservoir rocks that are composed of porous and permeable units make up the most important part of a geothermal system. They have gained secondary porosity by tectonic and lithological effects. In the Edremit-Güre area, marble levels of the Kazdağı Massif, Jurassic limestones, conglomerates within the Paleocene-Eocene sediments, sandstone, fractured volcanic rocks and pebbly sandy Miocene sediments comprise the reservoir rocks (Sarp et al., 1998). Avşar et al. (2013) reported the presence of two different aquifers in the Edremit geothermal field. They stated that the shallow aquifer is comprised of Quaternary and Plio-Quaternary unconsolidated sandstone, conglomerate and mudstone units. The units consisting of agglomerate and conglomerate over the Kazdağ Metamorphites are regarded as the second aquifer. According to Yalçın (2007), the Upper Jurassic-Lower Cretaceous limestone acts as a reservoir rock while the Karakaya Complex is of impermeable character. However, some of the wells receive thermal water from the Karakaya Complex. The Karakaya complex is impermeable and the fractured character as a result of tectonism increases the water-transfer capacity of the unit. Magmatism represented by Miocene volcanics and granitic rocks (Karacık and Yılmaz, 1998) constitutes the heat source for the geothermal system. The cover rock is another important component of the geothermal system, which is necessary for the storage of thermal fluid. In the Edremit basin, clayey, silty layers of sedimentary rocks, tuffs and volcanic rocks are the major cap rocks.

Edremit field is one of the important geothermal fields of Western Anatolia. In this field, almost 50 wells have been drilled by both private firms and government institutions (Erzenoğlu, 1985; Güner et al., 1994; Sarp et al., 1998; Ölmez et al., 2001; Dilemre et al., 2006; Avşar, 2011; Avşar et al., 2013). The depths of the wells are between 20-1350 m and the temperatures of waters from these wells varies between 21-65°C. Sarp et al. (1998) drilled 4 gradient wells in the Edremit field in order to determine the geothermal gradient and the locations of the deep production wells. The depths of the gradient wells vary from 122 to 300 m. As a result of the temperature measurements in the gradient wells, the geothermal gradient was calculated as 0.29ºC/10m-1.28ºC/10m (Sarp et al., 1998). The highest gradient value was obtained in the well drilled in granitoids that is the reservoir rock. Demet-1, ED-1, ED-2, ED-3, Güre-1, Güre-2 and BGK-2011/19 production wells were drilled by General Directorate Mineral Research and Exploration (Table 1). The drilled at a depth of 400 m and the bottom temperature of this well was determined 53ºC. The water produced from Demet-1 well has a flow rate of 1.5 l/s and a temperature of 40ºC (Erzenoğlu, 1985). The ED-2 well is at a depth of 495.5 m and the bottom temperature of the well is

Table 1- Temperature, depth and production information of some of the wells in the Edremit basin.

Well name	Depth (m)	Temperature (ºC)	Flow rate (l/s)	Coordinates			Reference
				Y	X	Z (m)	
Demet-1	400	40	1.5	-	-	-	Erzenoğlu (1985)
ED-1	189.5	60	75	4380395	503642	25	Ölmez et al. (2001)
ED-2	496.5	47	2	4380293	504014	27	Ölmez et al. (2001)
ED-3	495	59	18	4380335	03710	24	Ölmez et al. (2001)
EDJ-2	300	58	75	4380049	503916	24	Avşar et al. (2013)
EDJ-3	266	59	50	4380252	503634	21	Avşar et al. (2013)
EDJ-4	296	50	86	4380136	503458	19	Avşar et al. (2013)
Güre-1	196.20	55	6,5	490125	482300	10	Didik et al. (1994)
Güre-2	153.70	33	7	490300	482850	15	Didik et al. (1994)
İGJ-1	167	64	32	490224	4832366	-	Dilemre et al. (2006)
İGJ-2	250	56,3	50	490060	4382174	-	Dilemre et al. (2006)
İGJ-3	206	67	40	490215	4382392	-	Dilemre et al. (2006)
İGJ-3	250	67	40	490332	4382392	-	Dilemre et al. (2006)
İGJD-1	1350	96	30	490316	4382228	12	Dilemre et al. (2006)
BGK-2011/09	750	33,3	30	489133	4363577		Bulut et al. (2018)

55.4ºC. The gradient value calculated for this well is 0.26ºC/10 m. The thermal water was obtained from the well at a temperature of 47ºC and a flow rate of 2 l/s (Ölmez et al., 2001). The thermal water produced from the wells is used for heating of residences, thermal facilities and greenhouse and also for thermal tourism.

3. Methods

In this study, geothermal energy potential of the Edremit Basin is investigated using remote sensing method (LST, hydrothermal alteration and InSAR) and geological, tectonic and hydrogeological data. All the data were evaluated with a GIS application. The study was carried out in three stages (Figure 3).

The first stage comprises processing of the satellite images (anomalies maps of LST, hydrothermal alteration as well as InSAR analysis). During the field work, data were collected from the ground truth, faults, and various types of rock and sampling of thermal and cold waters. This is followed by the construction of geological and tectonic framework based on the geological map of the area which is mainly related to literature data. Descriptions of the units in the litostratigraphic section and faulting mechanism were obtained from previous studies and recent earthquakes data. The last step includes GIS study to combine, analyze and evaluate all the spatial data layer.

Three groups of analysis were carried out within the scope of remote sensing studies. The first is the preparation of surface temperature (LST) map from thermal bands of satellite data that is one of the most important remote sensing works widely used in the geothermal energy exploration. The second is the determination of hydrothermal alteration anomaly areas and the third one is defining the surface deformations by interferometric analysis of SAR images.

Field study is the ground truth step of all combined data. Geological, stratigraphical and structural mapping were checked during field study. Stratigraphical features are the key point for the heat source and reservoir rocks of thermal springs. Collection of field data includes measurements of striations and fault plane. A total of 133 fault plane/striations were measured at 19 different sites. Statistical analyses of faults and joints are processed in the lower hemisphere projection using the software employed for stress inversion of fault slip data (Angelier, 1979). During the fieldwork, thermal and cold water samples were collected from the wells and springs. Some physical

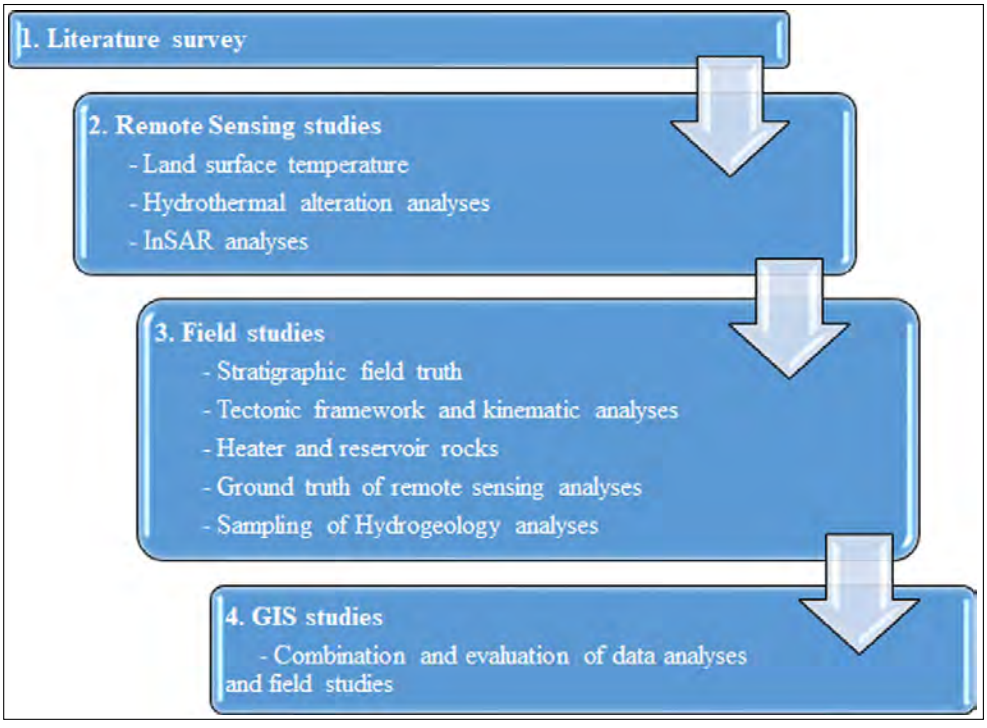

Figure 3- General methodological flowchart.

parameters were recorded during the collection of water samples (Table 2). The thermal water ES-1 was taken from the deepest well (1350 m) with the highest temperature at the northwest of field (in Güre). The ES-2 sample was collected from a well drilled in alluvium at a depth of 64 m (in Havran). The ES-3 sample that has a temperature of 32 ºC was taken from a well drilled that has a depth of 640 m in the south of the field. The E-4 sample was taken from a low-elevation stream. The sample E-5 is a cold water spring that discharges from high elevations. Their temperature was measured at the sampling site. From each spring, three samples are collected and 0.2 ml of HNO_3 was added to one of the samples to prevent precipitation of cations. Another batch was collected for isotope ($\delta^{18}O$, $\delta^{2}H$, ^{3}H) analysis. Chemical analysis of the waters was carried out at the laboratories of the General Directorate of Mineral Research and Exploration with the standard methods. The cations (Ca^{+}, Mg^{2+}, Na^{+}, K^{+}) and SiO_2 concentrations were determined by Inductively Coupled Plasma Optical Emission Spectrometry (ICP-OES). This method is also used in As, B and Li analysis. Titration method is used in HCO_3^{-} and CO_3^{2-} analysis. SO_4^{2-}, Cl^{-} and F^{-} analyses were made using the Ion Chromatography Method (ICM). $\delta^{18}O$ and δD (reported as V-SMOW) analyses were performed with laser spectrometry and tritium (^{3}H) analyses are made with a liquid count scintillation system at the General Directorate of State Hydraulic Works TAKK Laboratories. Lastly, the combination and evaluation of all data are presented on a final map constructed by GIS application.

4. Field Observations and Analysis

Four main study package have been applied in the content. Structural geology, remote sensing (calculation of surface temperature, determination of hydrothermal alteration, InSAR analysis), water chemistry and isotopic data (geochemical characteristics of Edremit and Güre waters, isotope geochemistry, geothermometer applications) and GIS application. They all were investigated and applied separately and then combined in GIS layers.

4.1. Structural Geology and Fault Kinematics from Field Study

The Edremit Basin located in the Biga Peninsula is a tectonically active area controlled by a normal faulting mechanism with right lateral component dominantly. It is formed in association with the North Anatolian Fault System (NAFS), Aegean Extensional System (AES) and the motion of plates around Türkiye (McKenzie, 1972; Jackson and McKenzie, 1988; Kaya, 1978; Gessner et al., 2013; Jolivet et al., 2013; Özkaymak et al., 2013; Uzel et al., 2013; Gürer et al., 2016; Gürer, 2023). The configuration implies that the peninsula moves to the west and southwest with a velocity of 2–3 cm/year (McClusky et al., 2000; Straub et al., 1997; Aktuğ et al., 2009). There are various mechanisms for the origin of basin: (a) strike-slip faulting associated with the NAFS (e.g. Okay and Satır, 2000), (b) normal faulting controlled by AES (Kurtuluş et al., 2009), and (c) coupled effects of both NAFS and AES (e.g. Yılmaz and Karacık, 2001; Boztepe-Güney et al., 2001; Gürer et al., 2016). Evolution of a basin has a great control on geothermal capacity. Not only the displacements along the active faults but also paleo structures act as passage for groundwater circulation. For this reason, the map of structural lineaments recorded during the field study and obtained from the literature are presented in Figure 4. The results show the existence of a dense

Table 2- Coordinates and physical parameters of the sampled waters in study field.

Sample No	Well Name	Coordinates			Well Depth (m)	T* (ºC)	pH	EC* µS/cm	References
		Y	X	Z					
ES-1	İGJD-1	490316	4382228	12	1350	86	8.5	1211	This study
ES-2	Altın Tohumcu	503078	4379448	22	64	32	7.4	1132	This study
ES-3	Gömeç	488235	4362501	52	640	32	8.1	1855	This study
ES-4	Hasanboğuldu	492945	4388545	259	Spring	15	8.1	229	This study
ES-5	Çamtepe Village	504970	4367950	487	Spring	19	7.4	449	This study
EDR-1*	EDR-1	490103	4381735	7	Spring	60	8.2	945	Yalçın, 2007
ED-3*	ED-3	503639	4380394	22	495	62	7.7	1060	Avşar et al., 2013
IGJ-2*	IGJ-2	490060	4382174	9	250	46.2	8.6	864	Kaçar et al., 2017

*: These samples are included here for comparison with samples taken in this study.

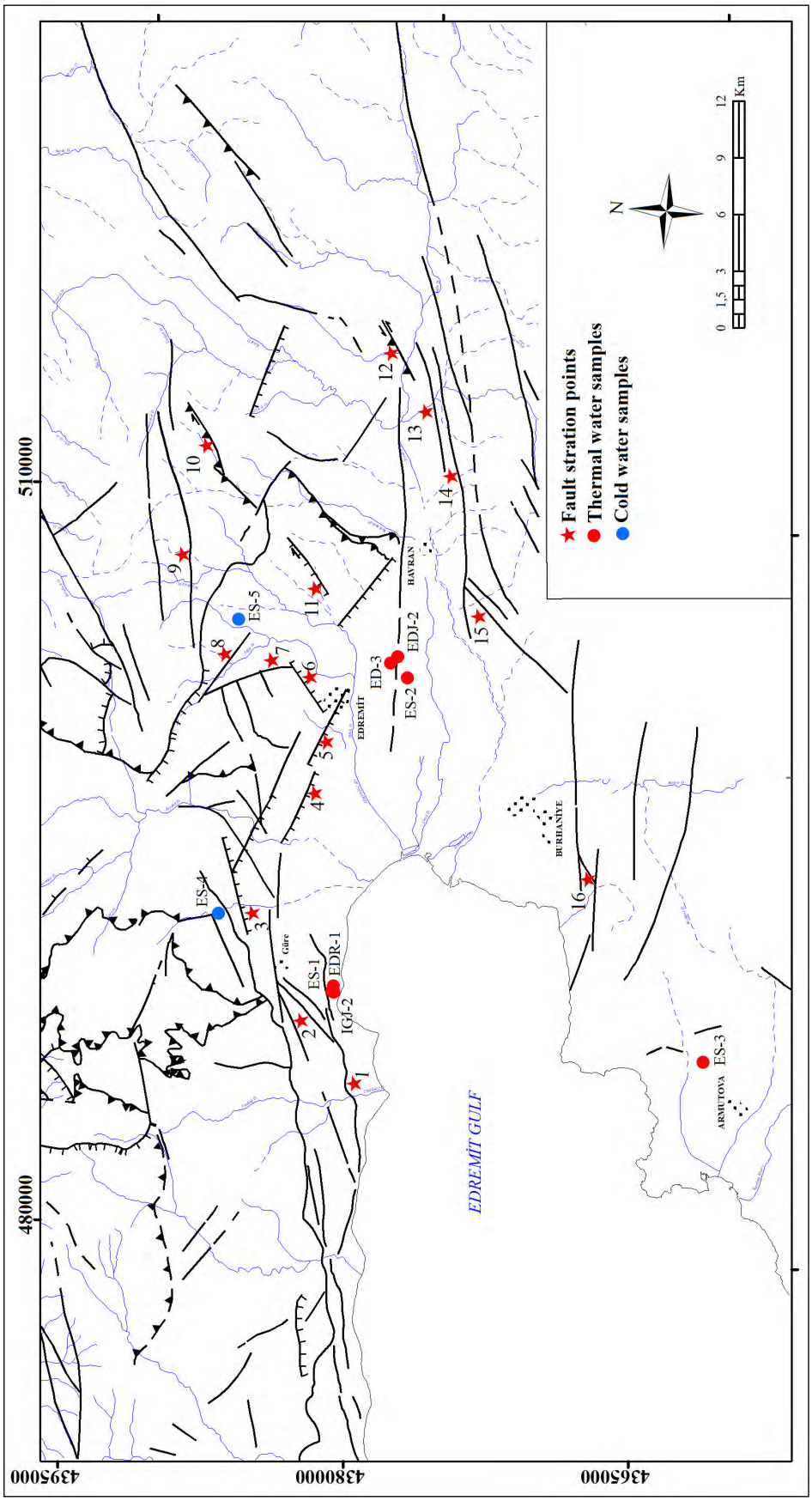

Figure 4- Main structures around the Edremit Basin; striation and water sample points (Faults and active faults: Duru et al., 2004; Duru et al., 2007*a, b*; Dönmez, 2013; Emre and Doğan, 2010; Emre et al., 2011; faults determined during the field study).

network of fractures that would affect the geothermal area in the Edremit Basin. Faults are crucial structures in groundwater moving to the surface. These structures' ability to convey fluid is directly impacted by the stress distribution under which they are created. Because of this, the development processes of the faults are identified, and crucial information on their lengths and groundwater capacities is gained based on the kinematic analysis of the fault striations taken over the fault surfaces. According to the older and current tectonic regimes, regional evaluation was made using the fault slip data. The locations of the places were marked with asterisks in Figure 4.

Kinematic analyses of fault striations are used to determine dominant stress directions operated on the faults. There is different software for the paleostress analysis based on the stress distribution. In this study, measured data obtained from the fault surfaces were analyzed according to methods proposed by Angelier (1984), T-TECTO. The data set was processed by the Direct Inversion Method (INVD) assuming that the slip is parallel to the calculated maximum shear stress. According to this assumption, the ratio of the principal stress differences is $R = (\sigma2 - \sigma3) / (\sigma1 - \sigma3)$. R has a range between 0 and 1, and when R goes to 0, faulting mechanism is dominated by σ1 as vertical (extensional), R closes to 1, faulting mechanism is dominated by σ3 as vertical (compressional) and in between σ2 is dominant and strike slip motion appears (Angelier, 1984). To analyze the striations for the stress distributions, we measured kinematic data along the fault planes, which are located particularly along the margin faults in the Edremit Basin (Figure 5). A total of 133 measurements from 19 different locations were used for stress configurations (Figure 6).

Structural geology should be the prime strategy for geothermal exploration studies. From this point of view, marginal faults in the Edremit Basin and some lineaments around the basin were measured and analyzed. Striations indicate that different types

Figure 5- Some field photographs and striations from fault surfaces; a) station 1, b) station 3, c) station 5, d) station 6, e) station 8 and f) field photographs from station 16 in Figure 5.

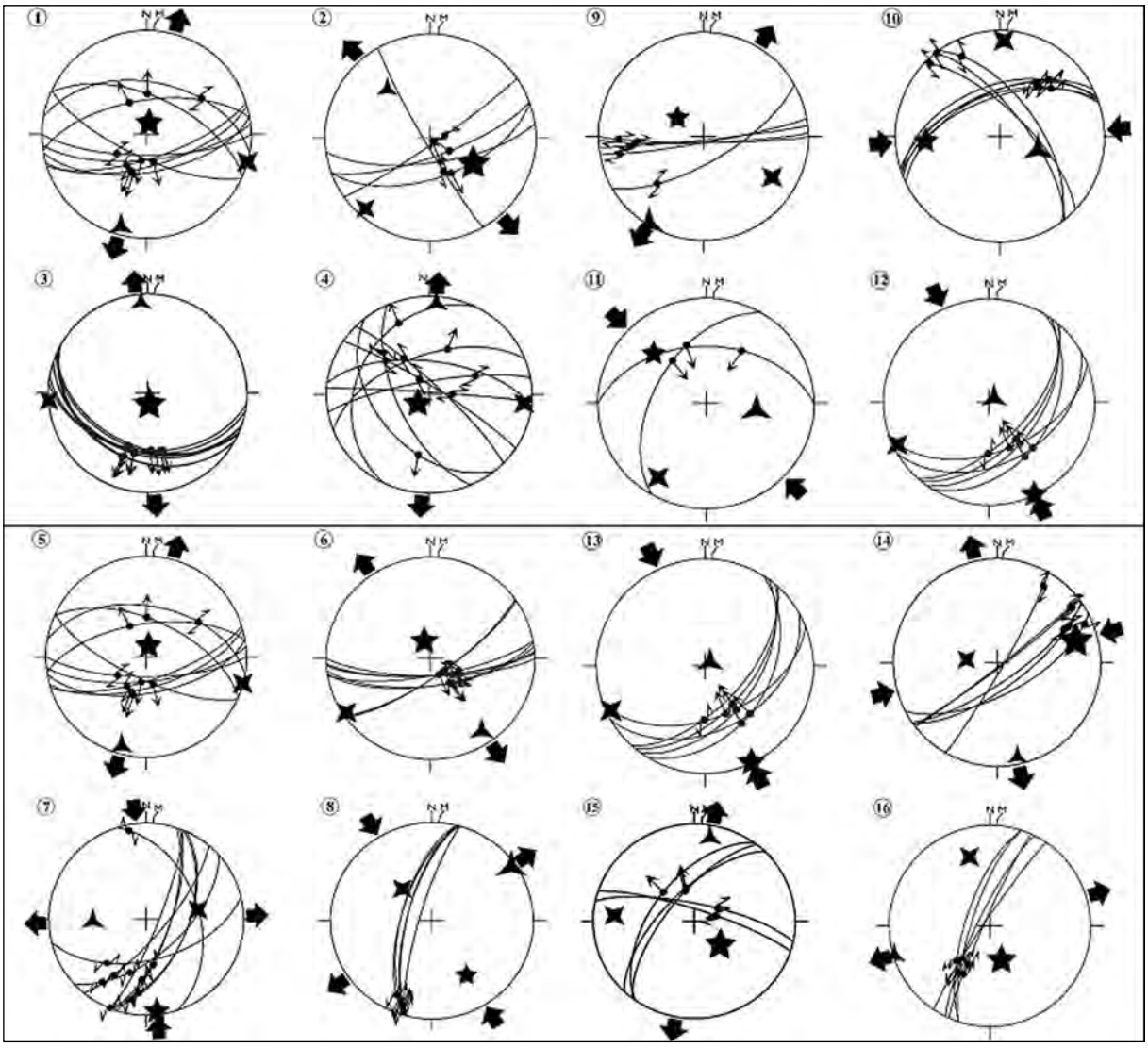

Figure 6- Kinematic analyses of fault striations measured at locations given in Figure 4.

of faulting mechanisms are effective in the area. Each point (1-16) and their kinematic results are presented in Figure 7 and according to the main faulting mechanism N-S extensional stress distribution is dominant around the Edremit Basin. In this case, the most probable faulting direction is around E-W and striking structures have normal motion such as the faults with measurement numbers of 1, 2, 3, 4, 5, 6, 9, 15 and 16 (Figures 5 and 6). On the other hand, 7, 8, 10, 11, 12, 13 and 14 indicate strike slip and reverse faulting mechanisms. Measurements 12 and 13 have reverse mechanism that are probably inherited from paleotectonic period.

4.2. Remote Sensing Studies

In this study, thermal bands of day/night time ASTER, Landsat 8 and Landsat 7 ETM+ satellite images were used to calculate LST values (Table 3). Two Landsat 8 TIRS (Thermal Infrared Sensor) images (acquisition date of 02.09.2017) with path-row number 181/033 were used. Two Landsat 7 ETM+ images with the same path-row number as Landsat 8 were obtained (10.09.2017). The acquisition date of two ASTER daytime thermal images is 20.09.2000 and the acquisition date of two ASTER nighttime thermal images is 27.06.2013. ASTER day and night times images are ASTER Surface Kinetic Temperature

Table 3- Satellite images used in this study.

Thermal Analysis				Alteration	InSAR Analysis
Landsat 8 OLI	**Landsat 7 ETM+**	**ASTER-day**	**ASTER-night**	**ASTER VNIR-SWIR**	**ALOS Palsar-1**
02.09.2017	10.09.2017	20.09.2000	27.06.2013	02.11.2004	04.01.2007-15.01.2011 (19 images)

(AST_08) data generated using the Temperature Emissivity Separation Algorithm (TES) (Gillespie et al., 1998). These data are from NASA Earth Science Data (NASA, 2019) while Landsat 8 TIRS and Landsat 7 ETM+ images were obtained from USGS (USGS, 2019).

Areas for the hydrothermal alteration anomalies associated with geothermal systems were determined applying band ratio method to spectral bands in the visible-near infrared (VNIR) (0.52-0.85 μm) and short-wave infrared (SWIR) (1.600-2.430 μm) region of the ASTER images (01.11.2004). The multi-temporal InSAR (MTInSAR) analysis of ALOS Palsar-1 (L-band) SAR images were used to define the surface deformations (subsidence, uplift) in the basin. In the MTInSAR analysis, ascending 19 ALOS Palsar-1 images taken between 04.01.2007 and 15.01.2011 were used (Table 4). ALOS Palsar-1 images were analyzed by applying the "Small Baseline Subset Interferometry (Small BASeline Subset-SBAS)" technique, which is one of the Multi-temporal InSAR (MTInSAR) methods.

Table 4- Acquisition dates of ALOS Palsar-1 images.

ALOS Palsar-1			
4.01.2007	9.10.2008	12.10.2009	30.05.2010
7.07.2007	9.01.2009	27.11.2009	15.07.2010
7.10.2007	24.02.2009	12.01.2010	30.08.2010
7.01.2008	12.07.2009	27.02.2010	15.01.2011
24.05.2008	27.08.2009	14.04.2010	

4.2.1. Calculation of Surface Temperature Values with ASTER Day/Night Times Thermal Images

Thermal infrared remote sensing analysis has been extensively used for the last years to identify surface temperature anomalies related with geothermal activity (Allis et al., 1999; Hook et al., 1999; Ayenew, 2001; Pieri and Abrams, 2005; Vaughan et al., 2012*a* and *b*; Haselwimmer and Prakash, 2013; Wessels et al., 2013). Satellite data such as MODIS, ASTER, Landsat 8 TIRS and Landsat 7 ETM+ and thermal cameras are widely used in this context. In order to obtain surface temperature values from the thermal bands of satellite images, many algorithms such as Radiative Transfer Equation (RTE), Single-Channel (SC), Split-Window (SW), temperature and emissivity separation (TES) have been developed (Gillespie et al., 1998; Qin et al., 2011; Li et al., 2013; Jiménez-Muñoz and Sobrino, 2003; Jiménez-Muñoz et al., 2014; Yu et al., 2014). ASTER day-time and night-time surface temperature maps were produced from AST08 surface kinetic temperature data. A scaling factor of 0.1 was applied to the surface kinetic temperature data of ASTER AST08 and the temperature values were converted to degrees Celsius. Then, the ASTER temperature maps of the study areas were prepared. Band 10 of Landsat 8 TIRS images and band 6 of Landsat 7 ETM+ images were used to calculate LST values. The procedures given the flowchart in Figure 7 were applied to compute the surface temperature values from the thermal bands of Landsat 8 TIRS and Landsat 7 ETM+ images. Landsat 8 TIRS and Landsat 7 ETM+ thermal bands were atmospherically corrected using parameters estimated by the atmospheric correction parameter calculator web tool (Barsi et al., 2003 and 2005). The emissivity (ε) values of Landsat 8 TIRS band 10 and Landsat 7 ETM+ band 6 are calculated using the NDVI Thresholds Method ($NDVI^{THM}$) (Sobrino et al., 2004; 2008) modified the existing land surface emissivity (LSE) calculation method based on Normalized Difference Vegetation Index (NDVI) (Van de Griend and Owe, 1993; Valor and Caselles, 1996). LST values were calculated using the single band algorithm generalized by Artis and Carnahan (1982) based on the Planck function using a single band (Equation 1).

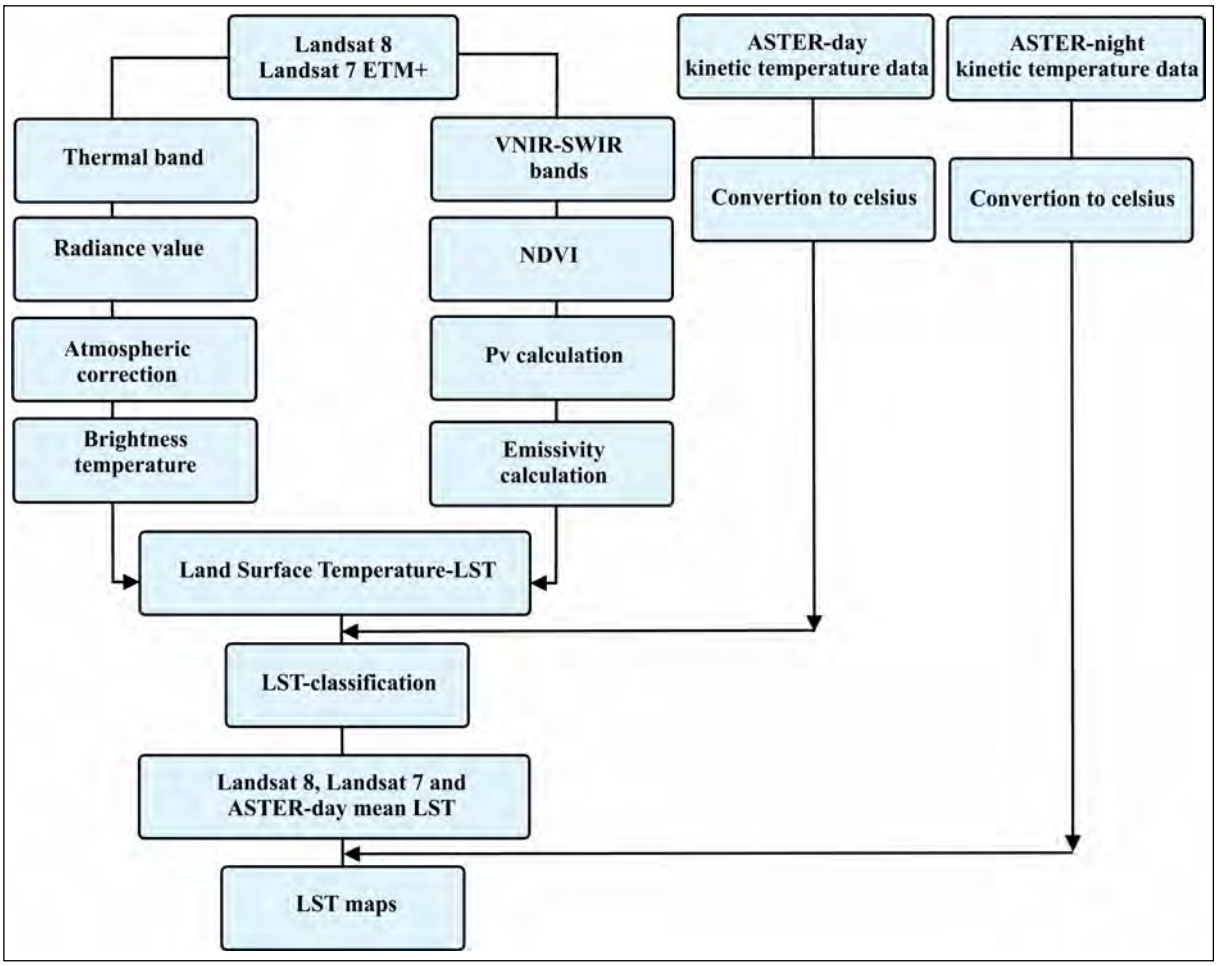

Figure 7- Flowchart of LST calculations.

$$T_s = \frac{BT}{\left\{1 + \left[\frac{\lambda \cdot BT}{\rho}\right] \cdot ln\varepsilon\right\}}$$ …….....…..Equation 1

Ts : land surface temperature (K)

BT: at-sensor brightness temperature (K)

λ : wavelength of the emitted radiance

● : h * c/s=1.438 x 10^{-2} m K

h : Planck's constant (6.626 x – 34 Js)

S : Boltzmann Constant (1.38 x – 23 J/K)

c : Velocity of light (2.998 x – 8 m/s)

ε : spectral emissivity

In order to increase the accuracy of LST results obtained from satellite data, approximately 10 highest temperature values on ASTER-daytime, Landsat 8 TIRS and Landsat 7 ETM+ LST maps were reclassified for each map. Then, the average daytime LST map was produced by taking the arithmetic average of these values (Figure 8).

4.2.2. Determination of Hydrothermal Alteration Anomaly Areas

In a geothermal system, changes known as alteration occur in the mineralogy, texture and chemistry of the rocks by the effect of thermal water, steam and fumaroles (Van der Meer et al., 2014). These changes are the indicators of underground geothermal systems on the ground surface. At certain temperatures, clay (kaolinite, illite), sulfate (alunite, gypsum), carbonate (calcite) and silica (opal, chalcedony) minerals are formed (Calvin et al., 2015). Therefore, mapping of hydrothermal alteration anomalies and identifying these minerals and/or mineral groups are important in terms of limiting the possible target areas (prospect

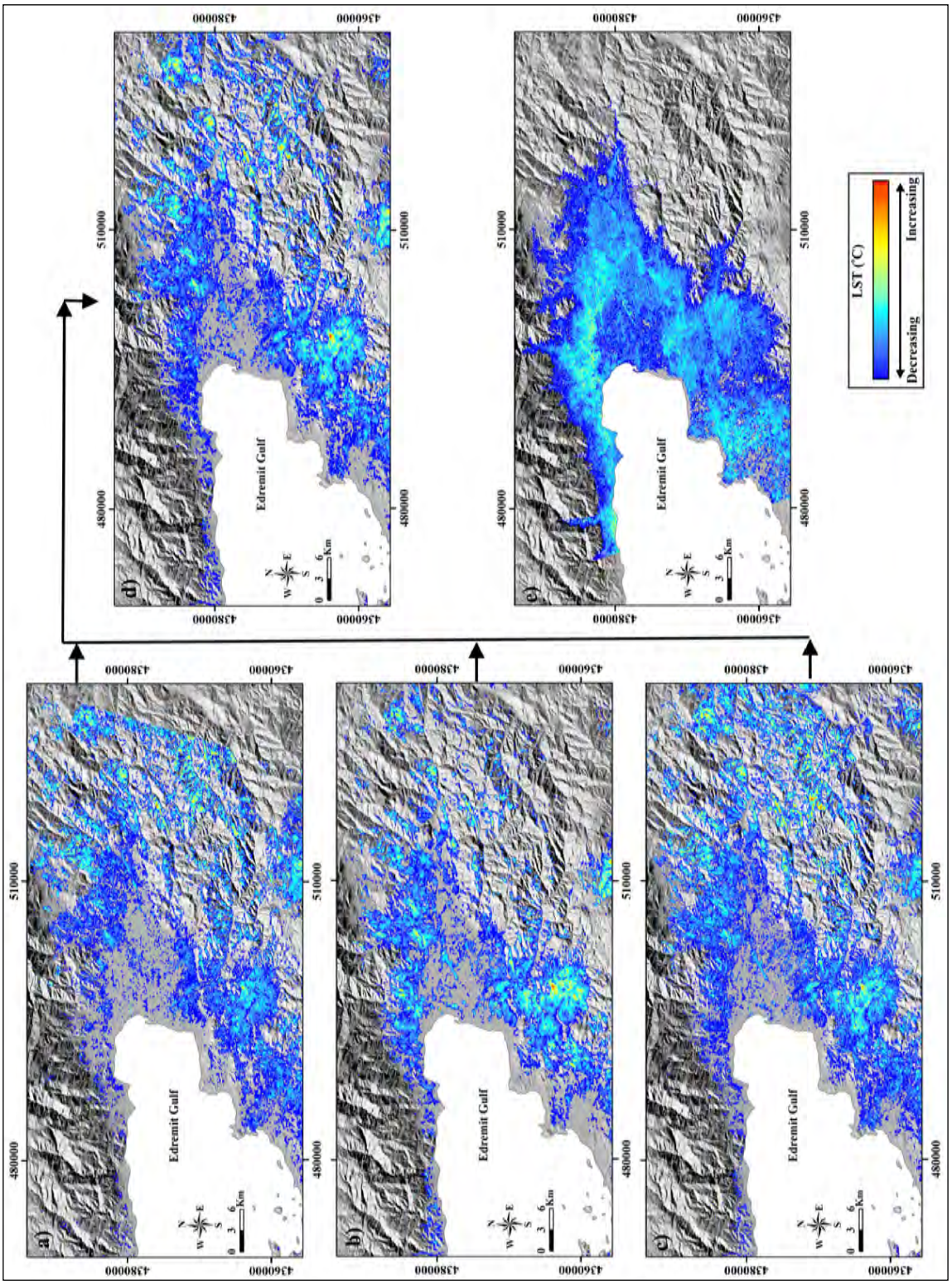

Figure 8- LST maps calculated from a) ASTER-daytime, b) Landsat 8 TIRS, c) Landsat 7 ETM+, d) average daytime and e) ASTER-nighttime (Approximately highest 10°C of temperatures values shown).

areas) for detailed studies in the early stages of geothermal exploration.

In the VNIR-SWIR region (0.4-2.5 μm wavelength), ASTER images have spectral bands corresponding to the diagnostic absorption features such as Fe^{+3}, Fe^{+2}, Al-OH, Fe-OH, Mg-OH, Si-OH and CO_3. Mineral and/or mineral groups can be determined using these descriptive absorption properties (Rowan and Mars, 2003; Rowan et al., 2003; Kalinowski and Oliver, 2004; Hewson et al., 2005). In order to define the anomaly areas of hydrothermal alteration in the Edremit basin, the VNIR-SWIR bands of the ASTER image were analyzed applying the band ratio technique. The bands in the VNIR-SWIR regions of the ASTER Level 1T image dated 02.11.2004 were combined and then the relevant part of the study area was obtained by cutting from the whole image. Afterwards, vegetation and water areas were masked and dark area subtraction (Lpath remove) was applied to image. With the band ratio analysis of the ASTER image, ironoxide/hydroxide minerals (hematite, goethite), Al-OH containing minerals such as clay minerals (illite, kaolinite vb.), alunite/kaolinite minerals, silica minerals (opal), Mg-OH minerals (chlorite, epidote) and $CaCO_3$ minerals (carbonate minerals) were mapped (Table 5 and Figure 9).

Table 5- Band ratio applied to ASTER image and mineral/mineral groups.

Mineral and/or minerals	Band Ratio
Ironoxide/hydroxide (hematite, goethite)	2/1
Al-OH-containing minerals (clay minerals)	4/6
Alunite/kaolinite minerals	4/5
Silica (opal)	4+5/6+7
Mg-OH -containing minerals (chloride, epidote) and $CaCO_3$ -containing minerals (carbonate minerals)	7+9/8

4.2.3. InSAR Analyses

Interferometric analyses (InSAR) were carried out in order to investigate the surface deformations such

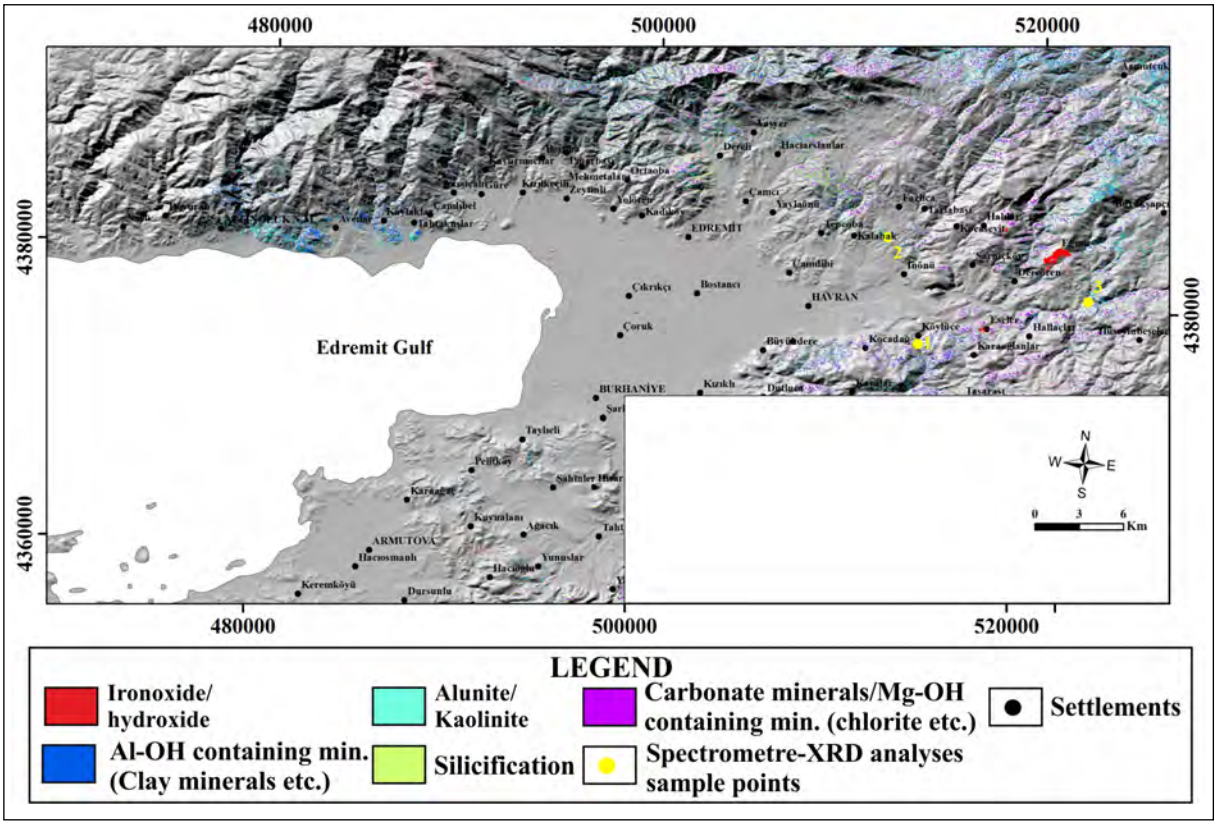

Figure 9- Hydrothermal alteration anomaly areas determined by ASTER band ratio analysis.

as subsidence, uplift etc. In this context, 19 ALOS Palsar-1 images were analyzed using SBAS method which is one of the Multi-temporal InSAR (MTInSAR) analysis techniques (Berardino et al., 2002). ALOS Palsar-1 images cover a time interval of 1518 days between the dates of 04.01.2007 and 15.01.2011 (Figure 10). By creating 132 interferometric pairs, ALOS Palsar-1 SBAS analysis was carried out.

As a result of ALOS Palsar-1 SBAS analysis, the amount of line of sight (LOS) surface deformations (mm) and the velocity rate (mm/year) were obtained. Results of analysis indicate that the LOS surface deformations (collapse-rise, etc.) are between about < -165 and >180 mm and the LOS velocity rates range from about < -26 to > 27 mm/year (Figure 11).

4.3. Water Chemistry and Isotopic Data

Major anion-cation and trace element concentrations of thermal and mineral waters sampled in the Edremit and Güre geothermal areas are given in Table 6. The analysis results were used to determine the chemical properties, reservoir temperatures, and mineral saturation of the waters. The results of isotope compositions ($\delta^{18}O$, δD and tritium) of the waters are presented in Table 7. The isotope results provide information on the water-rock interaction and the source of solutes in waters.

4.3.1. Geochemical Characteristics of Edremit and Güre Waters

The pH and temperature of the Edremit and Güre waters are 7.4-8.5 and 32-86°C, respectively. The measured electrical conductivity values are between 229-1855 µS/cm, and the total dissolved solid (TDS) contents range from 137 to 1341 mg/l.

The hydrogeochemical facies of the waters are defined by the dominant cation–anion pairs (concentrations in meq/l %). The Schoeller diagram shows that the thermal waters have the same origin and are mostly dominated by Na+K and SO_4 concentrations (Table 6 and Figure 12). However, cold waters (samples ES-4 and ES-5) are represented by Ca^{+2} and HCO_3^-. In the Piper diagram (Piper, 1944), the Edremit-Güre waters plot in two separate areas (Figure 13). The thermal waters fall into the $NaSO_4$ waters field, indicating a deep circulation and the cold-water samples plot into the field of $CaCO_3$ dominated waters.

Bor (B) concentration varies between 0.9-3 mg/l in thermal waters. B, due to its high solubility and volatility under high temperature, easily enters the composition of water. Tourmaline in igneous rocks is the source of boron. The presence of boron is an indication that water is interacting with granitic rocks. Brom (Br) is rare in geothermal waters. It is more common in seawater-fed or evaporitic waters. Br values in Edremit basin are quite low. Although arsenic is a mobile element, its solubility is low. As values in thermal waters in Edremit Field are quite low. It is thought that it is added to the composition of the water because of contact with the metal sulfides in the rocks through which the water passes.

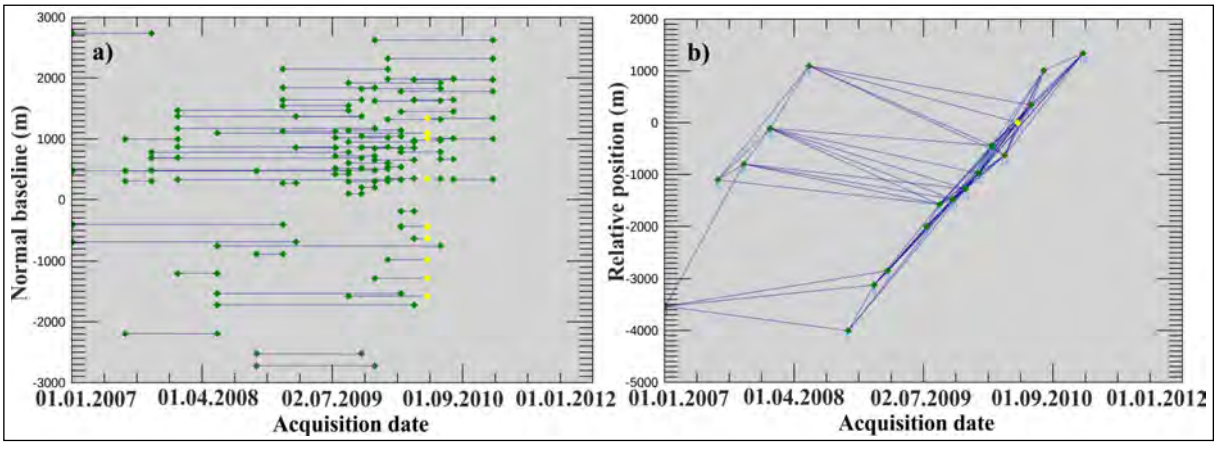

Figure 10- Plots of interferometric SAR image pairs versus time a) normal baseline and b) relative position graphs.

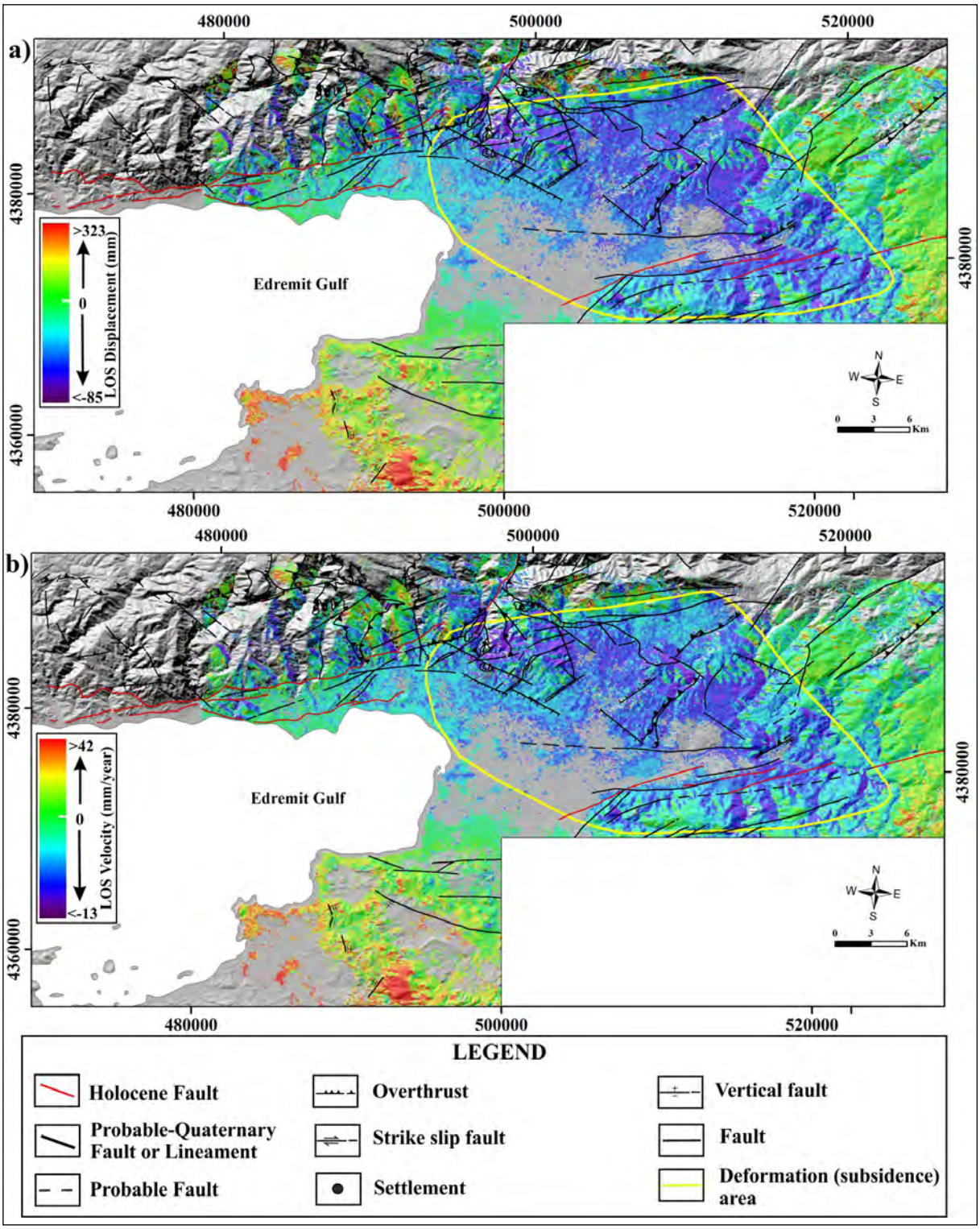

Figure 11- The result of ALOS Palsar-1 SBAS analysis a) LOS deformation (mm) amount, b) LOS velocity rates (mm/year) (faults and active faults: Duru et al., 2004; Duru et al., 2007*a, b*; Dönmez, 2013; Emre et al., 2011; faults determined during the field study).

Table 6- Results of chemical compositions of thermal and mineral waters from the study area.

Sample No	T* (ºC)	pH	EC µS/cm	Ca^{+2}	Mg^{+2}	Na^{+}	K^{+}	Cl^{-}	SO_4^{-2}	HCO_3^{-}	CO_3^{-2}	SiO_2	F^{-}	Br^{-}	B	As	Li	TDS	Water type (IAH)
ES-1	86	8.5	1211	23.7	<0.1	292	8.3	64.9	499	40.2	21.4	78.9	5.2	0.2	3	0.04	0.25	914	$Na+K-SO_4$
ES-2	32	7.4	1132	96.8	7.2	203	3.6	18.24	411	255	<10	33.17	1.7	0.2	0.9	<0.01	0.15	891	$Na+K-SO_4-HCO_3$
ES-3	32	8.1	1855	3.4	2.8	572	4.9	85	123	1127	44	32.9	1	0.2	1.5	0.01	0.18	1341	$Na+K-HCO_3-SO_4$
EDR-1[a]	60	8.2	945	23.8	0.6	276.3	5.9	59	506	61	<10	58.9	7.4	0.014	2.8	0.009	0.27	-	$Na+K-SO_4$
ED-3[b]	62	7.7	1060	25	0.2	193	3.4	48	360	54	-	32	-	-	1.6	-	-	-	$Na+K-SO_4$
EDJ-2[b]	58	7.6	1200	31	0.1	217	5.1	57	420	44	-	50	-	-	1.6	-	-	-	$Na+K-SO_4$
IGJ-2[c]	46.2	8.6	865.7	9.10	0.1	173	3.80	39	270	38.7	-	-	-	-	-	-	-	-	$Na+K-SO_4$
ES-4	15	8.1	229	44.1	8	4.8	<1	3.6	3.8	107	29.3	10.05	<0.1	<0.1	<0.1	<0.01	0.04	137	$Ca-Mg-HCO_3$
ES-5	19	7.4	449	73.8	8	32	1.3	20.7	6.4	326	<10	32.95	<0.1	<0.1	<0.1	<0.01	0.05	291	$Ca-Mg-HCO_3$

***** On-site (well-head and spring) measurements. Cation, anion and trace element concentrations are in mg/l. EC: Electric conductivity, TDS: Total dissolved solids (mg/l)

[a] EDR-1 is from taken Yalçın (2007), ED-3[b] and EDJ-2[b] are taken from Avşar et al. (2013), IGJ-2[c] is taken from Kaçar et al. (2017).

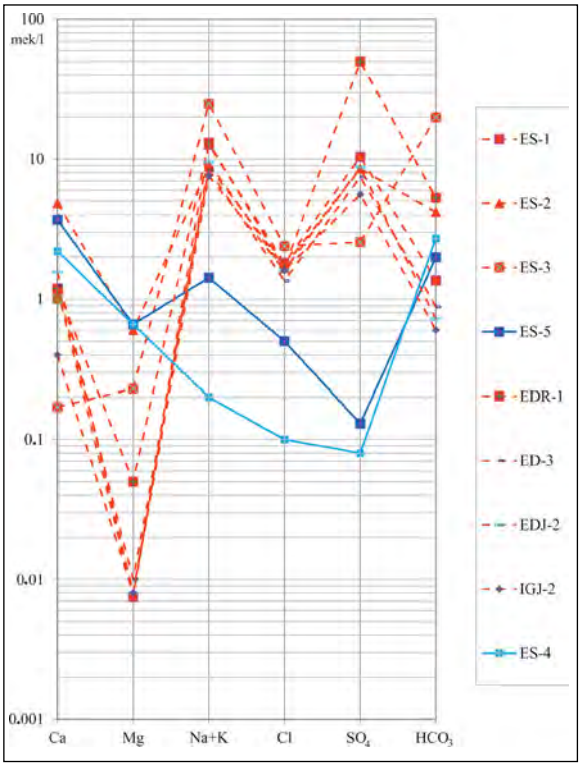

Figure 12- Semi-logarithmic Schoeller diagram for thermal (red dashed lines) and cold (blue lines) waters in Edremit and Güre areas. (Sample numbers refer to sample site numbers in Table 2 and Figure 5).

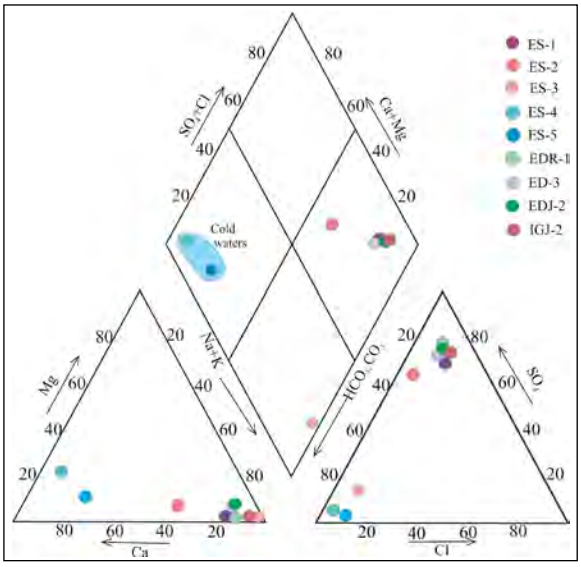

Figure 13- Piper diagram for thermal and cold waters in Edremit and Güre (Sample numbers refer to sample site numbers in Table 2 and Figure 5).

Table 7- Results for stable isotope (‰), tritium and Cl- for the Edremit-Güre waters.

Sample No	Temperature °C	Date of sampling	$\delta^{18}O$ (VSMOW)	δD (VSMOW)	Deuterium excess	^{3}H (TU)	Cl^- (mg/l)
ES-1	86	5.11.2019	-7.72	-47.04	14.7	0.46	64.9
ES-2	32	5.11.2019	-7.37	-43.71	15.3	5.84	61.3
ES-3	32	6.11.2019	-7.32	-43.91	14.7	1.11	82.1
ES-4	15	7.11.2019	-7.76	-41.64	20.4	2.97	3.6
ES-5	19	7.11.2019	-7.19	-41.71	15.8	1.4	20.7
EDR-1[a]	60	-	-7.26	-47.25	10.8	0	59
ED-3[b]	62	10.09.2008	-9.19	-52.19	21.3	-*	48

[a]: EDR-1 is from taken Yalçın (2007), [b]: ED-3 is from taken Avşar et al. (2013), *: This information is not available in the reference in question.

4.3.2. Isotope Geochemistry

The results of isotope analysis of water samples are given in Table 7. The values are presented in per mil (‰) deviations from the Vienna SMOW standard. In the $\delta^{18}O$–$\delta^{2}H$ graphic, isotope compositions of Edremit-Güre waters are plotted between the Marmara Meteoric Water Line (MMWL) ($\delta^{2}H=8\delta^{18}O+15$; Eisenlohr, 1995) and the Global Meteoric Water Line (GMWL) ($\delta^{2}H = 8\delta^{18}O + 10$; Craig, 1961). The $\delta^{18}O$ of thermal springs varies from –7.72 to –6.48‰ and from –7.76 to –5.87‰ for the cold waters. The δD values are in the range of –47.04 to –38.3‰7 for thermal waters and between –41.71 and –32.16‰ for cold waters (Figure 14). In general, $\delta^{18}O$–δD values of thermal waters are slightly lower than cold waters.

Much negative isotope values of thermal waters (enriched in light isotopes) indicate that they are recharged from higher altitudes than the cold waters (Figure 14). Accordingly, the waters might have negative isotope values on the Marmara meteoric water line and are not involved in a deep circulation, and cold surface waters may have mixed with these waters.

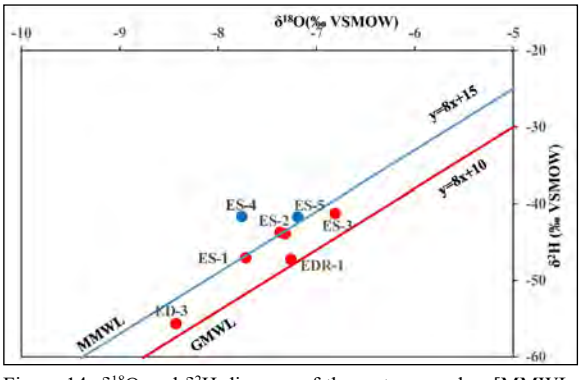

Figure 14- $\delta^{18}O$ and $\delta^{2}H$ diagram of the water samples. [MMWL: Marmara Meteoric Water Line (Eisenlohr, 1995); GMWL: Global Meteoric Water Line (Craig, 1961)]. Thermal waters are represented by red circles, while cold waters are represented by blue circles.

The deuterium excess of the samples calculated with the formula of $d= \delta D-8*\delta^{18}O$ varies between 14.7 and 21.3‰. The high values of deuterium excess indicate that waters in this region are recharged by marine precipitation. The sample ES-4 with the highest deuterium excess value is enriched in heavy isotope with respect to other samples and at the same time, it could be recharged from higher elevations and does not show any evaporation effect.

Tritium is an excellent tracer for water circulation. It is used for determining the relative age of groundwaters since it is radioactive (with half-life of 12.43 years) (Clark and Fritz, 1997). The concentration of tritium in meteoric waters is given in Tritium Unit (TU) (1 TU=1 atom $^{3}H/10^{18}$ atom H). The concentration of tritium in the atmosphere has changed by the nuclear tests. Atmospheric tritium concentration before 1963 was around 5 TU and it reached a maximum about 3000 TU in 1963 with tritium emitted into the atmosphere by nuclear tests (Mazor, 1991). According to these data, samples ES-1 and EDR-1 might be recharged by precipitation before 1963. The EDR sample has ^{3}H content of 0 TU, indicating a relatively deep circulation and a long residence time.

Tritium-Cl graph is very useful to examine the circulation depth of waters (Akıllı and Mutlu, 2018) (Figure 15). The low tritium value indicates that the waters are deeply circulated and have longer residence time underground. In addition, the tritium values of deep circulating waters are quite low and their chloride

content is high. Chloride is a widely used ion in the exploration and interpretation of geothermal systems. It directly characterizes geothermal water as it is not easily absorbed by other minerals once dissolved. This shows that thermal waters have longer residence time and their chemical composition is much more modified by the water-rock interaction (increasing chloride content). It is likely that sample ES-3 has a deeper circulation than other thermal water samples. The fact that the tritium content of the cold waters samples is higher than the geothermal waters (except for sample ES-2) indicates that these waters have a shallow circulation. The sample ES-2 was taken from a shallow well (64 m) drilled in alluvium. In terms of high tritiumm value and low chloride content, this sample suggests that there is a mixture of cold water with thermal water. The temperature of ES-2 sample is 32ºC. As seen in the Piper diagram (Figure 13), the ES-2 sample falls into a separate zone from other thermal waters. The high tritium and low chloride values of this sample might indicate a mixing with cold groundwater (Figure 15).

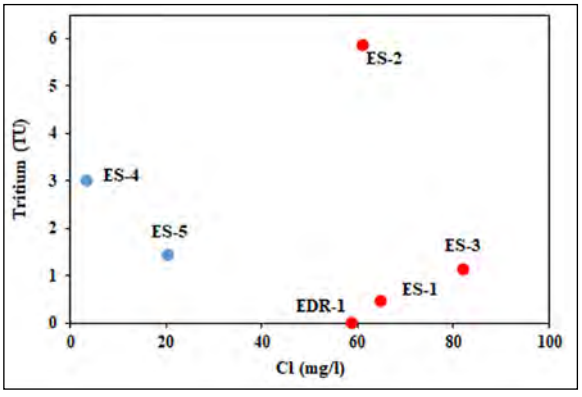

Figure 15- Tritium versus chloride diagram of water samples. Thermal waters are represented by red circles, while cold waters are represented by blue circles.

The relation between oxygen-18 and tritium is correlated with recharge elevation of the waters and their residence time in the aquifer. The residence time of waters increases as it approaches to the origin along the vertical axis of the graph. As seen in Figure 16, thermal water samples with low tritium value have a long residence time underground circulation, while cold waters with high tritium content have a shorter circulation. The sample ES -5 has a deeper circulation than ES-4 which is recharged from precipitation falling at higher elevations.

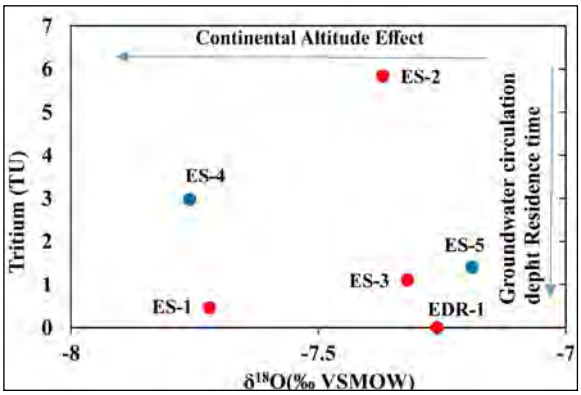

Figure 16- Plot of ^{3}H - $\delta^{18}O$ diagram of the water samples. Thermal waters are represented by red circles, while cold waters are represented by blue circles.

4.3.3. Geothermometer Applications

To determine the reservoir temperatures of the Edremit-Güre thermal waters, various geothermometers and mineral equilibrium models were used. First, we considered the maturity index (MI) to decide the applicability of Na-K geothermometers to the samples. The maturation index of the thermal waters, except for ES-2 sample, is found >2 and therefore, both cation and silica geothermometers were calculated (Figure 17). For samples with a maturation index less than 2, the application of cation geothermometers may yield erroneous results and therefore, silica geothermometers were preferred, which are based on mineral solubility and give better results at low temperatures (Akıllı and Mutlu, 2018) (Table 8). In Figure 17, sample ES-2 is close to the

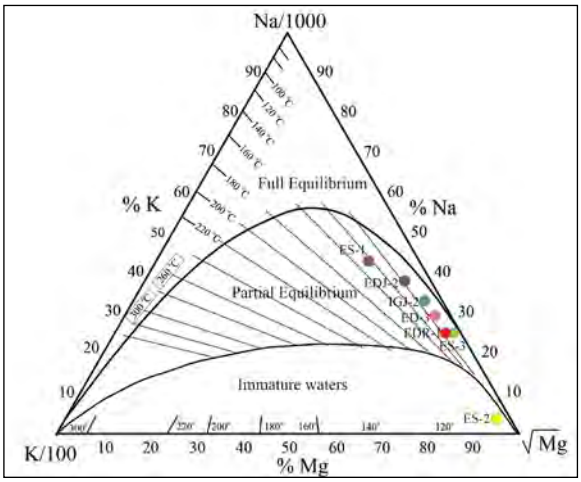

Figure 17- Na-K-Mg equilibrium diagram of Giggenbach (1988).

Table 8- Geothermometer estimates for Edremit thermal waters.

Sample No	T (ºC)	Quartz (Fournier and Potter, 1982)	Quartz (no steam loss) (Fournier, 1973)	Chalcedony (no steam loss, Fournier, 1977)	Chalcedony (no steam loss, Arnorsson et al., 1983)	K-Mg (Giggenbach, 1988)	Na-K (Fournier, 1979)	Na-K (Giggenbach et al., 1983)
ES-1	86	124	124	96	95	89	126	146
ES-2	32	84	83	52	55	-	-	-
ES-3	32	83	82	51	53	64	61	83
EDR-1	60	109	109	79	80	77	104	125
ED-3	62	83	82	51	53	65	97	117
EDJ-2	58	102	102	72	73	77	117	137

Mg corner and plots into the "immature waters" field. Only quartz and chalcedony geothermometers were applied to this sample. Other thermal water samples are plotted in the "partially equilibrated waters" field. For these waters, both cation and silica geothermometers were applied.

The temperatures of 82 and 124ºC were calculated by quartz (no steam loss) geothermometers of Fournier (1973) and Fournier and Potter (1982) (Table 8). For the chalcedony geothermometer, the equations of Fournier (1977) and Arnorsson et al (1983) were used. The reservoir temperatures of waters estimated by these geothermometers are 51-96ºC and 53-95ºC, respectively, which yielded very close values. The cation geothermometers are based on the distribution of alkaline elements between solid and liquid phases. The cation geothermometers are suitable for high-temperature waters where reservoir temperatures are > 180 ºC and may give incorrect results for low- temperature waters. The reservoir temperatures estimated with cation geothermometers vary between 61 and 137 ºC (Table 8). The cation geothermometers yielded different reservoir temperature values due to the interaction of the water with the host rocks and the mixing with cold water during the rise to the surface. Considering that silica saturation is controlled by chalcedony rather than quartz at temperatures below 180ºC (Fournier, 1991), the reservoir temperatures calculated by the chalcedony geothermometer are thought to be more realistic (Akıllı and Mutlu, 2018).

4.4. GIS Application

The geological features of the basin were investigated by applying five groups of studies. These are; 1) 1/100.000-1/25.000 scaled geological maps from the MTA archives, 2) lithological units in the basin with 1/100.000 scaled geological maps and literature data (MTA reports, articles, etc.), 3) stratigraphic succession of the basin, 4) determination of rocks that can be heaters and reservoirs in a geothermal system on the stratigraphic column section and 5) all these data is used to construct a conceptual model of the basin using the GIS analyses combined with thermal and alteration remote sensing results (Figure 18). The outputs are displayed on the SRTM-relief map for a final evaluation. Tectonic structures, kinematic analyses, geological units and stratigraphic sequence of the study area are the key components for such studies. Within the scope of hydrogeological studies, the samples collected from the thermal and cold waters in the area were evaluated using water chemistry, isotope analysis and various diagrams. As a result of these studies, data on chemical compositions of waters, circulation depths of thermal waters (shallow or deep), reservoir temperatures, types of reservoir rocks and recharge elevations were obtained. This information forms the hydrogeological spatial data layers in the study. The above-mentioned spatial data layers are composed of four main groups that are remote sensing, tectonics, geological and hydrogeological studies.

For the remote sensing studies, three groups of spatial data were produced. The first is the daytime average and the ASTER nighttime LST maps. The daytime average LST map was prepared taking the arithmetic average of the maximum 10ºC temperature values of the ASTER daytime, Landsat 8 TIRS and Lansdat 7 ETM+ maps to increase the accuracy. The second data layer is the band ratio analysis results of ASTER Level 1T satellite images to determine the hydrothermal alteration zones and minerals associated with geothermal systems. The SBAS analysis of ALOS Palsar-1 SAR images within the scope of remote sensing studies, the LOS displacement map of

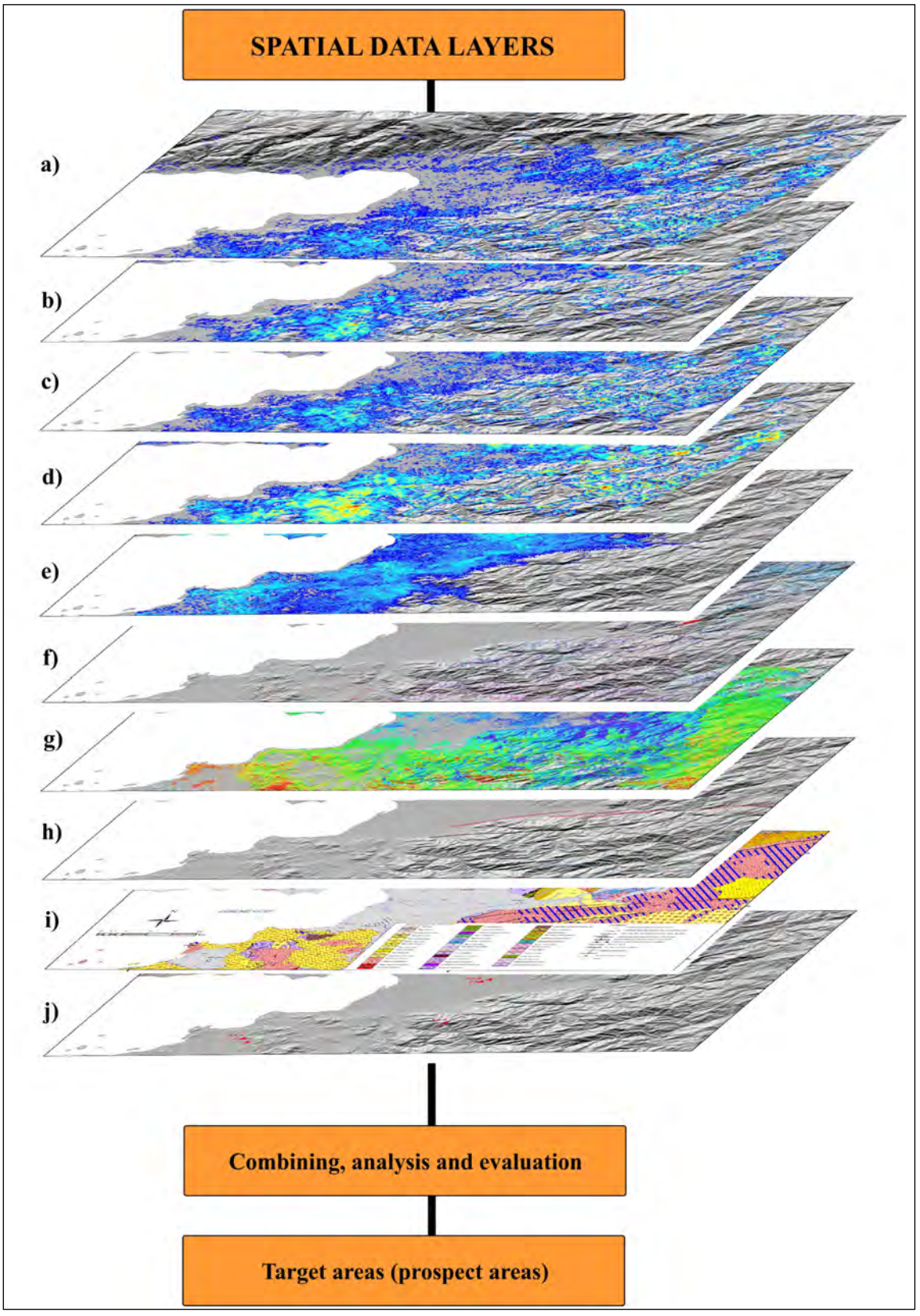

Figure 18- Spatial data layers and flow chart of GIS studies: a) ASTER-daytime LST, b) Landsat 8 TIRS LST, c) Landsat 7 ETM+ LST, d) Daytime-average LST, e) ASTER-nighttime LST, f) Hydrothermal alteration, g) ALOS Palsar-1 SBAS-deformation, h) Tectonic framework and kinematic analysis, i) Geology, j) Hydrogeology.

the surface deformations (subsidence, uplift, etc.) was prepared. All these results represent the combinations and assessment of the layers using the geographical information system (GIS), which is recently widely used in many disciplines for viewing, combining, organizing, querying, analyzing, and evaluating, spatial data layers (Bonham-Carter, 1994; Carranza, 2009). Finally, their combination, provides an, opportunity to define probable target areas (prospect areas) that might be important in terms of geothermal energy (Figure 19).

5. Discussion

During a geothermal energy exploration and evaluation study, several stages are progressed from initial exploration to production (Van der Meer et al., 2014). In this research, we carried out a pilot study in the Edremit Basin, Balıkesir, to evaluate the geothermal potential and to determine possible target areas with the use of a number of data, which include structural controls, hydrogeological features, and satellite image analyses.

Ten different layers were used to describe the possible target fields in the basin (Figure 19). Determining potential target areas (prospects) in terms of geothermal energy might provide significant gains in cost, labor and time. For this reason, we compared our results to known geothermal resources. Additionally, a fieldwork was carried out to check the reliability of thermal anomalies. For example, solar panels or man-made structures such as factory reflect huge thermal anomalies and mislead the data.

Surface temperature values calculated from ASTER-nighttime/daytime, Landsat 8 TIRS and Landsat 7 ETM+ thermal bands were validated using geothermal resources known in the region. Sample ES-3 located at northeast of Armutova has a temperature of 33ºC and reservoir temperature of this sample estimated by chalcedony geothermometer of is 53 ºC. In the average daytime LST map (without reclassification), the highest temperature was estimated 37 ºC. In this map, temperature values around the thermal springs are found in about the range of 30 to 32 ºC. In the average daytime LST map, that was obtained using highest temperature value of nearly 10 ºC and reclassification, we obtained temperatures of 4-5 ºC (the highest relative value is 12 ºC). Samples ED-3, ES-2 and EDJ-2 that are associated with E-W trending fault at the south of Edremit have temperatures of 62, 32 and 58 ºC, respectively. Reservoir temperatures of these samples estimated by chalcedony geothermometer are 53, 55 and 73ºC. In the average daytime LST map (without reclassification), temperature around the samples are estimated approximately 29-32ºC. In the average daytime reclassified LST map, temperatures values of about 4-7 ºC were obtained. ES-1 and EDR-1 samples associated with E-W trending active fault at the south of Güre have temperatures of 86 and 60ºC. Chalcedony reservoir temperatures of these samples are 95 and 80ºC. In the average daytime LST map (without reclassification) temperatures are estimated 28-30 ºC around these samples and in the average daytime reclassified LST map, temperatures are relatively found approximately 4-5 ºC.

Each of the areas that were selected for confirmation are represented by higher LST values with respect to surrounding parts. It is noticeable that high LST values are consistent with faults and fault systems that trend in E-W direction parallel to the main strike of NAFZ. The use of thermal satellite images for the correct identification of geothermal anomalies requires the integration of geological and tectonic data. The combination of all data considerably increases the determination of reliable information. According to the findings of the kinematic analysis, the expansion direction of the basin is in the N-S direction. As a result, E-W trending faults and their surrounding areas can be considered as potential areas for geothermal exploration and evaluation studies in the basin.

It is critical for the success of geothermal energy exploration studies to identify hydrothermal alteration minerals and/or mineral groups as surface indicators of geothermal activity. According to the results of the band ratio analysis of the ASTER images, in around geothermal springs in the west of the Güre, extensive argillization, silicification, and alunite/kaolinite anomaly areas were observed on granodiorite porphyry (PgoNkp) and Oligo-Miocene granodiorites (PgoNg), which are considered to be reservoir rocks (Figure 20). In the north of Edremit, Oligo-Miocene granodiorite (PgoNg) has been exposed to widespread hydrothermal alteration. ASTER band ratio analysis revealed argillization, silicification, and alunite/kaolinite anomaly areas on this unit.

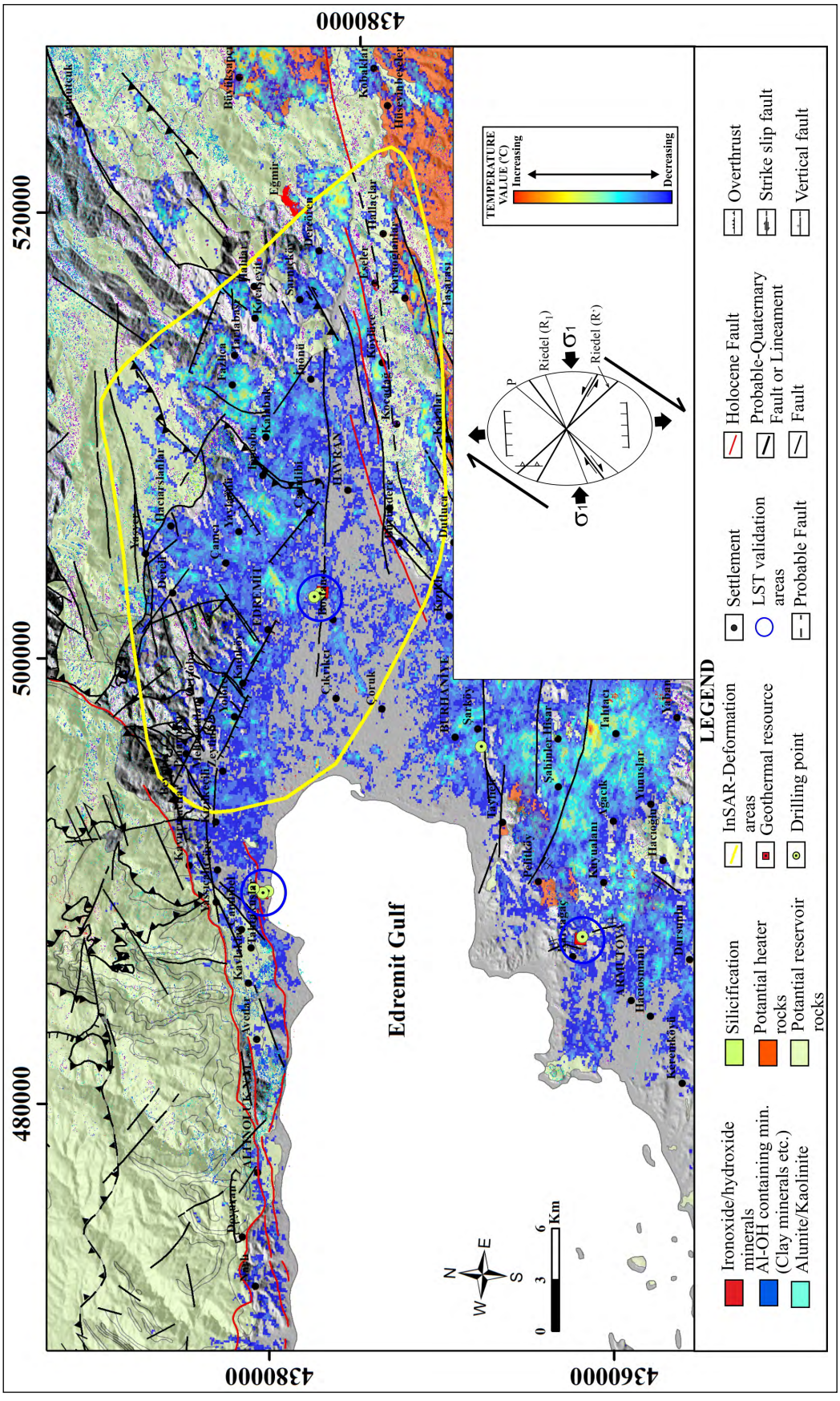

Figure 19- Final output map of the study area. Blue circles indicate the high possibility areas and recent geothermal resources (Faults and active faults: Duru et al., 2004; Duru et al., 2007*a*, *b*; Dönmez, 2013; Emre et al., 2011; faults determined during the field study).

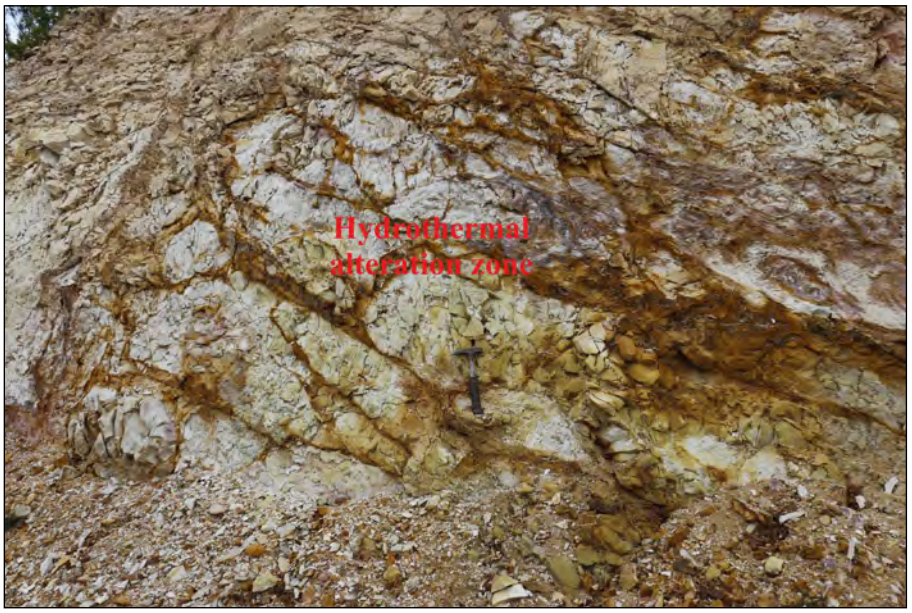

Figure 20- A view from the hydrothermally altered Granodiorite porphyry units in east of Havran.

In the Oligo-Miocene granodiorite (PgoNg) to the north of Edremit, extensive argillization, silicification, and alunite/kaolinite anomaly areas emerged. In addition, widespread argillization, silicification, and alunite-kaolinite anomaly areas were observed on the Yurekli Dacite (Nmy) and Bozdivlit volcanite (Nmb) which are considered as the heat source of geothermal resources in the northeast and southeast part of Armutova. In the field studies, samples were collected from these alteration areas. The alunite, illite, and montmorillonite minerals were identified in the spectral analysis of the samples (Figure 21). Ironoxide and hydroxide minerals are highly prevalent that can be related to hydrothermal and surface meteoric waters. As a result, all ironoxide and hydroxide mineral anomalies observed in ASTER image analysis should not be considered to be of a hydrothermal origin.

In the area between the faults bordering the south and north of the Edremit basin, subsidence has appeared as a distinctive feature of the ALOS Palsar-1 SBAS analysis results. This area is situated on the downward block of faults that border the north and south parts of the basin. Surface deformations observed in ALOS Palsar-1 SBAS analyses could have been caused by human activity, lithological features, or erosion in some areas. The subsidence event detected in the basin by the ALOS Palsar-1 SBAS analysis can be interpreted as an indicator of crustal thinning in pull-apart basins. Crustal thinning may contribute more to heat transport and conduction through tectonic structures in pull-apart basins than in other regions.

In the early stages of geothermal exploration and evaluation studies, satellite data analysis such as LST, the determination of hydrothermal alteration anomaly areas and mienrals is effective and useful approach to determine target prospect areas. The results of the studies have demonstrated that, in order to determine the prospect areas in pull-apart basins with greater accuracy and success, the LST results, in particular, should be evaluated considering the compression-extension directions in the basin.

6. Conclusions

Remote sensing, geological, tectonic, and hydrogeological research was carried out in the Edremit (Balıkesir) Basin in order to reveal geothermal energy potential and identify prospect areas for detailed surveys (drilling, geophysics, gas measurements, detail mapping, etc.). The findings of these studies were evaluated using GIS tools.

High temperature values were obtained in the LST maps around known geothermal resources in the basin, and they were found to be compatible. When the results of the study are evaluated considering the tectonic

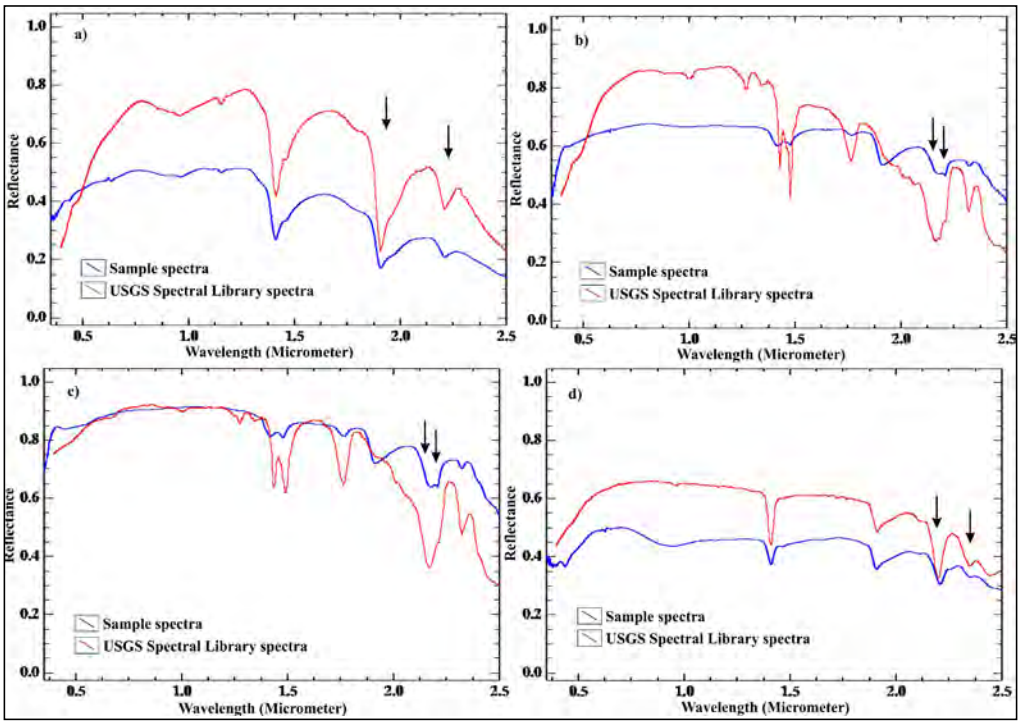

Figure 21- Spectra of hydrothermal alteration samples collected from east of Havran and mineral spectra in the USGS Spectral Library (USGS, 2007): a) Montmorillonite (sample no 1), b) and c) Alunite (sample no 2), c) illite (example no. 3) (sample locations are given in Figure 10)

structures and the compression-extension aspects of the basin, it is seen that the basin has a potential in terms of geothermal energy exploration. It is seen that there are many prospect areas that can be favorable for detailed studies within the basin. The applied approach and method were found to be effective based on the validation results of LST values computed from the daytime and nighttime thermal bands (ASTER-daytime, Landsat 8 TIRS, Landsat 7 ETM+ and ASTER-nighttime). The study also demonstrated that satellite data analyses (LST, hydrothermal alteration, MT-InSAR, etc.) achieve accurate, successful, and efficient results for identifying prospect areas in the preliminary phase of geothermal exploration and evaluation studies.

Acknowledgement

This study was financially supported by the General Directorate of Mineral Research and Exploration. The authors are grateful to anonymous referees for their critical comments that improved the manuscript. Project name is “Kuzey Anadolu Fay Sistemi Ve Doğu Anadolu Fay Sistemi Boyunca Gelişmiş Havzaların Jeotermal Enerji Potansiyellerinin Uzaktan Algılama ve Coğrafi Bilgi Sistemleri (CBS) Yöntemleri ile İncelenmesi: 3- Edremit (Balıkesir) Havzası”.

References

Akıllı, H., Mutlu, H. 2018. Polatlı ve Haymana (Ankara) sıcak sularının kökenine yönelik kimyasal ve izotopik sınırlamalar. Yerbilimleri 39 (1), 41-64.

Aktuğ, B., Nocquet, J. M., Cingoez, A., Parsons, B., Erkan, Y., England, P., Lenk, O., Guerdal, M.A., Kılıçoğlu, A., Akdeniz, H., Tekgüzel, A. 2009. Deformation of western Turkey from a combination of permanent and campaign GPS data: Limits to block-like behavior. Journal of Geophysical Research-Solid Earth, 114, B10404, doi:10.1029/2008JB006000.

Allis, R.G., Nash, G.D., Johnson, S.D. 1999. Conversion of thermal infrared surveys to heat flow: comparisons from Dixie Valley, Nevada, and Wairakei, NewZealand. Geothermal Resources Council – Transactions 23, 499–504.

Altunkaynak, Ş., Genç, S. 2008. Petrogenesis and time-progressive evolution of the Cenozoic continental volcanism in the Biga Peninsula, NW Anatolia (Turkey). Lithos 102, 316–340.

Angelier, J. 1979. Determination of the mean principal directions of stresses for a given fault population. Tectonophysics 56, T17-T26.

Angelier, J. 1984. Tectonic analysis of fault slip data sets. Journal of Geophysical Research 89, 5835-5848.

Arnorsson, S., Gunnlaugsson, E., Svavarsson, H. 1983. The Chemistry of Geothermal Waters in Iceland III, Chemical Geothermometry in Geothermal Investigations. Geochimica et Cosmochimica Acta 47, 567-577.

Artis, D.A., Carnahan, W.H. 1982. Survey of emissivity variability in thermography of urban areas. Remote Sensing of Environment 12(4), 313–329.

Avşar, Ö. 2011. Geochemical Evaluation and Conceptual Modeling of Edremit Geothermal Field. A Thesis Submitted to the Graduate School of Natural and Applied Sciences of Middle East Technical University, Ankara.

Avşar, Ö., Güleç, N., Parlaktuna, M. 2013. Hydrogeochemical characterization and conceptual modeling of the Edremit geothermal field (NW Turkey). Journal of Volcanology and Geothermal Research 262, 68-79.

Ayenew, T. 2001. Surface kinetic temperature mapping using satellite spectral data in Central Main Ethiopian Rift and adjacent highlands. Ethiopian Journal of Science 24, 51–68.

Aygül, M., Topuz, G., Okay, İ. A., Satır, M., Meyer, H.P. 2012. The kemer metamorphic complex (NW Turkey): A subducted continental margin of the Sakarya Zone. Turkish Journal of Earth Sciences 21, 19–35.

Barsi, J.A., Barker, J.L., Schott, J.R. 2003. An Atmospheric Correction Parameter Calculator for a Single Thermal Band Earth-Sensing Instrument. IGARSS03, 21-25 July 2003, Centre de Congres Pierre Baudis, Toulouse, France.

Barsi, J.A., Schott, J.R., Palluconi, F.D., Hook, S.J. 2005. Tool for Single Thermal Band Instruments. Earth Observing Systems X, Proc. SPIE 5882, August 2005, San Diego, CA.

Beccaletto, L. 2003. Geology, correlations, and geodynamic evolution of the Biga Peninsula (NW Turkey). Géologie appliquée. Université de Lausanne, Français.

Berardino, P., Fornaro, G., Lanari, R., Sansosti, E. 2002. A new algorithm for surface deformation monitoring based on small baseline differential SAR interferograms. IEEE Transactions on Geoscience and Remote Sensing 40/11, 2375–2383.

Bingöl, E. 1969. Kazdağ Masifinin merkezi ve Güneydoğu kesiminin jeolojisi. Bulletin of the Mineral Research and Exploration 72, 110-123.

Bingöl, E. 1971. Fiziksel yaş tayini metodlarını sınıflama denemesi ve Rb-Sr ve K-Ar metodlarının Kazdağ'da bir uygulaması. Türkiye Jeoloji Kurumu Bülteni 14, 1-16.

Bingöl, E., Delaloye, M., Ataman, G. 1982. Granitic intrusion in Western Anatolia; a contribution to the geodynamic study of this area. Eclo- Geol. Helv. 75/2, 437-446.

Bingöl, E., Delaloye, M., Pişkin, A., Genç, Ş. 1992. Significance of the granitoids of Eastern and Southern Marmara within the framework of the regional geotectonic evolution: Abstract of the Şnterna. Symp. Geol. Black Sea Region, Maden Tetkik ve Arama Genel Müdürlüğü.

Bonham-Carter, G.F. 1994. Geographic Information Systems for Geoscientists: Modelling with GIS. Pergamon: Elsevier Science Ltd Press.

Bozkurt, E., Mittwede, S.K. 2001. Introduction to the geology of Turkey - a synthesis. International Geology Review 43, 578–594.

Boztepe Güney, A., Yılmaz, Y., Demirbağ, E., Ecevitoğlu, B., Arzuman, S., Kuşçu, I. 2001. Reflection seismic study across the continental shelf of Baba Burnu promontory of Biga Peninsula, northwest Turkey. Marine Geology 176(1–4), 75–85.

Braddock, M., Biggs, J., Watson, I. M., Hutchison, W., Pyle, D. M., Mather, T. A. 2017. Satellite observations of fumarole activity at Aluto volcano, Ethiopia: Implications for geothermal monitoring and volcanic hazard. Journal of Volcanology and Geothermal Research 341, 10.1016/j.jvolgeores.2017.05.006.

Bulut, M., Purtul, E., Destur, M., Yılmaz, B.E. 2018. Karaağaç (Gömeç-Balıkesir) Ar:10/0003 Nolu Jeotermal Kaynak Arama Ruhsat Sahası Jeotermal Etüt (Jeoloji-Jeofizik) ve BGK-2011/9 jeotermal Araştırma Sondajı Kuyu Bitirme Raporu. General Directorate Mineral Research and Exploration Report No: 13716, Ankara (unpublished).

Calderon-Chaparro, R., Vargas-Cuervo, G. 2019. Determination of Hydrothermal Prospects in Paipa Geothermal Region (Boyacá, Colombia) Using Remote Sensing and Field Data. Earth Sciences Research Journal 23, 265-282. 10.15446/esrj.v23n4.77810.

Calvin, W.M., Littlefield, E.F., Kratt, C. 2015. Remote sensing of geothermal-related minerals for resource exploration in Nevada. Geothermics 53, 517-526.

Calvin, W., Pace, E. 2016. Mapping alteration in geothermal drill core using a field portable spectroradiometer. Geothermics 61. 10.1016/j.geothermics.2016.01.005.

Carranza, E.J.M. 2009. Geochemical anomaly and mineral prospectivity mapping in GIS, Handbook of Exploration and Environmental Geochemistry. Amsterdam: Elsevier 11, 351.

Chan, H.P., Chang, C. P. 2018. Exploring and monitoring geothermal and volcanic activity using Satellite Thermal Infrared data in TVG, Taiwan. Terrestrial, Atmospheric and Oceanic Sciences 29, 387-404. 10.3319/TAO.2018.01.22.01.

Chan, H. P., Chang, C. P., Dao, P. 2018. Geothermal Anomaly Mapping Using Landsat ETM+ Data in Ilan Plain, Northeastern Taiwan. Pure and Applied Geophysics 175. 10.1007/s00024-017-1690-z.

Clark, I., Fritz, P. 1997. Environmental isotopes in hydrogeology. Lewis Publishers, New York, 328.

Craig, H. 1961. Isotopic variations in meteoric waters. Science 133, 1833-1834.

Didik, S., Ölmez, E., Güner, A., Yıldırım, N. 1994. Balıkesir Edremit Güre G1 ve G2 Sıcak Su Sondajları Kuyu Bitirme Raporu. Maden Tetkik ve Arama Genel Müdürlüğü, Rapor No: 9837, Ankara (unpublished).

Dilemre, A., Gökalp, Y., Hakyol, S., Sarp, S., Orakçı, A. 2006. Balıkesir İli Jeotermal Kaynakları Değerlendirme Raporu. Maden Tetkik ve Arama Genel Müdürlüğü, Rapor No: 10858, Ankara (unpublished).

Dönmez. M. 2013. 1:100.000 Ölçekli Türkiye Jeoloji Haritaları, No:193 Ayvalık-J17 Paftası. Maden Tetkik ve Arama Genel Müdürlüğü, Ankara.

Dönmez, M., Akçay, A.E., Genç, Ş.C., Acar, Ş. 2005. Biga Yarımadası'nda Orta-Üst Eosen volkanizması ve denizel ignimbiritler. Bulletin of the Mineral Research and Exploration 131, 49-61.

Duru, M., Pehlivan, Ş., Şentürk, Y., Yavaş, F., Kar, H. 2004. New results on the lithostratigrapy of the Kazdağ Massif in nortwest Turkey. Turkish Journal of Earth Sciences "A special issue commemorating, Okan Tekeli", 177-186.

Duru, M., Pehlivan, Ş., Ilgar, A., Dönmez, M., Akçay, A.E. 2007*a*. 1:100.000 Ölçekli Türkiye Jeoloji Haritaları, No:98 Ayvalık-İ17 Paftası. Maden Tetkik ve Arama Genel Müdürlüğü, Ankara.

Duru, M., Pehlivan, Ş., Ilgar, A., Dönmez, M., Akçay, A.E. 2007*b*. 1:100.000 Ölçekli Türkiye Jeoloji Haritaları, No:97 Balıkesir-İ18 Paftası. Maden Tetkik ve Arama Genel Müdürlüğü, Ankara.

Eisenlohr, T. 1995. Die Thermalwässer der Armutlu-Halbinsel (NW Türkei) und deren Beziehung zu Geologie und aktiver Tektonik. Dissertation, ETH Zurich No: 11340, 165.

Emre, Ö., Duman, T. Y., Özalp, S. 2011. 1:250.000 Ölçekli Türkiye Diri Fay Haritası Serisi, Ayvalık (NJ 35-2) Paftası, Seri No:2, Balıkesir (NJ 35-3) Paftası, Seri No:4, Maden Tetkik ve Arama Genel Müdürlüğü, Ankara-Türkiye.

Erzenoğlu, Z., 1985. Balıkesir Edremit Güre (Demet)-1 sıcaksu sondajı kuyu bitirme raporu. Maden Tetkik ve Arama Genel Müdürlüğü Report, No. 7881 (in Turkish), Ankara (unpublished).

Faulds, J.E., Coolbaugh, M.F., Vice, G.S., Edwards, M.L. 2006. Characterizing Structural Controls of Geothermal Fields in the Northwestern Great Basin: A Progress Report. Geothermal Resources Council Transactions 30, 69–76.

Fournier, R.O. 1973. Silica in Thermal Waters: Laboratory and Field Investigations. Proceedings of the International Symposium on Hydrogeochemsitry and Biochemistry, Tokyo, Vol.1, Clark Co., Washington D.C. 122-139.

Fournier, R.O. 1977. Chemical Geothermometers and Mixing Models for Geothermal Systems. Geothermics 5, 41-50.

Fournier, R.O. 1979. A Revised Equation for the Na/K Geothermometer, Geoth. Res. Council. Transactions 3, 221-224.

Fournier, R.O. 1991. Water geothermometers applied to geothermal energy. In: D'Amore, F. (coordinator), Application of Geochemistry in Geothermal Reservoir Development. UNITAR/UNDP publication, Rome, 37-69.

Fournier, R.O., Potter, R.W. 1982. A Revised and Expanded Silica (Quartz) Geothermometer. Geoth. Res. Council Bull. 11-10, 3-12.

Genç, Ş.C., Dönmez, M., Akçay, A.E., Altunkaynak, Ş., Eyüpoğlu, M., Ilgar, Y. 2012. Biga Yarımadası

Tersiyer volkanizmasının stratigrafik, petrografik ve kimyasal özellikleri. In: Yüzer, E., Tunay, G. (Eds.), Biga Yarımadasının Genel ve Ekonomik Jeolojisi. Bulletin of the Mineral Research and Exploration 28, 122–162.

Gessner, K., Gallardo, L. A., Markwitz, V., Ring, U., Thomson, S. N. 2013. What caused the denudation of the Menderes Massif: Review of crustal evolution, lithosphere structure, and dynamic topography in southwest Turkey. Gondwana Research 24(1), 243-274.

Gillespie, A. R., Rokugawa, S., Matsunaga, T., Cothern, J. S, Hook, S., Kahle, A. B. 1998. A Temperature and Emissivity Separation algorithm for Advanced Spaceborne Thermal Emission and Reflection radiometer ASTER images. IEEE Transactions on Geoscience and Remote Sensing 36, 1113–1126.

Giggenbach, W.F. 1988. Geothermal Solute Equilibria, Derivation of Na-K-Mg-Ca Geoindicators, Geochim. Cosmochim. Acta 52, 2749-2765.

Giggenbach, W.F., Gonfiantini, R., Jangi, B.L., Truesdell, A.H. 1983. Isotopic and Chemical Composition of Parbatia Valley Geothermal Discharges, NWHimalaya, India. Geothermics 12, 199-222.

Giordano, G., Pinton, A., Cianfarra, P., Baez, W., Chiodi, A., Viramonte, J., Norini, G., Groppelli, G. 2013. Structural control on geothermal circulation in the Cerro Tuzgle-Tocomar geothermal volcanic area (Puna Plateau, Argentina). Journal of Volcanology and Geothermal Research 249, 77–94.

Gutierrez, F., Lemus, M., Parada, M., Benavente, O., Aguilera, F. 2012. Contribution of ground surface altitude difference to thermal anomaly detection using satellite images: Application to volcanic/geothermal complexes in the Andes of Central Chile. Journal of Volcanology and Geothermal Research 237-238, 69-80.

Güner, A., Didik, S., Ölmez, E., Yıldırım, N. 1994. Balıkesir-Edremit-Güre (G-1 ve G-2) sondajları kuyu bitirme raporu. Maden Tetkik ve Arama Genel Müdürlüğü Derleme Rapor No: 9837, 16, Ankara (unpublished).

Gürer, Ö. F., Sangu, E., Özburan, M., Gürbüz, A., Gürer, A., Sinir, H. 2016. Plio-Quaternary kinematic development and paleostress pattern of the Edremit Basin, western Turkey. Tectonophysics 679, 199–210.

Gürer, Ö. F. 2023. A new look at the origin of N-S trending young basins of western Anatolia. Bulletin of the Mineral Research and Exploration 170, 117-146.

Haselwimmer, C.E., Prakash, A. 2013. Thermal Infrared Remote Sensing of Geothermal Systems. In: Kuenzer, C., Dech, S. (Eds.), Thermal Remote Sensing: Sensors, Methods, and Applications 453–473.

Hewson, R.D., Cudahy, T.J., Mizuhiko, S., Ueda, K. and Mauger, A.J., 2005. Seamless geological map generation using ASTER in the Broken Hill-Curnamona province of Australia. Remote Sensing of Environment, 99, 159-172.

Hewson, R., Robson, D., Carlton, A., Gilmore, P. 2017. Geological application of ASTER remote sensing within sparsely outcropping terrain, Central New South Wales, Australia. Cogent Geoscience 3, 10.1080/23312041.2017.1319259.

Hook, S., Abbott, E., Grove, C., Kahle, A., Palluconi, F. 1999. Multispectral thermal infrared data in geological studies. In: Rencz, A.N., Ryerson, R.A. (Eds.), Manual of Remote Sensing, 3rd Ed. Remote Sensing for the Earth Sciences 3. Wiley 59–110.

Hulley, G., Hughes, C., Hook, S. 2012. Quantifying uncertainties in land surface temperature and emissivity retrievals from ASTER and MODIS thermal infrared data. Journal of Geophysical Research (Atmospheres), 117, 23113. 10.1029/2012JD018506

Ilgar, A., Demirci-Sezen, E., Demirci, Ö. 2012. Biga Yarımadası Tersiyer İstifinin Stratigrafisi ve sedimantolojisi. In: Yüzer, E., Tunay, G. (Eds.), Biga Yarımadasının Genel ve Ekonomik Jeolojisi. MTA Özel Yayın Serisi-28, 75-120.

Jackson, J., McKenzie, D.P. 1988. The Relationship between Plate Motions and Seismic Moment Tensors, and the Rates of Active Deformation in the Mediterranean and Middle East. Geophysical Journal 93, 45-73.

Jiménez-Muñoz, J.C., Sobrino, J.A.A. 2003. Generalized single-channel method for retrieving land surface temperature from remote sensing data. J. Geophys. Res. Atmos. 108, 4688.

Jimenez-Munoz, J. C., Sobrino, J. A., Skokovic, D., Mattar, C., Cristobal, J. 2014. Land surface temperature retrieval methods from Landsat-8 thermal infrared sensor data. IEEE Geosci Remote Sens Letter 11(10), 1840–1843.

Jolivet, L., Faccenna, C., Huet, B., Labrousse, L., Le Pourhiet, L., Lacombe, O., Lecomte, E., Burov, E., Denèle, Y., Brun, J.P., Philippon, M., Paul, A., Salaün, G., Karabulut, H., Piromallo, C.,

Monié, P., Gueydan, F., Okay, A.I., Oberhänsli, R., Pourteau, A., Augier, R., Gadenne, L., Driussi, O., 2013. Aegean tectonics: progressive strain localisation, slab tearing and trench retreat. Tectonophysics 597-598, 1–33. https://doi.org/10.1016/j.tecto.2012.06.011.

Kaya, O. 1978. Ege kıyı kuşağı (Dikili-Zeytindağı-Menemen-Yenifoça) Neojen stratigrafisi. Ege Üniversitesi Fen Fakültesi monografiler serisi, 17.

Kaçar, B., Özden, S., Ateş, Ö. 2017. Güre (Balıkesir) Jeotermal Alanının Jeolojisi, Hidrojeokimyası ve Aktif Tektonikle İlişkisi. Türkiye Jeoloji Bülteni 60, 243-258.

Karacık, Z., Yılmaz, Y. 1998. Geology of the ignimbirites and the associated volcanoplutonic complex of the Ezine area, Northwestern Anatolia. Journal of Volcanology and Geothermal Research 85 (1–4).

Kalinowski A., Oliver S. 2004. ASTER processing manual, Remote Sensing Applications, Geoscience Australia, internal report 39.

Kruse, F.A. 2012. Mapping surface mineralogy using imaging spectrometry. Geomorphology 137, 1, 41-56. https://doi.org/10.1016/j.geomorph.2010.09.032.

Kurtuluş, C., Doğan, B., Sertçelik, F., Canbay, M. M. 2009. Determination of the tectonic evolution of the Edremit Gulf based on seismic reflection studies. Marine Geophysical Research 30, 121–134.

Li, Z. L., Tang, B., Wu, H., Yan, G., W, Z., Trigo, I., Sobrino, J. 2013. Satellite-Derived Land Surface Temperature: Current Status and Perspectives. Remote Sensing of Environment 131, 14-37. 10.1016/j.rse.2012.12.008.

Littlefield, E., Calvin, W. 2014. Geothermal exploration using imaging spectrometer data over Fish Lake Valley, Nevada. Remote Sensing of Environment 140. 509–518. 10.1016/j.rse.2013.09.007.

Mazor, E. 1991. Applied chemical and isotopic groundwater hydrology. Open University Press, First Published, 264, Buckinghom.

McClusky, S., Balassanian, S., Barka, A. A., Demir, C., Ergintav, S., Georgiev, I., Gürkan, O., Hamburger, M., Hurst, K., Kahle, H., Kastens, K., Kekelidze, G., King, R., Kotzev, V., Lenk, O., Mahmoud, S., Mishin, A., Nadariya, M., Ouzounis, A., Paradissis, D., Peter, Y., Prilepin, M., Reilinger, R., Sanli, I., Seeger, H., Tealeb, A., Toksoz, M., Veis, G. 2000. Global positioning system constraints on plate kinematics and dynamics in the eastern Mediterranean and Caucasus. Journal of Geophysical Research 105(B3), 5695–5720.

McKenzie, D.P. 1972. Active tectonics of the Mediterranean region. Geophysical Journal of the Royal Astronomical Society 30, 109-158.

Mia, M. B., Nishijima, J., Fujimitsu, Y. 2014. Exploration and monitoring geothermal activity using Landsat ETM+images. A case study at Aso volcanic area in Japan. Journal of Volcanology and Geothermal Research 275. 10.1016/j.jvolgeores.2014.02.008.

Mia, M. B., Fujimitsu, Y., Nishijima, J. 2018. Monitoring of Thermal Activity at the Hatchobaru–Otake Geothermal Area in Japan Using Multi-Source Satellite Images-With Comparisons of Methods, and Solar and Seasonal Effects. Remote Sensing 10, 1430.

NASA. 2019. https://search.earthdata.nasa.gov/.

Norini, G., Groppelli, G., Sulpizio, R., Carrasco-Núñez, G., Davila-Harris, P., Pellicioli, C., Zucca, F., De Franco, R. 2015. Structural analysis and thermal remote sensing of the Los Humeros Volcanic Complex: Implications for volcano structure and geothermal exploration. Journal of Volcanology and Geothermal Research 301, 221-237. 10.1016/j.jvolgeores.2015.05.014.

Nukman, M., Moeck, I. 2013. Structural controls on a geothermal system in the Tarutung Basin, north central Sumatra. Journal of Asian Earth Sciences 74, 86-96. 10.1016/j.jseaes.2013.06.012.

Okay, A.I., Tüysüz, O. 1999. Tethyan sutures of northern Turkey. In: Durand, B., Jolivet, L., Horvath, F. and Seranne, M. (eds), Mediterranean Basins: Tertiary Extension within the Alpine Orogen. Geological Society, London, Special Publications 156, 475–515.

Okay, A. İ., Satır, M. 2000. Upper Cretaceous eclogite–facies metamorphic rocks from the Biga Peninsula, northwest Turkey. Turkish Journal of Earth Sciences 9, 47–56.

Okay, A. İ., Göncüoğlu, M. C. 2004. Karakaya complex: A review of data and concepts. Turkish Journal of Earth Sciences 13, 77–95.

Okay, A.İ., Siyako, M., Bürkan, K.A. 1990. Biga yarımadasının jeolojisi ve tektonik evrimi. Türkiye Petrol Jeologları Derneği Bülteni 2/1, 83-121.

Okay, A.İ., Siyako, M., Bürkan, K.A. 1991. Geology and tectonic evolution of the Biga Peninsula. Dewey, J.F. (ed). Special Issuse on tectonics. Bulletin of the Technical University of Istanbul 44, 191-255.

Okay, A. İ., Bozkurt, E., Satır, M., Yiğitbaş, E., Crowley, Q. G., Shang, C. K. 2008. Defining the

southern margin of Avalonia in the Pontides: Geochronological data from the late Proterozoic and Ordovician granitoids from NW Turkey. Tectonophysics 461, 252–264.

Okay, A.İ., Satır, M., Maluski, H., Siyako, M., Monie, P., Metzger, R., Akyüz, S. 1996. Paleo and Neo-Tethyan events in northwest Turkey: Geological and geocronogical constraints. Yin, A., Harrisson, M. (Eds). Tectonics of Asia: Cambridge Üniv. Pres 420-441.

Ölmez, E., Gökalp, Y., Ertürk, İ., Ekici, S., Yıldız, Ş., Demirel, V., Sözen, İ. 2001. Balıkesir Edremit Derman Jeotermal Alanı ED1, ED2, ED3 Sondajları Kuyu Bitirme Raporu. Maden Tetkik ve Arama Genel Müdürlüğü Rapor No: 10512, Ankara (unpublished).

Özkaymak, Ç., Sözbilir, H., Uzel, B. 2013. Neogene-Quaternary evolution of the Manisa Basin: Evidence for variation in the stress pattern of the İzmir-Balıkesir Transfer Zone, western Anatolia. Journal of Geodynamics 65, 117–135.

Parastatidis, D., Mitraka, Z., Chrysoulakis, N., Abrams, M. 2017. Online global land surface temperature estimation from landsat. Remote Sensing 9(12), 1–16, doi:10.3390/rs9121208.

Pieri, D., Abrams, M. 2004. ASTER watches theworld's volcanoes: a newparadigm for volcanological observations from orbit. J. Volcanol. Geotherm. Research 135 (1-2), 13–28.

Pieri, D., Abrams, M. 2005. ASTER Observations of Thermal Anomalies Preceding the April 2003 Eruption of Chikurachki Volcano, Kurile Islands, Russia. Remote Sensing of Environment 99, 1-2, 2005. 84-94.

Piper, A. M. 1944. A Graphic Procedure in Geochemical Interpretation of Water Analyses, American Geophysical Union Transactions 25, 914-923.

Qin, Q., Zhang, N., Nan, P., Chai, L. 2011. Geothermal area detection using Landsat ETM+ thermal infrared data and its mechanistic analysis—A case study in Tengchong, China. Int. J. Appl. Earth Observation and Geoinformation 13(4), 552-559. doi:http://dx.doi.org/10.1016/j.jag.2011.

Ramírez-González, L. M., Aufaristama, M., Jónsdóttir, I., Hoskuldsson, A., Thordarson, T., Proietti, N., Kraft, G., Mcquilkin, J. 2019. Remote sensing of surface Hydrothermal Alteration, identification of Minerals and Thermal anomalies at Sveifluháls-Krýsuvík high-temperature Geothermal field, SW Iceland. 7th ITB International Geothermal Workshop (IIGW2018). IOP Conf. Series: Earth and Environmental Science 254, 012005. doi:10.1088/1755-1315/254/1/012005.

Reinisch, E., Cardiff, M., Kreemer, C., Akerley, J., Feigl, K. 2020. Time-series Analysis of Volume Change at Brady Hot Springs, Nevada, USA using Geodetic Data from 2003 – 2018. Journal of Geophysical Research: Solid Earth 125.

Rowan, L.C., Mars J.C. 2003. Lithologic mapping in the Mountain Pass, California area using Advanced Spaceborne Thermal Emission and Reflection Radiometer (ASTER) data. Remote Sensing of Environment 84, 350–366.

Rowan, L.C., Hook, S.J., Abrams, M.J., Mars, J.C. 2003. Mapping hydrothermally altered rocks at Cuprite, Nevada, using the Advanced Spacebourne Thermal Emission and Reflection Radiometer (ASTER), a new satellite-imaging system. Economic Geology 98, 1019–1027.

Sarp, S. Burçak, M., Yıldırım, T., Yıldırım, N. 1998. Biga Yarımadasının jeolojisi ve jeotermal enerji olanakları ile Balıkesir-Havran-Derman kaplıca sahasının detay jeotermal etüdü ve gradyan sondajları. Maden Tetkik ve Arama Genel Müdürlüğü Rapor No: 10537. Ankara (unpublished).

Sheng, J., Wilson, J., Lee, S. J. 2009. Comparison of land surface temperature (LST) modeled with a spatially-distributed solar radiation model (SRAD) and remote sensing data. Environmental Modelling & Software. 24. 436-443. 10.1016/j.envsoft.2008.09.003.

Siyako, M., Bürkan, K. A., Okay, A. I. 1989. Tertiary geology and hydrocarbon potential of the Biga and Gelibolu peninsulas (in Turkish). Türkiye Petrol Jeologları Derneği Bülteni 1, 183–200.

Sobrino, J., Jimenez-Munoz, J.C., Sòria B.G., Romaguera, M., Guanter, L., Moreno, J., Plaza, A., Martinez, P. 2008. Land surface emissivity retrieval from different VNIR and TIR sensors. Geoscience and Remote Sensing, IEEE Transactions on, 46, 316-327. 10.1109/TGRS.2007.904834.

Sobrino, J. A., Jiménez-Muñoz, J. C., Paolini, L. 2004. Land surface temperature retrieval from LANDSAT TM5. Remote Sensing Environment 90, 4, 434–440.

Song, B., Park, K. 2014. Validation of ASTER Surface Temperature Data with in Situ Measurements to Evaluate Heat Islands in Complex Urban Areas. Advances in Meteorology 1-12. 10.1155/2014/620410.

Srivastava, P.K., Majumdar, T.J., Bhattacharya, A.K. 2009, Surface Temperature Estimation in Singhbhum Shear Zone of India using Landsat-7 ETM+ Thermal Infrared Data. Advances in Space Research 43, 10, 1563-1574.

Straub, C., Kahle, H.-G., Schindler, C. 1997. GPS and geologic estimates of the tectonic activity in the Marmara region, NW Anatolia. J. Geophys. Res., 102, 27 587-27601.

Şengör, A.M.C., Yılmaz, Y. 1981. Tethyan evolution of Turkey, a plate tectonic approach. Tectonophysics 75, 181-241.

USGS. 2019. https://earthexplorer.usgs.gov/.

USGS. 2007. Spectral Library. https://www.usgs.gov/labs/spectroscopy-lab/science/spectral-library.

TJVT Database. 1:25.000 ölçekli Türkiye Jeoloji Veri Tabanı (TJVT) verileri. Maden Tetkik ve Arama Genel Müdürlüğü, Ankara, Türkiye.

Uzel, B., Sözbilir, H., Özkaymak, Ç., Kaymakçı, N., Langereis, C.G. 2013. Structural evidence for strike-slip deformation in the İzmir-Balıkesir transfer zone and consequences for late Cenozoic evolution of western Anatolia (Turkey). Journal of Geodynamics 65, 94-116.

Valor, E., Caselles, V. 1996. Mapping land surface emissivity from NDVI: Application to European, African, and South American areas. Remote Sensing Environment 57, 167–184.

Van de Griend, A., Owe, M. 1993. On the relationship between thermal emissivity and the normalized difference vegetation index for natural surfaces. Int. J. Remote Sens. 14, 1119–1131.

Van der Meer, F., Hecker, C., van Ruitenbeek, F., van der Werff, H., de Wijkerslooth, C., Wechsler, C. 2014. Geologic remote sensing for geothermal exploration: A review. Int. J. Appl. Earth Observation Geoinformation 33, 255-269.

Vaughan, R., Calvin, W., Taranik, J. 2003. SEBASS hyperspectral thermal infrared data: Surface emissivity measurement and mineral mapping. Remote Sensing of Environment 85, 48-63. 10.1016/S0034-4257(02)00186-4.

Vaughan, R., Lowenstern, J., Keszthelyi, L., Jaworowski, C., Heasler, H. 2012*a*. Mapping temperature and radiant geothermal heat flux anomalies in the yellowstone geothermal system using ASTER thermal infrared data. Transactions - Geothermal Resources Council 36, 1403-1409.

Vaughan, R.G., Keszthelyi, L.P., Lowenstern, J.B., Jaworowski, C., Heasler, H. 2012*b*. Use of ASTER and MODIS thermal infrared data to quantify heat flow and hydrothermal change at Yellowstone National Park. J. Volcanol. Geotherm. Research 233–234, 72–89.

Waswa, A. K. 2017. Mapping of Hydrothermal Minerals Related to Geothermal Activities Using Remote Sensing and GIS: Case Study of Paka Volcano in Kenyan Rift Valley. International Journal of Geosciences 8(05), 711-725.

Wang, Q., Mwirigi, M.M., Kinoshita, I. 2014. A GIS-Based Approach in Support of Spatial Planning for Renewable Energy: A Case Study of Fukushima, Japan. Sustainability 6, 2087-2117. 10.3390/su6042087.

Wessels, R.L., Vaughan, R.G., Patrick, M.R., Coombs, M.L. 2013. High-resolution satellite and airborne thermal infrared imaging of precursory unrest and 2009 eruption at Redoubt Volcano, Alaska. Journal of Volcanol. Geotherm. Research 259, 248–269.

Yalçın, T. 2007. Geochemical characterization of the Biga Peninsula thermal waters (NW Turkey). Aquatic Geochemistry 13, 75-93.

Yılmaz, Y., Karacık, Z. 2001. Geology of the northern side of the Gulf of Edremit and its tectonic significance for the development of the Aegean grabens. Geodinamica Acta 14, 31–43.

Yu, X., Xulin, G., Zhaocong, W. 2014. Land Surface Temperature Retrieval from Landsat 8 TIRS—Comparison between Radiative Transfer Equation-Based Method, Split Window Algorithm and Single Channel Method. Remote Sensing 6, 10: 9829-9852. https://doi.org/10.3390/rs6109829.

Zannina, J., Loriab, A. F. R., Llabjania, Q., Laloui, L. 2020. Extension of Winkler's solution to non-isothermal conditions for capturing the behaviour of plane geostructures subjected to thermal and mechanical actions. Computers and Geotechnics 128, 1-20.

Bulletin of the Mineral Research and Exploration

http://bulletin.mta.gov.tr

Neotectonics and geothermal potential of the East Anatolian Tectonic Block: A case study in Diyadin (Ağrı) geothermal field, NE Türkiye

Ali KOÇYİĞİT[a]

[a]*Middle East Technical University, Department of Geological Engineering, Active Tectonics and Earthquake Research Lab, Ankara, Turkiye*

Research Article

Keywords:
Diyadin Geothermal Field, Thermogene Fissure-ridge Travertine, Active Volcano, Active Strike-slip Tectonic Regime.

ABSTRACT

Diyadin is situated 71 km ESE of Ağrı nearby the Turkish-Iranian State border in the east Anatolian tectonic block. It is only one of several type localities of promising geothermal fields in eastern Anatolia. The neotectonic regime and related fault zones in the eastern Anatolia are dominated by a strike-slip tectonic regime governed by a stress field state, in which the greatest principal compressive stress (σ1) is operating in NNW direction (N22°W) while the least principal stress axis (σ3) or extension direction is N68°E. This stress field state was proved once more by the tensor solution of the 12 June 2022 Akçift (Muradiye-Van) earthquake of Mw = 5.1. The strike-slip neotectonic regime started at the time of latest Pliocene-early Quaternary and then triggered the first occurrence of the fissure eruption along the NW trending Kaletepe open fracture. This event was followed by the development of both the two-peaked Tendürek strato-shild volcano and the Diyadin geothermal field (DGF). The most common manifestations of the DGF are the active tectonic regime and related faults, active volcanoes, fumeroles, numerous hot water springs to artesian wells, widespread iron-rich alteration zones, actively growing fissure-ridge travertines and the probable presence of the shallow-seated and unroofed hypabyssal felsic to intermediate intrusions of Quaternary age.

Received Date: 17.06.2022
Accepted Date: 07.02.2023

1. Introduction

In general, major factors, which control development of the geothermal fields, are active tectonic regime and related faults, plate boundaries and/or proximity to them, shallow-seated Curie point depth (CPD), high heat flow, young volcanic activity, young hypabyssal intrusions with felsic to intermediate chemical compositions, thinned crust and ascended asthenospheric mantle, a thick package of rocks with high porosity or reservoir rock (s), a package of impermeable rocks or cover rocks, and meteoric water supply enough. These factors also determine the distribution pattern of geothermal fields throughout the territory of Türkiye. For this reason, the most of geothermal fields (approximately 78%) are situated in the southwest Anatolia, i.e., at the back-arc region of the South Aegean-Cyprus subduction zone. In the same way, remainings are located within and adjacent to the active fault systems or plate boundaries such as the North Anatolian dextral strike-slip fault system, East Anatolian sisnistral strike-slip fault system and significant numbers of intraplate fault zones or systems such as the İnönü-Eskişehir, Akşehir-Afyon, and Central Anatolian active fault systems. The third and forth significant localities of the geothermal field are the central and eastern Anatolia respectively. They are characterized by the Quaternary volcanic activities (Innocenti et al., 1976; Ercan et al., 1993). According to Akın et al. (2014), the areas in which the heat flow

Citation Info: Koçyiğit, A. 2023. Neotectonics and geothermal potential of the East Anatolian Tectonic Block: A case study in Diyadin (Ağrı) geothermal field, NE Türkiye. Bulletin of the Mineral Research and Exploration 171, 33-68. https://doi.org/10.19111/bulletinofmre.1248712

**Corresponding author: Ali KOÇYİĞİT, alikocyigit45@gmail.com*

is between 0-125.7 mW/m^2 are called as normal fields, whereas the areas in which the heat flow is higher than 125.7 mW/m^2 are called as the geothermal fields. In addition, around Ağrı and its near environ in the eastern Anatolia, the average heat flow varies from 60 to 80 mW/m², i.e., it is low, and this area is not a geothermal field (Akın et al., 2014). Whereas, Aydın et al. (2020) reported that the eastern Anatolia is in the nature of low- or moderate-temperature geothermal systems based on some geological factors such as relatively thick crust, low surface heat flux and the absence of ideal cover units.

According to 2017 data, the energy consumption of Türkiye is provided by 31% from petrol, 28.2% from natural gas, 27.3% from coal and 12.5% from hydraulic and other renewable energy sources (Canbaz et al., 2020). The number of electricity energy production plants in the country reached 3098 by the end of July 2017. The country's energy needs are supplied by 288 natural gas, 186 wind, 613 hydraulic, 40 coal, 33 geothermal, 1.773 solar and 165 other power plants (MTA, 2018). The basic renewable energy sources are solar, wind, geothermal and hydroelectric. Theoretically, it is thought that the Türkiye's geothermal capacity is 31500 MWt, and its 77.9% is in the western Anatolia. The geothermal electricity potential is about 2000 MWe, whereas the installed capacity of electricity energy producted from geothermal resource is only 201.1 MWe at the end of 2017. The number of plants is 67 and its share in the primary energy balance is only 0.2% (Canbaz et al., 2020). Türkiye, there are 276 geothermal occurrences including nearly 110 fields with an average surface temperatures ranging from 22.5°C to 220°C (maximum 242°C). The surface temperatures in 80 of the occurrences are above 60°C, in 13 of them above 100°C and in 8 of ccurrences above 140°C (Basel et al., 2010). They have also reported that one of the major geothermal fields in the eastern Anatolia is the Diyadin (Ağrı) area where the average flow rate is 561 lt/s, the average surface temperature is 72°C, and the temperature interval at 1km depth is 55°-85°C.

In general, eastern Anatolia does not seem to present promising geothermal fields in spite of its extensive and young volcanism (Serpen et al., 2009). However, there are several well-known promising geothermal fields in the eastern Anatolia. These are the Nemrut Caldera, Başkale-Yiğit stratovolcano, Erciş-Zilan and the Tendürek volcano-Diyadin geothermal fields. The lack of good geothermal resources requires a geothermal-based multidisciplinary studies, i.e., there is a need for detailed hydrochemical, volcanological, tectonical and systematic geophysical investigations of the volcanic structures in the eastern Anatolia (Serpen et al., 2009). In the eastern Anatolia, geothermal-based detailed multi-disciplinary studies are very limited (Basel et al., 2010; Pasvanoğlu, 2013; Aydın et al., 2020; Şener and Şener, 2021). These studies are focusud to the geothermal potential of Ağrı region. Pasvanoğlu (2013) reported that the temperatures of the deep geothermal reservoirs in Diyadin range between 92° and 156°C based on quartz geothermometry. Same author has also stated that Diyadin waters are heated by magmatic activity associated with the Tendurek volcano based on chemical data. Şener and Şener (2021) reported that, the Ağrı provincial center, Patnos, Eleşkirt, and Doğubayazıt regions have high geothermal potential, while the Diyadin area has been identified as a very high geothermal potential based on the the Geothermal Potential Index (GPI) map of the Ağrı area (MTA, 2021).

Our study aims to present active tectonics, major surface manifestations, such as the fissure-ridge travertines, fumaroles and wide-spread alteration zones, of the Diyadin geothermal field, and the conceptual geothermal model for the eastern Anatolia under the lights of both the natural to international literature and detailed field geological data newly obtained from the field geological mapping studies carried out in Diyadin and its near environ. Thus, we think to fill the gap in the national and international geothermal literatures, and to increase the share of the renewable energy in the balance of primary energy used in our country.

2. Regional Geological Setting

The study area is situated very close to the Turkish-Iranian State border in the East Anatolian Tectonic Block (EATB). The EATB or the northwestern section of the Anatolian-Iranian high plateau (up to average 2 km above the sea level) is bounded by the Lesser Caucasus fold-thrust belt to the northeast, by the Kelkit-Çoruh sinistral strike-slip fault zone to the northwest, by both the North Anatolian and East Anatolian Fault systems to the west, by the Bitlis-Zagros Suture Zone (BZSZ) to the south and by the Turkish-Iranian State

border to the east (Figure 1). The eastern Anatolia is a seismically very active and geologically complicated region included in the Arabian-Eurasian collision zone (Figure 1a). The geological complexity is characterized by fold-thrust fault belts, strike-slip faults and related basin formations. These characteristics of the eastern territory of Türkiye represent a natural laboratory to observe multi-stage deformation. The geologically complicated multi-stage deformation pattern has been formed by the entirely demise of the Tethyan Seaway, the Bitlis Ocean, between the Indian Ocean and the east Mediterranean Sea followed by the continent-continent collision of northerly moving Arabian Plate and the Eurasian plate during the late Serravalian time (Şengör and Yılmaz, 1981; Dewey et al., 1986). These authors accepted that the late Serravalian time is the onset age of the neotectonic regime in Türkiye. However, after the final collision and formation of the Bitlis suture zone, the N-S-directed intracontinental convergence lasted over a time period of ~9 Ma. This time slice of ~9 Ma is here termed as the transitional period between the contractional palaeotectonic and the strike-slip neotectonic regimes (Koçyiğit et al., 2001; Aksoy et al., 2007; Çolak et al., 2012; Koçyiğit, 2013; Koçyiğit and Canoğlu, 2017). During this transitional period, a series of deformations took place. Some of them are the thickening of crust, regional tectonic uplift, E-W trending folds, thrust to reverse faults, resetting of new drainage system, disappearance of marine conditions, development of short-to long-term stratigraphic gaps and a widespread post-collisional volcanic activitity (Şengör and Kidd, 1979; Innocenti et al., 1980; Dewey et al., 1986; Şaroğlu and Yılmaz, 1986; Yılmaz et al., 1987; Ercan et al., 1990; Koçyiğit and Beyhan 1998; Koçyiğit et al., 2001; Koçyiğit, 2013; Koçyiğit and Canoğlu, 2017). The contractional deformation and development of fold-thrust belts lasted until the late Pliocene, and then they were replaced by a new tectonic regime, namely the contractional-extensional regime, i.e., the prominent strike-slip faulting-related tectonic regime. This is proved by the occurrence of a series of inversions. These are the inversions in the deformational style, types of geological structures, the nature of sedimentation and basin formation, geochemical characteristics of the volcanic activity (e.g., changing from calc-alkali nature to dominantly alkali composition), the nature of seismic activity triggered by the formation of two intracontinental transform fault boundaries (North Anatolian dextral strike-slip and the East Anatolian sinistral strike-slip fault systems), and finally west-southwestward escapement of the Anatolian platelet along these two megashears (Hempton, 1987; Koçyiğit and Beyhan 1998; Koçyiğit et al., 2001; Koçyiğit, 2013; Koçyiğit and Canoğlu, 2017). Hence the onset age of the strike-slip dominated neotectonic regime in eastern Anatolia is the late Pliocene (Koçyiğit et al., 2001; Koçyiğit, 2013; Koçyiğit and Canoğlu, 2017). In this neotectonic regime the greatest principal stress axis ($\sigma 1$) is operating in approximately NNW direction. In addition to the compression orientation, one other NE-SW secondary orientation is also observed which has been prevailing in the northeastern section of the EATB since the beginning of Quaternary period (Jackson, 1992; Copley and Jackson, 2006; Mokhoori et al., 2021). On a regional scale the principal stress axes orientations, which govern the strike-slip neotectonic regime in eastern Anatolia, are mainly controlled by the Arabian-Eurasian plate convergence. However, local stress orientations have been significantly influenced from the secondary blocks motions and their geometries (Avagyan et al., 2005). Based on the current stress field state, two major groups of strike-slip faulting-related structures occur in the EATB and its near environ. These are: (1) NE trending sinistral strike-slip faults, and (2) NW trending dextral strike-slip faults. From northwest to southeast the Kelkit-Çoruh, Erzurum, Dumlu, Çobandede, Digor and Başkale fault zones comprise the first group of active structures (Arpat et al., 1977; Şaroğlu and Yılmaz, 1986; Şaroğlu et al., 1987; Koçyiğit et al., 2001; Emre et al., 2012; Koçyiğit, 2013; Koçyiğit and Canoğlu, 2017; Emre et al., 2018). In contrast to this group, from northeast to southwest, the Aras, Iğdır, Balıkgölü, Ağrı, Çaldıran, North Tebriz, Karayazı, Erciş-Dorutay and the Yüksekova fault zones form the second group of active structures (Koçyiğit et al., 2001; Hessami et al., 2003; Karakhanian et al., 2004; Masson et al., 2006; Copley and Jackson, 2006; Dhont and Chorovicz, 2006; Djamour et al., 2011; Shabanian et al., 2012; Koçyiğit, 2013; Sharkov et al., 2014; Sağlam and Selçuk et al., 2016; Aghajany et al., 2017; Emre et al., 2018; Güneyli et al., 2020; Sağlam-Selçuk and Kul, 2021; Mokhoori et al., 2021). In addition to these structures, there are also a series of ~ N-S trending oblique-slip normal faults, and approximately E-W trending thrust to reverse faults, one of which reactivated and caused to the occurrence of a very destructive earthquake, the 23 October 2011 Tabanlı (Van) earthquake of Mw=7.2 (Koçyiğit, 2013). The most of these structures are outside of the present study. However, the Iğdır, Aras, Balıkgölü, Ağrı, Çaldıran, Erciş-Dorutay and the North Tebriz

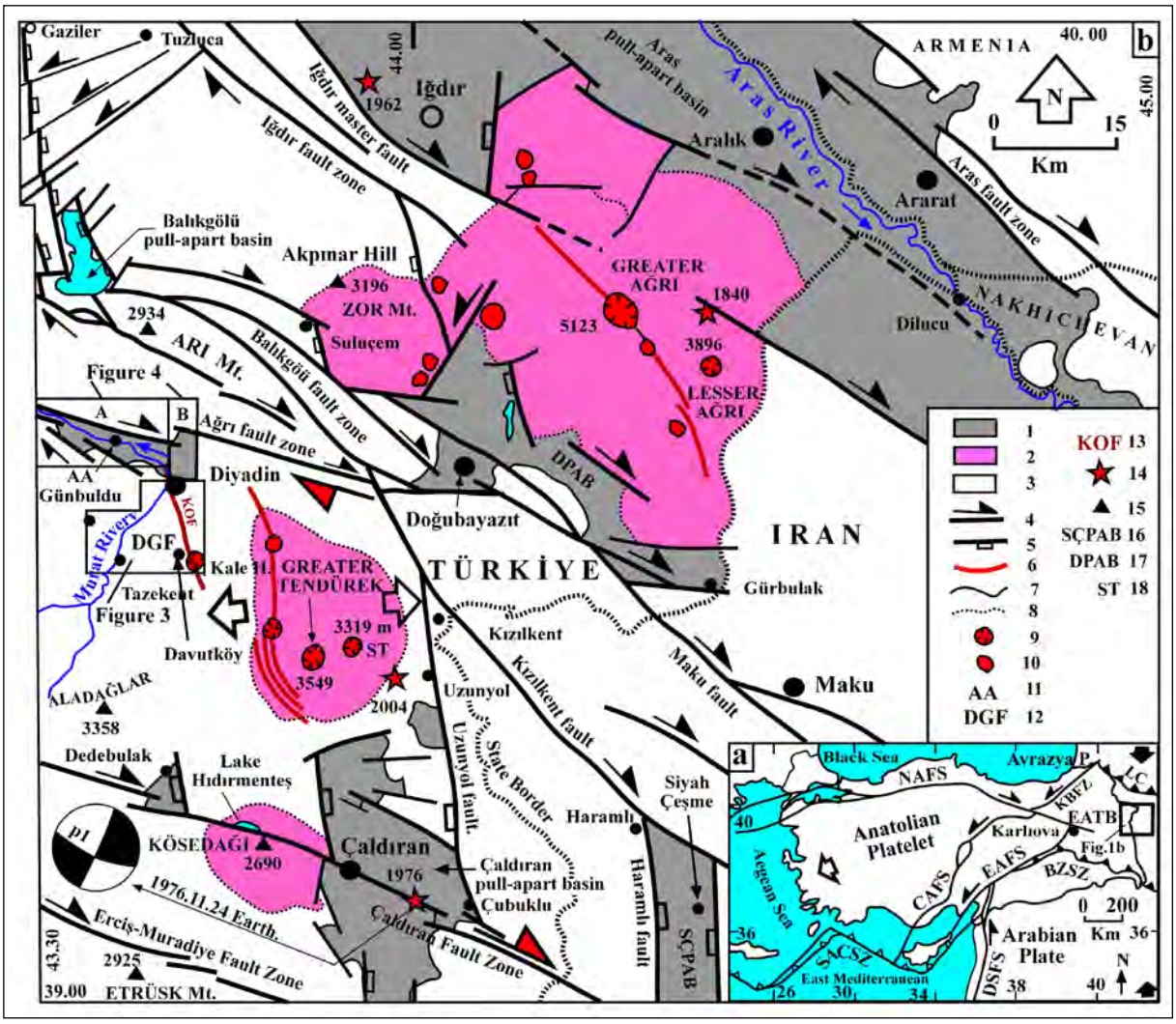

Figure 1- a) Simplified tectonic map illustrating significant neotectonic strucures in Türkiye and adjacent areas, and location of the study area. BZSZ: Bitlis-Zagros Suture Zone, EAFZ: East Anatolian Fault System, EATB: East Anatolian Tectonic Block, NAFS: North Anatolian Fault System, KBFZ: Kelkit-Bayburt Fault Zone, LC: Lesser Caucasus Fold-Thrust Belt, CAFS: Central Anatolian Fault System, DSFS: Dead Sea Fault System, b) Simplified regional neotectonic map of the study area and near environ. AA: Aşağıakpazar, DGF: Diyadin geothermal field, KOF: Kaletepe open fracture; 1. Quaternary pull-apart basin fill, 2. Quaternary volcanic cones, 3. Pre-Quaternary rocks, 4. Strike-slip faults, 5. Normal faults, 6. Open fractures, 7. Formation boundary, 8. Possible boundary, 9. Crater, 10. Other eruption centers, 11. Aşağı Akpazar, 12. Diyadin geothermal area, 13. Kaletepe open fracture, 14. Earthquakes epicenters, 15. Elevation above sea level; Large closed arrows indicate regional contraction directions, while large open arrows indicate regional extension directions (Note: contracion and extension are still going on).

fault zones are the key structures taking a part in the development of the Diyadin geothermal field (DGF). For this reason, they are described in detail in the following sections.

3. Stratigraphical Outline of Diyadin Geothermal Field (DGF)

The study area is the Diyadin geothermal field (DGF). It is situated at approximately 71 km east of the city of Ağrı along the Ağrı-Doğubeyazıt-Iran highway. It covers an area of approximately 100 km² surrounded by the Diyadin county, Davutköy, Tazekent, Dibekli, Altınkilit, Günbuldu and Aşağıakpazar villages respectively (Figure 1b). The development of the DGF is still lasting at the northwest foot of the polygenetic and double-peaked Tendürek volcano of late Quaternary age located at the upstream side of the 722 km long antecedent Murat River system (Figure 1b). The diagnostic characteristics of the DGF are

the occurrences of numerous hot water springs and actively growing fissure-ridge travertines in different directions. The reservoir is one of the key factors in the development of the geothermal field. For this reason, not only the younger neotectonic rock units, but also the older paleotectonic rock units are described here.

Based on ages, deformation pattern and the types of tectonic regimes, which controlled both the deposition and the deformation pattern of rocks, the rocks units exposing in and adjacent to the DGF are classified into two major categories: (1) paleotectonic units and (2) neotectonic units (Figure 2). The paleotectonic units,

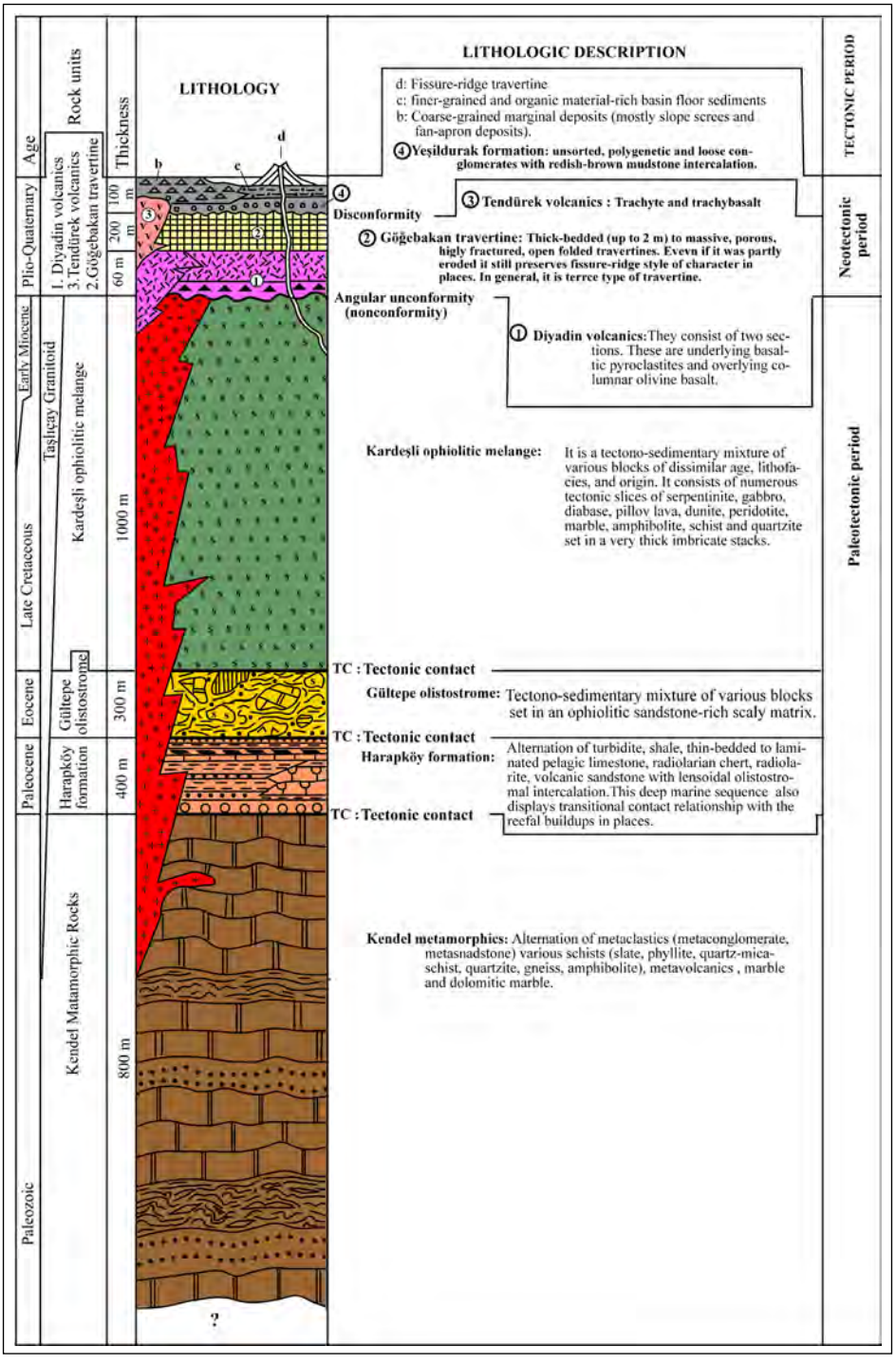

Figure 2- Columnar section of the Akpazar pull-apart basin and its near environs.

from oldest to youngest, are the Kendel Metemorphic Rocks, the Kardeşli ophiolitic mélange, the Harapköy formation, the Gültepe olistostrome, the Taşlıçay granitoid, the Dalören volcanic rocks, and the Mutlu formation. The neotectonic units are the Diyadin volcanic rocks, the Göğebakan travertines, the Yeşildurak fluvial sedimentary sequence, the Tendürek volkanic rocks, the Diyadin fissure-ridge travertines and the Quaternary alluvial sediments (Figures 3 and 4). Both the paleotectonic and neotectonic rock units are described separately below.

3.1. Paleotectonic Units

3.1.1. Kendel Metamorphic Rocks

This rock unit is exposed widely at the southwestern corner of the Akpazar pull-apart basin (Figure 4), near east of Günbuldu village and on the southwestern side of the Ulukent Town (Figure 3). Bottom of the Kendel metamorphic rocks is not exposed in the study area. However, at the visible lower section, the unit begins with the medium to thick bedded (30 cm-1.5 m),

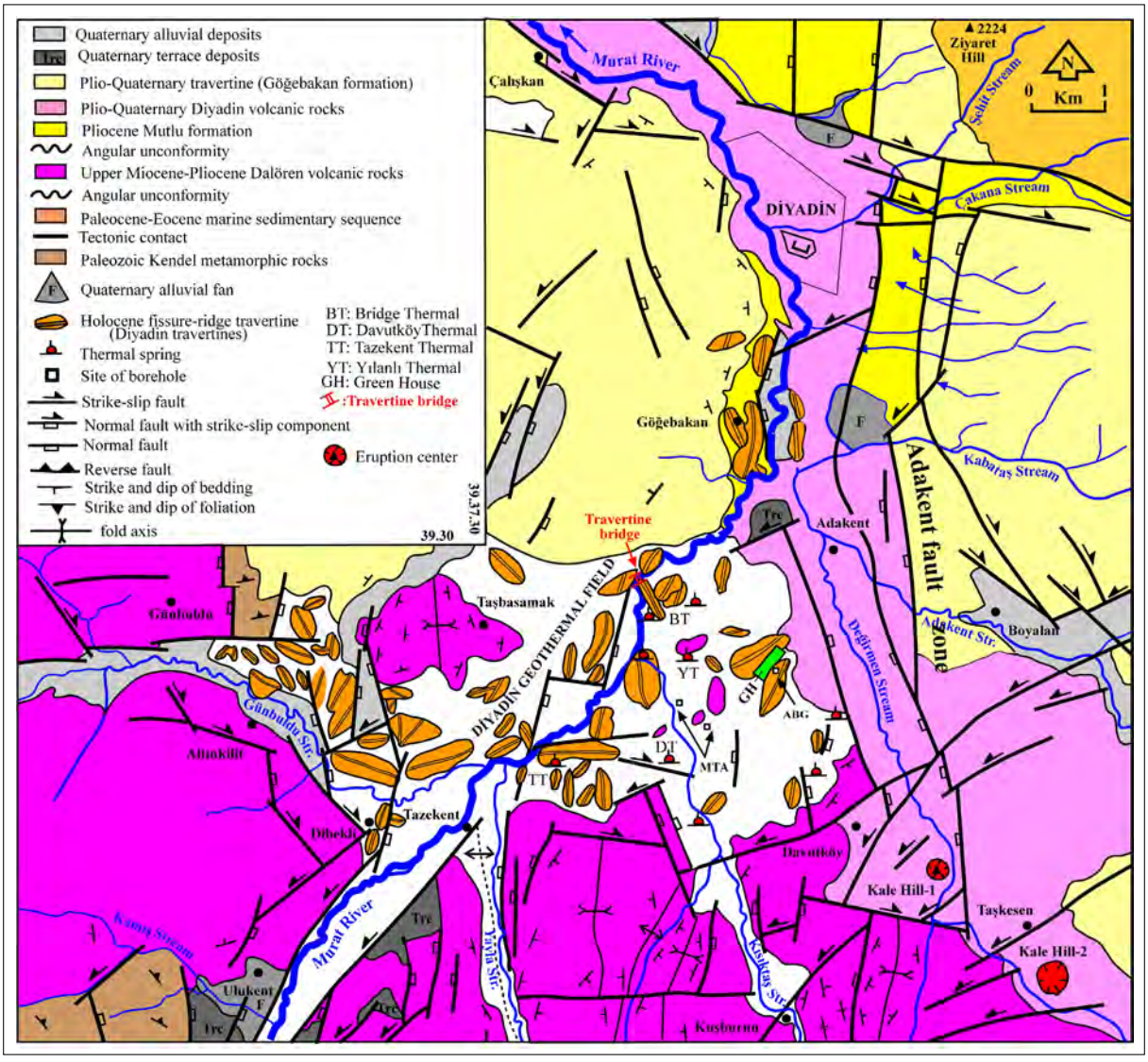

Figure 3- Geological map of the Diyadin geothermal field and its near environs.

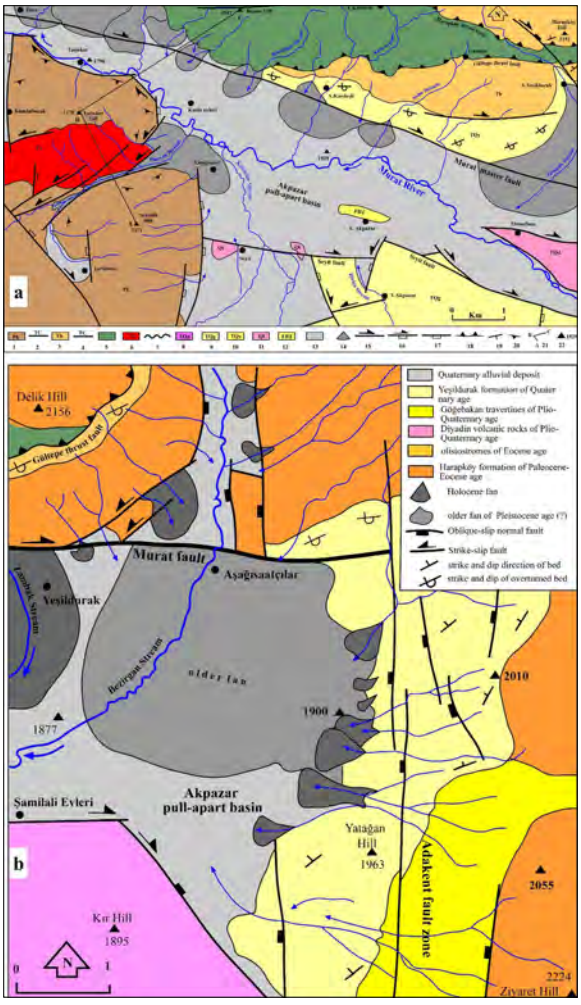

Figure 4- a) Geological map of the Akpazar pull-apart basin. 1- Paleozoic Kendel metamorphic rocks, 2- Tectonic contact, 3-Paleocene-Eocene marine sedimentary sequence, 4-Tectonic contact, 5-Upper Cretaceous ophiolitic melange, 6- Lower Miocene Taşlıçay Granitoid, 7- Angular unconformity (nonconformity), 8-Plio-Quaternary Diyadin columnar basalt, 9- Plio-Quaternary older travertine, 10- Plio-Quaternary fluvial conglomerate, 11- Quaternary Tendürek volcanics, 12- Quaternary alluvial sediments (basin fill), 13- Upper Quaternary fissure-ridge travertine, 14- alluvial fan, 15- Strike-slip fault, 16- Normal fault with strike-slip component, 17- Normal fault, 18- Thrust fault, 19- Strike and dip of bedding, 20- Strike and dip of foliation, 21- Line of geological cross-section, and 22- Elevations above sea level, b) Geological map of the eastern tip of the Akpazar pull-apart basin and its near environ.

in places massive, gray, blue and yellow colored dolomitic marbles, and then continues upwards with the alternation of marble, dolomitic marble, calcschist, mica-quartzschist, quartzite, amphibolite, gneiss and metaclastic rocks (metasandstone, metaconglomerate). At the topmost it ends with a thick package of recrystallized limestone. The visible total thickness of the Kendel metamorphic rocks is about 800 m. It is intruded and cut across by the Taşlıçay granitoid of the early Miocene age. However, it displays frequently faulted-contact relationships with younger rock units (Figures 3 and 4). The Kendel metamorphic rocks are also crossed frequently by the open fractures, shear planes and quartz veins owing to multiple deformation they have experienced. In addition, these rocks are full of caves of all size. For this reason, the Kendel metamorphic rocks, in particular marbels and quatrzites, are very porous and form main reservior of the geothermal fluid in the DGF. Based on previous works, age of the unit is Paleozoic (Esirtgen and Hepşen, 2018; Kansun et al., 2020).

3.1.2. Kardeşli Ophiolitic Mélange

This unit was previously reported as the "Kağızman Complex" by Kıral and Çağlayan (1980). It is exposed well in a large imbricate stack along the northern margin of the Akpazar pull-apart basin (Figure 4). The Kardeşli ophiolitic mélange displays tectonic contact relationships with the deep marine pelagic sedimentary sequence and olistostromes of Paleocene-Eocene age (Figure 5), while it is overlain with an angular unconformity by the Quaternary fluvial sedimentary sequence of the Akpazar pull-apart basin (Figure 6). The Kardeşli ophiolitic mélange consists of two major rock assemblages mixed by the tectono-sedimentery processes in a turbiditic scaly matrix. These are the deep-marine oceanic sedimentary sequence of pelagic limestone and radiolarian chert, and the spilite, pillove lava, basalt, diabase, gabbro, serpentinite and peridotite of oceanic crust to upper mantle lithosphere origin. It also contains rarely various blocks of marbles, quartzite, schists and shallow-water recrystallized limestones of continental crust origin. Whole of these rock assemblages are intensely sheared, brecciated and thrown into a series of wedge like imbricates. They display a southward-facing overturned to recumbent fold-thrust fault structure. This kind of outcrop pattern, chaotic internal structure and the thrust-faulted imbricate structure altogether reveal an accretionary prism formed at the inner wall of an oceanic trench situated adjacent to the overriding continental plate. Consequently, the Kardeşli ophiolitic mélange was

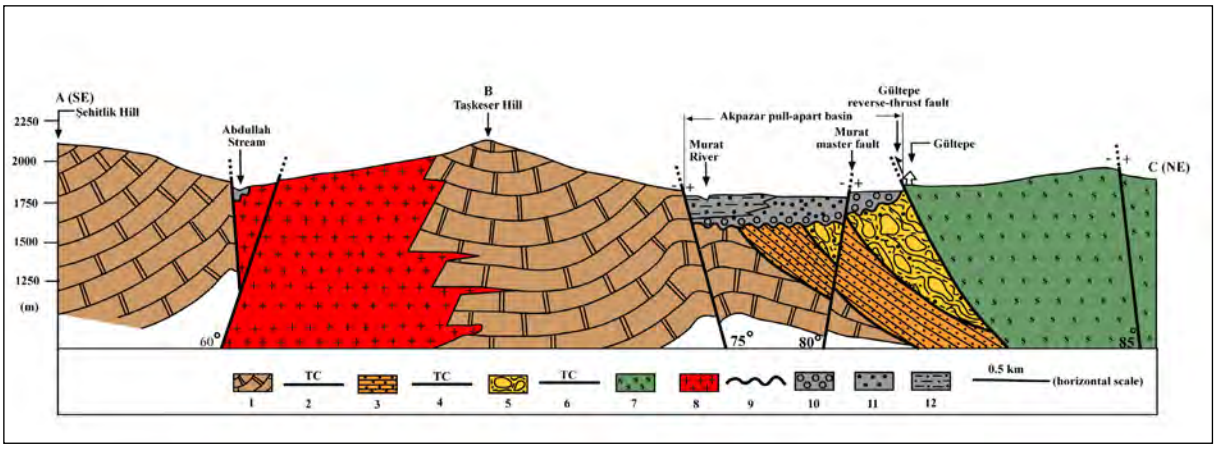

Figure 5- Geological cross-section along the line A-B-C on Figure 4; 1-Paleozoic Kendel metamorphic rocks, 2- Tectonic contact (TC), 3-Upper Paleocene Harapköy formation, 4- Tectonic contact (TC), 5-Eocene Gültepe olistostrome, 6- Tectonic contact (TC), 7-Upper Cretaceous Kardeşli ophiolitic melange, 8- Lower Miocene Taşlıçay Granitoid, 9-Angular unconformity (Nonconformity), 10-Plio-Quaternary polygenic fluvial conglomerate of the Yeşildurak formation, 11- Quaternary coarse-grained marginal deposits of basin, and 12- Finer grained depocentral deposits of the Akpazar pull-apart basin.

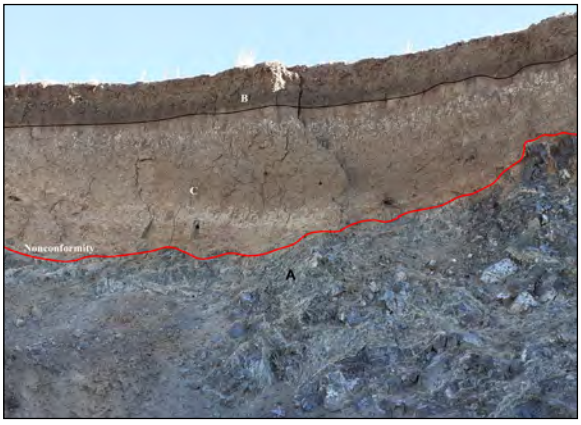

Figure 6- Close-up view of the nonconformity (angular unconformity) between the underlying serpentinite (A) of the Kardeşli ophiolitic mélange and the overlying fluvial sedimentary sequence (B) of the Yeşildurak formation, (C) Holocene soil horizon (near north of Yeşildurak village).

an originally accretionary prism or wedge resulted from sediments accreted onto the overriding tectonic plate along the convergent plate boundary. Most of the material in the accretionary wedge consists of marine sediments scraped off from the down-going slab of oceanic crust, but in some cases it also includes the erosional products of volcanic island arcs formed on the overriding plate.

The total thickness of the unit in the study area is 1 km. The deep sea pelagic limestones, mudstones and turbidites which comprise the matrix of the Kardeşli ophiolitic mélange. They contain rich foraminifers such as *Globotruncana stuarti, Globotruncana arca* and *Rugoglobigerina* sp (Aksoy and Tatar, 1990). Based on this fossil content, a Campanian-Maastrichtian age is assigned to the tectono-sedimentary mixture of the Kardeşli ophiolitic mélange. This unit is also reported widely as the East Anatolian Accretionary Prism (EAAP) in both native and international literature (Şengör and Yılmaz, 1981). The Kardeşli ophiolitic mélange, in particularly the mega-marble and carbonate blocks in it, represent the reservoir of the geothermal fluids in DGF.

3.1.3. Harapköy Formation and Gültepe Olistostrome

These rocks were previously named and reported as the "Pekiydere" and "Dirbi" formations, respectively, by Ercan and Sümengen (2018). In contrast to them, in the present study, they were renamed due to their different stratigraphical position in the study area (Figures 2 and 4). Both the Harapköy formation and the Gültepe olistostrome are exposed well around Ziyaret Hill to the near NE of Diyadin, and in the area among Aşağı Kardeşli, Gültepe, Aşağı Yeşildurak and Aşağısaatçılar villages and mostly on the Harapköy to Delik Hills along the northestern margin and eastern margins of the Akpazar pull-apart basin (Figures 3, 4a and 4b). At some localities, they were not mapped separately, because the Gültepe olistostrome also occurs as the intercalations within the Harapköy formation. Indeed, the Kardeşli ophiolitic mélange,

the Harapköy formation and the Gültepe olistostrome altogether form a thick imbricate stack separated by the intervening imbricate thrust faults (Figure 6). The Harapköy formation is composed of thin bedded to laminated deep marine shale, turbidite, palagic limestone, radiolarite and radiolarian chert alternation with polygenetic and unsorted olistostrome intercalations. This sedimentary succsession is intensely deformed (tight to overturned in position and also recumbent folded in places, especially against the tectonic contact with the Kardeşli ophiolitic mélange. The Harapköy formation contains thick-bedded to massive reefal limestone blocks of dissimilar size derived nearby steeply sloping wall of trench. The total thickness of the Harapköy formation is approximately 400 m. Based on the rich foraminifers content of the pelagic limestones and radiolarite, a late Paleocene-early Eocene age was assigned to the Harapköy formation (Ercan and Sümengen, 2018). The Gültepe olistostrome is exposed as an imbricate slice between the overlying ophiolitic mélange and the underlying Harapköy formation (Figures 4 and 6). It is a tectono-sedimentary mixture of various angular to sub-rounded blocks of all sizes set in a ophiolitic material-rich turbiditic matrix. Among blocks marble, quartzite, schists, reefal limestone, radiolarian chert, pelagic limestone, diabase, spilit, serpentinite, peridotite, gabbro, and pillow basalt can be mentioned. Based on the stratigarphical position and types of blocks included in it, an Eocene age was assigned to the Gültepe olistostrome.

3.1.4. Taşlıçay Granitoid

This igneous rock is exposed along the southern slope of the Taşteker Hill along the western margin of the Akpazar pull-apart basin (Figure 4). In addition, it also exposes at several localites on the upstream side and Aladağlar drainage divide to the south and outside of the study area (Figure 1b). At this locality (Çukuryala) the granodiorite displays a transitional contact relationship with the rhyolites and related pyroclastites. This contact relationship and their chemical composition reveal that their origin is same, i.e., it is a hypabyssal falsic intrusion. In general, the Taşlıçay granitoid is gray to pinkish in colour, and it has been densely fractured and cut across frequently by small-scaled faults, shear planes and quartz veins. The Paleozoic Kendel metamorphic rocks have also been intruded and metamorphosed once more by the Taşlıçay granitoid in the study area (Figure 5). On a regional scale, i.e., in the East Anatolian collision zone, there are a number of felsic intrusion outcrops similar to the Taşlıçay granitoid. They have also cut across the different rock packages of the East Anatolian Accretionary Prism (EAAP) (Keskin, 2003; Açlan and Duruk, 2018). The Taşlıçay granitoid is one of them, and it consists of two different rock assemblages. These are the I-type (host rock is igneous) and S-type (host rock is sedimentary) intrusive igneous rock assemblages. The I-type intrusive igneous assamblage consists of gabbro, diorite, quartzdiorite and monzodiorit with mildly intermediate composition. In contrast to them, the S-type assemblage are composed of tonolite, granodiorite and granite with felsic composition. The Taşlıçay granitoids display enrichment in large ion lithophile elements (LILE) (Cs, Rb, Ba, U, Th, Pb), light rare earth element (LREE) (I-type; LaN/YbN = 7.38–17.53; S-type; LaN/YbN = 6.27–26.73), and depleted in high field strength element (HFSE) (Nb, Ta, P, Ti) implying a subduction-related magmatic signature (Açlan and Duruk, 2018). Consequently, the origin of the Taşlıçay granitoid must be a calc-alcaline hybrid magma. Both the final collision of the Arabian and Erasian plates and the entire demise of the intervening ocean floor occurred during the late Serravalian time (Şengör and Yılmaz, 1981; Dewey et al., 1986, Yılmaz et al., 1998). However, both the intra-continental convergence and the subduction have also lasted after the collision and led to the thickening of crust and uplift in the East Anatolia (Pearce et al., 1990; Yılmaz et al., 1998; Keskin 2003; Barazangi et al., 2006; Elitok and Dolmaz, 2014). Accordingly, the oceanic slab of the Arabian plate persisted to subdect deeper and deeper below the accretionary prism. For this reason, the ocenic slab was first steepened and then broke off which led to the partial melting of both the continental crust and the lithospheric mantle. Thus two kinds of magma (falsic and basic magmas) developed and they begun to rise. Finally, a hybrid magma formed by the mixing of these upwelling two magmas (Keskin, 2003; Açlan ve Duruk, 2018). The Taşlıçay granitoid might have been formed by the cooling and solidification of this hybrid magma at shallower depth. The young hypabissal felsic magma reservoirs preserve their temperature for a long time. There are a number of dome and volcanic cones made-up of both

basic and felsic volcanic rocks of Plio-Quaternary age. The subsurface equivalents of the felsic domes and volcanic rocks may be the hypabissal intrusions, and they have not been unroofed yet. From this point of view, it is sugested that the heat source of the DGF, which is located at foot of the Tendürek polygenetic volcano and near by the Taşlıçay granitoid, may be such kinds of felsic hypabyssal intrusions.

3.1.5. Dalören Volcanic Rocks

These volcanic rocks are exposed widely to the southern margin of the DGF (Figure 3). The full volcanic succession, its synsedimentary (e.g., growth faults) and deformational structures (e.g., conjugate fractures and folds) are observed well around Aşağı and Yukarı Dalören villages (Figure 7). These settlements are outside of the study area but very close (at 1 km away) to the southern margin of the DGF. For this reason, this folded volcanic sequence was termed as the Dalören volcanic rocks in the present study. The Dalören volcanic rocks are composed mainly of rhyolite, andesite, trachyandesite, basaltic andesite, basalt and related pyroclastites (e.g., mostly ignimbrite, tuff and tuffite). The bottom of the Dalören volcanic rocks are not seen in the study area. However, it is observed well around Apro settlement to the southwest but outside the study area. At this locality, both the Kendel metamorphic rocks and the Taşlıçay granitoid are overlain with an angular unconformity by the Dalören volcanic rocks. The volcanic sequnce begins with the volcanic breccia and tufss onto the erosional surface of the older rocks, and then continues upwards with the alternation of ignimbrite, andesite, tuff, rhyolite, trachyte and volcanic breccia. At the topmost, the sequence is covered by a thick-bedded to massif ignimbrite horizon. In addition, the Dalören volcanic rocks display both erosional stratigraphical and also thrust-faulted contact relationships with the Pliocene Mutlu faormation. Tuff and tuffites are white, yellow, and green in color, thin bedded to laminated and not resistent to the weathering processes.

Therefore they display gentle topographic slope and can be easily recognized away from outcrop. In contrast to them, the ignimbrites are thick-bedded (up to 2m) to massif, dark browen to red in color and very resistent to the weathering. They are cut across frequently by vertical cracks, thus they display vertical to sub-vertical columnar structure and very steep scarps (up to 15 m high). The Dalören volcanic rocks are folded and cut across by the neotectonic structures (e.g., oblique-slip normal faults and strike-slip faults), In addition, they are overthrusted from north to south on the Pliocene Mutlu formation in places (Figure 8). The total thickness of the Dalören volcanic rocks is 700 m. Based on both the isotope and geochemical data, the origin of the Dalören volcanic rocks is a partly contaminated hybrid magma formed by the partial melting of lithospheric mantle (Keskin, 2003; Açlan and Turgut, 2017; Açlan and Duruk, 2018; Kansun et al., 2020). Consequently, the Dalören volcanic rocks have an impermeable texture due to the weathering. For this reason, they are one of the significant cover rocks of the DGF.

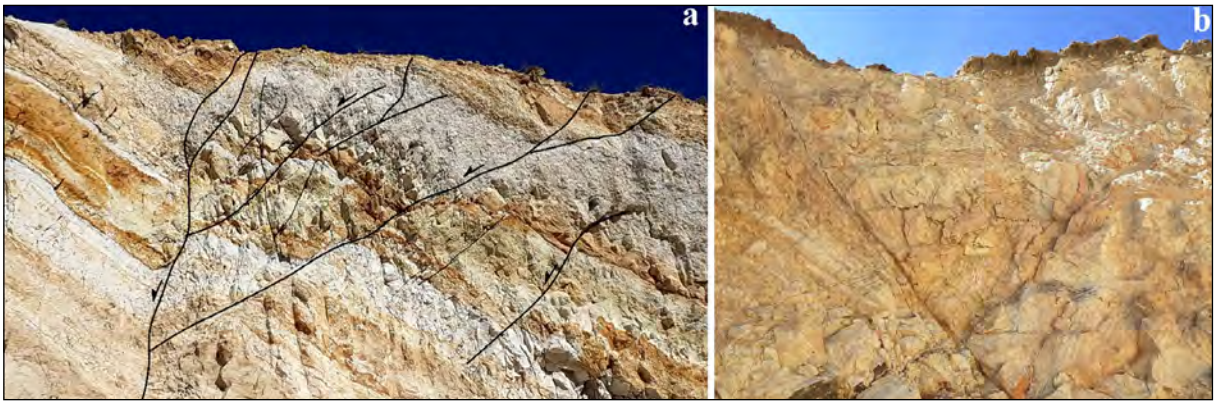

Figure 7- a) Close-up view of the normal growth-faulted tiffite of the Upper Miocene Dalören volcnic rocks (eastern limb of the Burgulu anticline), b) close-up view of intensely fractured (single shear planes and conjugate fractures) tuff-tuffite of the Dalören volcanic rocks.

Figure 8- a) General view of the tectonic contact (reverse fault) between the deformed (folded and oblique-slip normal-faulted) Dalören volcanic rocks (Td) and the Pliocene Mutlu formation (Tm) under the threatening of earth flow, SSW of the Burgulu Village (view to N), b) General view of the burgulu anticline with an approximately N-S trending axis. A. tuff-tuffite, B. ignimbrite, DGF. Diyadin geothermal field (view to N).

3.1.6. Mutlu Formation

In general, the Mutlu formation is represented by a loose and 400 m thick volcanosedimentary sequence of Pliocene age. It is exposed in a relatively small area to the near east-northeast of the Diyadin County in the study area. In contrast, it is the most widespread unit in the area, approximately 2-3 km away from the southern margin of the DGF, i.e., its major outcrops are observed around Mollakara, Aşağı-Yukarı Dalören, Mutlu, Gedik, Saitbeyli, Yolcupınarı, Gözüpek and Oğuloba villages to the south and outside the DGF (Koçyiğit, 2022). At the bottom, the Mutlu formation overlies with an angular unconformity the erosional surface of the Kendel metamorphic rocks. The top of the Mutlu formation is mostly free erosional surface, but some times it is a faulted contact with both the older and younger rocks units owing to the multiple deformation it experienced. Particularly, the top contact of the Mutlu formation is in the nature of thrust to reverse fault with the folded Dalören volcanic rocks of Miocene age (Figure 8). The Mutlu formation begins with a ten meters thick polygenetic to unsorted basal conglomerate on the erosional surface of the Kendel metamorphic rocks at the bottom, and then continues with the alternation of pebble-supported coarse-grained sandstone, siltstone, mudstone, tuff, tuffite, basaltic scoria, obsidian and claystone. The topmost of the sequence is covered by a loose conglomerate-sandstone alternation. Major clasts of basal conglomerate are marble, dolomite, quartzite, calcschist, granite, andesite, rhyolite, basalt and ignimbrite. They are sub- to well-rounded and range from 2 cm to 1.5 m in diameter. They also display

pebble imbrication. One of the major characteristics, which makes the recognition of the Mutlu formation easy, is the widespread earth flows took place within the formation owing to the secondary clay mineralization of claystones included in, and the oversaturation of the loose structure of the Mutlu formation. The second major characteristics of the Mutlu formation is the 3 m-150 m wide and iron-rich alteration zone (Figure 9). It occurs along and nearby the erosional contact separating the overlying Mutlu formation from the underlying marbles of the Kendel metamorphic rocks. From this point of view, this alteration zone reveals, from one hand, the existence of the subsurface geothermal fluid, from other hand, the key role of the Mutlu formation in the development of the DGF, because it is another cover rock of the DGF.

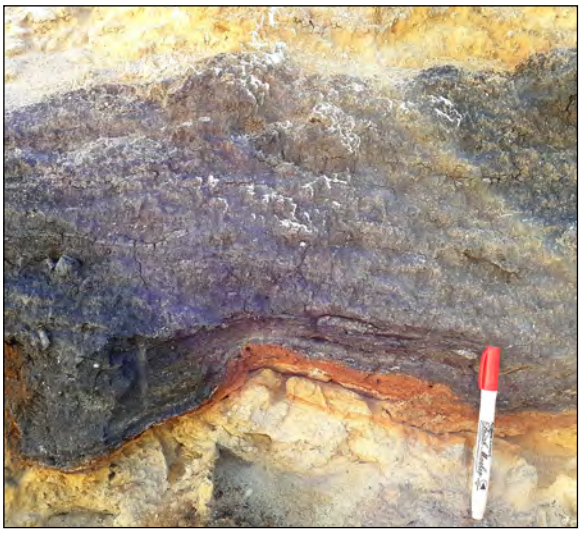

Figure 9- Close-up view of the irone-rich geothermal alteration zone formed in the marble of the Kendel metamorphic rocks close to the erosional bottom contact of the overlying Mutlu formation (SW of Ulukent Town).

3.2. Neotectonic Units: Major Manifestations of DGF

3.2.1. Diyadin Volcanic Rocks

They are exposed in a 0.2-1 km wide, 18 km long and NNW trending belt located between the Kale Hill in the south-southeast and the Omuzbaşı village in the north-northwest (Figures 3 and 4). The Diyadin volcanic rocks are composed of two sections. The lower section consists of basaltic breccia, lapilli, scoria, volcanic glass (obsidian) and tuff in a total thickness of 30-100 m. It is overlain with a sharp contact by the basaltic lava flow, i.e., the upper section of the Diyadin volcanic rocks (Figure 10a). It is dark black in color

Figure 10- a) Close-up view of the Diyadin volcanic rocks of Plio-Quaternary age. A. tuff-tuffite, B. volcanic breccia, and C. Columnar basalt, b) general view of the densely fractured basaltic columnar structure comprising the eastern wall of the Murat canyon (view to E).

and has a total thickness of 40 m. The basaltic lavas are densely fractured and display columnar to flow structures (Figure 10b). They are composed of several phenocrysts such as olivine, pyroxene (augite), apatite and some opaque minerals set in a finer-grained matrix made-up mostly of pyroxene microliths.

In general, the Diyadin volcanic rocks are underlain by the NNW trending open fracture termed here as the Kaletepe open fracture (KOF in Figure 1b). The first volcanic activity in and adjacent to the DGF initiated across two eruption centers, namely the Kaletepe eruption centers, situated at the SSE tip of the KOF around the Davutlar village at the southeast corner of the DGF (Figure 3). The olivine basaltic lavas were poured out of these two eruption centers and then started to flow in down-slope direction up to the Omuzbaşı village by using the KOF, thus the columnar olivine basalts formed by the cooling and solidification of this basaltic lava. The Diyadin volcanic rocks display thermal contact relationships with both the Upper Miocene Dalören volcanic rocks and the Pliocene Mutlu formation, i.e., Diyadin volcanic rocks are relatively younger than them. However, they show gradual top contact relationship with the Plio-Quaternary Göğebakan travertines (Figure 2). For this reason, the relative age of the Diyadin volcanic rocks is Plio-Quaternary. The alkali olivine columnar basalts are also very widespread rocks exposed in Malazgirt (Muş), Tutak (Van), Patnos and Hamur (Ağrı) regions within the east Anatolian tectonic block (EATB) (Türkecan et al., 1992; Esirtgen and Hepşen, 2018; Sümengen, 2009). The radiometric ages of the columnar basalts in these regions are 1.07 ± 0.12 my (Sanver, 1968), 2.0 ± 0.1 my and 3.9 ± 0.4 my (Innocenti et al., 1980), respectively. Consequently, the relative age of the Diyadin volcanic rocks is more or less same as the radiometrik age of these columnar basalts.

The Diyadin columnar basalt is one of the major manifestations of the DGF. Because, it is the production of first fissure eruption in the Diyadin region which triggered the onset of other eruptions and let to the development of nearby Tendürek polygenetic volcano (Figure 1b). In the same way, this event is also the initial key for the development of the strike-slip neotectonic regime and the Diyadin geothermal field. In addition, after this first fissure eruption and formation of the Diyadin columnar basalts, the upstream section of the 722 km long Murat River, which is one of the major branch of the Fırat drainage systemin in the east Anatolia, was settled down along the KOF and carved its bed deeply into the basalts and resulted in a 40 m deep and very narrow canyon, namely the Murat Canyon, during the development of the DGF under the control of strike-slip neotectonic regime. In the present, the Diyadin County is located on the eastern wall of this outstanding morphotectonic structure (Figure 11).

3.2.2. Göğebakan Travertines (Fossil travertines)

This unit was previously mapped and interpreted as a lacustrine limestone by Esirtgen and Hepşen (2018) and Kansun et al. (2020). In contrast to their interpretation, in the present study, it was identified that it is an older travertine deposited by the thermal fluids in the forms of plateau-, terrace-, mound- and

Figure 11- General view of the Murat canyon and the Diyadin County situated on its eastern wall (view to E).

fissure-ridge travertines within the DGF. Even though these travertines have lost the most of their original physical features due to the erosional period they have experienced, their original internal structures can be still observed inside the mining quarries opened in older travertines (Figure 12). In the present study, these older travertines were renamed as the Göğebakan travertine by the name of their type locality (Göğebakan village).

The Göğebakan travertines are the most widespread unit in the DGF (Figures 3 and 4). They cover an area of several tens of km². They show faulted- to erosional contact relationships with the pre-late Pliocene rocks. In contrast, the contact relationship between the Diyadin volcanic rocks and the Göğebakan travertines is conformable. For this reason, the relative age of the Göğebakan travertines is at least Plio-Quaternary. In general, the Göğebakan travertines are composed mostly of medium- to thick-bedded, but rarely massive travertines crossed frequently by open fractures. Total thickness of the Göğebakan travertines is 200 m.

3.2.3. Yeşildurak Formation

This unit is exposed well around Kardeşli, Yeşildurak and Aşağısaatçılar villages along the east-northeastern margin of the Akpazar pull-apart basin (Figures 4a and 4b). It overlies with an angular unconformity the serpentinites of the Kardeşli ophiolitic mélange (Figure 6) and the Paleocene-Eocene Harapköy formation at the bottom (Figure 5). However, it displays an overturned contact relationship with the Paleocene-Eocene Harapköy formation in places (Figure 4b). In general, it shows both the gradual and faulted-contact relationships with the Quaternary basin fill. At the bottom, it begins with the unsorted to polygenetic conglomerates, and then continues with the alternation of sandstones, mudstone, marl and again conglomerates (Figure 13a). Conglomerates are weakly lithified to loose and consists of sub-rounded to rounded clasts of mostly marble, limestone, serpentinite, quartz, andesite, basalt, granite, ignimbrite, chert, radiolarite, diabase (Figures 13b). They range from 2 cm to 75 cm in diameter. They set in a sandy matrix bounded weakly by both calcite and silica cement. Total thicknes of the sequence is 60 m. The yeşildurak formation is nearly flat-lying except for the area adjacent to the active faults. For istance, they are tilted up to 20° and overturned along the northern margin-boundary fault, the Murat fault (Figures 4 and 13a).

Figure 12- Close up view of the internal structure of the Göğebakan travertins (near ENE of the Göğebakan Village).

Figure 13- a) General view of the tilted Yeşildurak formation exposed against the active Murat fault, b) Close-up view of the sharp contact between the underlying mudstone and overlying polygenetic to unsorted conglomerate horizon.

3.2.4. Tendürek Volcanic rocks

The final continent-continent colision and formation of the Bitlis suture zone between the northerly located Eurasian and southerly-located Arabian plates were also accompanied by a post-colisonal volcanic activity of dissimilar chemical composition (Pearce et al., 1990; Ölmez et al., 1994; Yılmaz et al., 1998; Lebedev et al., 2016). This volcanic activity lasted untill the historical times with the occurrence of a series of isolated volconic cones such as Nemrut, Süphan, Tendürek and ağrı volcanoes situated in EATB. The Nemrut, Süphan and Ağrı are the stratovolcanoes formed by the alternation of both pyroclastites and lavas. In contrast to them, the Tendürek is a double-peaked strato-shield volcano covering an area of 650 km². The Tendürek volcano is located in an extensional area provided by the Ağrı, Balıkgölü and Çaldıran fault zones to the near east-southeast of the DGF (Figure 1b). The heights of greater and lesser Tendürek volcanoes are 3549 m and 3319 m respectively (Lebedev et al., 2016). The Tendürek volcano is composed mainly of trachytic lavas-pyroclastites (volcanic breccia, lapilli, tuff) and basaltic lavas to related pyroclastites (volcanic breccia, pumice and obsidian). The total thickness of volcanic sequence is about 1.7 km (Yılmaz et al., 1998). The volcanic sequence rests on both the Paleozoic Kendel metamorphic rocks and the Upper Cretaous east Anatolian accretionary prism (EAAP) at the bottom. The first volcanic activity started with the fissure eruption along the polygenetic Lesser Tendürek stratovolcano and then continued througout the Greater Tendürek shield volcano. The Lesser Tendürek volcano consists of both basic and felsic lavas, while the Greather Tendürek volcano is composed of intermediate to mildly felsic lavas. The present morphology of the Tendürek volcano has formed at five phases during the time slices of 250-200, 200-150, 150-100 and 50 thousand years before present (Lebedev et al., 2016). The Tendürek volcano is at the stage of caldera crossed and deformed by a seris of concentric to radial faults (open fractures). Widespread occurrence of gas and steam outputs (fumaroles) at the foot of the Tendürek volcano and the numerous hot water springs included in the nearby DGF reveal that it is still active in the present. In addition, based on the ratio of C- and He- istopes (C13/C12; He3/He 4), the origin of the gases coming out of the Tendürek volcano is mantle (Ölmez et al., 1994). Consequently, the active Tendürek volcano is another manifestation of the DGF (Figure 1b).

3.2.5. Diyadin Thermogene Fissure-Ridge Travertines

The most diagnostic manifestation of the DGF is the actively growing thermogene fissure-ridge travertines (Figure 3). Travertines are resulted from the deposition of the calcium- and bicarbonate-rich cold to hot waters coming out of the Earth by using the

open fractures, such as the normal faults, because they are the most suitable pathways for the circulation of ground waters. At depths, the CO_2 content of ground water is considerably high. For this reason, it makes the water oversaturated in CO_2, and thus inhibits both the precipitation of $CaCO_3$ and the formation of travertine. In contrast to the process at the depth, both the CO_2 and pressure suddenly release when ground water reaches to the ground surface. This makes the water unsaturated in CO_2, and thus the formation of travertine begins (Figure 14). In this frame, there is a close relationship between active faults and travertine occurrences. The fissure-ridge travertine is one of the most significant recorders of the neotectonic activity (Altunel and Hancock, 1993; Altunel, 1996; Hancock et al., 1999; Altunel and Karabacak, 2005; Koçyiğit, 2005; Brogi et al., 2005; Karabacak, 2007; Mesci et al., 2008; Temiz et al., 2009; Pasvanoğlu, 2013; Koçyiğit and Doğan, 2016; Brogi et al., 2021; Koçyiğit, 2022). For instance, Hancock et al. (1999) proposed the term "Travitonics" to emphasize the close relationship between the travertine formation and active tectonics. Indeed, there is a kinematic relationship between the general strike of the central fissure plane and the operation direction of the greatest principal stress axis (σ1) if the fissure-ridge travertine has developed under the control of σ1. In the case of strike-slip tectonic regime, the strike of the fissure plane is more or less parallel to the σ1 (Brogi and Capezzuoli, 2009; Koçyiğit and Doğan, 2016; Doğan et al., 2019; Brogi et al., 2021), but it is perpendicular to it in the case of tensional tectonic regime and related normal faulting

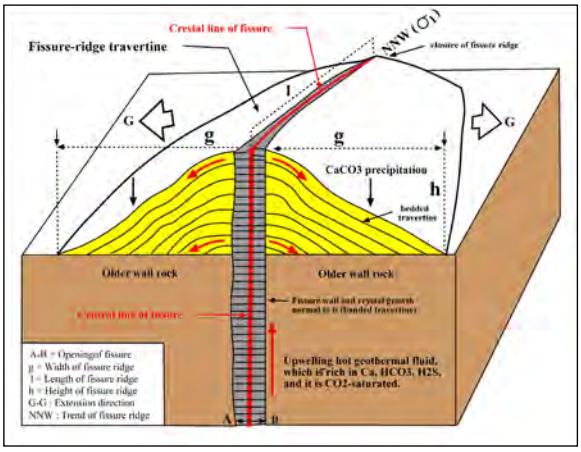

Figure 14- Sketched block diagram illustrating how the fissure ridge travertines are formed.

(Koçyiğit, 2005). The DGF is the type locality for the widespread fissure-ridge travertine occurrences. Therefore, fissure-ridge travertines in the study areas were first named as the Diyadin fissure ridge travertines (DFRT) and analyzed kinematically.

In general, except for several fissure-ridge travertines (Figure 4), most of them are situated in the area among Göğebakan, Taşbasamak, Günbuldu, Altınkilit, Dibekli, Tazekent and Davutköy villages and to the near south of the Diyadin County (Figure 3). For this region, this area was named as the Diyadin geothermal field (DGF). In the same way, the most of hot water springs and the shallow artesian wells are also located in the same area, i.e., the origin of the fissure-ridge travertines is hot water springs in the study area (Figures 3 and 14). Totally sixtyfive fissure-ridge travertines were mapped on 1/25.000 scaled map. They display a structural pattern like a doubly-plunging anticline (Figure 15a) with curvi-linear axis, which corresponds to the central fissure connecting a series of spring orifices (Figure 15b). Their sizes range from 160 m to 1200 m in length (maximum), from 6 m to 36 m in height, and from 66 m to 500 m in width, respectively.

In the same way, the openings of the central fissures range from 10 cm to maximum 13 m where the calcite crystals were grown in a direction normal to the walls of central fissures (Figures 14, 16a, 16b). They trend in N-S, NNE (up to 25°), NNW, NW (up to 65°), WNW and ENE directions. Some of the fissure-ridge travertines are conjugate in pattern where the vertical to sub-vertical open fractures of the fissure-ridge travertines intersect to each other under acute angles. The North East Anatolia (EATB) and the northwest Iran are seismically active regions deformed by both the strike-slip and thrust faulting sourced from the strike-slip neotectonic regime (Koçyiğit, 2013; Moghoori et al., 2021). These authors also determined that the stress field state in the same region is being dominated by N158° (N22°W) trending greatest horizontal compressive stress axis (σ1), sub-vertical intermediate stress axis (σ2) and the N068° (N68°E) trending least principal stress axis (σ3) by using the tensor solution diagrams of the 277 earthquakes took place in the same region. Based on this stress field state, the NNW, NW- NE- and ENE trending faults are the oblique-slip normal, dextral strike-slip, sinistral

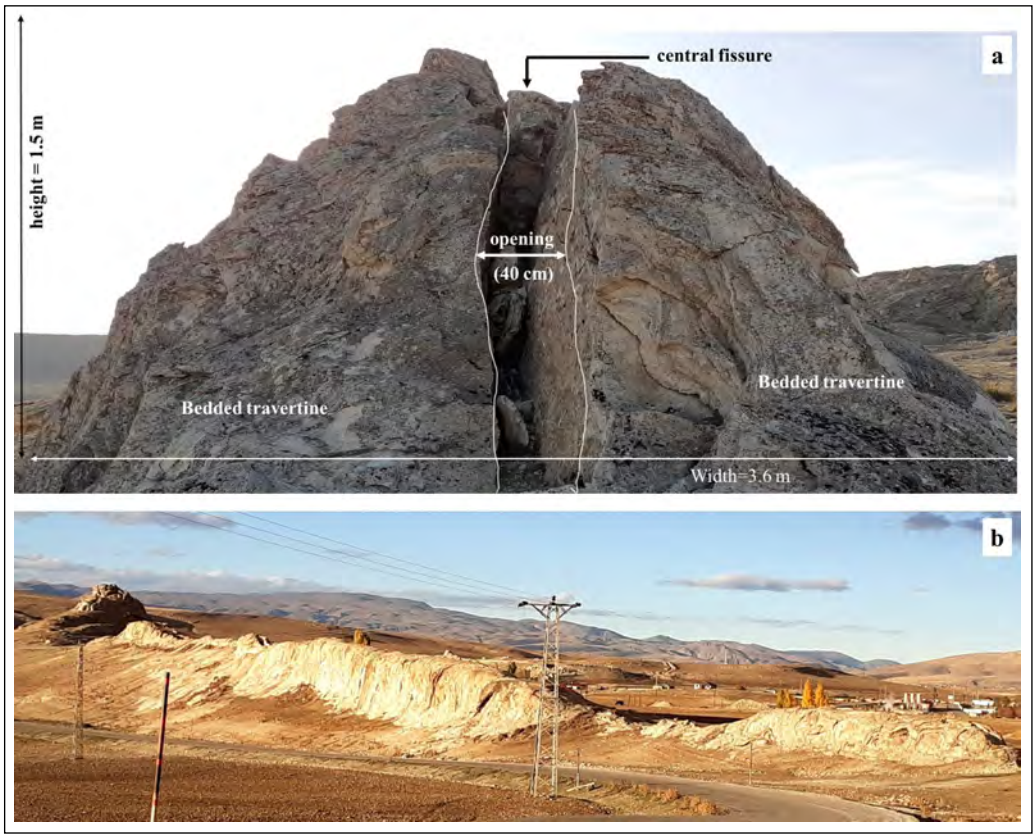

Figure 15-a) Cross-sectional view of the N50W trending fissure-ridge travertine (near north of Yılanlı thermal (YT in Figure 3), b) General view of the N50°W trending Yılanlı fissure-ridge travertine (view to NNE).

strike-slip and the thrust-to reverse faults, respectively. As is seen on geological maps (Figures 3 and 4), the fissure-ridge travertines formed not only along the NNW trending open fractures (normal faults), but also along the NW trending dextral to NE trending sinistral strike-slip faults and approximately ENE trending reverse faults, i.e., the DFRT are multi-directional based on the strikes of fissure-ridge axial planes. This occurrence pattern of the fissure-ridge travertines may imply to the abundance and high sub-surface pressure of the geothermal fluids in the DGF.

The fissure-ridge travertine deposits in the study area have not been dated radiometrically. However, they must be the late Pleistocene to Holocene in age based on the stratigraphical relationships among the travertine occurrences, the Plio-Quaternary columnar basalt and terrace deposits in the DGF (Figures 3 and 4). For instance, the fissure-ridge travertines show gradual contact relationships with the basin floor sediments of the late Quaternary age, while they cut across the Plio-Quaternary Diyadin columnar basalts (Figure 17), i.e., the relative age of the fissure-ridge travertines must be the late Quaternary-recent, because their formation is still lasting in the areas, where the level of regional water table is above ground surface.

In general, from the plate tectonic configuration point of view, fissure-ridge travertines are concentrated not only along the active plate boundaries, but also in both sides (out-and inside) the plate boundaries throughout the territory of Türkiye. The common and well-defined examples of them are as follows: (1) the Reşadiye fissure-ridge travertines (Mesci et al., 2020), (2) Akkaya (Eskipazar-Karabük) fissure-ridge travertines (Yıldırım, 2018), (3) Karakoyun-Yoğunağaç (Elazığ) fissure-ridge travertines (Kalender et al., 2015), (4) Sıcak Çermik (Sivas) fissure-ridge travertines (Mesci et al., 2008; 2018), (5) Kızıltepe (Avcıköy) and Sarıhıdır-Balkayası (Avanos) fissure-ridge travertines (Atabey, 2002; Koçyiğit and Doğan, 2016; Karabacak and Mutlu, 2019; Temiz et al., 2021), (6) Kırşehir fissure-ridge travertines (Atabey, 2002; Temiz et al., 2009), (7) Yaprakhisar-Ziga fissure-

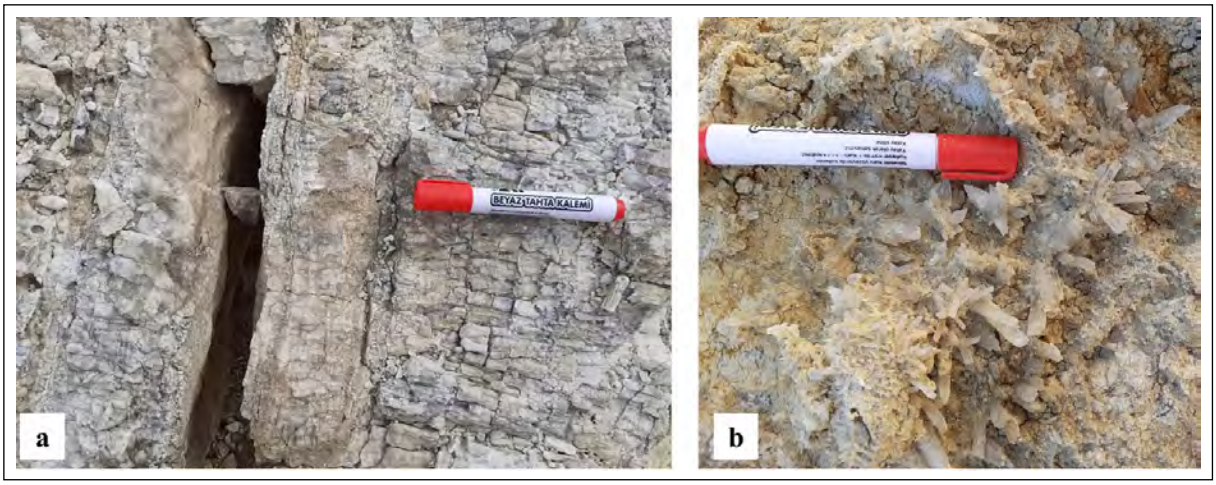

Figure 16- a) Close-up view of calcite minerals grown in a direction normal to the walls of the central fissure, b) Close-up view of calcite crystals.

ridge travertines (Doğan et al., 2019), (8) Urganlı (Manisa) fissure-ridge travertines (Demirkıran and Elçi, 2022), (9) Akhüyük (Ereğli-Konya) fissure-ridge travertines (Şener, 2018; Temiz and Savaş, 2018), (10) Hamamboğzı (Banaz) fissure-ridge (Koçyiğit, 2008), (11) Karahayıt-Pamukkale-Kaklık (Denizli) fissure-ridge travertines (Özkul et al., 2002; Koçyiğit, 2005; De Filippis et al., 2013; Özgür et al., 2017; Van Noten et al., 2018), and (12) Çamlık and Dereiçi (Başkale-Hakkari) fissure-ridge travertines (Sağlam-Selçuk et al., 2017; Yeşilova, 2021). The first two examples are located along the plate boundary, namely the NAFS, i.e. they are strike-slip faulting-induced fissure-ridge travertines. The examples 3 through 8 are intra-plate fissure-ridge travertines formed under the control of again active strike-slip faulting. The examples 9, 10 and 11 are also intra-plate fissure-ridge travertines, but they have developed under the control of tensional tectonic regime, in which the greatest principal stress axis (σ1) is sub-vertical in state. The last one, the example 12, is located in the EATB, and it's all characteristics are more or less same with those of the DFRT. The description of all these fissure-ridge travertines is outside of the paper. For this reason, readers, who are interested in fissure-ridge traverines, are kindly invited to see the above-mentioned papers and other literatures therein.

In general, one of the most diagnostic ground surface manifestations of geothermal fields is the thermogene fissure-ridge travertine. Recently, two well-defined fissure-ridge travertines were reported

Figure 17-General view of the N-S trending vertical fissure-ridge travertine (B) cutting across the Plio-Quaternary Diyadin columnar basalt (A) (eastern wall of the Murat Canyon).

from Italy, and introduced to the international literature. These are the Terme San Giovanni fissure-ridge travertine (Brogi and Capezzuli, 2009), and the Colle Fiorito fissure-ridge travertine (De Filippis et al., 2013). The first one is located in the Rapolano Terme area along the western margin of the Plio-Quaternary Siena basin shaping the interior side of the north-western Apennine chain. The second one is located at the southeastern tip of a NW-trending depression or paleograben (the Acque Albule Basin) drained by both the Tiber (Tevere) and Aniene Rivers cutting across the Roman magmatic system in the Tyrrhenian back-arc region or Tuscan geothermal field. Both of these fissure-ridge travertines have been formed along the normal faults under the control of a prominent

tensional tectonic regime accompanied secondly by the dextral strike-slip tectonic regime (Brogi and Capezzuli, 2009; De Filippis et al., 2013; Mancini et al., 2014; Porta et al., 2017; Vignaroli et al., 2020). The DFRT can be correlated with both of these two fissure-ridge travertines based on the age, hydro-chemical composition, morphology and the close-relationship with the active volcanoes. However, there are two basic contrasts among them: (1) The DFRT has developed in a pull-apart basin under the control of strike-slip neotectonic regime and related faults, (2) this fissure ridge travertine is multi-directional in the nature of it's strike of crestal fissure. In contrast to the DFRT, both the Terme San Giovanni fissure-ridge travertine and the Colle Fiorite fissure travertine are unidirectional and they have developed along the traces of active normal faults under the control of a tensional tectonic regime.

3.2.6. Thermal Springs and Artesian Wells

Recently a detailed geological to geochemical studies have been carried out on the natural mineral waters in both the central and periferal counties, such as Hamur, Patnos, Taşlıçay, Diyadin, Doğubayazıt, and Elekirt, of the city of Ağrı (Üçgün et al., 2014; Üçgün, 2019). They determined 37 thermal springs. 12 of them are in the nature of geothermal, the rest 25 are normal natural water springs. In addition, 15 of them are located in the Diyadin district. More or less, all of the hot water springs (Figure 18) and the artesian types of boreholes are concentrated in an approximately triangular area among Davutköy, Göğebakan and Tazekent villages (Figure 3) called so that "Diyadin Kaplıcaları" (Üçgün et al., 2014). Indeed, they are more widespread at four localities in this area. In terms of their names, these hot water springs were locally named as the Tazekent, Davutlar, Yılanlı and Bridge thermals respectively (TT, DT, YT and BT in Figure 3). The outlet temperatures of both hot water springs and wells range from 37°C to 78°C (Mutlu et al., 2013). Both the Yılanlı and Köprü thermals waters are also rich in sulfur. In a 35 m deep borehole drilled on the Mollakara-Gedik road (outside of the study area) passing along the western side of the Murat River flood plain, a hot water spring with the outlet temperature of 72°C erupted. In the present, hot waters of this artesian well are being used as an open air spa by the inhabitants of this region. In the same way, MTA drilled several boreholes with the depths ranging from 77 m to 215 m in the area between Yılanlı and Davutköy thermals (MTA in Figure 3). These wells also made artesian and hot waters with the outlet temperature of 62°C-78 °C poured out of the earth (Demirel and Özkan, 2000; Demir, 2006). Another borehole was drilled just on a NE trending fissure ridge travertine in the area very close to MTA wells (ABG in Figure 3), and a hot water with temperature of 65°C was obtained in the borehole at the depth

Figure 18- a) General view of a hot water spring with the outlet temperature of 50°C situated on the western side of the N50°W trending Bridge fissure ridge travertine in background (view to NE), b) close-up view of an again hot water spring among several mound-types of travertines up to 1.5 m high and 60 cm in diameter occurred at the same locality.

of 250 m. These waters are being used to heat the greenhouse (GH in Figure 3) constructed close to the well (Abdül Bahri Güzel, personal communication, 2021, Doğubayazıt). In general, hot and cold waters are in the composition of Na-HCO_3 and Ca-HCO_3 respectively. However, they also contain high amount of CO_2, H_2S and arsenic (As) in places. They are also meteoric in origin based on both oxygen- and hydrogen isotopes (Mutlu et al., 2013).

3.2.7. Quaternary Basin Fill

It consists of two major lithofacies based on their grain sizes and depositional settings. They are: (1) coarse-grained marginal facies, and (2) finer-grained basin floor facies. The marginal facies are represented by terrace deposits, older to recent superimposed alluvial fan deposits, and slope scree deposits. They are exposed widely along the fault-bounded margins of the Akpazar pull-apart basin (Figures 4a and 4b). Terrace deposits are observed well, in places, along the margins of the Murat River flood plain (Figure 3). The older flood plain deposits of the Murat River have been cut uplifted (up to 100 m) and then left as the fault terraces at different elevations (Figure 3). This observation reveals that both the flood plain of the Murat River drainage system and the margin-boundary faults of the Akpazar pull-apart basin are under the control of an active neotectonic regime. Alluvial fans show a fault-parallel aligned distribution pattern in different sizes ranging from several tens of m² to a few km². They consist of unsorted to polygenetic boulder blocks of mostly marble, schists, quartz, limestone, radiolarite, granite, diabase, spilite, ignimbrite, chert, and volcanic glass set in a sandy matrix at and nearby the apex of alluvial fans. Components of these loose conglomerate decrease in size and show a sorted texture towards the distal sections of alluvial fans. Some of the alluvial fans are in a superimposed pattern where older and larger fans are overlain by a number of smaller and younger alluvial fans. This pattern indicates that they have experienced a short term of non-depositional period followed by a sudden and high tectonic activity during their evolutionary history. One diagnostic example of these patterns is exposed well at the eastern tip of the Akpazar pull-apart basin (Figure 4b).

The second major lithofacies of the basin fill are composed of sandstone, siltstone, mudstone alternation with the intercalation of both the point- to mid-channel bar deposits, They show lateral and vertical gradational contact relationships with the organic material-rich claystone deposited in marsh and ponds. In addition, one of the largest fissure-ridge travertines (Akpazar fissure-ridge travertine) is included in the basin fill of the Akpazar pull-apart basin (Figure 4a). It is an about 1 km long, 200 m wide, 36 m high and trends N70°W direction. It cuts across the basin fill and still lasts to develop (Figure 19). Total thickness of the Quaternary basin fill ranges from 10 m to 100 m (maximum).

4. Akpazar pull-Apart Basin and Its Margin-Boundary Faults

In this region, the Akpazar pull-apart basin and its margin-boundary faults are other diagnostic manifestations of the DGF. It is drained by the Murat

Figure 19- General view of the N70°W trending Akpazar fissure-ridge travertine (View to WNW).

River drainage system (Figure 4a). The Akpazar pull-apart basin is an approximately 17.2 km long, 0.5 -5.5 km wide and WNW trending depression of Quaternary age. It is situated between the Esen settlement to the west-northwest (Figure 4a) and the near east of Aşağısaatçılar village to the east-southeast (Figure 4b). The northern margin of the basin is more or less linear, while its southern margin is uneven in shape. For this reason the northern margin is determined and controlled by only one and linear structure, namely the Murat master fault (Figures 4a and b). In contrast to the northern margin, the southern margin of the Akpazar pull-apart basin is determined and controlled by a number of fault segments of dissimilar length, type and trend (Figure 4a). They trend in N-S, E-W, NNE, NW, NE and WNW directions, while their lengths range from 0.5 km to 9 km (maximum). Based on the stress field state in this region (Mokhoori et al., 2021), these fault segments are in different character such as normal, dextral to sinistral strike-slip, and reverse faults. The Quaternary basin fill of the Akpazar pull-apart basin is tectonically juxtaposed with various basement rocks of dissimilar age, lithology and deformation pattern by these fault segments along the southern margin of the basin. The longest fault segment bounding the southeastern margin of the Akpazar pull-apart basin is the Seyit fault. It consists of two segments cut and offset by another short and N-S trending fault segment (Figure 4a). These two segments are totally 9 km in length, and located in the area between Seyit village to the WNW (Figure 4a) and Çalışkan Village to the ESE (Figure 3). The southeastern segment of the Seyit fault displays northerly facing stepped land shape and juxtaposes tectonically Quaternary alluvial sediments with the Plio-Quaternary Göğebakan travertines. The linear fault trace, steep fault scarp and fault-parallel aligned earthflows (Figure 20) imply to the existence and activeness of the Seyit fault segments.

The eastern margins of both the Akpazar pull-apart basin and the DGF are determined and controlled by the Adakent fault zone (AFZ). It is totally 20 km long, 2-4 km wide and N-S trending active fault zone situated between the Taşkesen village to the south and near east of the Aşağısaatçılar settlement to the north (Figures 3 and 4b). The AFZ consists of numerous fault segments of dissimilar lengths, trends and character. These are the N-S trending normal, NW to WNW trending dextral strike-slip and NE trending sinistral strike-slip fault segments. The N-S trending fault segments are prominent structures. Lengths of the fault segments range from 0.2 km to 11 km (maximum). They cut across both the paleotectonic units and the Plio-Quaternary basin fill, and tectonically juxtapose them with to each other. In general, western blocks of fault segments comprising the Adakent fault zone were thrown downward up to 400 m.

The northern margin of the Akpazar pull-apart basin is bounded and controlled by the master fault (Murat fault) of the Ağrı fault zone, which was first identified and reported in this study. The Ağrı fault zone is an about 5-22 km wide, 120 km long and

Figure 20- General view of the stepped Seyit faults, which bound and control southeastern margin of the Akpazar pull-apart basin (view to SSW). L. Earth flow.

WNW trending dextral strike-slip fault zone. It begins from the near north-east of the Eleşkirt County (Ağrı) to the west and outside of the study area, and then continues in ESE direction along the Ağrı pull-apart basin up to the Kumlubucak-Esen settlements, where it enters into the Akpazar pull-apart basin (Figures 4a and 4b). The Ağrı fault zone determines and controls northern margins of both the Ağrı and Akpazar pull-apart basins along its entire length. It consists of numerous, parallel to sub-parallel fault segments of different length, type and trend. The WNW trending dextral strike-slip fault segments are prominent. They cut across the Quaternary alluvial deposits, alluvial fans, stream beds and deflect to offset them in dextral directions. These relationships are observed well in the eastern section of the Ağrı pull-apart basin (Figure 21). In this area, the Murat River flows in WNW direction up to the city center of Ağrı, where it bends to SSE direction and exits the Ağrı pull-apart basin (Figure 21). In the eastern section of the Ağrı pull-apart basin, some sub-branches and their tributaries of the Murat River such as the Korşu stream and its tributaries, which flow in south direction along the northern margin of the basin, are cut, deflected and offset up to 21 km in dextral direction by the Ağrı fault zone and its master fault, the Murat fault, (A-A'= 21 km in Figure 21). This value indicates that the uniform slip rate along the Ağrı fault zone is 8.1 mm/yr (21 km/ 2.59 Ma = 8.1 mm/yr.) during the Quaternary neotectonic period. It also reveals that the magnitude of the peak earthquake to be sourced from the Ağrı fault zone is Mw = 6 or greater. To the near east of the Kumlubucak settlement, a N-S trending sill (highland) occurs and separates the easterly located Akpazar and westerly located Ağrı pull-apart basins from each other. However, the Murat fault cuts this high land and then continues up to 1 km northeast of the Omuzbaşı village where it jumps towards north and results in a left-stepping (restraining stepover) for 2 km distance around the Yeşildurak Village along the northern margin of the Akpazar pull-apart basin (Figures 4a and 4b). Here after, it runs in the same direction up to the near east of Aşağısaatçılar village, intersects with the N-S trending Adakent fault zone and then terminates at the easternmost tip of the Akpazar pull-apart basin (Figure 4b). The total length of the Murat fault in the study area is 17 km, and it consists of two segments. They determine and control the northern margin of the basin. As in the case of the Ağrı pull-apart basin, a number of alluvial fans of dissimilar size occur along the northern margin of the Akpazar pull-apart basin. They are also cut and deformed by the Murat fault (Figures 4a, 4b and 5).

5. Regional Fault Systems and Zones

These are the Tebriz (Tabriz), Erciş-Dorutay, Çaldıran, Ağrı, Balıkgölü (Gailatu), Siah Cheshmeh-Khoy, Iğdır, Aras and the Nakhichevan (Nahçivan) fault zones. Except for the Ağrı fault zone, remaining fault zones are situated outside of the study area. They have a key role in the development of the geothermal system in both the northwest Iran and northeastern Anatolia or EATB. For this reaon, their significant characteristics are described briefly below.

5.1. Tebriz Fault System

In general, the Tebriz fault system is an about 25 km wide, 210 km long, NW trending and seismologically very acctive dextral strike-slip fault structure. It is situated between the Bozkuş Mt. to the southeast and the near north-northwest of the Lake Urumiye to the norhwest (Figure 22). It consists of two major strands separated from one another by the intervening extensional right stepping (a pull-apart basin), where the City of Tebriz is situated (Figure 23) (Hessami et al., 2003; Aghajany et al., 2017). The western strand is known as the North Tebriz fault system, while the eastern one is termed as the South Tebriz fault system (Figure 22). Both the northwestern and southeastern sections of the North Tebriz fault system were moved by both the M 7.1 1721 and M 7.3 1780 historical earthquakes respectively; accordingly 35-50 km and 42-45 km long surface ruptures also occurred during these destructive earthquakes (Karakhanian et al., 2004). In addition, the slip rate on the North Tebriz fault system is 7 ± 1 mm/yr., and this value reveals that the return period of Mw 7.0 or greater earthquakes to be sorced from the North Tebriz fault system is between 250-300 yr. (Djamour et al., 2011). To the north-northwest of the Lake Urumiye, the North Tebriz fault system bifurcates into several fault zones, such as the Salmas, Erciş-Dorutay, Çaldıran, Balıkgölü-Siah Cheshmeh-Khoy, Iğdır, Aras and Nakhichevan fault zones, in the directions of E-W, WSW, NW and NNW, and then results in an extensional horse tail structures

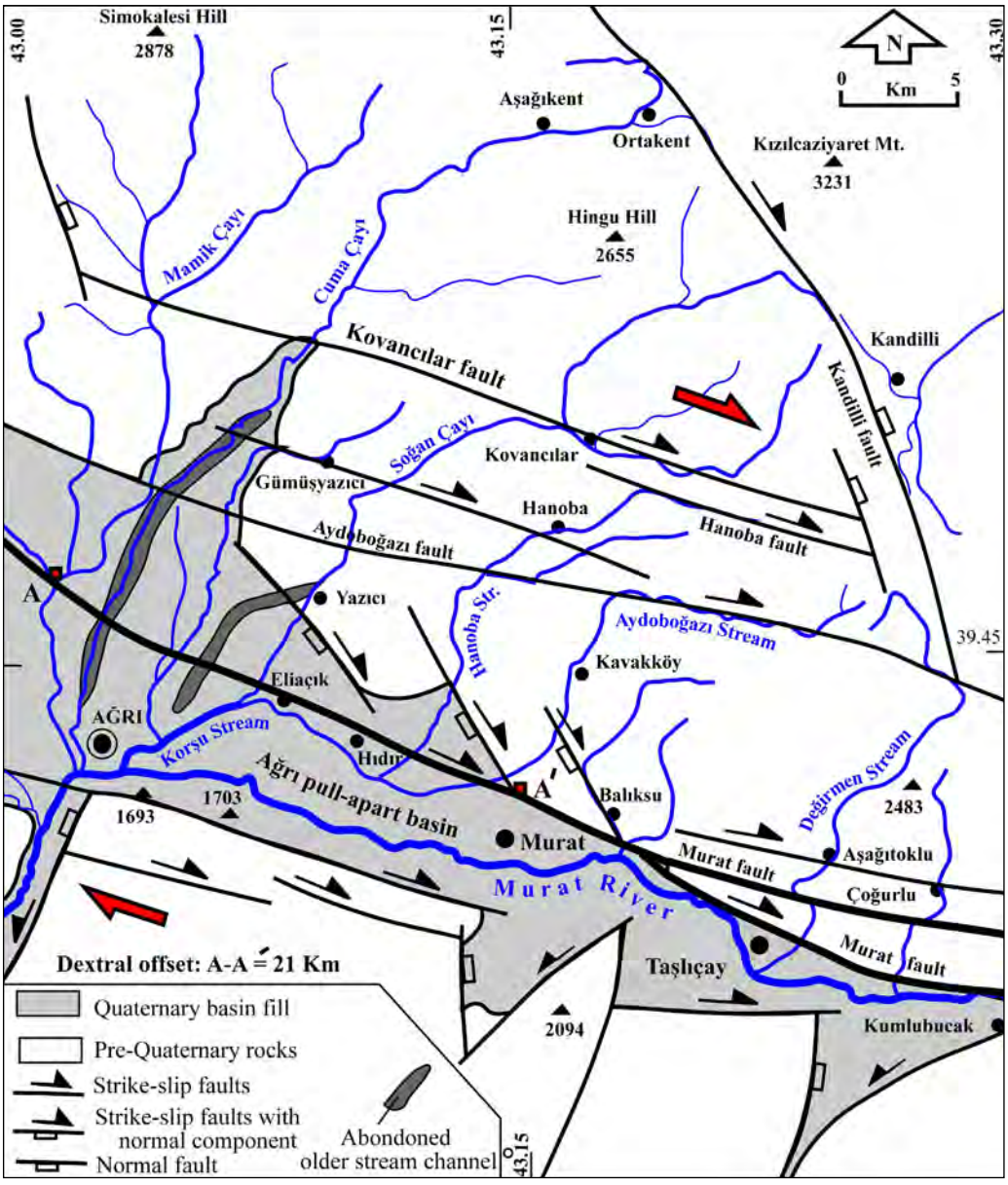

Figure 21-Neotectonic map of the eastern section of the Ağrı pull-apart basin and the offset drainage system (A- A'= 21 km) along the northern margin-boundary faults.

(Figure 22) (Copley and Jackson, 2006; Reilinger et al., 2006; Djamour et al., 2011). The most diagnostic menifestations of this extensional structueres are the DGF and the Tendürek to Ağrı volcanoes of Quaternary age. The most seismologically active one of these fault zones is the Çaldıran dextral fault zone, along which the motion on the North Tebriz fault system are being transferred towards northest Türkiye, i.e., into the EATB (Djamour et al., 2011).

5.2. Erciş-Dorutay Fault Zone

The Erciş fault zone is a 2-10 km wide, 90 km long and N40°-60°W trending active dextral strike-slip fault zone. It is located to the south and 45 km away from the study area It begins from the Patnos County to the northwest and outside the study area and then runs across the Erciş County, the Girekol, Etrüsk and Pirreşit volcanoes and Dorutay Town,

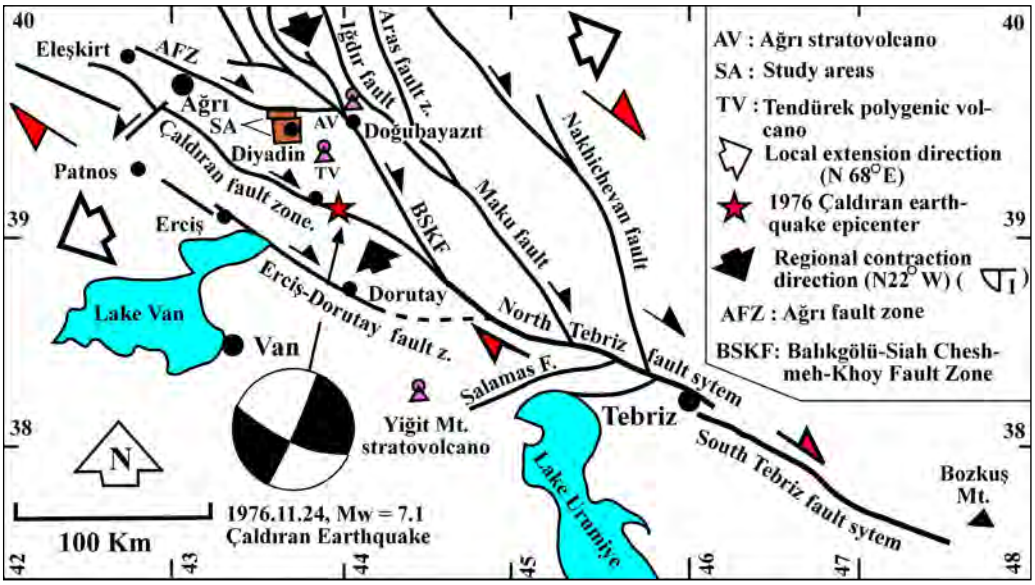

Figure 22-Simplified map illustrating the extensional horse tail structure (releasing type of horse-tail splay faults) in northeast Türkiye, Armania, Nakhichevan and northwest Iran.

Figure 23-General view of the Tebriz fault trace (F), its steep scarp and the city of Tebriz situated on the releasing stepover (view to N).

lastly. terminates near by the Turkish-Iranian State border to the southeast (Figures 22 and 24). The Erciş-Dorutay fault zone, which determines and controls the northeastern margin of the Van basin, consists of numerous, relatively short, parallel to sub-paralel and discontinuous fault segments of dissimilar length and trend. Among them the NW trending fault segments are prominent. The Erciş section was moved during the 23 October 2011 Tabanlı (Van) earthquake of Mw 7.2, and caused heavy damage and loss of life in these settlements (Koçyiğit, 2013). The small to intermediate seismic activity in and around this area are still lasting (Figure 24). Several stream beds (e.g., the Deliçay River) and alluvial fans are being cut, deformed and offset up to 850 m in dextral direction. Based on the offst morphotectonic features, the slip rate on the Erciş fault zone is 2.02 ± 0.12 mm/yr. (Sağlam-Selçuk and Kul, 2021).

5.3. Çaldıran Fault Zone

The Çaldıran fault zone was first determined and reported by Arpat et al. (1977). It is 2-8 km wide, 55 km long, N50°-80°W trending and northerly steeply dipping to convex dextral strike-slip fault zone. It begins from the Sarıkök settlement at the eastern foot of the Azizan volcano and then continues in southeast direction. Along its whole length it cuts across, in turn, the Kösedağ Volcano, the Hıdırmenteş sag pond, and the Çaldıran pull-apart basin, and offsets them in

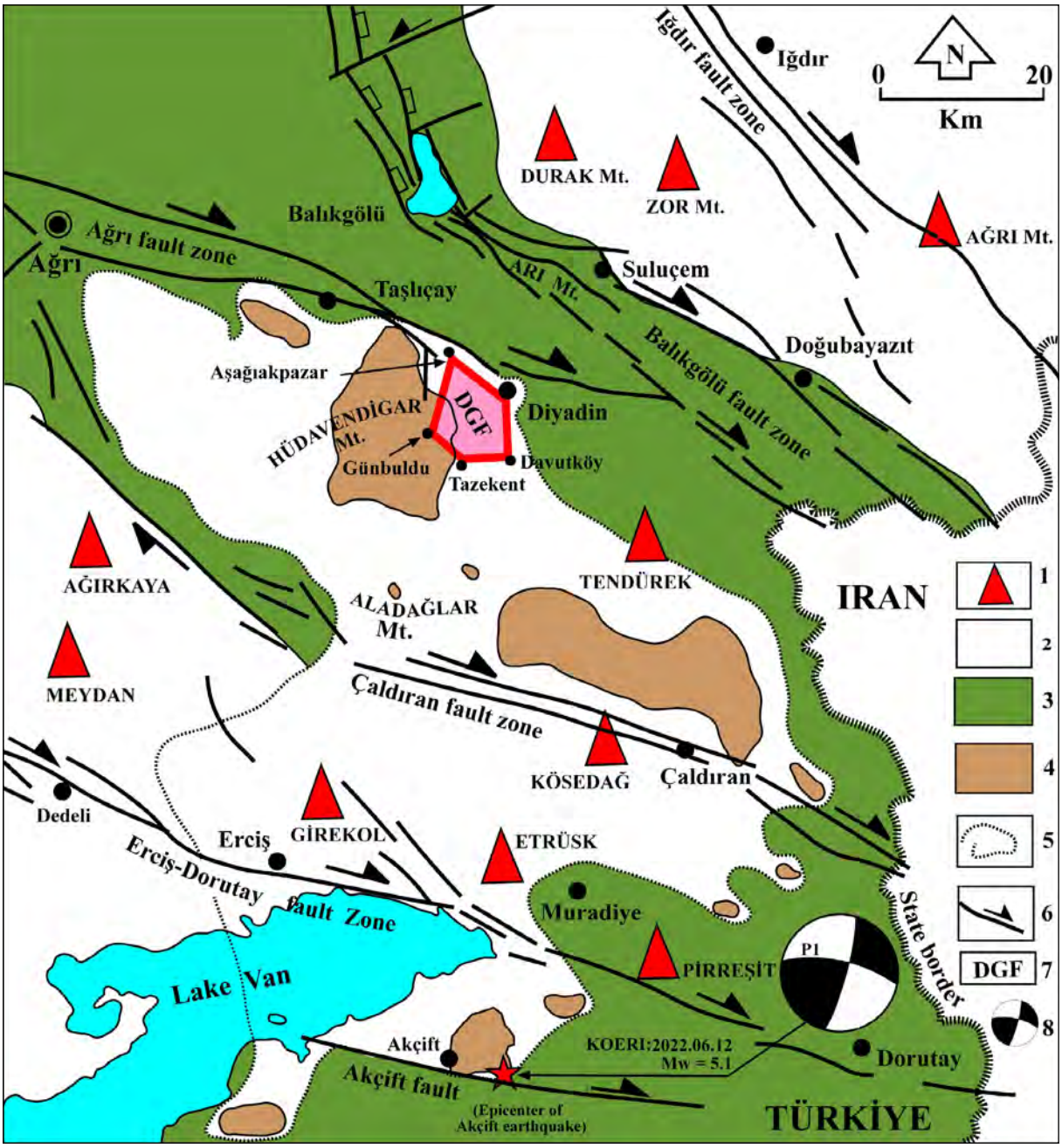

Figure 24-Simplified map illustrating distribution of both the reservoir and cover rocks of the geothermal system in eastern Anatolia. 1- isolated volcanic cones of Quaternary age, 2- post-collisional volcanic rocks sequence of late Miocene-Quaternary age, and the Neogene sedimentary sequence, 3- East Anatolian accretionary prism of Cretaceous-Paleocene age (EAAP), 4- Metamorphic rocks (Kendel metamorphic rocks) of Paleozoic age, 5-Approximate boundary of metamorphic rocks, 6- Active strike-slip fault zones, 7-Diyadin geothermal field and 8- Tensor solution diagram of Akçift earthquake (P1: source of earthquake-KOERI, 2022) (modified from Lebedev et al., 2016).

dextral direction. Lastly it joins with the North Tebriz fault system and terminates nearby the Gülderen to Baydoğan settlements at the Turkish-Iranian State border (Figures 1b and 22). The Çaldıran fault zone consists of numerous, parallel to sub-parallel, discontinuous fault segments of dissimilar length and trend. Along its whole length, the Çaldıran fault zone bifurcates and jumps to right and results in extensional steppings (releasing stepovers) such as the Dedebulak, Çaldıran and Siyahçeşme pull-apart basins (Figure 1b) (Şaroğlu et al., 1987; King and Nabelek, 1985; Sağlam-Selçuk et al., 2016). The Çaldıran fault zone was moved by the 24 December 1976 Çaldıran earthquake of Mw = 7.3 and led to the occurrence of an approximately 50 km long surface rupture with the coseismic dextral offset of 3.5 km (maximum) (Arpat et al, 1977; Toksöz et al., 1977; Ambraseys and Jackson, 1998; Tan et al., 2008). During the 1976 Çaldıran earthquake, whose epicenter is 25 km away from our study area, some settlements in the study area were heavily damaged. In addition, based on the GPS and morphotectonic data, both the Erciş-Dorutay and Çaldıran fault zones together were interpreted as the northwestern continuation of the North Tebriz fault system and reported that they are comprising the southwestern boundary of the Lesser caucasus-Talesh tectonic block moving in northeast direction (Copley and Jackson, 2006; Reilinger et al., 2006, Djamour et al., 2011). Same authors have also reported that the slip rate along this boundary, i.e., along the Erciş-Dorutay and Çaldıran fault zones, ranges from 7.2 mm/yr to 11mm/yr. In contrast to this values, it was determined and reported as the 3.27 ± 0.17 mm/yr based on the field geological data such as the offset formation boundaries (Sağlam-Selçuk et al., 2016). Based on a trench studies (paleoseismological studies) carried out on the master fault of the Çaldıran fault zone by Güneyli et al. (2020), the slip rate and the return period of the peak earthquake to be sourced from the Çaldıran fault were determined once more as the 5.36 mm/yr and 280 yrs., respectively. Both the Deliçay and the Zilan Çayı, which amonate from the peak of the Aladağlar Mt. highland and then flow down-slope direction towards south, are cut and offset by the Çaldıran fault zone up to 12 km in dextral direction. Based on field observation, the slip rate on the Çaldıran fault zone is about 4.8 mm/yr. As is seen obviously from these descriptions, there is still no a common agrement about the slip rate along the Çaldıran fault zone.

5.4. Balıkgölü Fault Zone

This structure is an abaout 4-20 km wide, 127 km long (Turkish section) and NNW to NW trending active dextral strike-slip fault zone. It was first determined and reported by Arpat et al. (1977). It was also renamed and introduced to the international literature as the Gailatu (Balıkgölü)-Siah Cheshmeh-Khoy Fault (GSKF) comprising the northwestern section of the North Tebriz Fault System (Karakhanian et al., 2004; Mokhoori et al., 2021). Based on both the type and general trend, the Balıkgölü fault zone consists of two major sections: (1) Balıkgölü section and (2) the Arı Mountain section. The 35 km long and NNW trending Balıkgölü section consists of several parallel to sub-parallel, short normal fault segments cut and offset in left-lateral direction by NE trending sinistral strike-slip faults. The Quaternary Balıkgölü pull-apart basin lasts to develop on the down-thrown blocks of the normal fault segments (Figure 1b). The 92 km long and NW trending Arı Mountain section is situated between the southern coastal area of the Balıkgölü to the northwest and the Kızılkent-Gürbulak settlements to the southeast nearby the Turkish-Iranian State border (Figure 1b). This section consists of numerous fault segments of dissimilar size, trend and character. However, the NW trending dextral fault segments are prominent with respect to others. They bifurcate, rejoin and result in several lensoidal blocks with long axes more or less parallel to the general trend of the fault zone. Several pushups and pull-apart basins formed by the uplifting and subsidence of the lensoidal blocks, respectively. The more diagnostic of them is the Arı Mountain Pushup and the Doğubayazıt pull-apart basin (DPAB in Figure 1b). The Arı Mountain section is divided into two sub-sections around Doğubayazıt. The northern one passes across the state border and then continues as the Maku fault in NW Iran. However, the southern sub-section (the Kızılkent fault) psses the state border near by the Kızılkent Town and then runs in again SE direction in Iran. Lastly it joins with the Siah Cheshmeh-Khoy fault zone, which is the northwestern section of the North Tebriz Fault System (Figure 1b). Around the Turkish-Iranian State border, both the northerly situated Balıkgölü and the southerly located Çaldıran

fault zones are linked to each other by the intervening and N-S trending normal faults and related pull-apart basins such as the Uzunyol to Haramlı normal faults and the Çaldıran to Siyah Çeşme pull-apart basins. In addition, two of the most diagnostic extensional structures, namely the Tendürek Volcano and related geothermal field (DGF) of the late Quaternary age, also occur in the same area (Figure 1b). Numerous morphotectonic features, such as the triangular facets, steep to sub-vertical fault scarps, fault terraces, fault valleys, offset drainage systems, fault parallel-aligned to deformed alluvial fans and deltas, narrow-long to deep fault corridors, fault-parallel-aligned sag ponds to springs althogether, reveal that the Balıkgölü fault zone is active (Öztürk, 2020). In addition, based on both the field geological and GPS data the slip rate on the Balıkgölü fault zone is 2-3 mm /yr (Copley and Jackson, 2006).

5.5. Iğdır and Aras Fault Zones

This is an about 3-4 km wide, 75 km long and N60°W trending dextral strike-slip fault zone. It is located between Tuzluca County to the northwest and east of the Ağrı stratovolcano to the southeast (Figure 1b). The Iğdır fault zone determines and controls the southwestern margin of the Aras pull-apart basin. It is an approximately15-35 km wide, 200 km long and NW trending pull-apart basin situated among Türkiye, Armania and Nakhichevan (Azerbaijan). The Aras pull-apart basin is drained by the Aras drainage system and has a very thick (up to 250 m) Quaternary basin fill. The northern and the southwestern margins of this large depression are shaped by the Quaternary Alagöz (Aragast) and Ağrı strato volcanoes respectively. The Iğdır fault zone begins near the Tuzluca County to the northwest and then continues in southeastwards in several paralel to sub-paralel discontinues dextral strike-slip fault segments. The longest and continuous one is termed here as the Iğdır master fault. It cuts across the Cretaceous ophiolitic mélange (Kardeşli ophiolitic mélange), Quaternary volcanic rocks of Durak, Zor and Ağrı Mountains as well as the Quaternary basin fill, and then tectonically juxtaposes them with to each others (Figure 1b). A series of morphotectonic features, such as the fault-parallel aligned and deformed alluvial fans, hanging valleys, fault terraces, deflected to offset stream beds, triangular facets and steep fault scarps, indicate that the Iğdır master fault is geologically active. This was also proved once more by both the 6 July 1840 very destructive historical earthquake and the 4 September 1962 instrumental Iğdır earthquake of Mw = 5.6 sourced from the Iğdır master fault (Soysal et al., 1981; Karakhanian et al., 2002; 2004; Bozkuş et al., 2010). The 1840 Ağrı historical earthquake has also led to heavy damage, loss of numerous lifes in the surrounding settlements and large-scale mass-wasting events such as earth flows, floodings, rockfalls, debris flows, creep, liquefactions to lateral spreading of ground in a boroad area. In addition, the Ağrı volcano was reactivated once more and it started to pour out lavas and pyroclastites (Soysal et al., 1981; Karakhanian et al., 2002; 2004).

The Aras fault zone is 4-7 km wide, 120 km long and NW trending dextral strike-slip fault zone. It begins from the near north of rhe Artaşat City to the norhwest and then runs in southeastwards across the western Armenia and Nakhichevan countries. In the further southeast it joins with the Maku fault zone and then terminates. Its only the 54 km long Ararat section (central section) is included in the study area (Figure 1b). The Aras fault zone determines and controls the southestern margin of the Aras pull-apart basin. It consists of several fault segments, which cut both older rocks and Quaternary basin fill and tectonically juxtaposes them with to each others (Figure 1b). The bed of the Aras River is shifted towards the Aras fault zone along its whole length which implies to the activeness of the Aras fault zone.

Consequently, the whole of above-mentioned regional dextral active fault zones are linked to each other by the intervening extensional structures, such as the Aras, Siyah Çeşme, Çaldıran and Akpazar pull-apart basins and the N-S to NNW trending oblique-slip normal faults (Figure 1b). These regional strike-slip fault zones also display a northwestward-opening extensional horsetail structure characterized by both the DGF and the Ağrı to Tendürek volcanic cones of the the late Quaternary age which owe their origins to the same faulting mechanism.

6. Discussion on Geothermal Potential and Conceptual Model of East Anatolia

In general major factors, which control development of the geothermal fields, are active

tectonic regime and related faults, plate boundaries and/or proximity to them, shallow-seated Curie point depth (CPD), high heat flow, young volcanic activity, young hypabyssal intrusions with felsic to intermediate chemical compositions, thinned crust and ascended asthenospheric mantle, a thick package of rocks with high porosity or reservoir rock (s), a package of impermeable rocks or cover rocks, and meteoric water supply enough. These criteria were interpreted under the light of both the above-mentioned field geological data and the international literature, and a conceptual model for the geothermal potential of the eastern Anatolia were prepared (Figure 25).

As is seen in Figure 22, some regional dextral fault zones situated in the EATB, Armenia and Nakhichevan continue throughout the northwestern territory of Iran, approach to each others, and lastly join with the North Tebriz Fault system in the further southeast (Figure 22). Another to say, the North Tebriz Fault system bifurcates into several fault zones at its northwestern tip, and then results in an extensional horse tail structure (a releasing type of horse-tail splay faults structure) (Copley and Jackson, 2006; Masson et al., 2006; Djamour et al., 2011; Shabanian et al., 2012; Mokhoori et al., 2021). In addition, the northern half of this horse tail structure together with the Lesser Caucasus are moving towards northeast, i.e., this area is beeing expanded in NE-SW direction (large open arrows in Figure 22) (Jackson, 1992; Copley and Jackson, 2006; Reilinger et al., 2006), On the other hand, based on the geophysical studies carried out in eastern Anatolia, the average thickness of the crust ia 45 km (Zor et al., 2003), and there is no a mantle lithosphere beneath the continental crust, i.e., the continental crust is floating on the ascended and very hot (1285°C) asthenospheric mantle (Keskin, 2003; Barazangi et al., 2006). In this frame, the continental crust in eastern Anatolia is represented by the East Anatolian Accretionary Prism (Figures 24 and 25). Consequently, the origin of the Upper Miocene-Quaternary volcanism is a hybrit magma resulted from the partial melting along the crust-astenospheric mantle contact and contamination of the upwelling magma (Keskin, 2003; Açlan and Duruk, 2018). The total thickness of these volcanic rocks is about 2 km, and they represent the most significant cover rocks of the geothermal system in East Anatolia (Figure 25). In addition, the isolated Quaternary volcanic cones of mostly alkaline to calc-alkaline characters, such as the Ağırkaya, Meydan, Girekol, Etrüsk, Pirreşit, Kösedağ, Tendürek, Zor Mt., Durak Mt. and Ağrı volkanoes (Figure 24), represent the last phase of

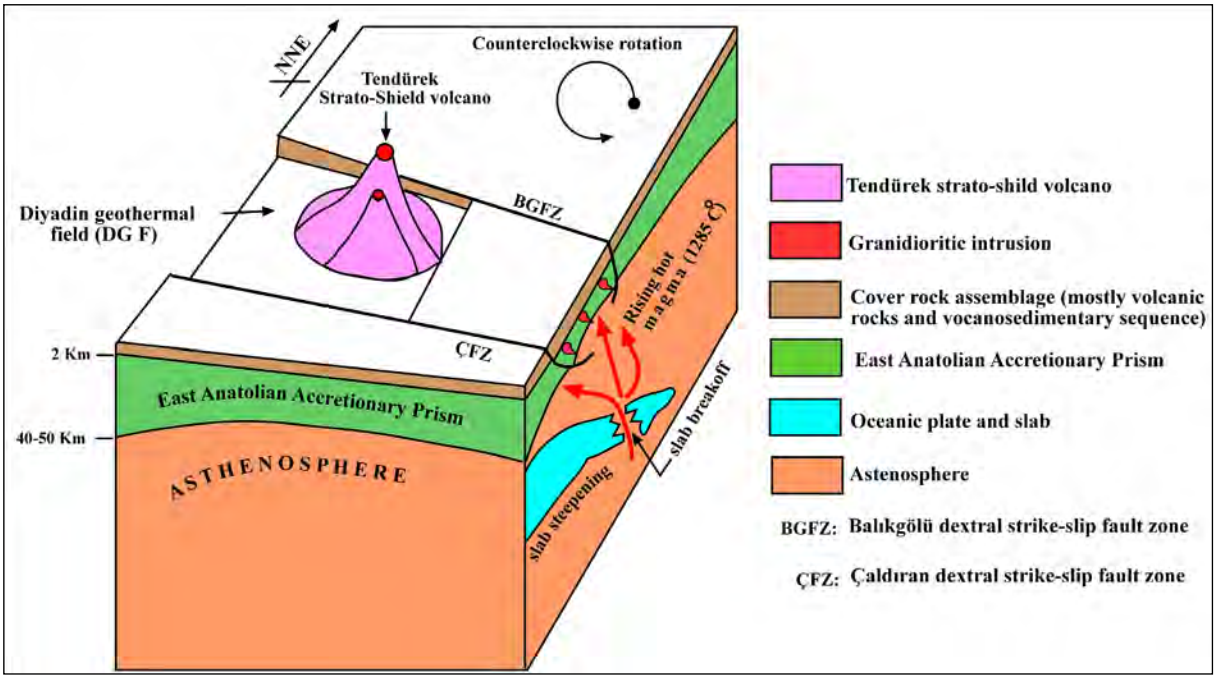

Figure 25- Sketched block diagram illustrating the geothermal heat source in eastern Türkiye.

the post-collisional magmatism in the east Anatolia. These isolated neotectonic volcanoes might have been underlain by a series of unroofed hypabyssal intrusions, which may also be the heat source of the geothermal fluid in the eastern Anatolia. For istance, the two-peaked Tendürek volcano is located near by the DGF. Its development lasted for about 0.7 Ma, and the last eruption on it took place 250.000 years ago, i.e., it is still active (Ölmez et al., 1994; Yılmaz et al., 1998; Lebedev et al., 2016). Another highest and neareast isolated volcano standing to the near northeast of DGF is the 5123 m high Ağrı stratovolcano. It was reactivated once more and poured out pyroclastites and lavas owing to the 1840 destructive historical Ağrı earthquake (Karakhanian et al., 2002). In particular, fumaroles along the foots of both volcanoes, numerous hot water springs to artesian wells and the actively forming fissure-ridge travertines in the DGF altogether reveal obviously that the geothermal potential of the DGF at the local scale, and the eastern Anatolia at regional scale are quite high (Basel et al., 2010; Pasvanoğlu, 2013; Şener and Şener, 2021). The temperature of the ascended asthenospheric mantle is about 1285°C (Figure 25). This value decreases in the opposite direction of geothermal gradient up to the 180°C at 1 km depth below the ground surface. Based on the studies carried out throughout the territory of Türkiye, the Curie temperature depth ranges between 14 and 18 km in the Ağrı region (Aydın et al., 2005; Akın et al., 2014, Elitok and Dolmaz, 2014). It is 16 km as an average. At this depth the Curie temperature is 585°C under normal conditions. In the same way, this value also decreases towards ground surface and becomes 210°C at one km depth below ground surface. In addition, the gases coming out of the Tendürek volcano is mantle in origin based on the isotope studies (Ölmez et al., 1994). Consequently, the source of the geothermal heat in eastern Türkiye is the ascended asthenospheric mantle (Keskin, 2003; Barazangi et al., 2006).

In general, the reservoir rocks in the East Anatolia are represented by the East Anatolian Accretionary Prism (EAAP). It was resulted from a series of tectono-sedimentary processes accompanied to the subduction and contint-continent collision between the northerly located Eurasian and southerly situated Arabian plate during the late Cretaceous-middle Miocene time. The EAAP is the tectono-sedimentary mixture of various rocks, such as the oceanic crust, deep-sea sedimentary sequence and the active to passive margins-drived older metamorphic rocks, in an ophiolitic materrial-rich finer-grained scaly matrix. It has been thrown into a series of imbricate stacks and overthickened at the time of obduction and tectonic transportation into its present-day position. The EAAP gained a considerable amount of permeability owing to the brittle deformation it experienced (Barazangi et al., 2006). The Kendel metamorphic rocks, made up of mostly marbles, are the blocks of dissimilar size floating rootless within the EAAP (Ölmez et al., 1994; Keskin, 2003; Lebedev et al., 2016). They are also very porus and full of caves owing to the easily dissolution of the $CaCO_3$. Thus, large-scale marble blocks also comprise another reservoir rock for the East Anatolian Geothermal System (Figure 25). The East Anatolia is also characterized by 2 km thick volcanic to volcanosedimentary rock sequence of dissimilar chemical compositions. In particularly pyroclastites, such as tuff and tuffite, are relatively finer-grained, and they result in secondary clay minerals owing to the chemical weathering processes. Thus they gain an impermeable texture. For this reason, the post-collisional volcanic to volcanosedimentary rocks comprise the cover rocks of the East Anatolian geothermal system (Figures 3, 7, 24 and 25).

The type locality, namely the DGF, is drained by the longest (722 km) drainage system, the Murat River, in the East Anatolia. It originates from the 3358 m high peak of the Aladağ Mt. in the further south and then flows downslow direction towards north and DGF (Figures 1b, 3 and 4a). The level of the water table around the upstream section (Aladağlar section) of the Murat River drainage system is about 20-25 m above the base level of the drainage system. However, it lowers up to 30 m and becomes 5-10 m below the base level in the further north around the DGF and the Akpazar pull-apart basin floor. Even though the precipitation in the type of snow and rain decreases in last 60 years, the elevation of the water table level is very close to the ground surface in the depressions. It is about 5 to 10 m below the ground surface in both the DGF and the Akpazar pull-apart basin. For istance, the elevation of the Akpazar pull-apart basin floor ranges from 1900 m to 1790 m, i.e., the water table elevation is between 1780 m and 1785 m. These observations reveal that the meteoric waters, which are necessary

for the development of the geothermal system in both the DGF and in the eastern Anatolia, are enough. These cold meteoric waters ara circulating deeper and deeper by using active faults and open fractures of active volcanoes untill they reach to the shallow-seated heeting source (e.g., most probably shallow-seated hypabyssal felsic to intermediate intrusions), and then turn back again towards ground surface as geothermal fluids by using the same kind of circulation paths.

The most of major Italian geothermal fields (IGF) are included in the Tyrrhenian back-arc region located on the western mountain front of the central Apennine orogeny chain (fold-thrust fault belt) (Batini et al., 2003; Giovanni et al., 2005). It is seen obviously that both the IGF and the DGF in eastern Türkiye have more or less same tectonic setting and ground surface manifestations, such as actively-growing to fossil fissure-ridge travertines, active volcanoes, fumeroles, numerous hot water springs to artesian wells, gas vents, widespread iron-rich alteration zones and active tectonic regimes and related faults, when they are compared (Giovanni, et al., 2005; Brogi and Capezzuoli, 2009; De Filippis et al., 2013, Porta et al., 2017). In contrary, there are also some significant contrasts between them. Among major contrasts, the followings can be mentioned: (1) the IGF has two basic reservoirs, which are the relatively shallow-seated (up to 2 km depth) sedimentary reservoir composed mostly of shallow-water platform to pelagic basin carbonates-turbidites of the late Triassic-Middle Miocene age and the deep-seated (up to 4 km depth) metamorphic basement rocks of Permian-early Triassic age (Giovanni et al., 2005; Santilano, 2016); whereas, the reservoir of the DGF is the accretionary prism of late Cretaceous age and the large-scale Upper Paleozoic-Mesozoic carbonate blocks to wedges in it experienced a multi-phased brittle deformation, (2) the cap rocks or the impermeable cover rocks of the IGF are represented by shallow-marine to terrestrial finer clastics of shale, marl, siltstone and volcanic tuff to tuffite intercalations of Plio-Quaternary age, whereas the DGF is characterized by a thick (up to 2 km) volcano-sedimentary sequence of Miocene-Quaternary age, (3) the geothermal fluids of the IGF are the superheated waters and gas (up to 350°-400°C) (Giovanni et al., 2005), whereas, the temperature of geothermal fluid of the DGF is relatively low (up to 150°C at the depth of 1 km), (4) the heat source of the IGF is relatively shallow-seated (up to depths of 3 and 6 km below ground surface) felsic to intermediate intrusions (Santilano, 2016), whereas the heat source of the DGF is still under debate.

7. Conclusions

Under the light of the above-mentioned dataset, the followins are concluded**:** (1) the strike-slip neotectonic regime in eastern Türkiye commenced at the time of latest Pliocene-early Quaternary time, and it triggerred the development of both the Tendürek strato-shild volcanoe and the Diyadin geothermal field, (2) the presence of main factors, which control the development of the geothermal system, was also determined in the eastern Türkiye; they obviously reveal that the geothermal potential of the eastern Türkiye is quite high as much as those in southwestern Anatolia. This is proved once more by its surface manifestations such as the active tectonic regime and related faults (e.g., extensional horsetail strucure), active volcanoes (Tendürek and Ağrı volcanoes), fumeroles, numerous hot water springs to artesian wells, widespread iron-rich alteration zones and actively growing thermogene fissure-ridge travertines. However, the heat source of the DGF is still under debate. For this reason, the probable presence of the unroofed hypabyssal felsic to intermediate intrusions at the roots and their near environs of the isolated Quaternary volcanoes in the eastern Türkiye have to be researched in detail by the geophysical methods.

Acknowledgements

This work has been financially supported by the Zorlu Energy Electricity Production Company, İstanbul. For this reason, authors of these paper are gratefull to the Zorlu Energy Company executives.

References

Açlan, M., Duruk, H. İ. 2018. Geochemistry, zircon U-Pb geochronology, and tectonic setting of the Taşlıçay Granitoids, Eastern Anatolia, Turkey. Arabian Journal of Geosciences 11 (36) 1-19.

Açlan, M., Turgut, İ. K. 2017. Şekerbulak (Diyadin-Ağrı) dolaylarında yüzeyleyen volkanik kayaçların mineralojik-petrografik ve jeokimyasal özellikleri. Çukurova Üniversitesi Mühendislik Mimarlık Fakültesi Dergisi 32 (4) 163-174.

Aghajany, S. H., Voosoghi, B., Yazdian, A. 2017. Estimation of north Tabriz fault parameters using neural networks and 3D tropospherically corrected surface displacement field. Geomatics, Natural Hazards and Risk 8 (2) 918-932.

Akın, U., Ulugergerli, E. U., Kutlu, S. 2014. Turkiye jeotermal potansiyelinin ısı akısı hesaplamasıyla değerlendirilmesi. Bulletin of the Mineral Research and Exploration 149, 205-214.

Aksoy, E., Tatar, Y. 1990. Van ili doğu-kuzeydoğu yöresinin stratigrafisi ve tektonigi. TÜBITAK Doğa Dergisi 14**,** 628-644.

Aksoy, E., İnceoz, M., Koçyiğit, A. 2007. Lake Hazar basin: a negative fl ower structure on the East Anatolian fault system (EAFS), SE Turkiye. Turkish Journal of Earth Sciences 16, 319–338.

Altunel, E. 1996. Pamukkale travertenlerinin morfolojik özellikleri, yaşları ve neotektonik önemleri. Bulletin of the Mineral Research and Exploration 118, 47-64.

Altunel, E., Hancock. P. L. 1993. Active fissuring and faulting in Quaternary travertines at Pamukkale, western Turkey. Geomorphology 94, 285-302.

Altunel, E., Karabacak, V. 2005. Determination of horizontal extension from fissure-ridge travertines: a case study from the Denizli Basin, southwestern Turkey. Geodinamica Acta 18, 333-342.

Ambraseys, N. N., Jackson, J. A. 1998. Faulting associated with historical and recent earthquakes in the Eastern Mediterranean region. Geophysical Journal International 133, 390-406.

Arpat, E., Şaroğlu, F., Iz, H. B., 1977. Çaldıran depremi. Yeryuvarı ve İnsan 2, 29-41.

Atabey, E. 2002. The formation of fissure ridge type laminated travertine-tufa deposits microscopical cheacteristics and diagenesis, Kirşehir, central Anatolia. Bulletin of the Mineral Research and Exploration 123-124,59-65.

Avagyan, A., Sosson, M., Philip, H., Karakhanian, A., Rolland, Y., Melkonyan, R., Rebai, S., Davtyan, V. 2005. Neogene to Quaternary stress field evolution in Lesser Caucasus and adjacent regions using fault kinematics analysis and volcanic cluster data. Geodinamica Acta 18 (6) 401-416.

Aydın, H., Karakuş, H., Mutlu, H. 2020. Hydrogeochemistry of geothermal waters in eastern Turkey: Geochemical and isotopic constraints on water-rock interaction. Journal of Volcanology and Geothermal Research 390, 106708.

Aydın, İ., Karat, H. İ., Koçak, A. 2005. Curie point depths map of Turkey. GJI Volcanology, geothermics fluids and rocks 162, 633-640.

Barazangi, M., Sandvol, E., Seber, D. 2006. Structure and Tectonic Evolution of the Anatolian Plateau in Eastern Turkey. Geological Society of America, Special Paper 409, 463–473.

Basel, E. D. K., Serpen, U., Satman, A. 2010. Turkey's geothermal Energy potential: updated results. Proceedings, Thirthy-Fifth Workshop on Geothermal Reservoir Engineering. Stanford University, Stanford, California, February 1-3.

Batini, F., Brogi, A., Lazzarotto, A., Liotta, D., Pandeli, E. 2003. Geological features of Larderello-Travale and Mt. Amiata geothermal areas (Southern Tuscany, Italy). Episodes 26(3), 239-244.

Bozkuş, C., Demir, M., Kurtuluş, B. 2010. Iğdır ve yakın çevresinin depremselliği. ReaserchGate, 15.

Brogi, A., Capezzuoli, B. 2009. Travertine deposition and faulting: the fault-related travertine fissure-ridge at Terme S. Giovanni, Rapolano Terme (Italy). International Journal of Earth Sciences 98, 931-947.

Brogi, A., Capezzuoli, A., Costantini, A., Gandin, A., Lazzarotto, A. 2005. Tectonics and travertines relationship in the Rapolano Terme area (Northern Apennines, Italy). Proceedings of the First International Symposium on Travertine, 142-148.

Brogi, A., Capezzuoli, E., Karabacak, V., Alçiçek, M.C., Luo, L. 2021. Fissure Ridges: A Reappraisal of Faulting and Travertine Deposition (Travitonics). Geosciences 2021, 11, 278.

Canbaz, C. H., Temizel, C., Palabiyik, Y., Balıkçıoğlu, A., Yılmaz, I. Ö., Aytuna, S., Ranjith, R. 2020**.** Evaluation of Geothermal Potential of Turkey as an Alternative Source of Energy Under Demand and Supply Dynamics of Other Energy Resources. Conference paper. Turkey IV. Scientific and Technical Petroleum Congress, 20 December 2020 in Turkey.

Copley, A., Jackson, J. 2006. Active tectonics of the Turkish-Iranian Plateau. Tectonics 25, 1–19.

Çolak, S., Aksoy, E., Kocyiğit, A., Inceoz, M. 2012. Palu-Uluova strike-slip basin on the East Anatolian Fault System, Turkey: transition from paleotectonic period to neotectonic period. Turkish Journal of Earth Sciences 21 (4), 547-570.

De Filippis, L., Anzalone, E., Billi, A., Faccenna, C., Poncia, P. P., Sella, P. 2013. The origin

and growth of a recently-active fissure ridge travertine over a seismic fault, Tivoli, Italy. Geomorphology 195,13–26.

Demirel, V., Ozkan, H. 2000. Ağri-Diyadin MT-2, 3 and 4 Geothermal Well Drilling, Completion Report. Maden Tetkik ve Arama Genel Müdürlüğü Report No. 10451, 1-14 (in Turkish).

Demir, S. 2006. Hydrogeological investigation and Detection of the Origin of Thermal Waters in Diyadin. Istanbul Technical Univ. MSc Thesis (in Turkish).

Demirkıran, Z., Elçi, H. 2022. Urganlı (Manisa) Travertenlerinin Morfolojik Özellikleri ve Tektonizma ile İlişkisi. Mühendislik Bilimleri ve Tasarım Dergisi 10(3), 1027-1042.

Dewey, J. F., Hempton, M. R., Kidd, W. S. F., Şaroğlu, F., Şengör, A. M. C. 1986. Shortening of continental lithosphere: the neotectonics of eastern Anatolia-a young collision zone. Collision Tectonics. Geological Society of London Special Publication 19, 3-36.

Doğan, U., Koçyiğit, A., Yılmaz, E. 2019. Geomorphological evolutionary history of the Melendiz River Valley, Cappadocia, Turkey .Mediterranean Geoscience Reviews 1, 203-222.

Dhont, D., Chorowicz, J. 2006. Review of the neotectonics of the Eastern Turkish-Armenian Plateau by geomorphic analysis of digital elevation model imagery. International Journal of Earth Sciences 95, 34-49.

Djamour, Y., Andrnant, P., Nankali, H. R., Tavakoli, F. 2011. NW Iran-eastern Turkey present-day kinematics: Results from the Iranian permanent GPS network. Earth and Planetary Science Letters 307, 27–34.

Elitok, Ö., Dolmaz, M. N. 2014. Mantle flow-induced crustal thinning in the area between the easternmost part of the Anatolian plate and the Arabian Foreland (E Turkey) deduced from the geological and geophysical data. Gondwana Research 13, 302-318.

Emre, Ö., Duman, T. Y., Elmacı, H., Olgun, Ş., Özalp, S. 2012. 1/250.000 ölçekli Türkiye Diri Fay Haritası Serisi, Doğubayazıt (NJ 38-2) nolu pafta seri No. 54, Maden Tetkik ve Arama Genel Müdürlüğü, Ankara, Türkiye.

Emre, Ö., Duman, T. Y., Özalp, S., Şaroğlu, F., Olgun, Ş., Elmacı, H., Çan, T. 2018. Active fault databese of Turkey. Bulletin of Earthquake Engineering 16(8), 3229-3275.

Ercan, T., Fujitani, T., Madsuda, J., Nodsu, K., Tokel, S., Tadahide, U. I. 1990. Doğu ve Güney-doğu Anadolu Neojen-Kuvaterner volkanitlerine ilişkin yeni jeokimyasal, radyometrik ve izotopik verilerin yorumu. Bulletin of the Mineral Research and Exploration 110, 143-164.

Ercan, T., Keskin, İ., Dönmez, M. 1993. Eleşkirt (Ağrı) Yöresindeki Tersiyer Yaşlı Volkanizmanın Jeokimyasal Özellikleri ve Bölgesel Yayılımı. Jeoloji Mühendisleri Dergisi 42, 74-88.

Ercan, T., Sümengen, M. 2018. Türkiye Jeoloji Haritaları Serisi, Doğubayazıt Paftası, No. 254. Maden Tetkik ve Arama Genel Müdürlüğü, Jeoloji Etütleri Dairesi, Ankara (unpublished), Türkiye.

Esirtgen, T., Hepsen, N. 2018. Türkiye Jeoloji Haritaları Serisi, Doğubayazıt J51 Paftası, No. 256. Maden Tetkik ve Arama Genel Müdürlüğü, Jeoloji Etütleri Dairesi, Ankara, Türkiye.

Giovanni, B., Guido, C., Adolfo, F. 2005. Characteristics of Geothermal Fields in Italy. Giornale di Geologia Applicata 1, 247 -254.

Güneyli, H., Yaman, M., Yıldırım, V. 2020. Çaldıran Fayı'nın Çaldıran İlçesi Dolayında Paleosismolojik ve Neotektonik Özellikler. Çukurova Üniversitesi Mühendislik Mimarlık Fakültesi Dergisi 35(2), 279-293.

Hancock, P. L., Chalmers, R. M. L., Altunel, E., Çakır, Z. 1999. Travitonics: using travertines in active fault studies. Journal of Structural Geology 21, 903-916.

Hempton, M. R. 1987. Constraints on Arabian plate motion and extensional history of the Red Sea. Tectonics 6, 687-705.

Hessami, K., Pantosti, D., Tabassi, H., Shabanian, E., Abbassi, M. R., Feghhi, K., Solaymani, S. 2003. Paleoearthquakes and slip rates of the North Tabriz Fault, NW Iran: Preliminary results. Annales de Geophysique, 46, 903-916.

Innocenti, F., Mazzuoli, R., Pasquare, G., Radicati, F., Villan, L. 1976. Evolution of the volcanism in the area of interaction between the Arabian, Anatolian, and Iranian plates (Lake Van., Eastern Turkey). Journal of Volcanology and Geothermal Research 1,103-112.

Innocenti, F., Mazzuoli, R., Päsquare, G., Scrri, G., Villari, L. 1980. Geology of the volcanic area north of Lake Van (Turkey). Geologische Rundschau 69(1), 292-323.

Jackson, J. 1992. Partitioning of strike-slip and convergent motion between Eurasia and Arabia in eastern Turkey and the Caucasus. Journal of Geophysical Research: Solid Earth 97, 12471-12479.

Kalender, L., Öztekin, Ö., İnceöz, M., Çetindağı. B., Yıldırım, V. 2015. Geochemistry of travertine deposits in the Eastern Anatolia District: an example of the Karakoçan-Yoğunağaç (Elazığ) and Mazgirt-Dedebağ (Tunceli) travertines, Turkey. Turkish Journal of Earth Sciences 24, 1-20.

Kansun, G., Afzali, A. O., Üçgün, F. 2020. The Stratigraphic and Petrographic Properties of the Rocks in Davut -Tazekent Vicinity, Diyadin-Ağrı-Turkey. European Journal of Science and Technology Special Issue 528-551.

Karabacak, V. 2007. Ihlara vadisi (Orta Anadolu) travertenlerinin genel ozellikleri ve kabuksal deformasyon açısından onemleri. Eskişehir Osmangazi Universitesi Muhendislik Mimarlık Fakultesi Dergisi 20, 65-82 (in Turkish).

Karabacak, V., Mutlu, H. 2019. Sarıhıdır Travertenlerinin (Avanos) jeokronolojik ve İzotopik Sistemleri: Acıgöl ve Erciyes Volkanizmasına Ait Geç Kuvaterner Kabuk deformas-yonu tarihlendirilmesi. Maden Tetkik ve Arama Genel Müdürlüğü Project Number:118Y069, 96.

Karakhanian, A., Djrbashian, R., Trifonov, V., Philip, H., Arakelian, S., Avagian, A. 2002. Holocene-historical volcanism and active faults as natural risk factor for Armenia and adjacent countries. Journal of Volcanology and Geothermal Research 113 (1– 2), 319-344.

Karakhanian, A. S., Trifonov, V. G., Philip, H., Avagyan, A., Hessami, K. 2004. Active faulting and natural hazards in Armenia, eastern Turkey and northwestern Iran. Tectonophysics 380,189-219.

Keskin, M. 2003. Magma generation by slab steepening and slab-breakoff beneath a subduction accretion complex: an alternative model for collision-related volcanism in eastern Anatolia, Turkey. Geophysical Research Letters 30, 8046–8050.

King, G. C. P., Nabelek, J. L. 1985. Role of Fault Bends in the Initiation and Termination of Earthquake Rupture. Science 228, 983-987.

Kıral, K., Çağlayan, A. 1980. Kağızman (Kars)-Taşlıçay (Ağrı) dolayının Jeolojisi. Maden Tetkik ve Arama Genel Müdürlüğü, Jeooji Etütleri Dairesi, Report Number: 154 (unpublished).

Koçyiğit, A. 2005. Denzili Graben-Horst System and the eastern limit of the West Anatolian continental extension: basin fill, structure, deformational mode, throw amount and episodic evolutionary history, SW Turkey. Geodinamica Acta 18, 167-208.

Koçyiğit, A. 2008. Orta Anadolu'nun Aktif tektoniği ve jeotermal enerji potansiyeli. Middle East Technical University, Faculty of Science, Deaprtment of Geological Engineering Project Number: 07-03-091-00-23, Final Report, 135.

Koçyiğit, A. 2013. New field and seismic data about the intraplate strike-slip deformation in Van region, East Anatolian plateau, E. Turkey. Journal of Asian Earth Sciences 62, 586-605.

Koçyiğit, A. 2022. Diyadin (Ağrı) ilçe sınırları içinde yer alan 30 Nolu Gedik Köyü ve 31 Nolu Mutlu Köyü Ruhsat sahalarının jeotermal potansiyeli ile ilgili saha jeolojisi çalışmaları: Technical Report, 75 (unpublished).

Kocyiğit, A., Beyhan, A. 1998. A new intracontinental transcurrent structure: the Central Anatolian Fault Zone, Turkey. Tectonophysics 284, 317–336.

Koçyiğit, A., Canoğlu, C. 2017. Neotectonics and seismicity of the Erzurum pull-apart basin, East Turkey. Russian Geology and Geophysics 58, 99-122.

Koçyiğit, A., Doğan, U. 2016. Strike-slip neotectonic regime and related structures in the Cappadocia region: a case study in the Salanda basin, Central Anatolia, Turkey. Turkish Journal of Earth Sciences 25, 393–417.

Koçyiğit, A. Yılmaz, A., Adamia, S., Kuloshvili, S. 2001. Neotectonics of East Anatolian Plateau (Turkey) and Lesser Caucasus: implication for transition from thrusting to strike-slip faulting. Geodinamica Acta 14, 177-195.

KOERI 2022. Akçift (Muradiye-Van) earthquake. Boğaziçi Üniversitesi, Kandilli Rasat-hanesi ve Deprem Araştırma Enstitüsü, İstanbul.

Lebedev, V. A, Sharkov, E. V., Ünal, E., Keskin, M. 2016. Late Pleistocene Tendürek Volcano (Eastern Anatolia, Turkey):I. Geochronology and Petrographic Characteristics of Igneous Rocks. Petrology 24(2), 127-152.

Mancini, M., Marini, M., Moscatelli, M., Pagliaroli, A., Stigliano, F., Di Salvo, C., Simionato, M., Cavinato, G. P., Corazza, A. 2014. A physical stratigraphy model for seismic microzonation of the Central Archaeological Area of Rome (Italy). Bulletin of Earthquake Engineering 12, 1339 – 1363.

Masson, F., Djamour, Y., Van Gorp, S., Chery, J., Tatar, M., Tavakoli, F., Nankali, H., Vernet, P. 2006. Extension in NW Iran driven by the motion of the South Caspian Basin. Earth and Planetary Science Letters 252, 180-188.

Mesci, B. L., Erkmen, A. C., Gürsoy, H., Tatar, O. 2018. Fossil findings from the Sıcak Çermik fissure ridgetype travertines and possible hominid tracks, Sivas, Central Turkey. Geodinamica Acta 30(1), 15-30.

Mesci, B. L., Gürsoy, H., Ghaleb, B., Tatar, O. 2020. An Extensional Fracture Acting as Hot Water Source for Travertine Deposition on the North Anatolian Fault Zone, Turkey: the Reşadiye Fissure-Ridge. Geological Bulletin of Turkey 63, 145-1607.

Mesci, B. L., Gürsoy, H., Tatar, O. 2008. The evolution of travertine masses in the Sivas area (Central Turkey) and their relationships to active tectonics. Turkish Journal of Earth Sciences 17, 219-240.

Mokhoori, A. N., Rahimi, B., Moayyed, M. 2021. Active tectonic stress field analysis in NW Iran-NE Turkey using earthquake focal mechanism data. Turkish Journal of Earth Sciences 30, 235-246.

MTA 2018. General Directorate of Mineral Research and Exploration, Energy Maps.

MTA 2021. Turkey Geothermal Resources Distribution and Application Map.

Mutlu, H., Aydın, H., Kazancı, A. 2013. Diyadin (Ağrı) jeotermal sahasına yönelik jeokimyasal ve izotopik bulgular. 11. Ulusal Tesisat Mühendisleri Kongresi, İzmir, 47-67.

Ölmez, E., Ercan, T., Yıldırım, T. 1994. Tendürek (Doğu Anadolu) Jeotermal Alanının (Diyadin, Zilan, Çaldıran) Volkanolojisi ve Jeotermal Enerji Olanakları, 47. Türkiye Jeoloji Kurultayı Bildiriler Kitabı, 49-55.

Özgür, N., Kıymaz, I., Uzun, E., Kutlu, D. S. 2017. Hydrogeological modelling of geothermal waters in Pamukkale, western Anatolia, Turkey. European Geologist 43, 52-58.

Özkul, M., Varol, B., Alçiçek C. 2002. Deposıtıonal Envıronments and Petrography of Denizli travertınes. Bulletin of the Mineral Research and Exploration 125, 13-29.

Öztürk, Y. 2020. Aktif fayların tanımlanmasında jeomorfik belirteçlerin rolü: Balıkgölü fay zonu örneği. Jeomorfolojik Araştırmalar Dergisi 5, 101-117.

Porta, G. D., Croci, A., Marini, M., Kele, S. 2017. Deposıtıonal Architecture, Facies Character and Geochemical Sıgnature of the Tıvoli Travertines (Pleistocene, Acque Albule Basin, Central Italy). Rivista Italiana di Paleontologia e Stratigrafia (Research in Paleontology and Stratigraphy) 123(3), 487-540.

Pasvanoğlu, S. 2013. Hydrogeochemistry of thermal and mineralized waters in the Diyadin (Ağrı) area, Eastern Turkey. Applied Geochemistry 38, 70-81.

Pearce, J. A., Bender, J. F., de Long, S. E., Kidd, W. S. F., Low, F. J., Güner, Y., Şaroğlu, F., Yılmaz, Y., Moofbath, S., Mitchell, J. G. 1990. Genesis of collision volcanism in Eastern Anatolia, Turkey. Journal of Volcanology and Geothermal Research 44,189-229.

Reilinger, R., McClusky, S., Vernant, P., Lawrence, S., Ergintav, S., Cakmak, R., Ozener, H., Kadirov, F., Guliev, I., Stepanyan, R., Nadariya, M., Hahubia, G., Mahmoud, S., Sakr, K., ArRajehi, A., Paradissis, D., Al-Aydrus, A., Prilepin, M., Guseva, T., Evren, E., Dmitrotsa, A., Filikov, V., Gomez, F., Al-Ghazzi, R., Karam, G. 2006. GPS constraints on continental deformation in the Africa-Arabia-Eurasia continental collision zone and implications for the dynamics of plate interactions. Journal of Geophysical Research 111, B05411.

Sağlam-Selçuk, A., Kul, A. Ö. 2021. Long-term slip rate estimation for Ercis Fault in East Anatolian Compressive Tectonic Block from geologic and geomorphologic field evidence. Geological journal 56, 5290-5310.

Sağlam-Selçuk, A., Erturaç, M. K., Nomade, S. 2016. Geology of the Çaldıran Fault, Eastern Turkey: Age, slip rate and implications on the characteristic slip behavior. Tectonophysics, 680, 155-173.

Sağlam-Selçuk, A., Erturaç, M. K., Uner, S., Özsayınç, E., Pons-Branchud, E. 2017. Evolution of Çamlık fissure-ridge travertines in the Başkale basin (Van, Eastern Anatolia) Geodinamica Acta 29(1), 1-19.

Santilano, A. 2016. Deep geothermal exploration by means of electromagnetic methods: New insights from the Larderello geothermal field (Italy). PhD. thesis in the Graduate School of Politecnico di Torino, 242.

Serpen, U., Aksoy, N., Ongurc, T., Korkmaz, E. D. 2009. Geothermal energy in Turkey: 2008 update. Geothermics 38, 227-237.

Shabanian, E., Acocella, V., Gioncada, A., Ghasemi, H., Belieri, O. 2012. Structural control on volcanism

in intraplate post collisional settings: Late Cenozoic to Quaternary examples of Iran and Eastern Turkey. Tectonics 31, TC3013.

Sharkov, E., Lebedev, V., Chugaev, A., Zabarinskaya, L., Rodnikov, A., Sergeeva, N., Safonova, I. 2014. The Caucasian-Arabian segment of the Alpine-Himalayan collisional belt: geology, volcanism and neotectonics. Geoscience Frontiers 6, 513-522.

Soysal, H., Sipahioğlu, S., Kolçak, D., Altınok, Y. 1981. Türkiye ve Çevresinin Tarihsel Deprem Kataloğu (2100 B.C.–1900 A.D.). TÜBİTAK, TBAG-341.

Sümengen, M. 2009. 1/100.000 ölçekli Türkiye Jeoloji Haritaları Serisi, Kars H50 Paftası. Maden Tetkik ve Arama Genel Müdürlüğü, Report Number:108, Ankara, Türkiye.

Şaroğlu, F., Yılmaz, Y. 1986. Doğu Anadolu›da neotektonik dönemdeki jeolojik evrim and havza modelleri Bulletin of the Mineral Research and Exploration 107,73-94.

Şaroğlu, F., Emre, Ö., Boray, A. 1987. Türkiyenin Diri Fayları ve Depremselliği. Maden Tetkik ve Arama Genel Müdürlüğü, Report Number: 8174 Ankara (unpublished).

Şener, M. F. 2018. Akhüyük (Konya) Jeotermal Alanındaki Hidrotermal Akışkan Dolaşımı ve Traverten Oluşum Mekanizması, Orta Anadolu, Türkiye. Türkiye Jeoloji Bülteni 61, 193-206.

Şener, E., Şener, Ş. 2021. Exploration of geothermal potential using integrated fuzzy logic and analytic hierarchy process (AHP) in Ağrı, Eastern Turkey. Turkish Journal of Earth Sciences 30,1134-1150.

Şengör, C., Kidd, W. S. F. 1979. Post-collisional tectonics of the Turkish-Iranian plateau and a comparison with Tibet. Tectonophysics 55, 361-376.

Şengör, C., Yilmaz, Y. 1981. Tethyan evolution of Turkey A plate tectonic approach. Tectonophysics 75, 181-241.

Tan, O., Tapırdamaz, M. C., Yörük, A. 2008. The Earthquake Catalogues for Turkey. Turkish Journal of Earth Sciences 17, 405-418.

Temiz, U., Savas, F. 2018. U/Th Dating of the Akhuyuk fissure ridge travertines in Ereğli, Konya (Central Anatolia, Turkey): their relationship to active tectonics. Arabian Journal of Science and Engineering 43,3739-3749.

Temiz, U., Gokten, E., Eikenberg, J. 2009. U/Th dating of fissure ridge travertines from the Kırşehir region (Central Anatolia Turkey). Structural relations and implications for the Neotectonic development of the Anatolian block. Geodinamica Acta 22, 201-213.

Temiz, H., Koçak, İ., Öksüz, N., Akbay, S. 2021. Significance of neotectonic and paleoclimatic Late Pleistocene-Holocene travertine and origins: Balkayası, Avanos-Nevsehir, Central Anatolia/ Turkey. International Journal of Earth Sciences 110(6), 2157-2177.

Toksöz, M. N., Arpat, E., Şaroğlu, F. 1977. East Anatolian Earthquake of 24 November 1976. Nature 270, 423-425.

Türkecan, A., Dönmez, M., Özgür, T. B., Mutlu, G., Sevin, D., Bulut, V. 1992. Patnos-Tutak-Hamur (Ağın) yöresinin jeolojisi ve volkanik kayaçların petrolojisi. Maden Tetkik ve Arama Genel Müdürlüğü Report Number: 9434 Ankara (unpublished).

Üçgün, F. 2019. The Petrography-Geochemistry of Volcanic Rocks Around in Davut- Tazekent Villages (Diyadin-Ağrı) and the Characteristics of the Diyadin Geothermal Field, MSc, Selcuk University, Konya, Turkey (in Turkish).

Üçgün, F., Kurt, M., Karagöz, K., Kocaman, S., Zilbeyaz,, N., Göçer, H., Erol, F., Tanışır, E., Çeker, S. 2014. Ağrı İli Minerallı Sular Araştırması. T.C. Serhat Kalkınma Ajansı Ağrı Destek Ofisi, Proje Sonuç Raporu, 164.

Van Noten, K., Soete, J., Claes, H., Foubert, A., Özkul, M., Swennen, R. 2013. “Fracture networks and strike-slip deformation along reactivated normal faults in Quaternary travertine deposits, Denizli Basin, Western Turkey”. Tectonophysics 588, 154-170.

Vignaroli, G., Mancini, M., Brilli, M., Bucci, F., Cardinali, M., Giustini, F., Voltaggio, M., Yu, T. L., Shen, C. C. 2020. Spatial-Temporal Evolution of Extensional Faulting and Fluid Circulation in the Amatrice Basin (Central Apennines, Italy) During the Pleistocene. Frontiers in Earth Science 8, 130.

Yeşilova, Ç. 2021. Potential geoheritage assessment; Dereiçi travertines, Başkale, Van (east anatolian Turkey). MANAS Journal of Engineering 9(1), 66-71.

Yıldırım, G. 2018. Akkaya-Eskipazar (Karabük) travertenine yönelik jeokimyasal ve izotopik bulgular. Ankara Üniversitesi Jeoloji Mühendisliği Bölümü, Yüksek Lisans Tezi, 87.

Yılmaz, Y., Güner, Y., Şaroğlu, F. 1998. Geology of the Quaternary volcanic centers of the east Anatolia. Journal of Volcanology and Geothermal Research, 85, 173-210.

Yılmaz, Y., Şaroğlı, R., Güner, Y. 1987. Initation of the neomagmatism in East Anatolia. Tectonophysics 134, 177-199.

Zor, E., Sandvol, E., Gürbüz, C., Türkelli, N., Seber, D., Barazangi, M. 2003. The crustal structure of the East Anatolian plateau (Turkey) from Receiver functions. Geophysical Research Letters 30 (24), 8044.

Bulletin of the Mineral Research and Exploration

http://bulletin.mta.gov.tr

The potential, utilization and development of geothermal energy in Türkiye

Mehmet Furkan ŞENER[a*], Taygun UZELLİ[b], İbrahim AKKUŞ[c], Orhan MERTOĞLU[d] and Alper BABA[e]

[a]*Izmir Bakircay University, Faculty of Arts and Sciences, Department of Geography, İzmir, Türkiye*
[b]*İzmir Institute of Technology, Geothermal Energy Research and Application Center, İzmir, Türkiye*
[c]*Beytepe District, 5442 Street, 2, Sukent Beytepe Houses, F Block, 17/65, Çankaya, Ankara, Türkiye*
[d]*Turkish Geothermal Association, And Street, 8/2, Çankaya, Ankara, Türkiye*
[e]*İzmir Institute of Technology, Department of International Water Resources, İzmir, Türkiye*

Research Article

Keywords:
Geothermal Energy, Türkiye, Strategy Report, HDR/EDGS, Future Policy.

ABSTRACT

Geothermal energy is a natural resource that can be utilized directly or by converting to other types of energy. Considering the diversity of the geological structure of Türkiye, the geothermal systems have developed depending on young tectonic and volcanic active rock. Western and Central Anatolia are especially rich in geothermal resources. The geothermal well with the hottest well-bottom temperature was drilled in Central Anatolia, and the well-bottom temperature was measured as 341°C at a depth of 3845 meters. In 2022, Türkiye's electricity generation capacity and the total installed direct heat use reached 1663 MWe and 5113 MWt, respectively. Considering Anatolia's Curie depth and heat flux, the probable thickness of the batholith can be regarded as 10 km. For example, the total granitoid area of Western Anatolia is 4221 km^2 and at least 2% of this granitoid can provide approximately 8x10^7 MWh of electricity by Enhanced Deep Geothermal Systems **(**EDGS). When all granites in Türkiye are considered, it is expected that the future capacity of Türkiye will be much higher with drilling research and development studies and the discovery of new fields. This capacity will exceed 100.000 MWt levels in the medium term, especially with the addition of EDGSs.

Received Date: 10.08.2022
Accepted Date: 03.01.2023

1. Introduction

The ever-increasing population density, industrialization and rising living standards increase the energy demand. Fossil fuels meet a large part of the energy requirement worldwide. The fact that fossil fuels pose risks to the environment and will run out in the future has shown that renewable energy sources should replace them. Problems that concern all humanity, especially global warming and climate change, are increasing. As emphasized in the Paris Agreement, it has become necessary to move away from traditional carbon-based energy sources as primary energy resources worldwide to keep the global temperature increase below 2°C. Therefore, in recent years, all countries have focused on developing new, renewable, and sustainable energy sources. Geothermal energy is one of the renewable energy sources. Geothermal energy is a natural resource that can be utilized directly or by converting it to other types of energy. It can also be transported through fractures and cracks in the rock by the water, steam, and gas energy created by the heat accumulated in various depths of the Earth's crust.

Using geothermal energy for different purposes such as electricity, residential heating, greenhouses,

Citation Info: Şener, M. F., Uzelli, T., Akkuş, İ., Mertoğlu, O., Baba, A. 2023. The potential, utilization, and development of geothermal energy in Türkiye. Bulletin of the Mineral Research and Exploration 171, 69-90. https://doi.org/10.19111/bulletinofmre.1229381

**Corresponding author: Mehmet Furkan ŞENER, furkan.sener@bakircay.edu.tr*

thermal tourism, fishing, and heating roads has become widespread in many countries (Figure 1). According to the change in renewable-sourced, domestic installed power in Türkiye over the years, significant increases were achieved in power capacity between 2006 and 2022 thanks to the effective incentive mechanisms. Geothermal installed power, calculated at 23 MWe in 2006, increased to 1663 MWe as of 2022 (EPDK, 2022).

Türkiye is among the leading countries in terms of existing geothermal energy resources and the use of these resources, ranking 4th globally in energy production and 2nd in the world for direct use (Şener et al., 2022). In addition, according to the 2020 data from the General Directorate of Mineral Research and Exploration (MTA), the usable capacity of Türkiye is approximately 38.000 MWt. Due to the wells whose production data is not documented in the official records, the total current capacity is not known precisely. Nevertheless, according to the data obtained, the total possible theoretical heat potential is 62.000 MWt. Considering the potential of geothermal energy, it creates an inter-sectoral synergy with the heat energy alternative regarding supply security. It offers implementation in urban heating, agriculture, thermal tourism, manufacturing, and urban infrastructure opportunities. In this context, scientific studies were carried out in various regions of Türkiye (Eşder and Şimşek, 1977; Filiz, 1982; Yılmazer, 1984; Şimşek, 1985; Mutlu and Güleç, 1998; Gemici and Filiz, 2001; Gemici and Tarcan, 2002; Özgür, 2002; Baba et al., 2003; Tarcan et al., 2005; Gültekin et al., 2007; Tayfur et al., 2008; Baba et al., 2010; Özkan et al., 2011; Karakuş and Şimşek, 2013; Aksoy, 2014; Tarcan et al., 2016; Uzelli et al., 2017; Şener et al., 2017; Hatipoğlu Temizel and Gültekin, 2018; Şener, 2019; Baba et al., 2019; Şener and Baba, 2019; Şener, 2019; Aydın et al., 2020; Pasvanoğlu, 2020; Uzelli et al., 2021; Şener et al., 2021; Uzelli et al., 2021; Baba and Chandrasekharam, 2022). Along with significant progress in geothermal electricity supply, Türkiye also has great potential to be used in heat energy supply. This study includes Türkiye's current geothermal potential, usage areas, projections, and suggestions for the future.

2. Current Situation of Energy Resources

The world's total energy supply (TES) increased approximately 2.6 times between 1971 and 2018 (REN21, 2021). Most of this energy consumption belongs to developed countries such as the United States of America (USA), China, and Russia. On the other hand, although oil, one of the fossil fuels, still maintains its stability, the consumption rate decreased from 44% to 32%, while natural gas increased from 16% to 23% and took third place. As of 2021, oil, coal, and natural gas are still the world's primary energy sources and correspond to approximately 80.2% of the

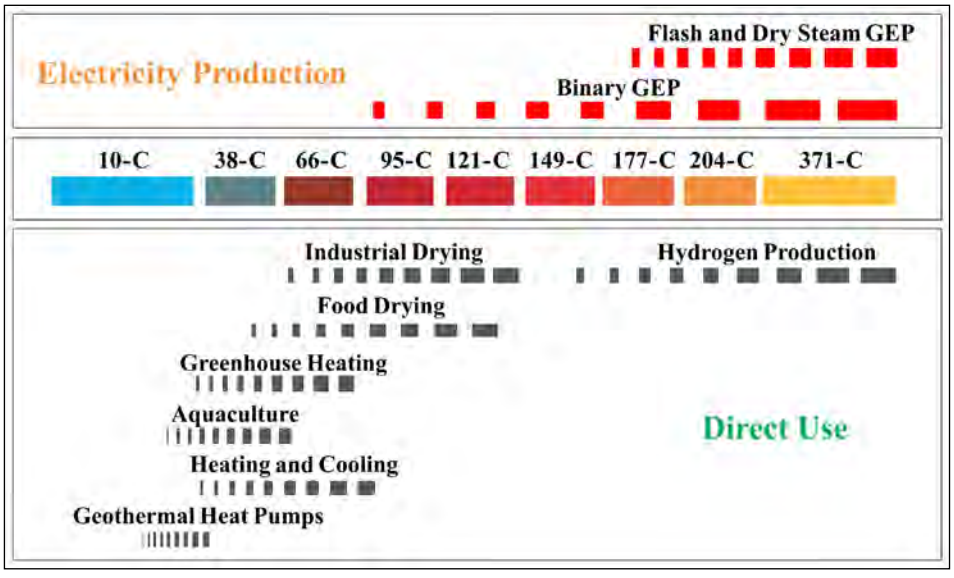

Figure 1- Direct and indirect usage of geothermal energy resources (modified from Lindal, 1973).

total energy consumption. According to the data, at the end of 2019, the rate of renewable energy sources is around 11.2% (REN21, 2021).

In 2020, electricity generation from geothermal sources, one of the renewable energy sources, reached a total of 97 TWh, and the direct use of geothermal heat reached approximately 128 TWh. In that year, geothermal power capacity grew slightly compared to recent years (partly due to disruptions caused by the Covid-19 pandemic), and almost all new facilities are located in Türkiye (REN21, 2021). Although the industry continues to face challenges owing to the pandemic, a total of 246 MW of additional capacity has been added worldwide with the inclusion of countries such as Colombia (small-scale ORC units from co-produced oil) and Taiwan (a 4.2 MW power plant) (Thinkgeoenergy, 2022).

$40 billion was invested in new geothermal energy developments worldwide from 2010 to 2020. By the end of 2021, the total installed geothermal power generation capacity was 15,854 MW, with an increase of 246 MW compared to 2020 (Thinkgeoenergy, 2022). Today's installed geothermal capacity is dominated by the USA with approximately 3722 MWe, followed by Indonesia, the Philippines, Türkiye, and New Zealand. Türkiye's share in electricity generation is around 11% (Şener et al., 2022). The top 10 geothermal producers contribute almost 90% of the world's total market, and many countries, especially Europe, plan to invest in geothermal energy soon.

Considering the direct use of geothermal energy for thermal heat applications, only four countries (China, Türkiye, Iceland, and Japan) account for three-quarters of the energy consumed. Direct use has grown by around 8% recently, with heating being the primary driver (Lund and Tóth, 2020).

Geothermal power generation plants are essential for Türkiye. With global warming and pandemic conditions, fossil fuel power plants have faced emission and supply problems. In addition, solar, wind, and hydraulic power plants have also been affected by climatic and regional meteorological events and experienced differences in their production (EPDK, 2019; 2022). The capacity factor, expressed mathematically, is the division of the total energy produced by a power plant in each period by the total capacity energy produced. Considering the capacity factor of geothermal power plants (GPP), the highest capacity factor among renewable energy sources belongs to geothermal power plants, according to the August 2021 data of Energy Markets Management Inc. (EMMI) (EPİAŞ, 2021; Selenka, 2021).

According to the capacity factor data for plants in Türkiye, wind power is 35.1%, solar power is 26.8%, hydroelectric power is 20.6%, biomass is 49.7%, and the GPP is 60.1% (Figure 2). The fact that power plant types have variable capacity factors has been one of the most critical indicators that geothermal power plants should be seen as the base load for power plants in Türkiye.

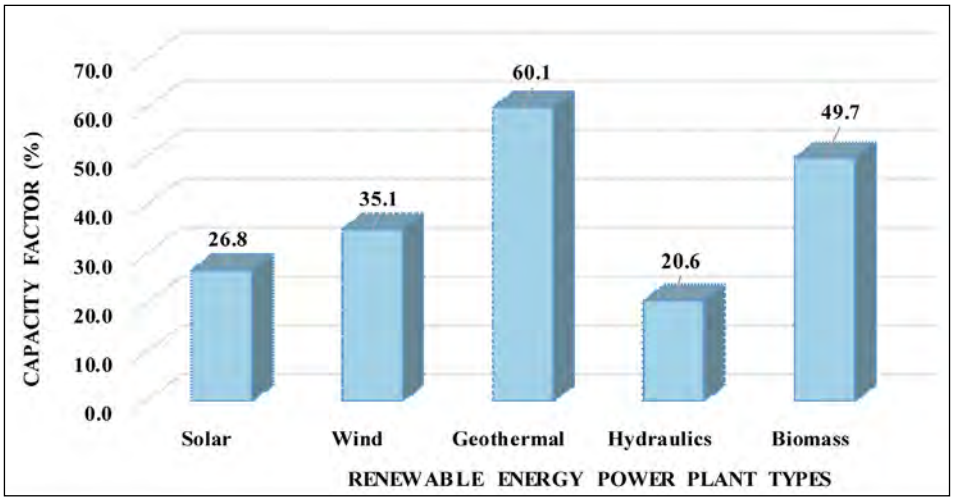

Figure 2- Renewable energy sources and capacity factors (Selenka, 2021).

2.1. Hydrothermal Geothermal Systems

The MTA research in 1960 is considered the beginning of Türkiye's geothermal energy research. Since than fields containing fluids suitable for different purposes, such as energy production and direct use, have been discovered. The period between 1970-2000 is primarily known for the reconnaissance of high-temperature reservoirs (Akkuş, 2017).

There are currently 415 geothermal fields with a temperature of 30°C and above. The number of geothermal fields includes both natural resources and drilled wells. According to their distribution, based on natural spring and well bottom temperature values, 84% consists of medium and low-temperature areas, and 16% consists of high-temperature areas.

The Western Anatolian Extensional Neotectonic Zone is well-known for its geothermal resources and numerous hot springs. The geothermal fields around Manisa, Denizli, Aydın, İzmir, and Muğla constitute the essential resources in this region (Figure 3).

The geothermal resources in İzmir Bay and its northern part were formed under the control of both the extensional tectonic regime and strike-slip faults (İZKA, 2022). In some regions, such as Manisa (Kula), Afyon, and Çanakkale, the geothermal system can also be seen to be affected by volcanism and magmatism. In addition, geothermal systems in Çanakkale, Balıkesir, Bursa, Bolu, and Yalova are located within a neotectonic region.

Geothermal areas are also located in the Central Anatolian Region, under the influence of the North Anatolian Fault Zone (NAFZ) to the north, the East Anatolian Fault Zone (EAFZ) to the east, and the Tuzgölü Fault Zone (TGFZ) to the west. Additionally, Tertiary granite intrusions, local and regional block faulting, and Pliocene volcanism form the geothermal systems (Şener et al., 2017). Ankara, Niğde, Yozgat, Nevşehir, Kırşehir, Aksaray, and Sivas geothermal fields are the most important geothermal resources in this region (Şener, 2019).

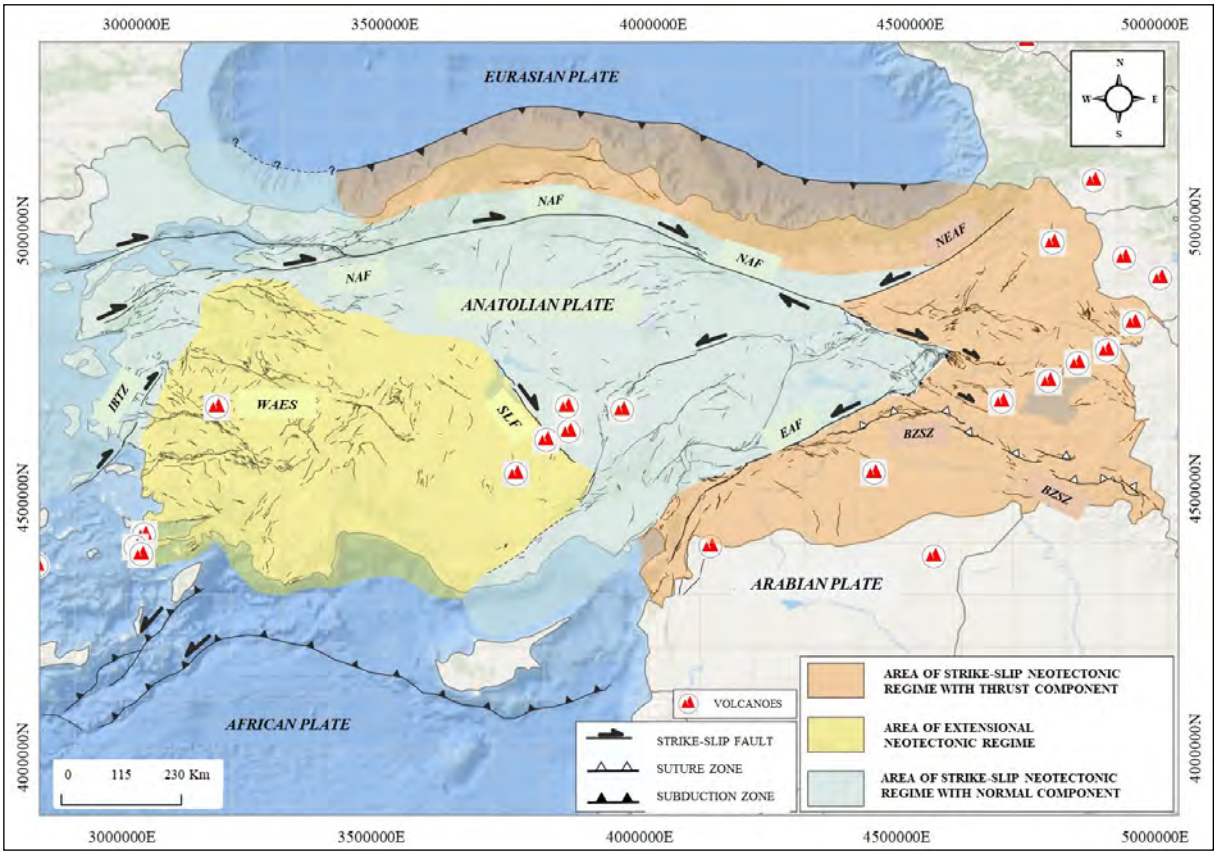

Figure 3- Neotectonic regions and structural features of the Anatolian Plate (modified from Baba et al., 2021, after Şengör and Dyer, 1979; Barka, 1992; Bozkurt, 2001; Koçyiğit and Özacar, 2003).

A dominant strike-slip neotectonic regime controls the geothermal systems along the NAFZ up to Bingöl-Karlıova and around the EAFZ. Geothermal fields in Hatay, Mersin, Kahramanmaraş, Osmaniye, Elazığ, Bingöl, and Muş were primarily formed under the control of EAFZ and its segments. In addition, the Bitlis-Zagros Suture Zone (BZSZ) and young volcanism areas have enriched the Southeast regarding geothermal resources and other geological events (Baba et al., 2021; Şener et al., 2021; Uzelli et al., 2021).

Many tectonic, volcanic, and magmatic factors such as caldera, domes, extension cracks, and magma chambers are located in the eastern part of the Anatolian Plate and are limited by the control of BZSZ and EAFZ. The essential areas formed under the compressional tectonic regime are Erzurum, Kars, Ağrı, Van, Bitlis, and Muş (Uzelli et al., 2021).

In the Southeastern Anatolia Region to the south of the BZSZ, the Karacadağ volcanism and compressional tectonics have led to the formation of critical geothermal fields in Gaziantep, Adıyaman, Diyarbakır, Şırnak, Batman, and Siirt. Since the Southeastern Anatolia Region is an oil region, it has been studied by many researchers. Medium-high temperature geothermal fluids have been found in many oil wells drilled around Adıyaman, Diyarbakır, and Batman. In this study, it has been determined that the wells that have not been discovered and are not currently in use are quite suitable and vital resources for geothermal applications in the region. It has been emphasized that they should be reintroduced to the region's economy in the future (Baba et al., 2019).

2.2. Hot Dry Rock (HDR) - Enhanced Deep Geothermal Systems (EDGS)

Hot dry rock can be defined as impermeable or semi-permeable rocks that reach a high temperature created by themself, such as granite-granodiorite. Using engineering methods, the utilization of unconventional geothermal resources to obtain an economical and appropriate amount of heat is called Enhanced Deep Geothermal Systems (EDGS).

The Anatolian Plate is in an important geological position for obtaining geothermal energy from hot and radiogenic granitoid using EDGS technology (Figure 4). EDGS is based on the principle of cracking the impermeable rocks at depth with pressure, creating an artificial reservoir, and then sending water to the fractured stones and using the energy of the heated water.

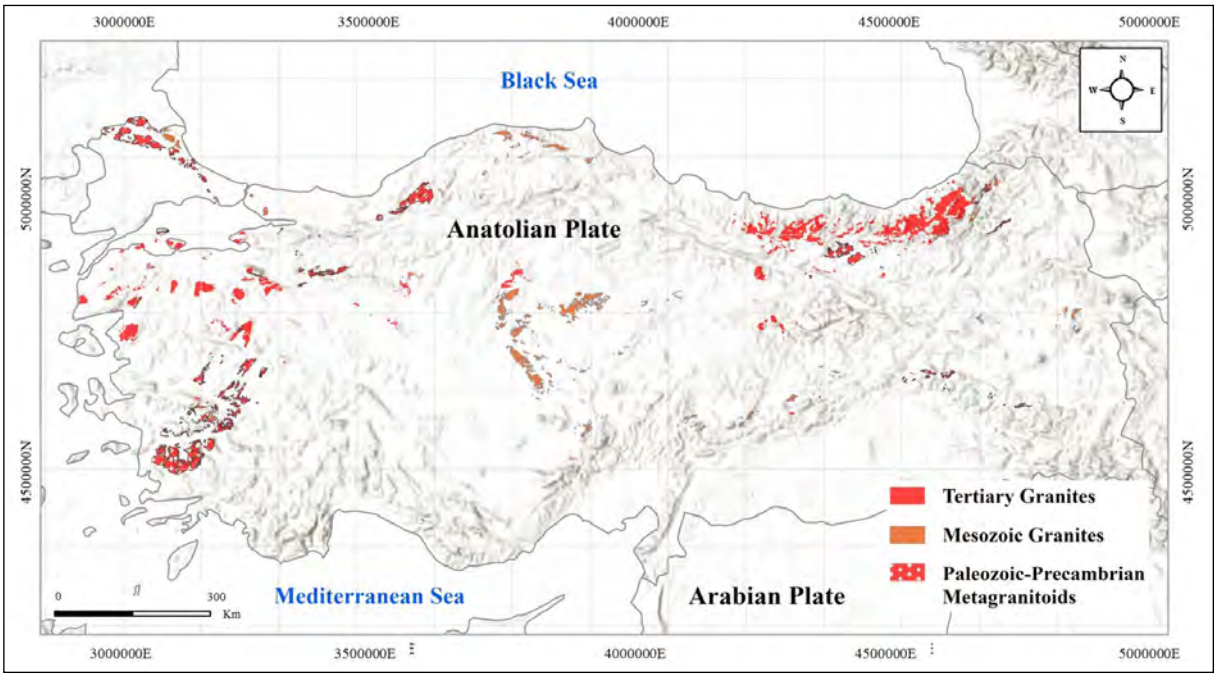

Figure 4- Granitoid distribution of Anatolian Plate (Chandrasekharam and Baba, 2021).

The following criteria must be carried out for successful EDGS;

- The underground crack network is sufficient for high temperatures.
- The permeable area should be large enough to provide an adequate amount of fluid flow between the wells and the contact surface of the fluid, and the hot rock should be large enough to allow the rock to heat the fluid without cooling.
- Geothermal energy can be brought to the surface and used in electricity generation and/or heating.

Since granites in Türkiye contain high concentrations of U, Th, and K, they have above-average calorific values and generate significant heat. The heat generation value (A) is obtained based on the Rybach Equation:

$$A(\mu W/m^3) = 10^{-2} * \rho * (9.52C_U + 2.56C_{Th} + 3.48C_K) \quad (1)$$

($\rho(g/cm^3)$: density of the rock; C_U, C_{Th} and C_K: uranium (ppm); thorium (ppm) and potassium (%) concentrations).

Surface heat flux values are calculated using the Lachenbruch (1968) Equation:

$$Q = Q_0 + D * A \quad (2)$$

(Q: heat flux at the surface; Q_0: the initial value of a heat flux; D: rock thickness; A: radioactive heat generation).

Considering the Curie depth and heat flux of Western Anatolia, the probable thickness of the batholith can be regarded as 10 km. Considering that the total granitoid area of Western Anatolia is 4221 km^2, at least 2% of these granitoid rocks can provide electricity by EDGS, then EDGS. Electricity generation potential in Western Anatolia is approximately $8x10^7$ MWh. When all granites in Türkiye are considered, it is clear that the latent energy which could be obtained is very high (Chandrasekharam and Baba, 2021, 2022).

In the Bozköy district of Niğde, a 3845-meter-deep well was drilled by a private company in 2016, and the highest well-bottom temperature (341°C) was measured. Hence the highest well-bottom temperature indicates that the EDGS energy potential of Central Anatolia is high and it is predicted that the geothermal system in Central Anatolia can be developed using EDGS Technologies (Şener et al., 2017).

2.3. Distribution, Utilization, and Potential of Geothermal Energy Resources in Türkiye

Türkiye has more than 2000 wells and 415 geothermal fields, in which the lower temperature limit is accepted as 30°C. In 2022, Türkiye's electricity generation capacity reached 1663 MWe, and the total direct heat use (installed thermal power) reached 5113 MWt. Considering the diversity of the geological structure of Türkiye, the geothermal systems have developed depending on young tectonic and volcanic active rock. Western and Central Anatolia are especially rich in geothermal resources (Figure 5). The geothermal well with the hottest well-bottom temperature was drilled in Niğde (located in Central Anatolia), and the well-bottom temperature was measured as 341°C at a depth of 3845 meters. Different parts of the country, such as Nevşehir, Sivas, Yozgat, Erzurum, Ankara, Batman, Van, and Şırnak, also have medium-high temperature springs.

In this study, the fluid temperature and flow rate in 2089 wells with accessible data were taken as the basis. According to the obtained data, the capacity is around 36025.81 MWt. However, because of the differences in the first measurement values required for the license in the well data, values may have changed later in the production process. The well data not being shared for commercial reasons as well as unsaved well data, the capacity will be above the registered value.

According to the distribution of the number of wells by region, the Aegean Region ranks first with 1635 wells, followed by Central Anatolia and Marmara (Figure 6). In terms of capacity, the Aegean Region ranks first by far with 34.920 MWt. The 673 wells in Aydın, 384 in Manisa, 228 in Denizli, and 209 in İzmir indicate the high potential in the Aegean Region (Table 1).

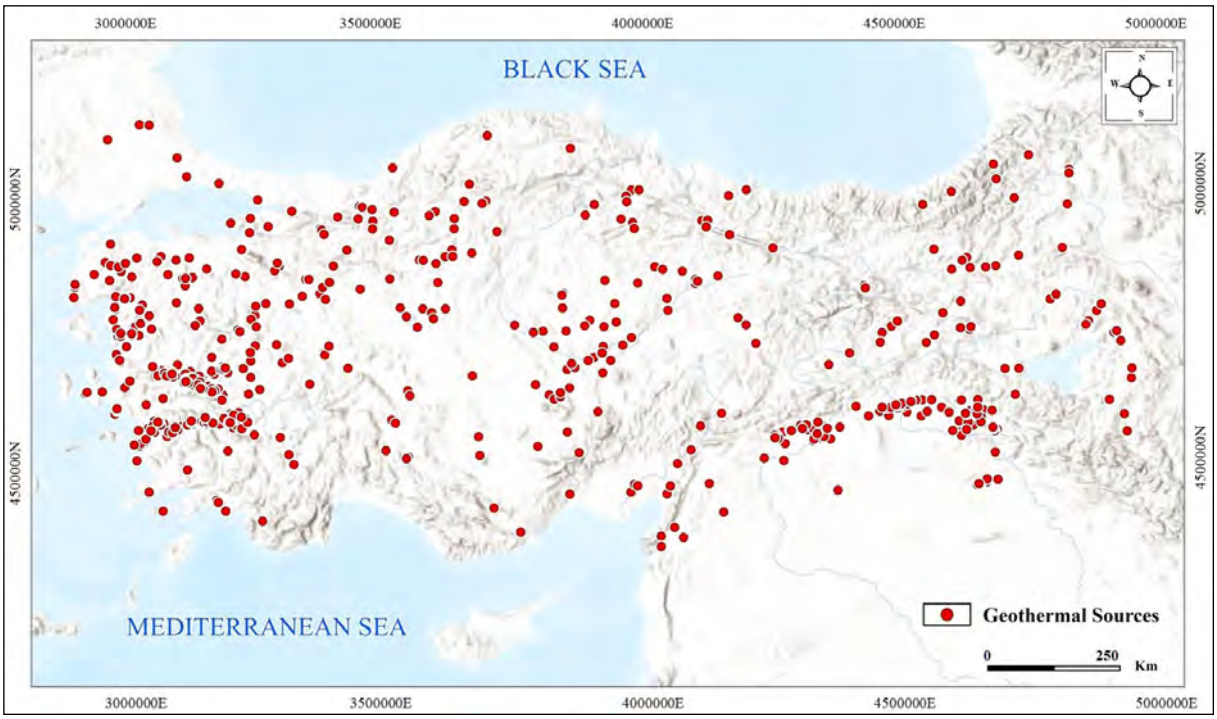

Figure 5- Geothermal sources of the Türkiye (Updated from Akkuş et al., 2005; Baba et al., 2019; EBRD, 2020*a*).

Table 1- Geothermal well capacity values of provinces in Türkiye (Baba et al., 2019; EBRD, 2020*a*).

Province	Number of Wells	Capacity (MWt)	Province	Number of Wells	Capacity (MWt)	Province	Number of Wells	Capacity (MWt)
Afyon	52	334.1	Erzincan	1	0.00	Muğla	5	11.38
Ağrı	6	87.04	Erzurum	11	21.82	Nevşehir	13	90.26
Aksaray	5	1.12	Eskişehir	14	20.83	Niğde	14	15.38
Amasya	7	4.79	Gaziantep	1	0.00	Ordu	1	0.00
Ankara	62	108.65	Hatay	8	0.22	Osmaniye	1	0.00
Aydın	673	19143.53	İstanbul	9	0.79	Rize	4	4.84
Balıkesir	33	90.25	İzmir	209	874.10	Sakarya	5	56.52
Batman	1	3.21	Kahramanmaraş	7	8.61	Samsun	12	12.92
Bilecik	1	0.22	Karabük	1	0.33	Siirt	1	0.29
Bingöl	4	6.00	Kayseri	6	2.62	Sivas	16	58.38
Bolu	23	20.84	Kırklareli	2	2.76	Şanlıurfa	25	57.21
Bursa	5	17.43	Kırşehir	21	66.46	Tokat	7	5.82
Çanakkale	21	180.44	Kilis	1	0.00	Tunceli	2	0.81
Çankırı	5	5.91	Kocaeli	2	0.00	Uşak	5	15.64
Çorum	10	0.80	Konya	18	20.92	Van	7	26.85
Denizli	228	4906.63	Kütahya	84	392.36	Yalova	6	19.75
Diyarbakır	7	6.30	Manisa	384	9242.40	Yozgat	40	74.83
Elazığ	1	0.63	Mersin	2	2.82			
TOTAL NUMBER OF WELLS								2089
TOTAL CAPACITY (MWt)								36025.81

In recent years, the potential of the Central Anatolia Region (especially in Nevşehir, Aksaray, and Niğde) has been increasing, while other regions are still waiting for investment (Figure 7).

The current usage areas and capacities of geothermal energy in Türkiye are presented in the Türkiye Geothermal Strategy Report, prepared in 2022. According to the report, the total installed heat power in direct use is 5113 MWt (Table 2).

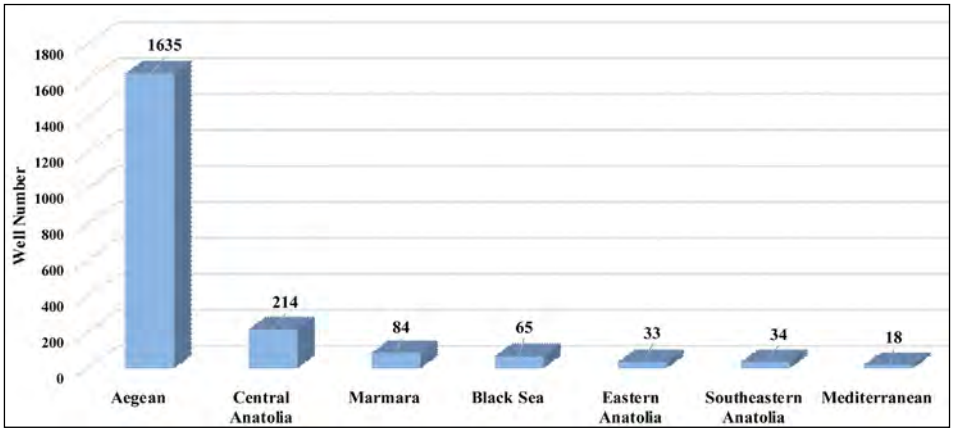

Figure 6- Distribution of the number of wells by region (Akkuş et al., 2005; Şener et al., 2017; Baba et al., 2019; EBRD, 2020*a*).

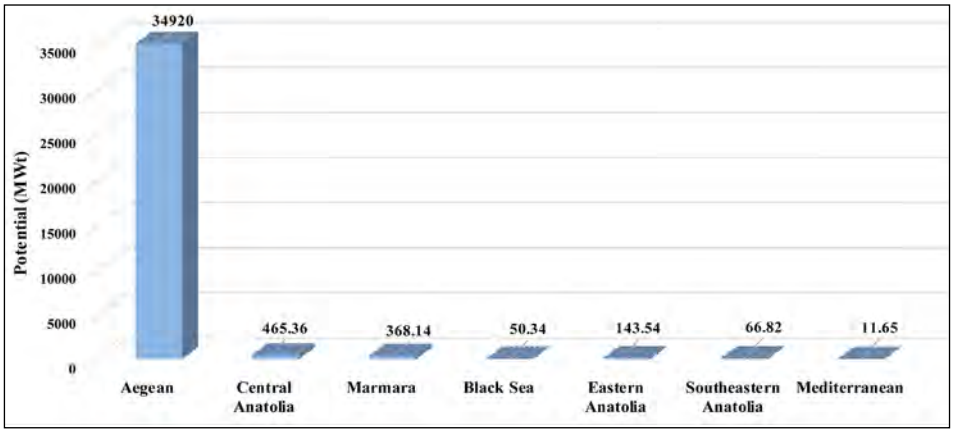

Figure 7- Regional capacity distribution from existing well data (Akkuş et al., 2005; Şener et al., 2017; Baba et al., 2019; EBRD, 2020*b*).

Table 2- The current situation of geothermal evaluations in Türkiye.

Evaluation	**Capacity**
Geothermal District Heating (city, residential)	158.000 Housing Equivalent (1422 MWt)
Greenhouse Heating	5293 Acres (1230 MWt) 146.600 Housing Equivalents
Spa Facilities, Thermal Hotels and Timeshare Facilities Heating	68.000 Housing Equivalents (680 MWt)
Thermal Energy of Thermal Water used in Hotels, Spas, Timeshares	520 Spas(1763 MWt) (23 million People Per Year)
Fruit and Vegetable Drying	9.5 MWt
Cooling	0.35 MWt
Geothermal Heat Pump (ground source)	8.5 MWt
Total Heat Usage (installed thermal power)	5113 MWt
Total Electricity Production (installed power)	1663 MWe
Industrial Liquid CO_2, Dry Ice Production	400.000 Tons/Year

2.4. Electricity Generation

Türkiye has been dependent on fossil fuels for more than 60% of electricity generation until recent years. Since oil and natural gas production is too low to serve the purpose, this deficit is resolved through imports. Increasing global prices and policies to reduce foreign dependency have increased investment and incentives to exploit Türkiye's natural resources. For this reason, in addition to using domestic sources from fossil fuels, the trend toward new technologies has accelerated, and investments in solar, wind, hydraulic and geothermal energy have increased. Electricity production from geothermal energy has grown rapidly, especially with the Türkiye Renewable Energy Resources Support Mechanism (YEKDEM) (Figure 8).

The sector has recorded significant growth by including the private sector in energy production from geothermal resources. As of 2022, the number of geothermal power plants in Türkiye is 65, and the installed geothermal power capacity is 1663 MWe (EPDK, 2022). Today, all geothermal power plants are located in the western part of Türkiye. While most of the power plants are situated in Aydın, Denizli, and Manisa, new power plants have started to be established in developing areas of İzmir, Afyon, and Çanakkale (Figure 9).

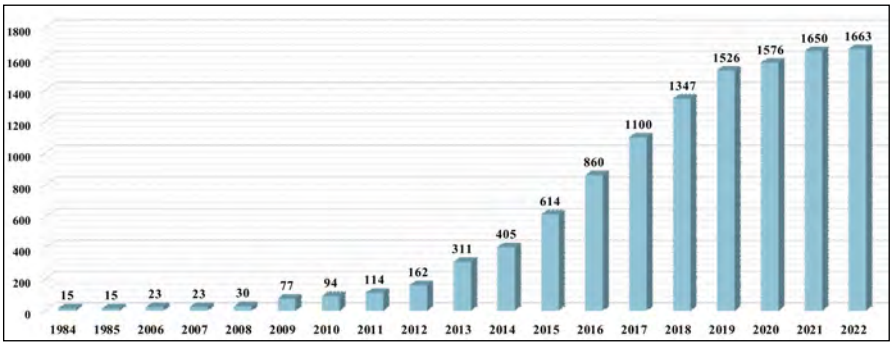

Figure 8- Capacity development of geothermal power plants in Türkiye (MWe; EPDK, 2022).

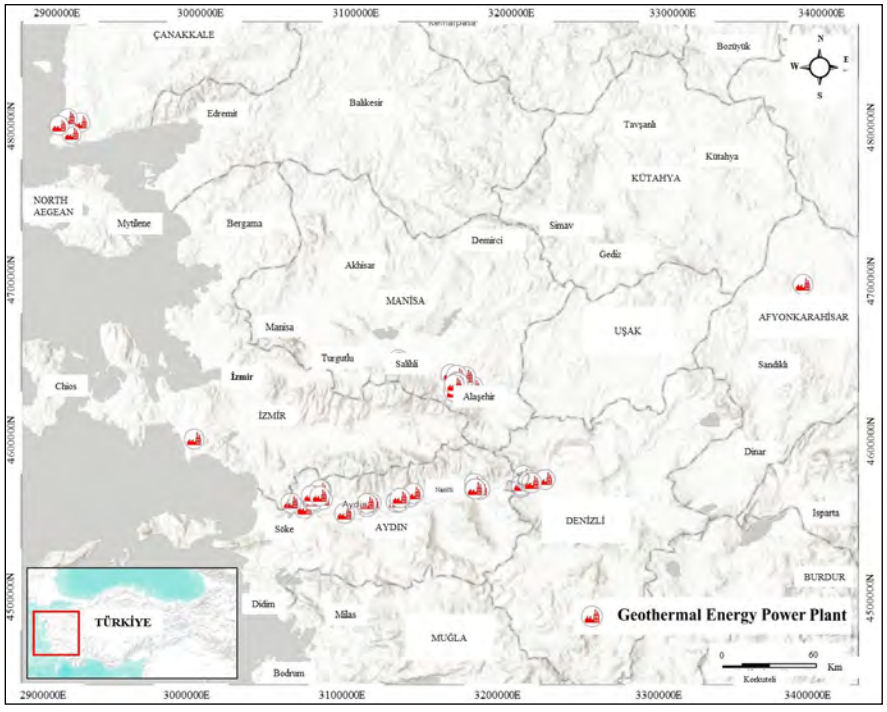

Figure 9- Location map of existing geothermal power plants in Türkiye.

Geothermal power plants in Türkiye and their operating capacities are presented in Table 3. Table 3 also shows that 98% of the existing power plants are in Western Anatolia. According to Energy Market Regulatory Authority (EMRA) data, apart from the existing power plants, there are 12 projects which have received a pre-license, with a total capacity of 310 MWe at the beginning of 2022. In addition, two projects are under construction, and the total capacity of geothermal power plants is approximately 62 MWe.

2.5. Direct Use

The installed direct-use geothermal capacity in Türkiye has been calculated as 5113 MWt within the scope of the Türkiye Geothermal Resources Strategy Report. Approximately 47.8% is thermal tourism applications, 27.8% is central heating applications, 24.1% is greenhouse heating applications, and 0.4% is heat pumps, drying, and cooling applications (Figure 10).

Table 3- Geothermal power plants and their operating capacities (EPDK, 2022).

Province / District		**Field Name**	**Company**	**Operating Capacity (MWe)**
Denizli	Sarayköy	Kızıldere-Karataş	Zorlu Elek.	260
			Bereket Enerji	6.85
		Tekkeköy	Greeneco Enerji	77.2
		Tosunlar	Akça	3.804
Manisa	Alaşehir	Kurudere-Alkan	Zorlu Elek.	45
			Türkerler Jeot.	78
		Kemaliye	Enerjeo	24.9
		Alaşehir-Soğukyurt	Sis Enerji	47.52
		Alaşehir-Kavaklıdere	Maspo Enerji	44
		Alaşehir-Baklacı	Akça Enerji	19.4
		Piyadeler	Soyak Enerji	60.3
Manisa	Salihli	Caferbey-Hasalan-Sart	Sanko	64
Aydın	Germencik	Ömerbeyli	Gürmat Elek.	259.9
		Hıdırbeyli/ Bozköy	Kipaş Holding	218.6
		İncirliova	3 S Kale	25
		Turanlar	Beştepeler Enj.	24
		Gümüşköy	Gümüşköy Jeot.	13.2
	Nazilli	Güzelköy-Durasıllı	Kipaş Holding	10
Aydın	Kuyucak	Yöre	Turcas	18
		Pamukören	Çelikler Jeot.	176.55
Aydın	Sultanhisar	Sultanhisar		36.31
			Menderes Geot.	7.951
Aydın	Köşk	Salavatlı		60.5
Aydın		Umurlu	Karkey	24
Aydın	Buharkent	Buharkent	Limgaz	13.77
İzmir	Seferihisar	Kavakdere	RSC Elektrik	12
Çanakkale/Ayvacık Tuzla Babadere		Tuzla	Yerka	11.75
		Tuzla Jeot.	7.5	
		MTN Enj.	7.95	
Afyon		Ömer-Gecek	AFJET	2.755
Denizli	Sarayköy	Gerali	Jeoden	2.52
Total Production				1663.23

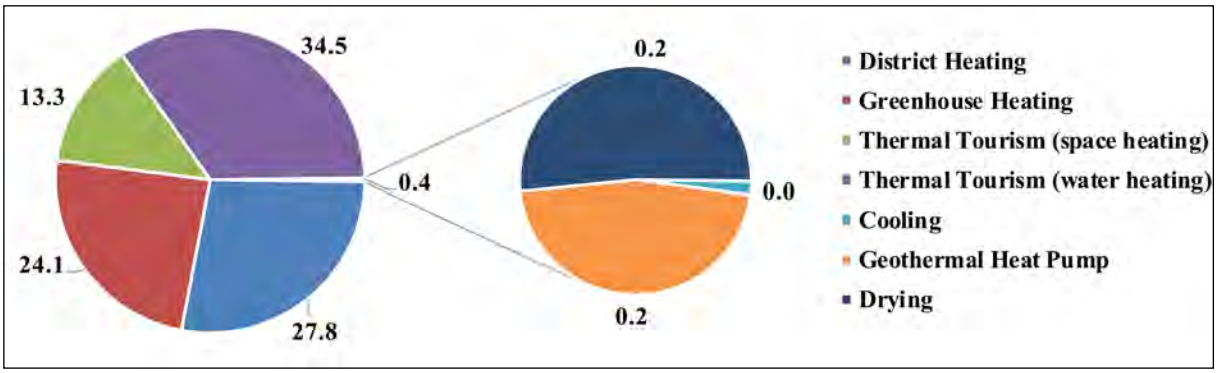

Figure 10- Percentage of current direct use applications (MWt) in Türkiye.

The capacities of direct-use applications in MWt determined in this study are shown in Figure 11. Considering the general distribution of usage, heating applications come to the fore. The thermal energy capacity of the thermal water used in thermal spas and pools is 1763 MWt, and the heat energy capacity used for geothermal heating of the thermal facility and related spaces is 680 MWt. The heat energy capacity of central heating systems in cities and districts has reached 1422 MWt. In agricultural applications, the heat energy capacity for greenhouse heating is 1230 MWt, while the heat energy capacity for drying agricultural products is 9.5 MWt. The heat energy capacity of the heat pumps is 8.5 MWt, and the cooling application capacity with the geothermal fluid is 0.35 MWt.

2.6. Urban Heating and Cooling

According to the Energy Cities Association (EKB, 2022) data, heating systems for cities and commercial buildings/facilities are Türkiye's most common direct use of geothermal energy today (Figure 12 and Table 4). The total capacity of central geothermal heating and thermal facility space heating applications is 2102 MWt.

2.7. Thermal and Health Tourism

As of today, more than 520 active spa facilities use geothermal resources. These facilities host approximately 20-23 million people per year. This contributes to the rise of Türkiye to 3rd place in the world in thermal facility applications of geothermal

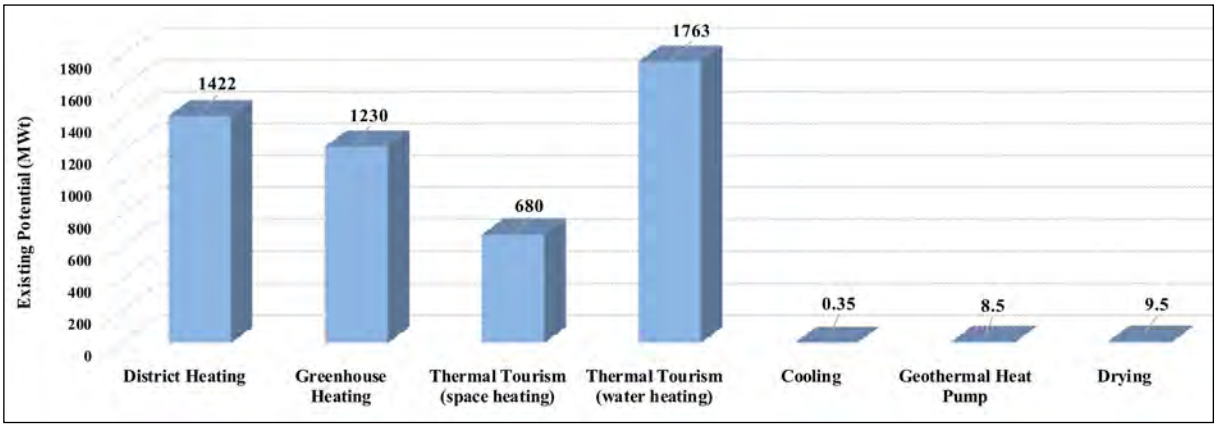

Figure 11- Current capacities of geothermal direct use applications in 2022.

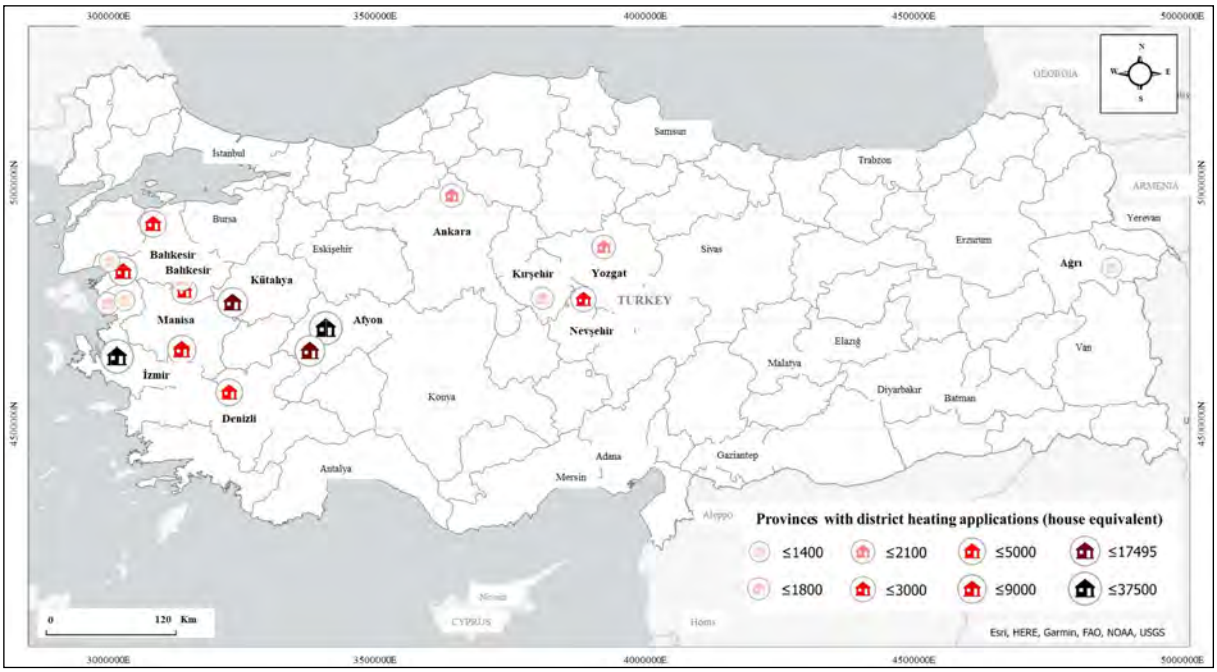

Figure 12- Provinces with district heating in Türkiye and housing equivalents (created from EKB, 2022 data).

Table 4- District heating applications.

Application Field	Temperature ºC	House Equivalent	Application Field	Temperature ºC	House Equivalent
Balıkesir-Gönen	80	3.400	İzmir-Dikili	125	1.530
Kütahya-Simav	120	18.612	Nevşehir-Kozaklı	92	3.800
Ankara-Kızılcahamam	80	2100	Ağrı-Diyadin	70	970
İzmir-Balçova-Narlıdere	98-125	38.899	Manisa-Salihli	94	10067
Afyon-Sandıklı	70	30.000	Denizli-Sarayköy	140	5000
Kırşehir-Terme	57	1.800	Balıkesir-Edremit	60	5.100
Afyon-Ömer-Gecek	95	25.610	Balıkesir-Bigadiç	96	1.500
Balıkesir-Güre	65	1400	Yozgat-Sorgun	80	2100
Balıkesir-Sındırgı	98	4.000	İzmir-Bergama	65	866
TOTAL					156.754

* Considering the current growth, the total value is approximately 158.000. Energy Cities Association data has been updated and used.

energy. The countries most known for health tourism operating under medical supervision are the USA, Germany, Thailand, India, and Türkiye. The geothermal fluid was examined that heats the thermal pools, health and cure centers, natural outlets-spas, and historical and renovated thermal pools. The thermal applications and facilities of the provinces in Türkiye are shown in Figure 13.

Thermal tourism is the oldest sector of geothermal application in Türkiye. Thermal facilities use geothermal fluid for baths, pools, and spas. As 520 hot springs use approximately 1763 MWt of capacity and serve 20 million people annually, the estimated future thermal requirements are also in line with the current condition and geothermal resource potential (WB, 2021).

Figure 13- Provinces with thermal tourism facilities or spas in Türkiye and the approximate number of facilities (Ministry of Health, 2021).

2.8. Greenhouse Heating and Agricultural Drying

Türkiye has made rapid progress in the greenhouse sector since 1970. In recent years, greenhouse cultivation has adopted geothermal direct-use applications for developing technology, innovative approaches, and inexpensive economic heating. Currently, the Turkish greenhouse sector ranks 4th in Europe in total production. According to the data compiled in this study, geothermal use (greenhouse heating and drying) is being applied in 17 provinces of Türkiye (Figure 14).

Most of the existing greenhouses are located in the southern provinces, where the climatic conditions are more favorable. The lack of improvement in colder climates is due to the cost of conventional energy sources. However, in recent years, a growing geothermal greenhouse sector has started to develop in cold climate regions (such as Sivas, Afyon, Kırşehir, and Ağrı-Diyadin) due to the widespread use of geothermal energy in greenhouses.

Annual energy use rates for greenhouse heating with geothermal resources worldwide almost tripled from 1995 to 2020. In line with the global trend, Türkiye increased its geothermal greenhouse heating capacity to 1230 MWt and the total greenhouse area to 5293 decares in 2022. However, high-tech greenhouse cultivation (by all kinds of heat sources) accounts for less than 2% of the total. As of 2022, geothermally-heated greenhouses have a significant share of 30% of the total heated greenhouse area.

In addition to geothermal greenhouses, geothermal energy is also used for drying the products. The use of geothermal sources in the food drying process aims to reduce food loss all over the world. According to the 2021 UN Food Waste Index Report, a total of 931 million tons of food is wasted worldwide yearly (UNEP, 2021). According to the same report, more than 7.7 million tons of food are wasted in Türkiye annually. Traditional drying methods, such as sun drying in an open area, are still the most common

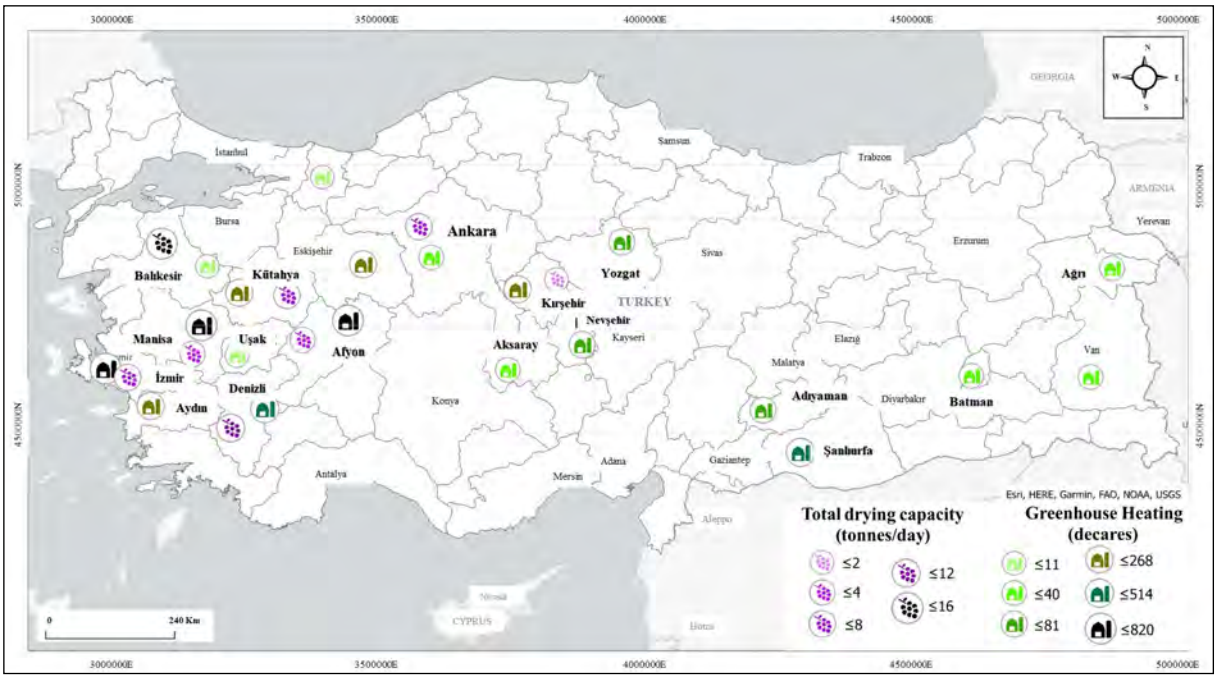

Figure 14- Current geothermal greenhouse heating and drying applications in Türkiye.

drying methods in Türkiye. However, contamination by dust, soil, and insects and unmanageable drying parameters such as temperature and wind speed can cause excessive drying and decrease the quality of the dried product. Therefore, renewable energy sources such as geothermal energy play an essential role in controlled drying methods. In the current situation, as in the examples of İzmir, Balıkesir, and Kırşehir, agricultural drying practices have increased in recent years, and the 2022 capacity has reached the level of 9.5 MWt.

2.9. Integrated Systems

Integrated (gradual) use of geothermal resources is defined as electricity generation, distribution and use of thermal energy, drying and dehydration processes, recreational uses, and sequential use of geothermal heat in applications by integrating different technologies (Rubio-Maya et al., 2015).

Some of Türkiye's existing geothermal power plants provide good investments and fluid support for integrated use. For instance, in Çanakkale-Babadere, Aydın-Ortaklar, Germencik, Salavatlı, and Denizli-Sarayköy, the geothermal fluid from the geothermal power plant is used in a cascade manner in greenhouse heating and urban heating before being sent for re-injection (Figure 15).

3. Contribution of Geothermal Energy to National Economies, Support Mechanisms, and Investment Costs

One of the most important economic aspects of geothermal energy is that it reduces the dependency on imported energy by using domestic resources. Thus, domestic investments will reduce trade deficits and keep capital in the country.

No matter how high a country's technical potential for geothermal electricity generation is, technology and incentives for the market and production are the primary determining role. For instance, although electricity generation from a 180°C geothermal well in the Kızıldere Geothermal Field in the 1980s was not considered economically and technically appropriate, today, it is regarded as desirable and economical. Therefore, the critical factors are an incentive, purchase price, purchase period, and financial opportunities.

In addition to environmentalism and security of supply, the cost of geothermal heating is at least 60% cheaper than fossil fuels. Today, geothermal heat is 70% cheaper than natural gas in many places (local house tariff). Considering the state's subsidy to natural gas for residential heating, it becomes clear how much geothermal energy contributes to the country's economy. Compared to the actual natural gas cost

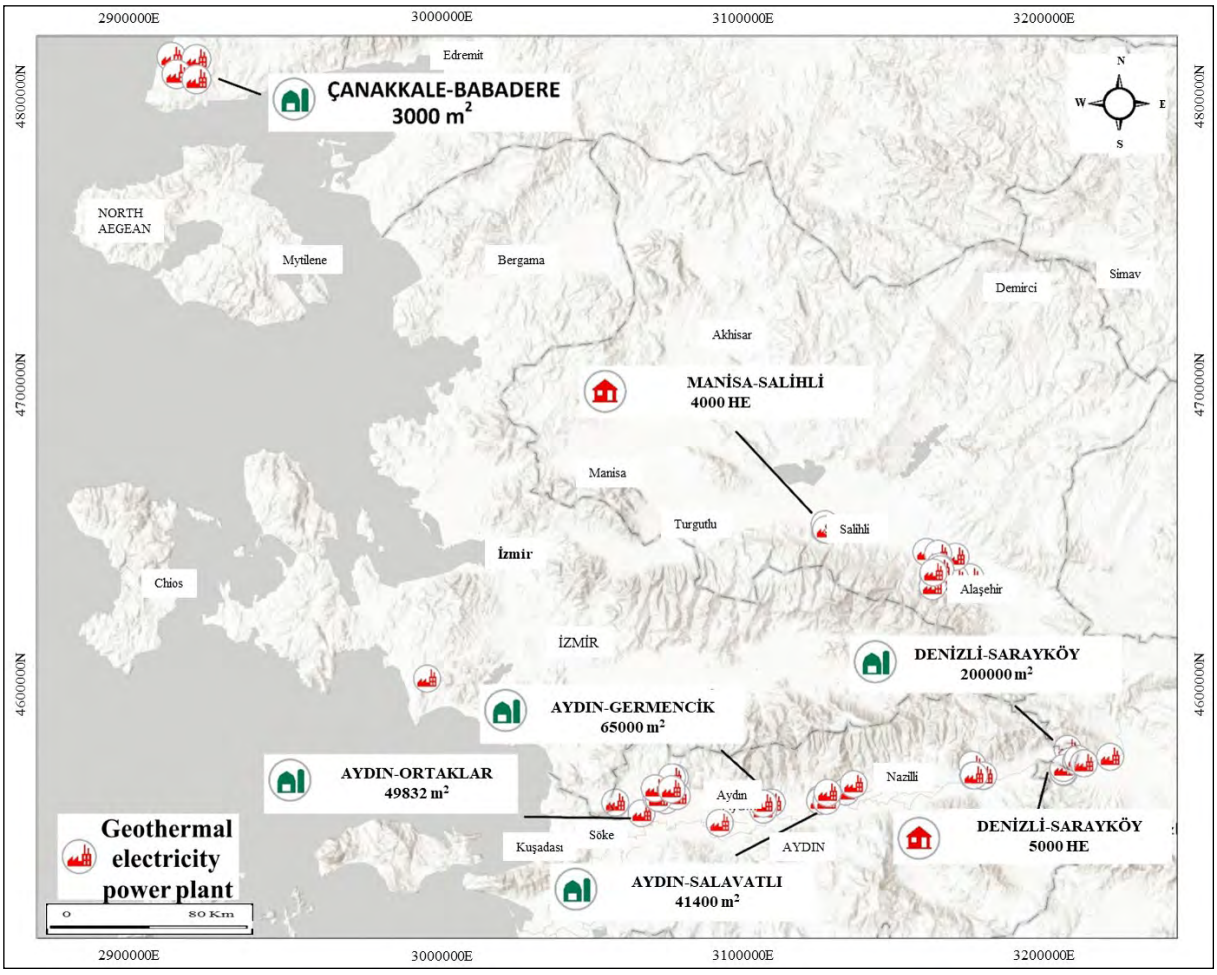

Figure 15- Examples of existing geothermal integrated applications in Türkiye (WB, 2021). HE: House Equivalent.

of 9.135 TL/m^3 (6.3 TL/m^3 x 1.45 (45% BOTAŞ increase as of 01.04.2022)), a very economical price of approximately 1/8 is in favor of the state and population. Data on the contribution of geothermal energy to the annual economy regarding electricity and direct use are presented in Table 5 and Figure 16.

The direct contribution of geothermal applications calculated above to the economy is 54,857,760,000 TL in total (excluding contribution to employment, natural gas savings, and CO_2 emission reduction). Also, when 5% is added for the unknown and unregistered, the direct contribution of the geothermal applications to the economy can be considered as approximately 58 billion TL/year.

3.1. Current Incentive System

The Ministry of Industry and Technology has an incentive system for investments of a specific size. Customs duty exemption, Value Added Tax (VAT) exemption, permission for loan allocation, etc., are applied within this incentive system; these parameters change annually according to the circumstances.

3.2. Investment Costs of Geothermal Energy Applications

The approximate amount invested in some basic geothermal energy applications were calculated in this study.

3.3. Geothermal District Heating System General Investment

Since the late 1980s, geothermal central city heating applications have been ongoing and significantly contributed to the Turkish economy. Geothermal central heating investments are made under the leadership of provincial governors, development

Table 5- The annual contribution of electricity generation and direct use of geothermal energy to the economy.

Geothermal Energy Application	Calculation Details	Economic Contribution (TL/ Year)
Electricity Generation	1663 MWe x 103 x 0.8 (domestic consumption factor) x 0.95 (production reduction factor and others in summer) x 8500 hours/year x 2.5 TL/kWh (average sales to the end consumer)	26.857.400.000
House, Hotel, Spa, Thermal Facility, Central Heating	Equivalent to 216.000 residences x 330 TL/month x 12 months	855.360.000
Greenhouse Heating and Production	5293 acres x 103 x 50 kg/m^2 season x 20 TL/kg	5.293.000.000
Liquid CO_2 and Dry Ice Production	400.000 tons/year x 300 dollars/ton x 14 TL/US$	1.680.000.000
Mineral Water Production and Sales	MASUDER, 2022	6.500.000.000
Thermal Tourism (Ministry and Municipality certified Hotels and Spas)	~ 80.000 beds x 0.7 occupancy rate x 400 TL/day person (room + meal + treatment) x 365 days/year	8.176.000.000
Thermal Tourism (Spa, Cure Center, Physiotherapy, Daily Spa Facilities)	320 spa facilities x 500 people/day x 130 TL/day person (including treatment, etc.) x 365 days/year x 0.7 occupancy rate	5.314.400.000
Thermal Tourism (Thermal Timeshare Facilities)	Facilities Using Geothermal Heating and Thermal Water (Except for the amount paid for the purchase of time-share property (for investment)) 10.000 rooms x 2500 TL/year (Operation and maintenance expenses) x 23 terms (350/15 days)	575.000.000

agencies, YIKOB (Department of Investment Monitoring and Coordination), and municipalities in Türkiye. Two examples of the cost of geothermal heating applications are presented below.

The first is an investment made by the governorship, municipality, and partially the private sector with the public's participation. The approximate amount includes the main investment, wells, and distribution, thus:

158.000 residences (equivalent to 100 square meters per residence) x 35.000 TL/house = 5,530,000,000 TL.

Second is the calculation of global investment by citizens for indoor installations in geothermal central heating. This is calculated according to the internal installation of at least 158.000 residential equivalents in geothermal central heating (low-temperature system). The 158.000 residences are considered new indoor installations. According to the figures of January 2022, this installation, including under-building pumps, piping, calorimeters, room radiators, hot water boilers, etc. for a 100 m^2 house, is accepted as 17.000 TL, as below:

158.000 x 17.000 TL = 2,686,000,000 TL invested.

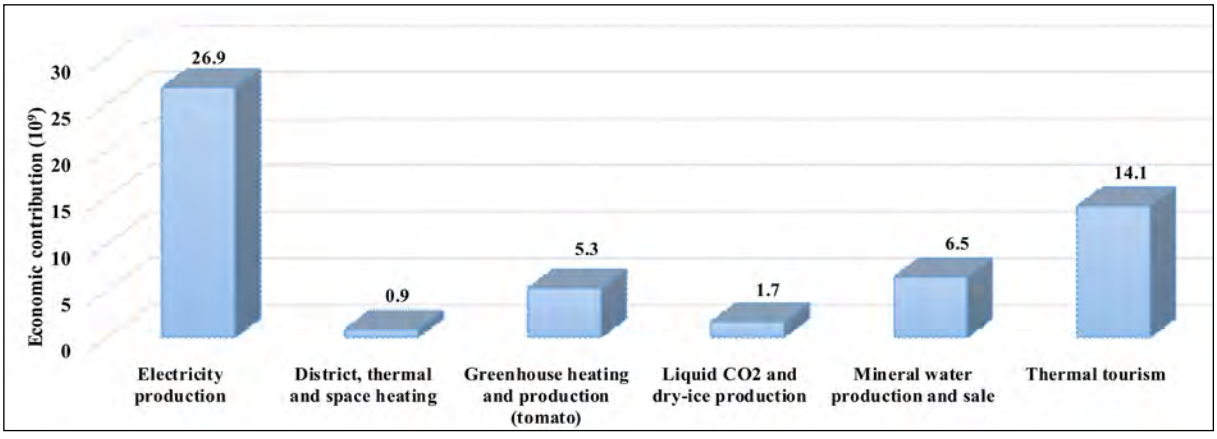

Figure 16- The annual contribution of geothermal energy to the Turkish economy in terms of electricity and direct use (TL/year).

3.4. Geothermal Power Plants Investment

All the existing geothermal power plants in Türkiye, except the Kızıldere-Denizli power plant, were built by the private sector. If we assume the total electricity generation capacity as 1663 MWe and calculate an average investment cost of 4 million dollars per MWe, the result is:

1663 MWe x 4 million USD/MWe x 14 TL/USD = 93,128,000,000 TL.

3.5. Investment in Thermal Tourism, Thermal Hotels, Cure Centers, Spas, etc.

Today, it is difficult to calculate the total investment cost for these sectors because the investments were made in different years, and new investments are still being made. Furthermore, since these investments are not in a certain classification and standard, making a standard calculation is impossible.

3.6. Geothermal Greenhouse Investment

Currently, the total of geothermal heated greenhouses is 5293 decares. Türkiye is the world leader in terms of geothermal-heated greenhouses. The cost of a 1 m^2 greenhouse investment is between 80-120 dollars. This cost varies according to the region where the greenhouse is installed in terms of the type, size, and condition of the land, the characteristics of the geothermal field, and the type of heat used. However, if the average is calculated as 100 dollars per m^2:

5293 acres x 10^3 (m^2) x 100 USD/m^2 x 14 TL/USD = 7,410,200,000 TL.

4. Recommendations and Strategies for the Sustainability of Geothermal Resources

Geothermal resources are an important renewable energy source for Türkiye's economy if they are systematically and technically explored, operated, and inspected within legal regulations. Today, the geothermal resource is widely used directly and indirectly in Türkiye. Electricity produced in geothermal power plants from a geothermal fluid is termed indirect use, while urban heating and cooling, greenhouse heating, agricultural drying, thermal and health tourism, CO_2, and dry ice production applications are used directly (Figure 17).

In view of the geological data obtained, an evaluation of which applications can be made in which provinces in Türkiye is presented in Figure 18. Geothermal energy power plants, electricity production, and integrated production can be implemented in many cities in Western Anatolia. Agricultural applications, thermal tourism, and heating are becoming common in Western and Central Anatolia. Thermal tourism and integrated facilities,

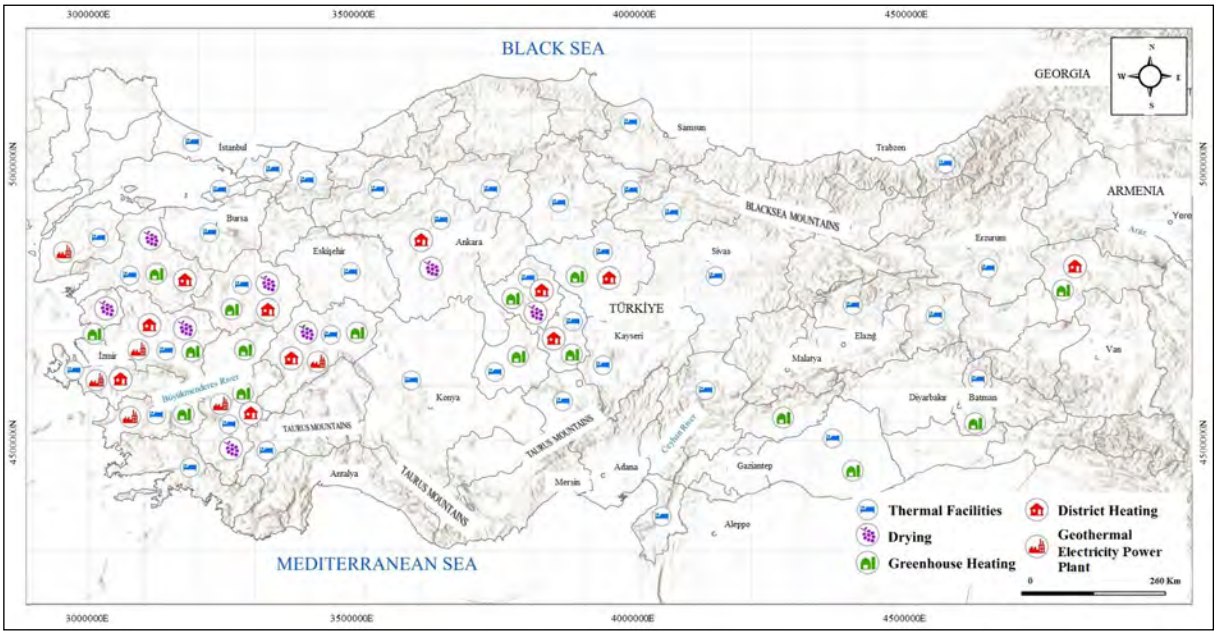

Figure 17- Current direct and indirect use of geothermal energy sources in Türkiye.

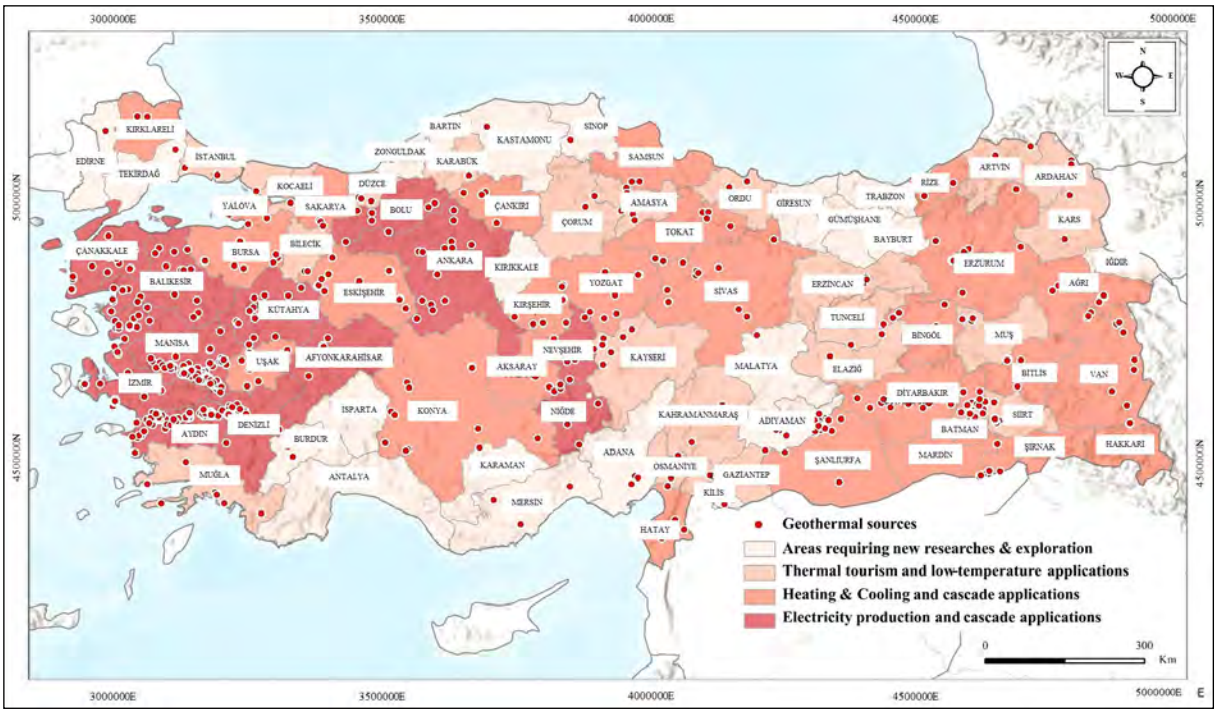

Figure 18- Projection of future fields using direct and indirect geothermal energy sources in Türkiye.

and heating and cooling applications can be seen in different regions of Türkiye. In addition to these, geothermal potential should be investigated in some provinces of the Mediterranean and the Black Sea regions.

Considering the total potential of 62.000 MW currently, a short- and medium-term approach can be made. These approaches have been calculated based on the present situation and the continuity of economic conditions in the world geothermal energy sector (assuming no pandemics, wars, or other catastrophic events). Accordingly, a total of 51.492 MWt usage is foreseen in the medium term (Table 6).

Although hot dry rock (HDR) and EDGS have not been considered in the short and medium term, the projections have a high potential in this application. In the calculations made in this study, when the EDGS value is added, it is predicted that Türkiye's total potential will be at least 400.000 MWe. In addition, when the potential targets and estimated investment are realized, it is thought that the contribution of geothermal energy to the economy will be 210 billion

Table 6- Short- and medium-term plans for the use of existing geothermal energy.

		Direct Use (MWt)	Current Status (2022)	Short Term (2030)	Medium Term (2040)	Long Term (2050)
Total geothermal energy capacity (62.000 MWt)	Total electricity generation capacity (MWe)		1663	3000	4500	6000
	14% MWt conversion efficiency		11878	21428	32142	42586
	Direct use capacity (MWt)	Residential Heating	2102	5000	9000	14000
		Greenhouse	1230	2800	4600	6600
		Thermal Tourism	1763	2000	4500	6000
		Drying	9.5	80	300	1000
		Cooling	0.35	350	800	2000
		Geothermal Heat Pump	8.5	40	150	1500
	Total	MWt	16991.35	31698	51492	73956

TL/year, with direct and indirect employment for approximately 450,000 people (Table 7).

Geothermal energy should be implemented in the short and long term on both the supply and demand sides with the national and local authorities. The private sector, universities, institutes, and research centers should prepare short-, medium- and long-term strategies for developing and effectively using geothermal resources.

In geothermal systems, wells have not yet been drilled in all areas determined by the studies carried out to date. Therefore, it is expected that the future capacity of Türkiye will be much higher when encompassing drilling research and development studies and discovering new fields. This capacity will exceed 100,000 MWt levels in the medium term, especially with the addition of EDGSs.

The following factors were deemed critical in the Science and Technology Commission's Policy Recommendations and Actions meeting held by the climate council in 2022 by the Ministry of Environment, Urbanization, and Climate Change:

- Development of materials resistant to high temperature and high pressure.
- Concentrating on deep and directional drilling technology studies.
- Measuring and monitoring geothermal seismic data.
- Developing models and technologies that will solve the problems of collapse and microseismicity in geothermal fields.
- Increasing and developing studies on obtaining minerals from geothermal fluids.
- Development of borehole designs.
- Developing innovative technologies to eliminate environmental impacts.
- Studies and development of technologies for the direct use of geothermal fluid.
- Dissemination and development of geothermal source heat pumps.
- Creating detailed heat maps of the earth's crust.
- Increasing studies on HDR/EDGS systems and developing technologies for using gases instead of fluids in these systems.

In addition to the Policy Recommendations and Actions of the Science and Technology Commission, it is essential to carry out the following strategies:

- Developing the geothermal energy sector in

Table 7- Potential targets and estimated investment amounts for geothermal applications.

Geothermal Application	**Estimated Goals for 2030**	**Additional Investment (USD) (from 2022 to 2030)**
Electricity Generation (Hydrothermal)	3000 MWe (24 Billion kWh)	5,4 billion USD
Heating (housing, hotel, thermal facilities, etc.)	5000 MWt (500,000 Housing equivalent)	1,2 billion USD
Greenhouse Heating	2800 MWt (12,000 Acres)	1,3 billion USD
Drying, etc.	80 MWt (300,000 tons/year)	30 billion USD
Thermal Tourism	2000 MWt Total of 520 thermal springs, Health Tourism Facilities, ect.	1 billion USD
Cooling	350 MWt (20,550 residences equivalent)	140 million USD
Fishing+Other Uses (Mineral extraction, etc.)	400 MWt	100 million USD
Total Investment		9,170,000,000 USD
The natural gas equivalent of all geothermal uses above		6 billion USD /Year
Amount of economic growth created by applications such as geothermal electricity production, heating (housing, thermal facilities, etc.), thermal tourism (spa), greenhouse cultivation, drying, fishing, etc. if goals in 2030 are reached		210 billion USD /Year
Direct and Indirect Employment		450,000 people

cooperation with the private sector and local government.

- Expanding the sector and making research-development plans with the participation of the MTA, TÜBİTAK, universities, institutes, and the private sector.
- Promoting further development of the industry through the development of industry standards, information sharing, and transparency.
- Ensuring local and national consensus within the community on geothermal energy.
- Developing laws and regulations, an administrative structure, and incentive mechanisms.
- Ensuring that sufficient capacity is increased in central and local government to process permit applications in a fast, open, systematic, and transparent manner.
- Establishment of heating networks in a region-oriented manner in coordination with local governments.
- Determination of stable and predictable long-term finance-oriented energy policies to ensure sustainable direct-use practices and sectoral improvement.

5. Results

Geothermal energy is a natural resource that can be utilized directly or by converting to other types of energy. Using geothermal energy for different purposes, such as power, residential heating, thermal tourism, and greenhouses has become widespread in Türkiye. Türkiye is in a crucial geological position for obtaining geothermal energy from hot and radiogenic granitoid using EDGS technology. Türkiye energy problem can be minimized in a short time with the effective and correct use of geothermal resources. For this reason, it is extremely important to increase and support geothermal research in Türkiye.

References

Akkuş, İ. 2017. Neden jeotermal enerji? Türkiye için önemi, hedefler ve beklentiler. Mavi Gezegen Dergisi, 23, 25-39.

Akkuş, I., Akıllı, H., Ceyhan, S., Dilemre, A., Tekin, Z. 2005. Türkiye Jeotermal Kaynaklar Envanteri. Maden Tetkik ve Arama Genel Müdürlüğü Envanter Serisi, 201, Ankara.

Aksoy, N. 2014. Power generation from geothermal resources in Turkey. Renewable Energy 68, 595-601.

Aydın, H., Karakuş, H., Mutlu, H. 2020. Hydrogeochemistry of geothermal waters in eastern Turkey: Geochemical and isotopic constraints on water-rock interaction. Journal of Volcanology and Geothermal Research 390, 106708.

Baba, A., Chandrasekharam, D. 2022. Geothermal resources for sustainable development: A case study. International Journal of Energy Research 46(14), 20501-20518.

Baba, A., Kaya, A., Birsoy, Y. K. 2003. The effect of Yatağan thermal power plant (Muğla, Turkey) on the quality of surface and ground waters. Water, Air, and Soil Pollution 149, 93-111.

Baba, A., Gürdal, G., Şengünalp, F. 2010. Leaching characteristics of fly ash from fluidized bed combustion thermal power plant: case study: Çan (Çanakkale-Turkey). Fuel Processing Technology 91(9), 1073-1080.

Baba, A., Şaroğlu, F., Akkuş, I., Özel, N., Yeşilnacar, M. İ., Nalbantçılar, M. T., Demir, M. M., Gökçen, G., Arslan, Ş., Dursun, N., Uzelli, T., Yazdani, H. 2019. Geological and hydrogeochemical properties of geothermal systems in the southeastern region of Türkiye. Geothermics 78, 255-271.

Baba, A., Uzelli, T., Sözbilir, H. 2021. Distribution of geothermal arsenic in relation to geothermal play types: A global review and case study from the Anatolian plate (Turkey). Journal of Hazardous Materials 414, 125510.

Barka, A. A. 1992. The North Anatolian Fault zone. Annalas Tectonicae 6, 164–195.

Bozkurt, E. 2001. Neotectonics of Türkiye-a synthesis. Geodinamica Acta 14, 3-30.

Chandrasekharam, D., Baba, A. 2021. High heat generating granites of Kestanbol: future enhanced geothermal system (EGS) province in western Anatolia. Turkish Journal of Earth Sciences 30, 1032-1044.

Chandrasekharam, D., Baba, A. 2022. Carbon dioxide emissions strategy through enhanced geothermal systems: Western Anatolia, Turkey. Environmental Earth Sciences 81(8), 235.

EBRD. 2020*a*. Early Stage Geothermal Support Framework: (PLUTO)-Cumulative Impact Assessment Report of Cumulative Impact Assessment of Geothermal Resources in Türkiye. European Bank for Reconstruction and Development.

EBRD. 2020*b*. European Bank for Reconstruction and Development, Türkiye: Feasibility Study On The Potential For Geothermal District Heating And Cooling Systems.

EKB. 2022. Enerji Kentleri Birliği, Türkiye jeotermal kentsel ısıtma verileri 2021.

EPDK. 2019. T.C. Enerji Piyasası Düzenleme Kurumu 2019 yılı Elektrik Piyasası Sektör Raporları.

EPDK. 2022. Elektrik Piyasası Üretim Lisansları. T.C. Enerji Piyasası Düzenleme Kurumu.

EPİAŞ. 2021. https://seffaflik.epias.com.tr/transparency/.

Eşder, T., Şimşek, Ş. 1977. The relationship between the temperature-gradient distribution and geological structure in the İzmir-Seferihisar Geothermal Area, Turkey. Proceedings of the Symposium on the Geothermal Energy, Ankara, 93-114.

Filiz, Ş. 1982. Ege Bölgesi'ndeki önemli jeotermal alanların 18O, 2H, 3H, 13C izotoplarıyla incelenmesi. Assoc. Prof. Thesis, E.Ü.Y.B.F., İzmir (in Turkish).

Gemici, Ü., Filiz, Ş. 2001. Hydrochemistry of the Çeşme geothermal area, Turkey. Journal of Volcanology and Geothermal Research 110, 171-188.

Gemici, Ü., Tarcan, G. 2002. Distribution of boron in thermal waters of western Anatolia, Turkey and examples on their environmental impacts. Environmental Geology 43, 87–98.

Gültekin, F., Firat Ersoy, A., Ersoy, H. 2007. Hydrochemical and isotopic investigation of Trabzon mineral springs, Ayder (Çamlihemşin-Rize) and Ilıcaköy (İkizdere-Rize) hot springs. Yerbilimleri 50–51, 11–25 (in Turkish).

Hatipoğlu Temizel, E., Gültekin, F. 2018. Hydrochemical, isotopic, and reservoir characterization of the Pasinler (Erzurum) geothermal field, eastern Turkey. Arabian Journal of Geosciences 11, 1–20.

İZKA. 2022. İzmir ilindeki jeotermal kaynakların potansiyeli, kullanım alanları, ekonomik ve çevresel etkilerinin belirlenmesi araştırması projesi final raporu. İzmir Kalkınma Ajansı.

Karakuş, H., Şimşek, Ş. 2013. Tracing deep thermal water circulation systems in the E-W trending Büyük Menderes Graben, western Turkey. Journal of Volcanology and Geothermal Research 252, 38–52.

Koçyiğit, A., Özacar, A. 2003. Extensional neotectonic regime through the NE edge of the Outer Isparta Angle, SW Türkiye: New field and seismic data. Turkish Journal of Earth Science 12, 67–90.

Lachenbruch, A. H. 1968. Preliminary geothermal model of the Sierra Nevada. Journal of Geophysical Research 73, 6977-6989

Lindal, B. 1973. Industrial and other applications of geothermal energy. Geothermal Energy, UNESCO, Paris.

Lund, J., Tóth, A. N. 2020. Direct utilization of geothermal energy 2020 worldwide review. Geothermics 90, 101915.

Ministry of Health, 2021. Sağlık Bakanlığı Halk Sağlığı Genel Müdürlüğü Çevre Sağlığı Daire Başkanlığı, Türkiye Kaplıcaları, Kaplıca Arama Portalı.

Mutlu, H., Güleç, N. 1998. Hydrogeochemical outline of thermal waters and geothermometry applications in Anatolia (Turkey). Journal of Volcanology and Geothermal Research 85, 495–515.

Özgür, N. 2002. Geochemical signature of the Kızıldere geothermal field, Western Anatolia, Turkey. International Geology Review 44(2), 153 – 163.

Özkan, R., Şener, M., Helvacı, C., Şener, M. F. 2011. Hydrothermal alterations and relationship with thermal waters at Aliağa (İzmir) geothermal field, Yerbilimleri Dergisi 32(1), 141-168.

Pasvanoğlu, S. 2020. Geochemistry and conceptual model of thermal waters from Erciş – Zilan, Geothermics 86, 101803.

REN21. 2021. Renewables 2020 Global Status Report. (Paris: REN21 Secretariat). Global Overvıew.

Rubio-Maya, C., Ambríz Díaz, V. M., Pastor Martínez, E., Belman-Flores, J. M. 2015. Cascade utilization of low and medium enthalpy geothermal resources − A review. Renewable and Sustainable Energy Reviews 52, 689-716.

Selenka. 2021. https://selenkaenerji.com/blog/ulkemizdeki-yenilenebilir-kaynakli-santrallerin-kapasite-faktoru-agustos-2021-17.html

Şener, M. F. 2019. A new approach to Kırşehir (Türkiye) geothermal waters using REY, major elements and isotope geochemistry. Environmental Earth Sciences 78, 3.

Şener, M. F., Baba, A. 2019. Geochemical and hydrogeochemical characteristics and evolution of Kozaklı geothermal fluids, Central Anatolia, Turkey, Geothermics 80, 69-77.

Şener, M. F., Baba, A., Uzelli, T., Akkuş, İ., Mertoğlu, O. 2022. Türkiye Jeotermal Kaynaklar Strateji Raporu. Maden ve Petrol İşleri Genel Müdürlüğü.

Şener, M. F., Şener, M., Uysal, I. T. 2017. The evolution of the Cappadocia Geothermal Province, Anatolia (Türkiye): geochemical and geochronological evidence. Hydrogeology Journal 25(8), 2323-2345.

Şener, M. F., Yiğit, B., Şener, M. 2021. Geochemical proxies and formation mechanism of Hatay (Başlamış) travertine and relation with Dead Sea Fault Zone (S-Türkiye). Journal of African Earth Sciences 177, 104126.

Şengör, A. M. C., Dyer, J. M. N. 1979. Neotectonic provinces of the Tethyan orogenic belt of the eastern Mediterranean; variations in tectonic style and magmatism in a collision zone. Eos, Transactions, American Geophysical Union 60(18), 390.

Şimşek, Ş. 1985. Geothermal model of Denizli, Sarayköy-Buldan area. Geothermics 14(2-3), 393 – 417.

Şimşek, Ş. 2003. Hydrogeological and isotopic survey of geothermal fields in the Büyük Menderes graben, Turkey. Geothermics 32, 669–678.

Tarcan, G., Gemici, Ü., Aksoy, N. 2005. Hydrogeological and geochemical assessments of the Gediz Graben geothermal areas, western Anatolia, Turkey. Environmental Geology 47(4), 523 – 534.

Tarcan, G., Özen, T., Gemici, Ü. 2016. Geochemical assessment of mineral scaling in Kızıldere geothermal field, Turkey. Environmental Earth Science 75, 1317.

Tayfur, G., Kirer, T., Baba, A. 2008. Groundwater quality and hydrogeochemical properties of Torbalı Region, Izmir, Turkey, Environmental Monitoring and Assessment 146(1), 157-169.

Thinkgeoenergy, 2022. https://www.thinkgeoenergy.com/thinkgeoenergys-top-10-geothermal-countries-2021-installed-power-generation-capacity-mwe/.

UNEP. 2021. United Nations Environment Programme. Food Waste Index Report 2021.

Uzelli, T., Şener, M. F., Dölek, İ., Baba, A., Sözbilir, H., Dirik, K. 2021. Structural controls and hydrogeochemical properties of geothermal fields in the Varto region, East Anatolia. Turkish Journal of Earth Sciences 30, 1076-1095.

Uzelli, T., Baba, A., Mungan, G. G., Dirik, R. K., Sözbilir, H. 2017. Conceptual model of the Gülbahçe geothermal system, Western Anatolia, Turkey: based on structural and hydrogeochemical data. Geothermics 68, 67-85.

Yılmazer, S. 1984. Ege Bölgesi'ndeki bazı sıcak su kaynaklarının hidrojeoloji ve jeokimyasal incelemeleri (in Turkish). Master Tezi, Dokuz Eylül Üniversitesi, Fen Bilimleri Enstitüsü, İzmir.

WB. 2021. WorldBank-Türkiye-Assessment of Opportunities and Interest in Direct Uses of Geothermal Energy, Project Final Report Workshop Presentation, ESMAP, Stantec and Reykjavik Geothermal.

Bulletin of the Mineral Research and Exploration

http://bulletin.mta.gov.tr

Comparative analysis of water and carbon dioxide injection for the thermohydraulics of an EGS project in Dikili Geothermal Field, Türkiye

Ali Cemal BENİM[a] and Aydın ÇİÇEK[b*]

[a]*Düsseldorf University of Applied Sciences, Department of Mechanical and Process Technology, Center of Flow Simulation, Düsseldorf, Germany.*
[b]*General Directorate of Mineral Research and Exploration of Türkiye, Department of Energy Raw Materials, Ankara, Türkiye.*

Research Article

Keywords:
EGS, Thermohydraulics, Computational Analysis, Supercritical Carbon Dioxide.

ABSTRACT

A comparative numerical analysis of the thermohydraulics of an enhanced geothermal system (EGS) project in Türkiye in Dikili area is presented. The fractured granodiorite is modelled as porous media, utilizing the numerically suggested data of other authors for the corresponding hydraulic characteristics. As the heat transmission fluid, two different mediums are alternatively considered. These are the more classical medium, water and the supercritical carbon dioxide (sCO_2). Transient calculations are performed for a time period of twenty years, comparing the temporally developing results obtained for water and sCO_2 with each other. Based on modeling parameters and assumptions, higher production temperatures are observed with sCO_2, in comparison to water, implying an advantage for sCO_2 usage as a working fluid in EGS. This is accompanied by the further advantage of a lower pressure drop for sCO_2. On the other hand, the temperature advantage is relativized by the lower specific heat capacity of sCO_2 causing a decrease in the production thermal power. In general, the present results are found to be encouraging for a further and more detailed analysis of the employment of sCO_2 as working fluid in EGS.

Received Date: 22.08.2022
Accepted Date: 27.04.2023

1. Introduction

Türkiye attracted many scientists due to its spectacular geology during the last century. Neotectonics, active tectonics and related geothermal potential of western Anatolia has scientifically been a hot place since the 2007 following the enactment of the "Geothermal Resources and Natural Mineral Waters (Law No: 5686)". Dikili geothermal field, located nearly 75 km north of İzmir city in westernmost Türkiye, is a significant conventional geothermal field (Figure 1). The Dikili geothermal field is bounded by Madra mountain to the north, Karadağ mountain to the south and Yuntdağ mountain to the southwest (Figure 2).

Although there are a number of formations in the study area, geological units of the geothermal field are subdivided here into 4 units for the sake of simplicity (Figure 2). From older to younger, (1) Pre-Tertiary (Permian-Triassic) basement rocks with siltstone, mudstone, silty limestone and limestones, (2) late Oligocene to early.

Miocene Kozak magmatic complex composed mainly of granodiorites, (3) early Miocene to Quaternary basic to asidic volcanics and sedimentary rocks (siltstone, mudstone and limestones) and (4) Quaternary-aged relatively loose sediments.

Citation Info: Benim, A. C., Çiçek, A. 2023. Comparative analysis of water and carbon dioxide injection for the thermohydraulics of an EGS project in Dikili Geothermal Field, Türkiye. Bulletin of the Mineral Research and Exploration 171, 91-105. https://doi.org/10.19111/bulletinofmre.1288731

**Corresponding author: Aydın ÇİÇEK, aydincicek2003@gmail.com*

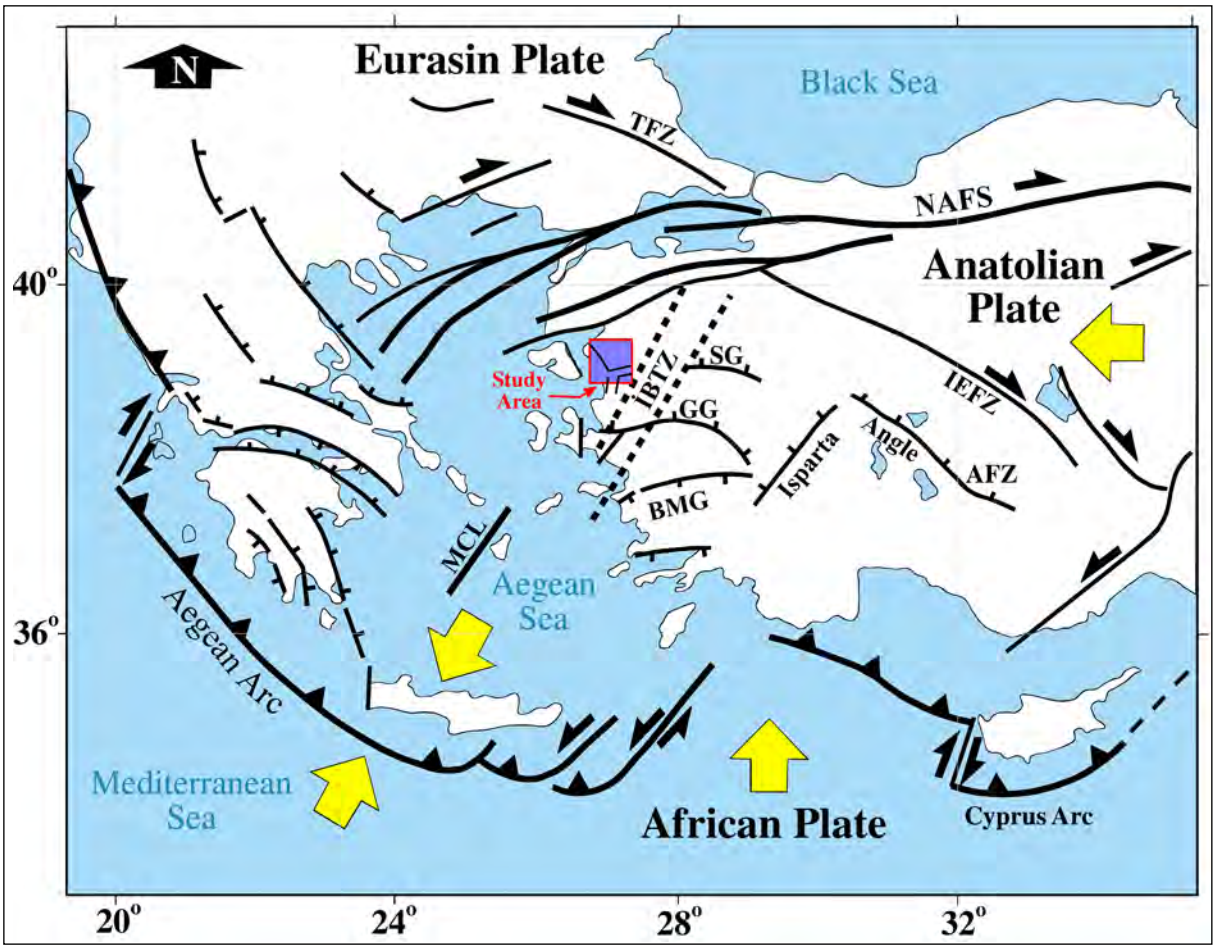

Figure 1- Simplified map showing the major (plate) tectonic elements and configuration of the Aegean region. NAFS, North Anatolian Fault System; TGF, Tuz Gölü Fault; IEFZ, İnönü-Eskişehir Fault Zone; AFZ, Akşehir Fault Zone; BMG, Büyük Menderes Graben; GG, Gediz Graben; SG, Simav Graben; MCL, Mid-Cycladic Lineament; TFZ, Thrace Fault Zone; İBTZ, İzmir-Balıkesir Transfer Zone (Re-drawn from Uzel, 2013).

The geothermal potential and the tectonics of the study area is also previously studied well by many researchers (e.g. JICA, 1987; Hou et al., 2015; Baba et al., 2022; Gürer, 2023). The Dikili geothermal field tectonically lies in the junction of Altınova, Bakırçay and Çandarlı basins (Figure 2). In addition, the area seems to be affected partly by strike-slip İzmir-Balıkesir Transfer Zone (İBTZ) (Figure 1) (Altunkaynak and Yılmaz, 1998; Uzel, 2013; Hou et al., 2015). Based on the lineament analysis done here using 1/25,000 and 1/250,000 topographic maps, it seems that the study area is mainly dominated by the NE-SW and relatively less dominated by the NW-SE-trending structural features (Figure 3).

The reservoir rocks of conventional geothermal system in the Dikili geothermal field is made of mainly by volcanics (Parlaktuna and Avşar, 2014). Although JICA (1987) proposed that the recharge area is located in the north (Madra mountains), the Yuntdağ and Karadağ mountains have also some potential as recharge area based on the surface geology and topography. The geothermal waters found inside the Dikili geothermal field are meteoric in origin based on some isotopic studies (JICA, 1987).

Baba et al. (2022) reported 27 geothermal wells with various depths and 4 springs as of February 2022. According to them, surface temperatures and flow rates of the springs vary between 57-80 ºC and 2-180 l/s, of geothermal wells between 37-131.5 ºC and 15-60 l/s, respectively. Although there are many economically producing conventional geothermal wells, some hot and economically dry wells were reported as well

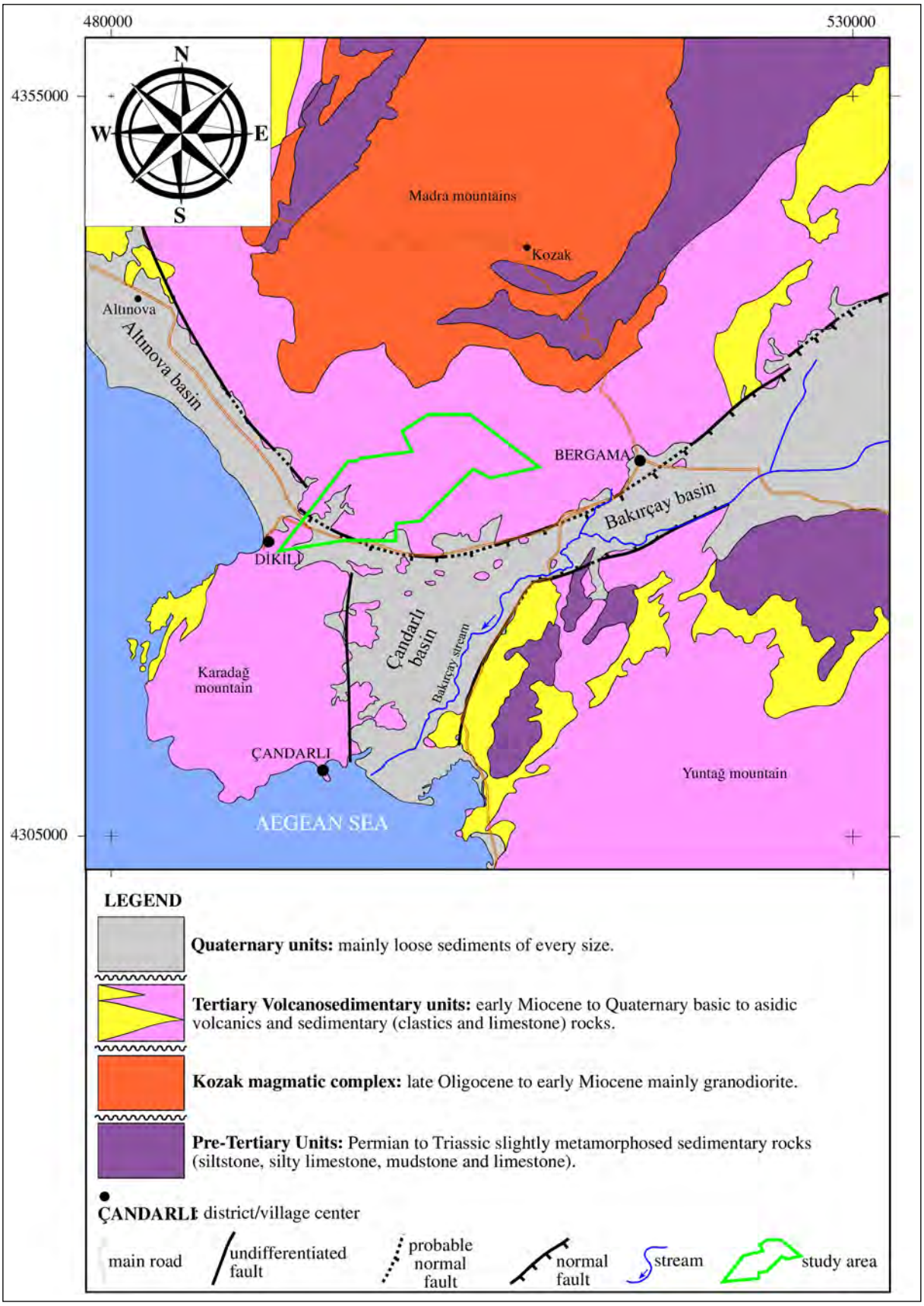

Figure 2- Simplified geological map of the study area and its vicinity (simplified from JICA, 1987).

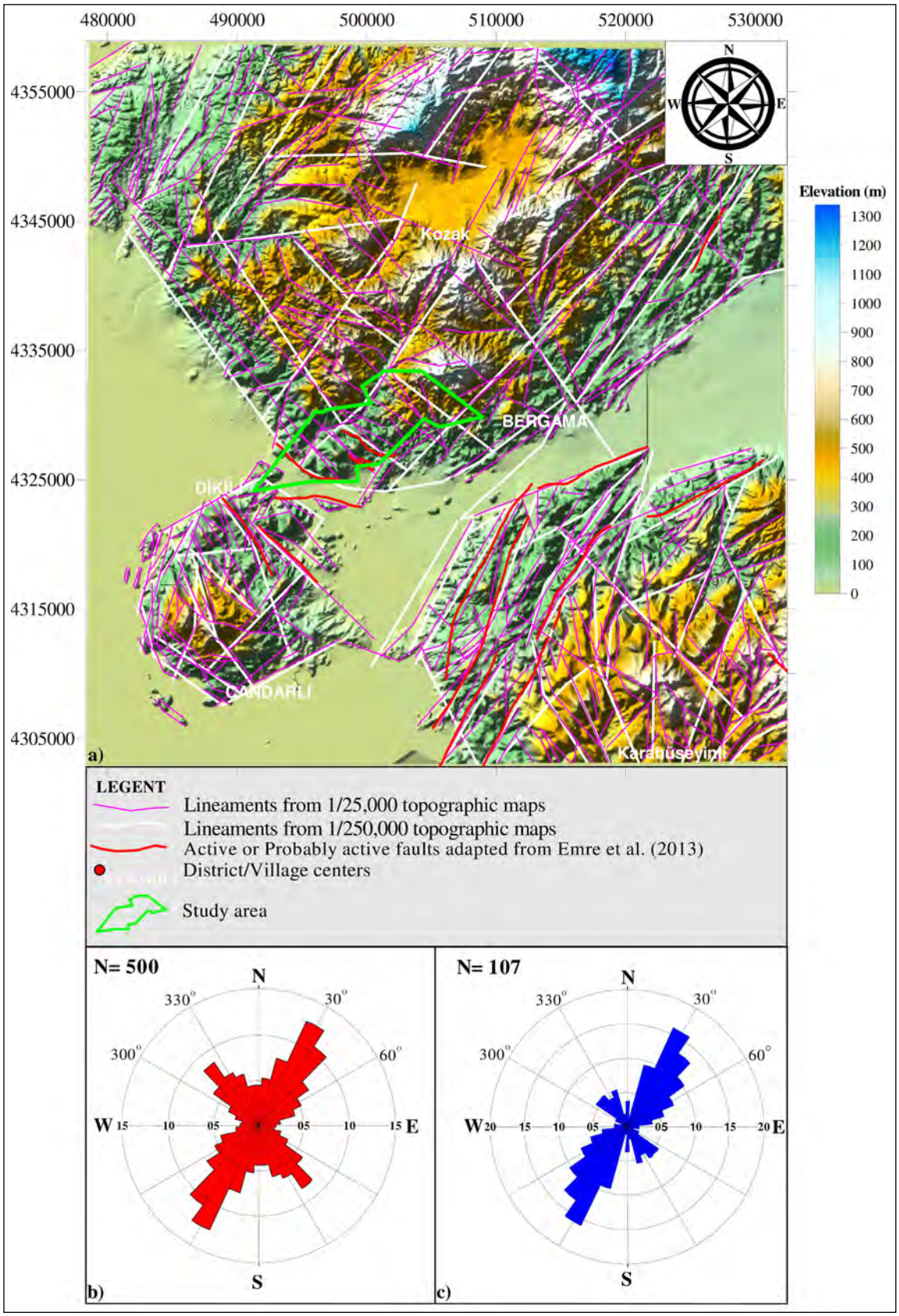

Figure 3- DEM of the study area and its vicinity, b) rose diagram of the lineament anaylsis obtained from 1/25.000 topographic maps and c) 1/250.000 topographic maps.

(Baba et al., 2022; Parlaktuna and Avşar, 2014). The bottom hole temperatures of the wells reach up to 135 ºC at a depth of 1,500 m (Yılmazer et al., 1990).

Based on previous studies, some radioactive element-bearing rocks such as Yuntdağ volcanics and Kozak granodiorite are common in the study area (Yarar et al, 2005). In addition, deep-circulation related convection cells as evidenced by fluctuating geothermal gradients at shallow depths are widespread (Parlaktuna and Avşar, 2014). Based on this, the heat sources may at least be attributed to radioactivity and deep-circulated meteoric waters (i.e. convective geothermal system).

Hou et al. (2015) presented the preliminary geology, geophysics and geochemistry results of the study area. They used FLAC3D software, a code adapted for geotechnical analysis, in their study (FLAC3D, 2019). In modelling fracturing, the strain-hardening/-softening ubiquitous-joint model was used, in which the mechanical behavior of matrix and joint was described by the Mohr-Coulomb criteria with a tension cutoff that can harden or soften according to specific laws. Hou et al. (2015) did not provide any detailed mathematical and numerical modelling aspects of the study for the modeling the flow. More detailed investigations of the thermohydraulics of the EGS project, with emphasis on numerical modelling aspects, such as grid independence and domain size, spatial and temporal resolution, were provided by Benim et al. (2018 *a, b*). Turan et al. (2021) calculated the EGS potential of the study area using probabilistic assessment method. In this study, we focus on the classical type Enhanced Geothermal Systems (EGS) potential of a part of the Dikili geothermal field by comparing water and sCO_2 as a working fluid using numerical code Ansys Fluent 18.0 (Figure 4). Here we present the results, advantages and disadvantages of sCO_2 as a working fluid over water in a classical type EGS of Çiçek (2020) for the first time in Türkiye.

The above-mentioned studies on the EGS project were carried out for water as the working fluid. If super critical carbon dioxide sCO_2 is used as heat transfer fluid, the utilization of geothermal energy can advantageously be combined with simultaneous sequestration of the carbon dioxide, a greenhouse gas (Brown, 2000). Therefore, the use of carbon dioxide in EGS is among the current hot research topics in energy technology and is being studied by a number of researchers. A higher capacity to use CO_2 as a working fluid compared to water was predicted by Pruess (2006, 2010) for an analyzed case. A study is presented on the problem of clogging due to high salinity working fluid by Borgia et al. (2012). A more recent study presented by Liu et al. (2019) comparing the efficiencies of water and sCO_2 as working fluid in a Chinese case. An investigation into the utilization of sCO_2 in the above-mentioned EGS project in Dikili area, in İzmir, Türkiye, was recently presented by Benim and Çiçek (2022). The present investigation is a continuation of this work, where a more detailed analysis is presented. The main difference to the previous study lies in the postprocessing and interpretion of the results. In the present paper, the temperature fields of sCO_2 injection are compared directly with those of water injection, and in additional planes that reveal the penetration of the temperature wave in the direction perpendicular to the plane of the walls, which were not the case in Benim and Çiçek (2022). In addition, a comparative analysis between sCO_2 and water injection is presented for the useful thermal power, total produced energy as function of time, as well as the required pumping power, which were not elaborated in Benim and Çiçek (2022).

In the studies of other authors on CO_2 injection in EGS projects mentioned above, specialized software designed for geothermal reservoir calculations, such as TOUGH2 (Pruess, 1991) and T2Well (Pan and Oldenburg, 2014) were used. As it was the case in the previous work of the Benim et al. (2018*a, b*), Benim and Çiçek (2022), the current analysis is based on the general-purpose Computational Fluid Dynamics (CFD) Software ANSYS Fluent 18.0 (ANSYS Fluent, 2018).

2. The Investigated EGS Configuration and Solution Domain Definition

The envisaged injection-production configuration is a triplet one, where two production wells are symmetrically arranged around a single injection well, as depicted in Figure 4a. The configuration exhibits two symmetry planes, which are also indicated in the figure. These are utilized in the mathematical modelling to reduce the computational overhead. Thus,

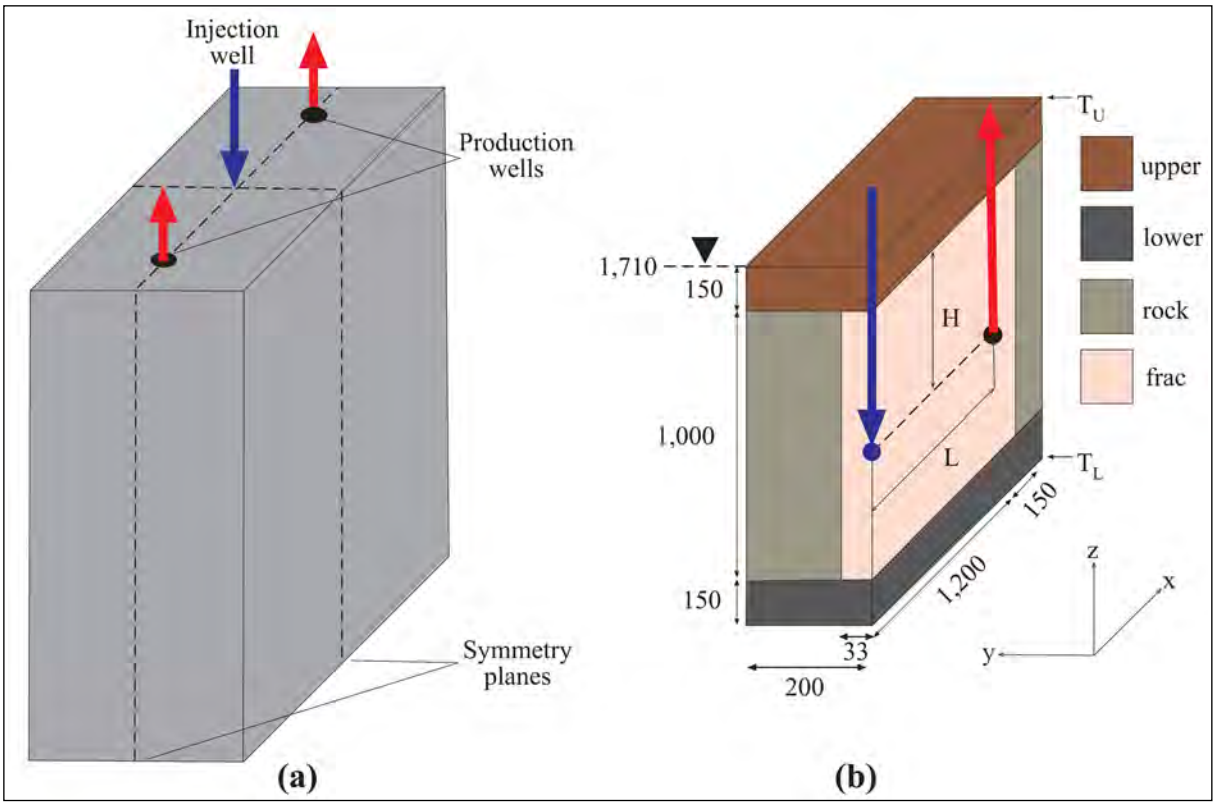

Figure 4- The considered EGS configuration; a) locations of production and injection wells, b) solution domain (in meter) and rock zones.

a quarter of the region shown in Figure 4a is defined to be the solution domain, which is bounded by two symmetry planes. The solution domain is illustrated in Figure 4b, where the dimensions (in meter) as well as the topology of the assumed rock structures are also indicated, along with the orientation of the used Cartesian coordinate system.

The dimensions of the fractured region (1200 x 33 x 1000 m) are borrowed from Hou et al. (2015). Except the symmetry planes, there is, of course, a certain arbitrariness in choosing the positions of the surfaces that bound the solution domain. They should be chosen sufficiently far away from the region of interest, so that the applied boundary conditions don't interfere with the process, i.e. don't falsify the results. In a previous study, a study was carried out by Benim et al. (2018*a*) by considering different domain sizes in the same configuration and it was ensured that the present choice (Figure 4b) provides an adequate domain size. Please also note that the upper horizontal boundary of the domain (Figure 4b) is not positioned at the ground surface but a position at 1710 m depth.

3. Mathematical and Numerical Modelling Outline

The Computational Fluid Dynamics (CFD) software Fluent (ANSYS Fluent, 2018) is used during computational modelling. The software uses the Finite Volume Method (FVM) of discretization (Versteeg and Malalasekera, 2007).

3.1. Mathematical Modelling

The solution domain contains solid and fluid materials. Although the real physics may imply a certain "dynamical" fluid-solid interaction, the solids are assumed to be non-deformable. Possible chemical interactions between the fluid and solids are also neglected. Thus, the fluid-solid interaction is solely "thermal" in nature in the present model. The total transport processes that are involved in the solution domain are of energy, mass and momentum described by the corresponding differential balance equations (Bird et al., 2006). Mass, momentum as well as conductive and convective energy transport processes govern the flow of the heat transfer fluid. The energy transport from the hot solid into the colder fluid occurs

by means of conduction and convection heat transfer (Bhattacharyya et al., 2016) through the surfaces of the fractures in the rocks. This energy extraction by the fluid and the corresponding local temperature drop triggers energy transport i.e. heat transfer, from the farther and hotter rock regions towards the colder zones, feeding the system. In the present case, due to the extremely large disparity between the geometric scales of the fractures and the solution domain, it is not possible to model the heat transmission by resolving fluid-solid interfaces, as it is commonly done in many other smaller scale convective heat transfer applications (Bhattacharyya et al., 2016). Therefore, the rocks are modelled as porous medium, where the individual fractures are not geometrically resolved, but their integral effect in larger scales is accounted for by means of characterizing parameters such as the porosity and permeability, through which the corresponding transport equations are accordingly amended (Civan, 2011).

Turbulent flow in porous media flow is a further challenging topic (Wood et al., 2020), and commonly employed turbulence modelling approaches (Benim, 1990; Xia et al., 1997) cannot readily be adopted to flow in porous media. In the current modelling, the influence of flow turbulence is neglected. This assumption can be seen to be justified, at least in part, by the very low superficial and physical velocities expected within the tiny fractures. According to the Darcy law, the porous solid region influence onto the fluid hydrodynamics is accounted for by introducing a momentum sink into the Navier-Stokes equations that corresponds to a static pressure drop (Whitaker, 1986).

3.2. Material Properties

For the characterizing parameters of the porous medium, the data provided in Hou et al. (2015) is utilized. In reference to the rock regions depicted in Figure 4b, the employed values are listed in Table 1, where the given values are assumed to remain constant within each zone. The permeabilities and porosities are generally rather low as shown in Table 1. It should also be noted that the permeability of the fractured zone (frac) is anisotropic unlike the remaining zones. In the fractured zone, the permeability is several orders of magnitude larger in the main fracturing direction compared to the other directions.

Table 1- Porosities and permeabilities (in m^2) of rock zones (Figure 1b).

	Upper	**Frac**	**Rock**	**Lower**
porosity	0.013	0.02	0.02	0.02
permeability (x)	4×10^{-18}	1×10^{-13}	4×10^{-18}	4×10^{-18}
permeability (y)	4×10^{-18}	4×10^{-18}	4×10^{-18}	4×10^{-18}
permeability (z)	4×10^{-18}	4×10^{-14}	4×10^{-18}	4×10^{-18}

An important component of the mathematical modelling is the material properties of the considered media. For the case with water as the heat transfer medium, compressibility of the water is neglected. The water used as the working fluid may evaporate inside the system due to high temperatures and can also be followed by a condensation as it is known to occur in some EGS projects. Nevertheless, in the current configuration, an analysis of the prevailing pressures and temperatures with respect to the thermodynamic water properties has implied that the water remains in liquid phase throughout modeling. The compressibility of injected supercritical Carbon Dioxide (sCO_2) is also considered during modeling as described below. The used material properties, namely the specific heat capacity (c), thermal conductivity (λ), density (ρ) and dynamic viscosity (μ) of water are assumed to be constant. The thermophysical rock properties are also considered to be constant. The used material properties for the water and solid rocks are summarized in Table 2.

Table 2- Material properties of water and solid rocks.

	μ [Pa·s]	ρ [kg/m^3]	c [J/(kg·K)]	λ [W/(m.K)]
water	0.00019	940	4176	0.717
rock	-	2670	965	2.83

Special attention is required to model the thermophysical material properties of sCO_2. In the current modeling, NIST (National Institute of Standards and Technology) Thermodynamic and Transport Properties Refrigrants and Refrigrant Mixtures Database Version 9.1 (REFROP v9.1) (Lemmon et al., 2018) is used for the thermophysical behavior of the sCO_2. Thus, in calculating the case with sCO_2 as the heat transfer fluid, the pressure and temperature dependence of the material properties are accurately considered. Here, a further important question is, if the medium remains within the

supercritical regime throughout complete solution domain, or if local temperature and pressure values cause a local transition into a different state such as superheated gas or subcooled liquid. The occurrence of such transitions would cause some problems in numerical analysis. The values for the critical pressure and temperature carbon dioxide (CO_2) are known to be 73.82 bar and 31.04°C, respectively. The superheated state prevails above this. Since the lowest temperature in the system is 60°C (inlet temperature of the heat transfer liquid), a deviation from the superheated state can only happen if the pressure attains to a lower value in comparison to the critical pressure. In the present solution, the minimum static pressure at the passage to the production well intake is nearly 540 bars. The value is quite above the critical one. Thus, a sCO_2 can be used throughout the entire solution domain.

3.3. Initial and Boundary Conditions

Six surfaces bound the prismatic solution domain, where two vertical surfaces are defined to be symmetry planes as already mentioned above (Figure 4b). The remaining four surfaces are modelled as solid walls with prescribed temperature. The temperatures at the upper and lower horizontal walls that bound the domain are indicated as T_U and T_L, respectively, in Figure 4b. These temperatures are assumed to be constant and prescribed as boundary conditions at these surfaces with the values T_U=138°C and T_L=240°C according to the data provided by Hou et al. (2015), along with the assumption of stagnant fluid. At the beginning of the process, a linear variation of the temperature between the upper and lower walls is assumed, which is applied as initial condition throughout the whole domain, as well as the boundary condition on the vertical wall boundaries.

There is a large-scale difference between domain size and borehole diameters. This makes a coupled modelling of the piping with the rest of the domain very difficult due to extreme grid resolution requirements. Therefore, at present, it is seen that calculating the heat transfer and flow in the pipes in a coupled manner with the outer domain is not appropriate. This may be considered to be a reasonable assumption for current purposes, since the borehole casing is cemented with very low thermal conductivity. As a result, the modeled outer surface of the casing of the wells is considered as adiabatic walls. The inlet boundary of the solution domain is positioned at the outlet of the injection pipe (indicated by a blue dot in Figure 4b). The outlet boundary of the solution domain is positioned at inlet plane of the production pipe (indicted by a red dot in Figure 4b). At the inlet surface, a constant 60°C temperature and 215 kg/s mass flow rate are applied as boundary conditions. At the outlet, a constant static pressure and a zero-gradient condition are applied for the velocities. The problem is analyzed for a configuration, where the inlet and outlet boundaries are 1000 m apart (L=1000, Figure 4b) and 590 m lower than the upper rock layer (H=590 m, Figure 4b).

3.4. Numerical Modelling

In the numerical modelling, a 2nd order accurate, bounded backward differencing scheme (Versteeg and Malalasekera, 2007) is applied for time discretization. In general, the time step size to be employed should be carefully checked not only for reasons of stability but also with regard to temporal accuracy. Even if stability criteria might have been met, smaller time steps may still be needed for accuracy (Bit et al., 2020). Since the presently applied discretization scheme is unconditionally stable, not necessarily the stability, but the accuracy is of concern. In the present calculations, a time step size of 6h is applied. This time step size may appear to be too large compared to other transient phenomena encountered in different applications (Bit et al., 2020). However, in the previous analysis (Benim et al., 2018 *a, b*), it was shown that this time step size is adequate to obtain very accurate temporal resolution for the present problem. This time-step size results in cell Courant and Fourier numbers (Peyret, 1996) that are much smaller than 1.0 and 0.5, respectively. Thus, with this time step size, even an explicit scheme would lead to a stable solution. In the spatial discretization, the formally a 2nd order accurate upwind scheme is used (Glaister, 1993) except for density, for which a 1st order upwinding is used. The PRESTO! interpolation scheme is used for pressure (Peyret, 1996). The velocity-pressure coupling is treated by the PISO scheme (Versteeg and Malalasekera, 2007). The velocity components are under-relaxed in the iterative procedure within a time step. The underrelaxation coefficient is 0.5. None of the further variables are under-relaxed. For the

convergence criteria for each time step, the threshold values of the normalized residuals are set to 10^{-12} for the energy equation. It is set to 10^{-6} for the remaining equations. The solution domain is discretized by essentially equidistant, orthogonal, block-structured grid with hexahedral finite volumes. The utilized computational grid consists of 185,000 nodes. Benim et al. (2018*a*) found out that the grid ensures sufficiently grid independent solutions.

4. Results and Discussion

The calculated temperature (T) distribution in the y-z symmetry plane through the injection well (Figure 4b) following half a year, one year, five years, and fifteen years of production are shown in Figure 5 and Figure 6 for H_2O and sCO_2 as working fluid, respectively.

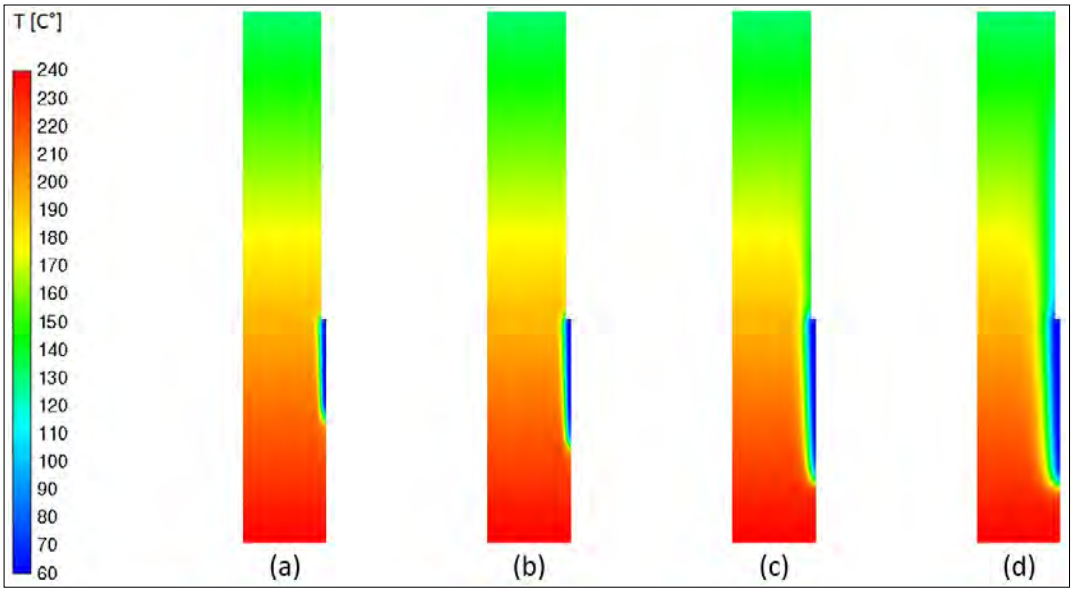

Figure 5- Water as heat transfer fluid: Temperature (°C) variation in y-z symmetry plane (Figure 4b) through the injection well after; a) half a year, b) one year, c) five years, d) fifteen years of production.

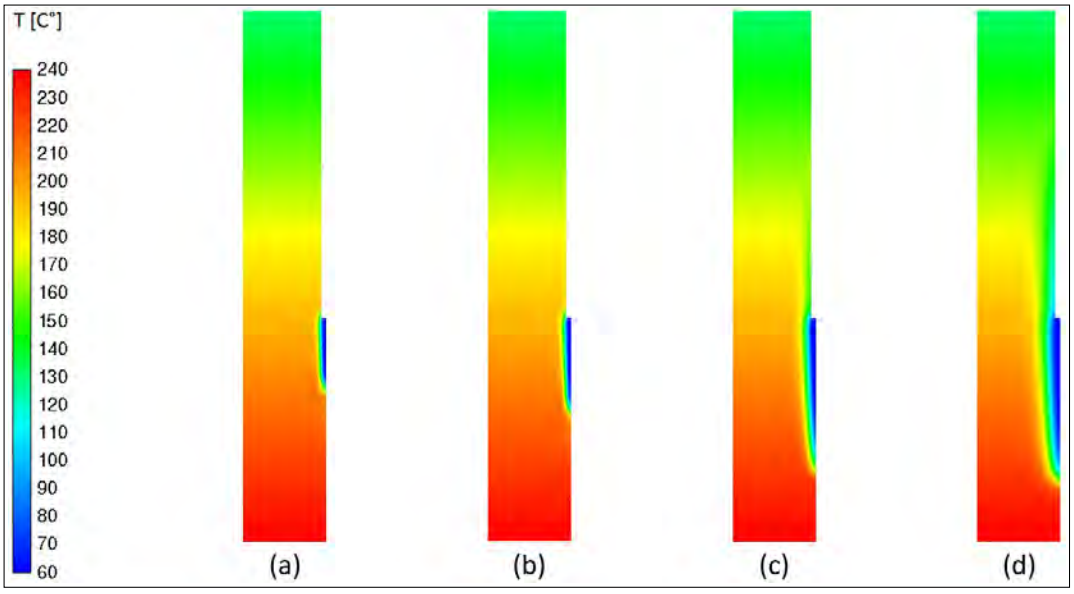

Figure 6- sCO_2 as heat transfer fluid: Temperature (°C) variation in y-z plane (Figure 4b) through the wells; a) half a year, b) one year, c) five years, d) fifteen years of production.

In this plane, with relatively low permeability, the dominant heat transfer mode is conduction (Table 1). The penetration of the temperature front is rather low in y direction. It is rather restricted to the environs of the fractured area. Qualitatively similar behavior is observed for both heat transfer fluids (Figures 5, 6). Quantitatively, the size of the reduced temperature region is smaller for the sCO_2 compared to the water in the early phases of production, and it gradually approaches to that of water in time.

The calculated temperature distribution in the x-z plane (Figure 4b) after half a year, one year, five years, and fifteen years are shown in Figure 7 and Figure 8 for H_2O and sCO_2 as working fluid.

The qualitative features of the temperature patterns are similar for both heat transfer fluids (Figures 7 and 8). After half a year of production, a quite round, nearly elliptic, low temperature region is observed around the injection well (Figures 7a and 8a), which expands further in time while preserving its qualitative shape (Figures 7b, 8b). After five years of production, it can be observed that the shape of the cold zone is distorted with respect to the previous one. In addition, the temperature front has met the lower boundary of the fractured zone and reached the production well (Figures 7c, 8c). After fifteen years of production, one observes that the low temperature zone has further expanded and also reached the lateral boarder of the fractured zone (Figures 7c, 8d). Despite the fact that the cold waterfront reached the production well after about five years, the production temperature still remains above the injection temperature due to the mixing of heated water by its environs of the fractured zone and convective transport of the warmer water into the production well.

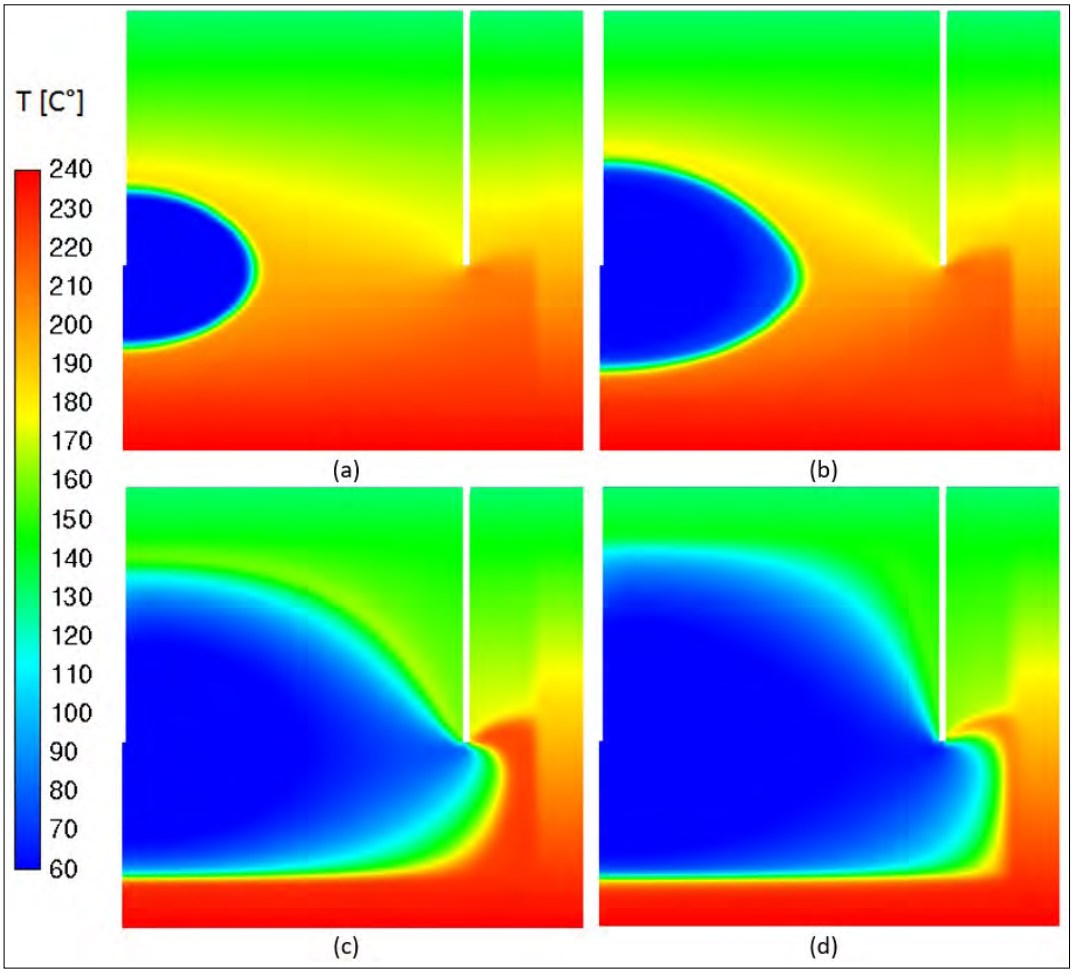

Figure 7- Water as heat transfer fluid: temperature [°C] variation in x-z plane (Figure 4b) through the wells after; a) half a year, b) one year, c) five years, d) fifteen years of production.

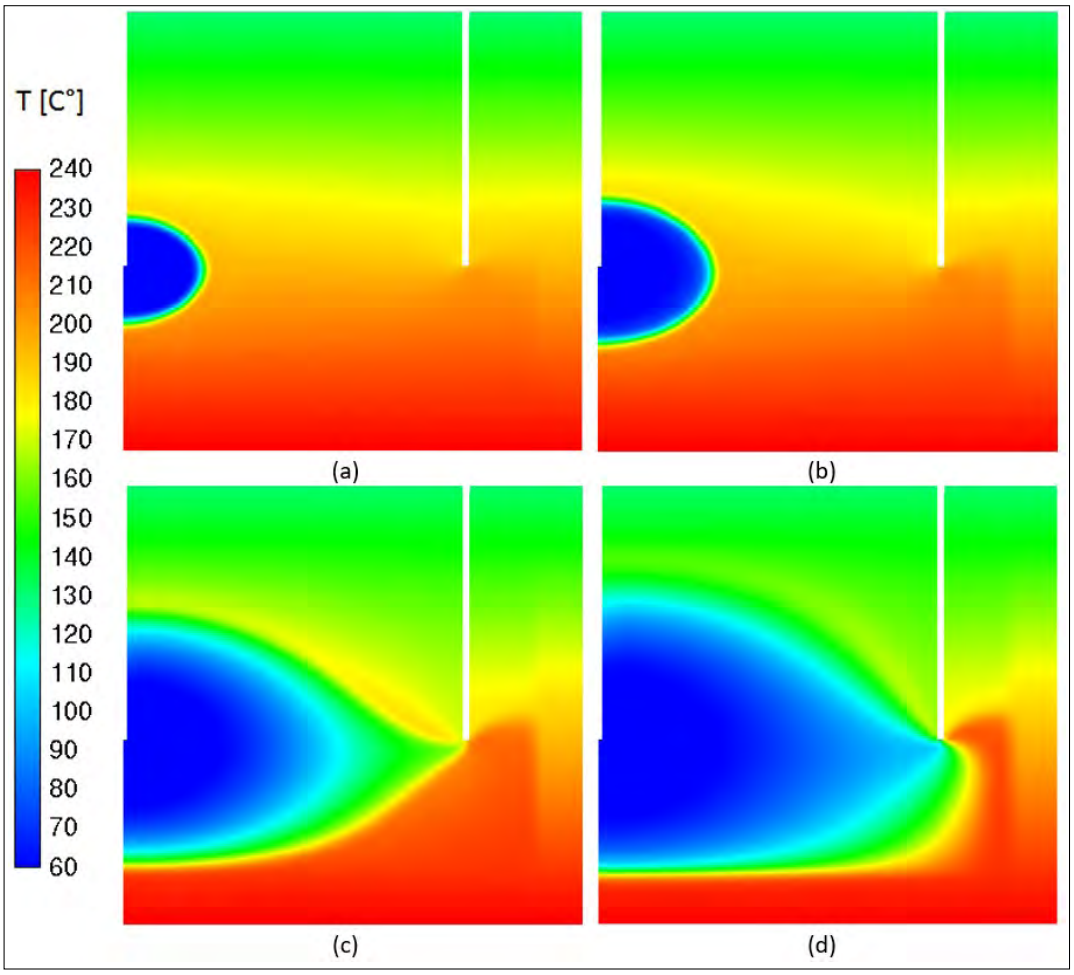

Figure 8- sCO_2 as working fluid: temperature (°C) variation in x-z plane (Figure 4b) through the wells after; a) half a year, b) one year, c) five years, d) fifteen years of production.

One of the significant differences between sCO_2 and water injection is the liquid density variation. The density may vary locally and temporarily depending on temperature-pressure conditions of the working fluid. An obvious result of a variable density is that the CO_2 may be retained in the reservoir, implying that the production flow rate may show a temporal variation and does not need to remain equal to the inlet mass flow during the process. For sCO_2 injection, the calculated flow rate at the production is shown in Figure 9 for 20 years of production. In addition, the constant value for the incompressible water is indicated (any potential loss in working fluid to the ground, a common phenomenon in a real case, is neglected during modeling).

In Figure 9, it is observed that the production flow rate for the sCO_2 is quite low at the beginning, approximately fifty percent of the injection flow rate.

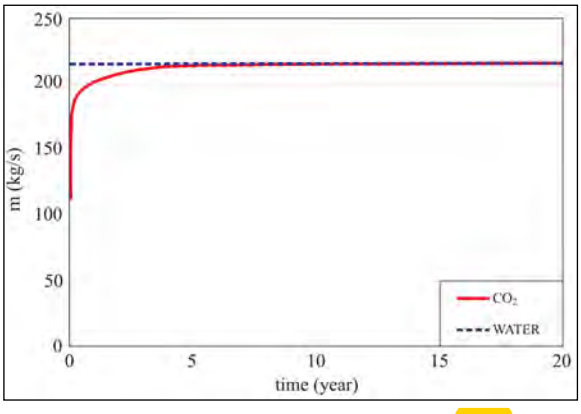

Figure 9- Variation of H_2O and sCO_2 production rates [kg/s] in time.

The value increases quite rapidly in the initial six months and reaches the injection value nearly five years later. Therefore, the storage effect mentioned for sCO_2 is particularly striking within the first five years.

Projected production temperatures for H_2O and sCO_2 during 20 years of production are presented in Figure 10.

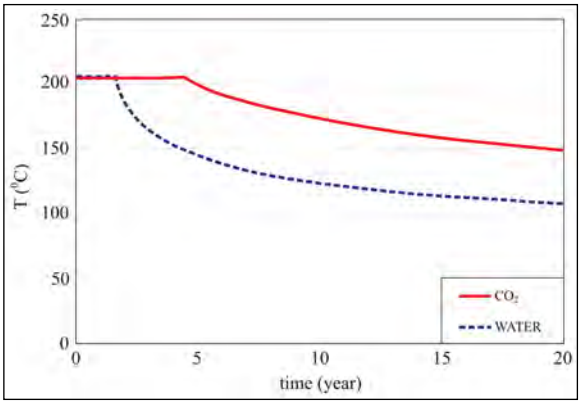

Figure 10- Variation of H_2O and sCO_2 production temperatures (°C) in time.

In the figure, one can see that the temperatures remain constant for an initial period of time and start to decrease thereafter, which is qualitatively the same for both fluids. This time period is shorter for H_2O (nearly one year) compared to subcritical CO_2 (nearly five years). It may be seen in Figure 10 that a much higher production temperature is achieved with sCO_2 over the 20 years of production compared to water. The higher temperatures observed for sCO_2 can be traced back to the differences in the material properties, especially in the thermal conductivity (higher for CO_2) and specific heat capacity (lower for CO_2). At the end of 20 years, the CO_2 production temperature (about 150 °C) is approximately 40 °C higher with respect to water (about 110 °C). In this respect, it is more advantageous to use carbon dioxide instead of H_2O.

The "useful" thermal energy flow rate, i.e. the useful thermal power (P_{TH}) at the production well can be expressed as (Baehr, 2005).

$$P_{TH} = m_P\, c\, (T_P - T_{ref}) \quad (1)$$

where m_P and T_P stand for the production mass flow rate and temperature, respectively, while c denotes the fluid's isobaric specific heat capacity. The reference temperature T_{ref} is taken to be 80°C, with the assumption that this value represents the lowest useful production temperature for which a subsequent energy conversion with acceptable efficiency is possible. The variations of P_{TH} over 20 years for sCO_2 and water injection are presented in Figure 11.

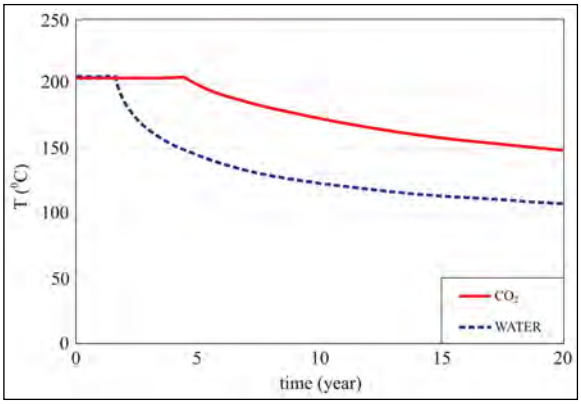

Figure 11- Variation of useful thermal power (MW) in time, for injected H_2O and sCO_2 production.

Although the production temperature of injected water is lower compared to that of sCO_2 (Figure 10), this is compensated and exceeded by the higher specific capacity of water compared to CO_2 so that the production thermal power of water injection turns out to be larger than that of sCO_2 injection, as seen in Figure 11. This is more pronounced in the initial phase of production, where the lower production mass flow rate of sCO_2 (Figure 9) contributes additionally to the lower values of the CO_2 curve. The water curve gradually approaches to the CO_2 curve in time, and reaches practically the same level at the end of the production time of 20 years. At the very beginning of production, the power obtained by water is more than 5 times larger compared to CO_2 for a short time. This ratio rapidly decreases and gets stabilized at about 3 for the first two years of production. Thereafter, the ratio starts to decrease quite rapidly. After five years, the power obtained by water is only about 1.5 times larger compared to CO_2. Beyond fifteen years, the difference is negligible and vanishes towards the end of twenty years period (Figure 11).

The total geothermal energy production using water and sCO_2 as heat transfer fluid over 20 years are depicted in Figure 12, where the curves shown are based on the useful thermal power variations shown in Figure 11. One can see that the total energy produced by CO_2 at the end of 20 years is about 70% of that of water (Figure 12).

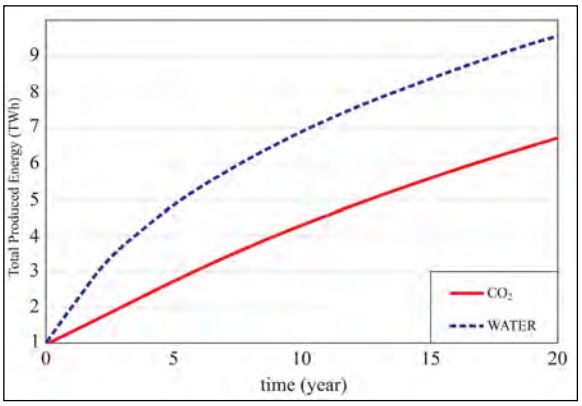

Figure 12- Variation of total produced energy (TWh) in time, for water and sCO_2 as working fluid.

The pressure drops (Δp) in the system and the related loss of mechanical energy is a further important issue, from the energetic point of view. The pressure drops within the solution domain, i.e. between the inlet boundary (at the bottom of the injection well) and the outlet boundary (at the bottom of the production well) can be obtained from the performed numerical calculations. For water injection, the pressure drop in the system remains fairly constant during the whole injection period. In case of sCO_2, a mild increase about 12% is observed within the 20 years of operation time (a mean value is used below).

The mechanical power (P_M), i.e. the pumping power associated with the pressure drop can be estimated from (Streeter and Wylie, 1975).

$$P_M = V\,\Delta p \qquad (2)$$

where V denotes the volume flow rate through the system. In case of sCO_2, the volume flow rate, as well as Δp exhibit local and temporal variations so that spatial and temporal integration processes would be needed to obtain an accurate, representative mean value for P_M. However, since the variations are not too large, an indicative estimation can still be obtained by using approximately averaged values of V and Δp, which is also done currently.

The average pressure drop (Δp) through the system and the associated average mechanical power (P_M) for pumping are presented in Table 3, for water, and sCO_2 as heat transfer fluids.

Table 3- Pressure drop and pumping power for water and sCO_2 injection.

	Δp [Mpa]	**P_M [MW]**
Water	54	12
CO_2	26	8

As one can see in Table 3, the pressure drop for CO_2 is 48% that of water, which may be seen as an advantage for sCO_2 as a working fluid. This difference may obviously be attributed to the difference in the viscosities of both mediums, as the kinematic viscosity of the sCO_2 (on the average) is nearly the half of water. Consequently, the associated mechanical power is smaller for CO_2, compared to water (Table 3). However, ratio of CO_2-to-water is 67% for P_M (Table 3). This is due to the larger volume flow rate (V) of sCO_2. For the same mass flow rate, larger volume flow rates occur for subcritical CO_2, due to its smaller density (on the average) compared to water, causing this trend.

Hou et al. (2015), Benim et al. (2018 *a, b*) studied the EGS potential of the Dikili geothermal field using only water as circulation fluid for 90 days (3 months), 1000 days (nearly 3 years), 10 years and 20 years of production whereas we studied here for 6 months, 1 year, 5 years and 15 years of production for both water and sCO_2. In addition, they used 100, 150, 200 and 250 kg/s steady injection mass flow rates whereas we used only 215 kg/s steady injection mass flow rates during this study. Although the production durations and mass flow rates are different one another, the temperature distributions along x-z and y-z symmetry planes, total produced energy and temperature variations in the outlet of the reservoir seem identical for water. The studies that deal with water and sCO_2 at the same time are scarce even in the world. Based on limited existing studies, some of our findings such as production temperatures, cumulative produced energy and pressure drops for water vs. sCO_2 are comparable with previous studies performed in some other EGS sites such as Zhacanggou, Northeastern Tibet, China (Liu et al., 2019) although geological and modeling parameters are quite different.

5. Conclusions

Higher production temperatures are achieved with sCO_2 as working fluid in comparison to water according to current estimates. It is mainly due to its higher thermal conductivity and lower specific heat capacity, according to current assumptions. However, the thermal energy content of the production may turn out to be lower for sCO_2 as mainly caused by the lower specific heat capacity. On the other hand, as the thermal power varies quite remarkably over the whole production time for water, a more stable production power in time is obtained for sCO_2, which may be seen as an advantage for the latter. A further advantage of the sCO_2 injection is the lower pressure drop due to its lower kinematic viscosity, implying a lower pumping power. The present results encourage a more detailed and comprehensive analysis of the usage of sCO_2, as heat transfer fluid in EGS, including overall system analysis and optimization, which is intended to be considered in the future work. The fact that the use of sCO_2 in EGS may also contribute to the CO_2 storage issue in relationship with the greenhouse effect, the utilization of CO_2 in EGS surely deserves further attention.

References

Altunkaynak, Ş., Yılmaz, Y. 1998. The Mount Kozak magmatic complex, Western Anatolia. Journal of Volcanology and Geothermal Research 85, 211-231.

ANSYS Fluent, 2018. Release 18.0, Theory Guide. https://www.ansys.com/products/fluids/ansys-fluent.

Baba, A., Sözbilir, H., Demir, M. M., Akkurt, G. G., Özşen, A. Y., Şener, M. F., Hancıoğlu, E., Uzelli, T., 2022. İzmir ilindeki jeotermal kaynakların potansiyeli, kullanım alanları, ekonomik ve çevresel etkilerinin belirlenmesi araştırması. Project Report, 194, İzmir.

Baehr, H. D. 2005. Thermodynamik. 12th Edition Springer Verlag, 651.

Benim, A. C. 1990. Finite element analysis of confined turbulent swirling flows. International Journal for Numerical Methods in Fluids 11(6), 697-717.

Benim, A. C., Çiçek, A. 2022. Investigation of the thermohydraulics of an EGS project in Turkey: comparative assessment of water and CO_2 as heat transfer fluid. The International Symposium on Convective Heat and Mass Transfer 5-10 June 2022, İzmir, Turkey.

Benim, A. C., Çiçek, A., Eker, A. M. 2018*a*. A computational investigation of the thermohydraulics of an EGS project. Journal of Thermal Science 27(5), 405-412.

Benim, A. C., Çiçek, A., Eker, A. M. 2018*b*. A Preliminary numerical study of the thermohydraulics of an EGS project in Turkey. MATEC Web of Conferences 240 (1).

Bhattacharyya, S., Chattopadhyay, H., Benim, A. C. 2016. Heat transfer enhancement of laminar flow of ethylene glycol through a square channel fitted with angular cut wavy strip. Procedia Engineering 157, 19-28.

Bit, A., Alblawi, A., Chattopadhyay, H., Quais, Q. A., Benim, A. C., Rahimi-Gorji, M., Do, H. T. 2020. Three-dimensional numerical analysis of hemodynamic of stenosed artery considering realistic outlet boundary conditions. Computer Methods and Programs in Biomedicine 185, 105163.

Bird, R. B., Stewart, W. E., Lightfoot, E. N. 2006. Transport Phenomena. 2nd edition, Wiley, 780.

Borgia, A., Pruess K., Kneafsey, T. J., Oldenburg, C. M., Pan, L. 2012. Numerical simulation of salt precipitation in the fractures of a CO_2 enhanced geothermal system. Geothermics 44(67), 13-22.

Brown, D. 2000. A hot dry rock geothermal energy concept utilizing supercritical CO_2 instead of water, Twenty-Fifth Workshop on Geothermal Reservoir Engineering 24-26 January 2000, Stanford University, 233-238.

Civan, F. 2011. Porous Media Transport Phenomena. Wiley, 488.

Çiçek, A. 2020. The electric power production targeted Unconventional Geothermal Systems (UGS), some conceptual designs and their thermodynamics classification. Bulletin of the Mineral Research and Exploration 163, 211-228.

Emre, Ö., Duman, T. Y., Özalp, S., Elmacı, H., Olgun, Ş., Şaroğlu, F. 2013. 1/250.000 ölçekli Türkiye diri fay haritası. The General Directorate of Mineral Research and Exploration of Türkiye, Special Publications Series, 30, Ankara, Türkiye.

FLAC3D, 2019. Fast Lagrangian Analysis of Continua in Three-Dimensions, Ver. 7.0, Itasca Consulting Group, Minneapolis.

Gürer, F. Ö. 2023. A new look at the origin of N-S trending young basins of western Anatolia. Bulletin of the Mineral Research and Exploration 170, 117-146.

Glaister, P. 1993. Second order accurate upwind difference schemes for scalar conservation laws with source terms. Computers and Mathematics with Applications 25(4), 65-73.

Hou, Z., Şen, O., Gou, Y., Eker, A. M., Li, M., Yal, G. P., Cambazoğlu, S., Were, P. 2015. Preliminary geological, geochemical and numerical study on the first EGS project in Turkey. Environmental Earth Sciences 73, 6747-6767.

Japan International Cooperation Agency (JICA) (1987). Pre-feasibility study on the Dikili Bergama geothermal development project in The Republic of Turkey, Ankara. MTA, Progress Report II, Final Report, 229 .

Lemmon, E. W., Bell, I. H., Huber, M. L., McLinden, M. O. 2018. NIST Standard Reference Database 23: Reference Fluid Thermodynamic and Transport Properties-REFPROP, Version 10.0, National Institute of Standards and Technology, Standard Reference Data Program, Gaithersburg.

Liu, Y., Wang, G., Yue, G., Zhang, W., Zhu, X., Zhang, Q. 2019. Comparison of enhanced geothermal system with water and CO_2 as working fluid: a case study in Zhancanggou, Northeastern Tibet, China. Energy Exploration and Exploitation 37(2), 736-755.

Pan, L., Oldenburg, C. M. 2014. T2 Well -an integrated wellbore-reservoir simulator. Computers and Geosciences 65, 46-55.

Parlaktuna, M., Avşar, U. 2014. Dikili jeotermal sahası kaynak koruma alanları etüt raporu. Middle East Technical University, 163 p., Ankara (unpublished).

Peyret, R,. 1996. Handbook of Computational Fluid Mechanics. Academic Press, 480.

Pruess, K. 1991. TOUGH2: A general-purpose numerical simulator for multiphase fluid flow and heat flow, Lawrence Berkeley Lab., California, USA.

Pruess, K. 2006. Enhanced geothermal systems (EGS) using CO_2 as working fluid – a novel approach for generating renewable energy with simultaneous sequestration of carbon. Geothermics 35, 351-367.

Pruess, K. 2010. Enhanced geothermal systems (EGS) with CO_2 as heat transmission fluid – a scheme for combining recovery of renewable energy with geologic storage of CO_2.World Geothermal Congress 25-29 April 2010, Bali, Indonesia.

Streeter, V. L., Wylie, E. B. 1975. Fluid Mechanics, 6th edition, McGraw-Hill, 752.

Turan, A., Artun, E., Saner, S. 2021. Probabilistic assessment of geothermal resources and their development in Dikili-İzmir region. Earth and Environmental Sciences: Green Energy for Environmental Sustainability, 3, 634.

Uzel, B. 2013. Geological Evolution of İzmir-Balıkesir Transfer Zone: A crustal-scale structure reorganizing extensional tectonics in western Anatolia. Dokuz Eylül University, PhD Thesis, 236.

Versteeg, J. K., Malalasekera, W. 2007. An Introduction Computational Fluid Dynamics – The Finite Volume Method, 2nd edition Pearson, 503.

Whitaker, S. 1986. Flow in porous media I: a theoretical derivation of Darcy's law. Transport in Porous Media 1(1), 3-2.

Wood, B D., He, X., Apte, S. V. 2020. Modeling turbulent flows in porous media, Annular Review of Fluid Mechanics 52, 171-203.

Xia, J. L., Smith, B. L., Benim, A. C., Schmidli, J., Yadigaroğlu, G. 1997. Effect of inlet and outlet boundary conditions on swirling flows. Computers and Fluids 26(8), 881-823.

Yarar, Y. Günaydı, T., Çelebi, N., 2005. Determination of Radon Concentrations of The Dikili Geothermal Area in Western Turkey. Radiation Protection Dosimetry (2006), 118(1), 78-81

Yılmazer, S., Gevrek, A. İ., Sünger, Z., Üstün, Z., Çetiner, L., 1990. İzmir-Dikili-Kaynarca Jeotermal Sahası Kaynarca-1 Derin Jeotermal Sondajı Kuyu Jeolojisi Bitirme ve Değerlendirme Raporu, Maden Tetkik ve Arama Genel Müdürlüğü Report No: 9466, Ankara (unpublished).

Bulletin of the Mineral Research and Exploration

http://bulletin.mta.gov.tr

Neotectonics of Türkiye and its geothermal implication

Naci GÖRÜR[a*] and Şebnem ÖNDER[b]

[a]*Member of the Academy of Science, İstanbul, Türkiye*
[b]*Çanakkale Onsekiz Mart University, Faculty of Engineering, Department of Geophysical Engineering, Çanakkale, Türkiye*

Research Article

Keywords:
Neotectonic, Geothermal Springs, Neotectonic Provinces, Hot-Dry Rock, Temperature Map.

ABSTRACT

Favorable conditions for geothermal energy were created in Türkiye during its neotectonic episode from Neogene to Quaternary. This episode is characterized mainly by fluvio-lacustrine sedimentation and strike-slip tectonics with associated magmatism. Under these conditions, a great number of geothermal areas have formed in the neotectonic provinces in association with major tectonic features, including the North and East Anatolian Fault Zones (NAFZ and EAFZ, respectively). Today, the geothermal resources of Türkiye are mainly located in the West Anatolian Extensional Province associated with the graben systems. However, the Central Anatolian Ova Neotectonic Province is considered one of the most promising geothermal targets which are characterized by the presence of widespread hot dry rock systems. This study mainly aims to throw light on the possible potentiality of these resources at Kırşehir Block by emphasizing the neotectonic evolution of the country.

Received Date: 30.09.2022
Accepted Date: 16.12.2022

1. Introduction

Geothermal energy is natural heat that can be extracted from the earth. The earth's interior is hot and temperature increases with increasing depth. The increase is about 30 ºC per km of depth (1 ºC per 33 m of depth). The relationship between the variation in temperature and depth is called the geothermal gradient (Nwankwo and Ekine, 2009; Kwaya et al., 2019). The geothermal gradient may show regional variations depending on geological conditions. In areas where there are active tectonism and volcanism, the geothermal gradient is much higher than in other areas. Such areas are known as geothermal areas where more earth's internal heat is transferred to shallow depths or surfaces by conduction or convection mechanisms. The former mechanism is the transfer of heat by means of molecular action within the earth's crust, whereas the latter involves fluid movements. Conductively heated geothermal areas are generally represented by hot dry rocks where there is no sufficient geothermal fluid to transport heat to the surface. Such geothermal resources are exploited by creating an artificial reservoir in these hot rocks at depth so that water can be pumped into them at the surface. Convectively heated geothermal areas have adequate hot fluids to rise close to the surface (Rybach, 2010).

Importance of the geothermal energy increases in the world every day. The main reasons for this are related to global energy crises and climate change. Climate change is caused by the emission of greenhouse gases, mostly carbon dioxide and methane. Burning fossil fuels for energy production creates most of these emissions. Greenhouse gases lead to global

Citation Info: Görür, N., Önder, Ş. 2023. Neotectonics of Türkiye and its geothermal implication. Bulletin of the Mineral Research and Exploration 171, 107-122. https://doi.org/10.19111/bulletinofmre.1219987

**Corresponding author: Naci GÖRÜR, gorurna@gmail.com*

warming and thus to climate change. Climate change has already started in the world and perhaps will result soon in an expansion of deserts, wildfires, storms, droughts, glacial retreats, sea-level rise, flooding, etc. Climate change threatens people with food, water scarcity, disease, economic loss, human migration, etc. Deep cuts in the emission of greenhouse gases are vital and require switching from using fossil fuels to green energy resources. Geothermal energy is one of the green energy resources. It doesn't much create carbon dioxide during production, but it can emit a slight amount of greenhouse gases and air pollution. It will likely play a huge role in Türkiye in the transition to renewable energy because the thermal energy stored in the shallow earth crust of this country may be enough to provide a major part of its energy demand. Today, Türkiye is ranked 4th in the world in terms of installed geothermal capacity, but effective geothermal investigations and explorations may promote her to the first division (Miranda-Barbosa et al., 2017).

2. Geothermal Systems

Geothermal systems are hot petrological features at shallow depths with three primary components: a heat source, reservoir rock, and cap rock. The heat source is dominantly characterized by a volcanic intrusion or shallowly emplaced magma in volcanically and tectonically active areas. These conditions make a large heat transfer from deep in the Earth to relatively shallow depths where usually convective circulation of ground waters takes place. Reservoir rock is actually a hot rock with or without porosity and permeability. If it is permeable and fractured, it may contain fluid and allow it to flow into the production wells. Cap rocks are impermeable rocks above the reservoir rocks. They trap and prevent the loss of the fluid that exists in the reservoir rocks. As understood from the description above, fluid is not a primary component of a geothermal system. Geothermal energy may be present in a geothermal system even with no permeable reservoir or circulating fluid. Such a system is known as hot-dry rock. In this system, the impermeable rocks above the heat source are heated to extremely high temperatures through an abnormally high conductive heat flow. Utilization of the system can be done only after creating an artificial geothermal reservoir by using hydro-fracturing to form or enhance permeability and porosity in the hot rocks. To make energy production, two wells (one injection and one production) must be drilled into the hot rock. Hot dry rock resources seem virtually unlimited in magnitude but only those at shallow depths are preferable because the production cost of energy from this system is higher than that of conventional geothermal systems. However, the advent of new technologies for drilling and production may improve its economics in the near future (Mortensen, 1978; Stefansson, 2000; Duchane and Brown, 2002; Saemundsson et al., 2009; Çiçek, 2020).

From the description above, it is clear that geothermal systems form where active tectonics and magmatism prevail. Such conditions were created in Türkiye in the middle Miocene and have been ruling since then. This period represents the neotectonic phase of the country and without its detailed knowledge, it is not possible to evaluate the geothermal potential of Türkiye. Therefore, this topic will be dealt with first in the following paragraphs.

3. Neotectonics of Türkiye

Neotectonics of Türkiye was established in the middle Miocene after the closure of the southern branch of the Neo-Tethys Ocean (Bitlis Ocean) along the Bitlis-Zagros Suture Zone in Southeast Anatolia. Following the closure, Eastern Anatolia started to be squeezed between the Arabian and Eurasian plates, leading to a progressive thickening and shortening of the crust and forcing an Anatolian wedge (Anatolian Plate) to move westward away from the high-strain area. This movement took place along two major strike-slip fault zones, the dextral North Anatolian and the sinistral East Anatolian Transform Faults, NAFZ and EAFZ, respectively (Figure 1). It led to the deformation and oblique overthrusting of the Anatolian Plate onto the oceanic lithosphere of the Mediterranean along the Hellenic-Cyprus subduction zone.

It was the main cause of the formation of the neotectonic provinces of Türkiye, including East Anatolian Contractional, Central Anatolian Ova, West Anatolian Extensional, and North Anatolian Provinces (Figure 2).

The neotectonic regime had very profound effects on the geological evolution of Türkiye during the

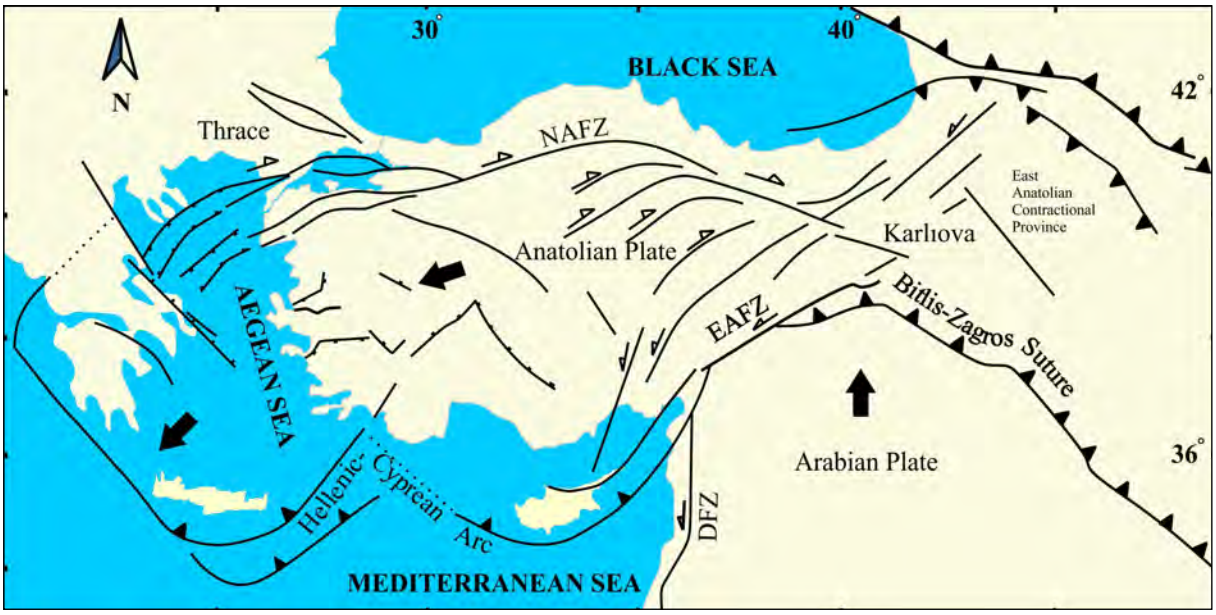

Figure 1- Neotectonics of Türkiye (modified from Gürer et al., 2003; NAFZ: North Anatolian Fault Zone, EAFZ: East Anatolian Fault Zone, Dead Sea Fault Zone).

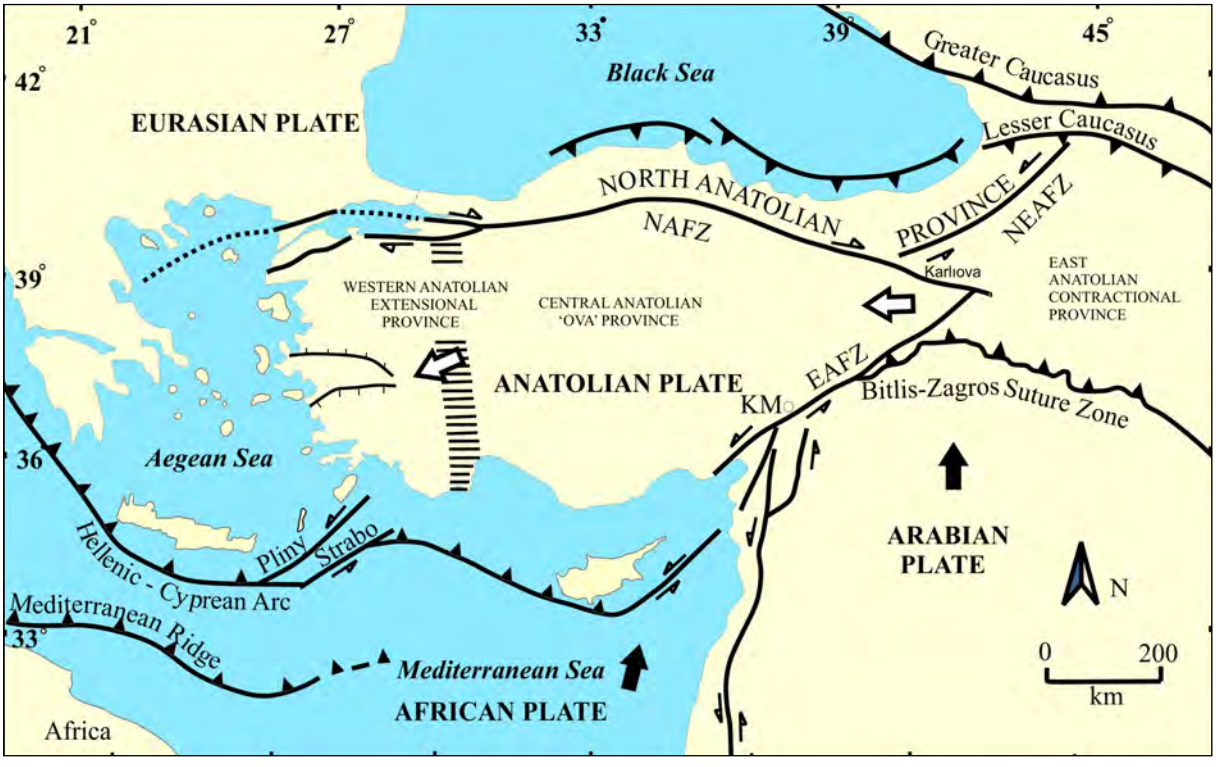

Figure 2- Neotectonic provinces of Türkiye (modified from Bozkurt, 2001; NAFZ: North Anatolian Fault Zone, NEAFZ: Northeast Anatolian Fault Zone, EAFZ: East Anatolian Fault Zone, KM: Kahramanmaraş).

Neogene to Quaternary. It was dominated in the neotectonic provinces by extension and strike-slip faulting with widespread continental sedimentation and calc-alkaline magmatism. Closure of the Bitlis Ocean resulted in the East Anatolian Contractional Province crustal thickening and generation of many compressional and extensional structures, such as east-west trending thrust, reverse, and strike-slip faults with associated ramp basins. The westward motion of the Anatolian Plate caused in the eastern part of the Central Anatolian Ova Province internal deformations and the formation of many second-order faults and associated basins, arising from the NAFZ. In the rest of this province, a strike-slip dominated ova regime became established. Ovas are extensional basins bounded by dextral or sinistral oblique-slip faults. In the West Anatolian Extensional Province, the extensional regime has been established due to the obstruction of the westerly motion of the Anatolian Plate both by the abrupt south-westerly bend of the NAFZ in the Marmara Region and the Grecian mainland. The North Anatolian Province is tectonically the quietest region among the others and appears to be undergoing E-W shortening with a number of strike-slip faults with strong E-W thrust components (Şengör, 1979, 1980; Şengör and Yılmaz, 1981; Özgül, 1984; Görür et al., 1984; Şengör et al., 1985; Görür and Tüysüz, 2001; Bozkurt, 2001; Gürer et al., 2003; Okay, 2008).

4. Neotectonic Provinces of Türkiye

The neotectonic provinces developed on top of the different palaeotectonic terrains of Türkiye that had mostly formed a united land mosaic before the elimination of the Bitlis Ocean. Each of the neotectonic provinces has a distinctive set of structures and stratigraphy with characteristic tectonism and magmatism (Şengör et al., 1985; Bozkurt, 2001; Okay, 2008). Their Neogene stratigraphy is more or less similar but the pre-Neogene stratigraphy is different because it developed when the terrains were separate blocks and undergoing different tectono-stratigraphic evolution. Unless the pre-Neogene stratigraphy of the palaeotectonic terrains is understood, it is difficult to evaluate their geothermal potential because, in most of the geothermal fields in Türkiye, the pre-Neogene formations constitute the reservoir rocks. Therefore, the pre-Neogene stratigraphy of each province is summarized below first and then their Neogene stratigraphy is discussed collectively.

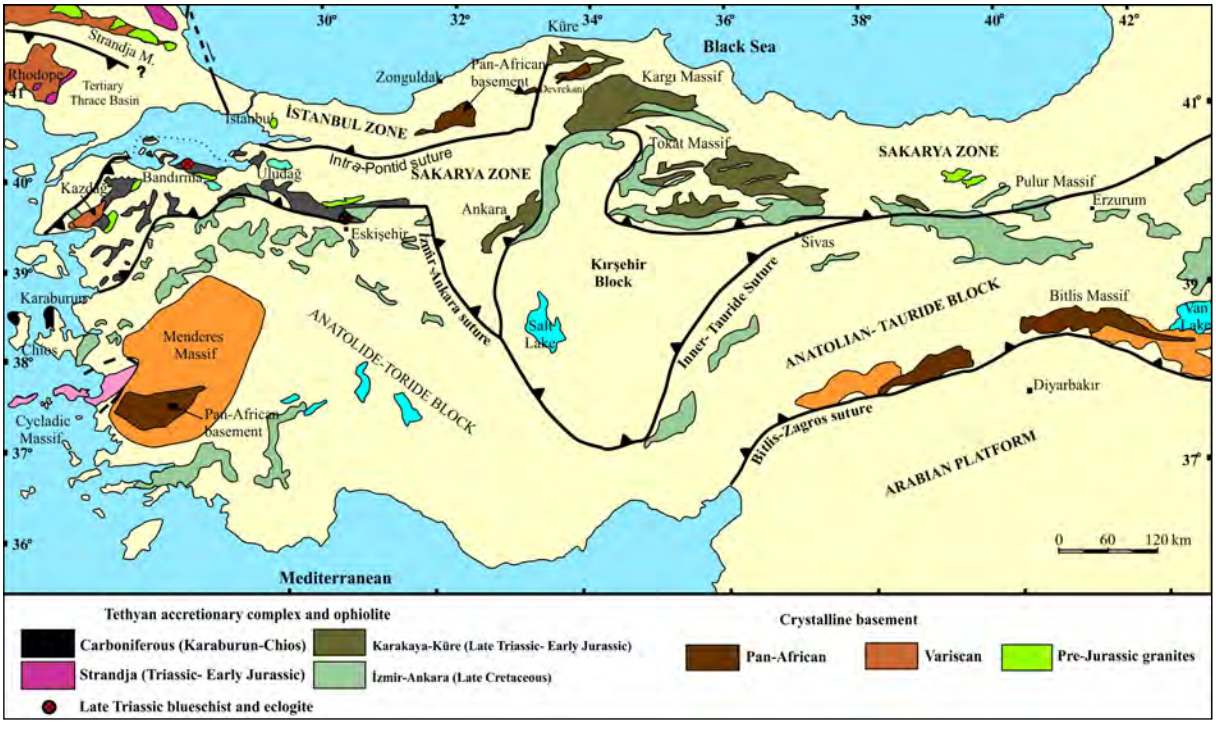

Figure 3- Palaeotectonic terrains of Türkiye (modified from Okay, 2008).

4.1. East Anatolian Contractional Province

This province covers Southeast and East Anatolia and developed on two palaeotectonic terranes of Turkey, namely the Arabian Platform and East Anatolian Accretional Complex (Figures 2 and 3). The Arabian Platform has a Pan-African type basement overlain with an angular unconformity by a sedimentary sequence, ranging in age from Cambrian to Tertiary. The pre-Permian sediments of the sequence are composed mainly of clastic rocks, whereas the post-Permian deposits consist of carbonates. Eastern Anatolia is characterized by a basement, comprising an ophiolitic accretional melange of Upper Cretaceous age. This basement is unconformably overlain by Palaeocene to Eocene flysch and olistostrome that shallow upward and pass into Neogene continental deposits with widespread calc-alkaline volcanics (Şengör and Yılmaz, 1981; Perinçek, 1990; Yılmaz, 1993; Okay, 2008).

4.2. Central Anatolian Ova Neotectonic Province

This province has developed dominantly on Kırşehir Block, one of the main palaeotectonic terrains of Türkiye (Figures 2 and 3). The Kırşehir Block consists of a metamorphic basement and cover rocks. The metamorphic basement comprises gneisses, micaschists, metaquartzites, and marbles, whereas the cover rocks include partly preserved Upper Cretaceous ophiolite nappes and sedimentary rocks of Upper Cretaceous to Neogene age. Both the metamorphic basement and the ophiolite nappes are intruded by Cretaceous granite intrusions (Beyazpirinç et al., 2022). Ophiolite nappes are comprised of basalt, radiolarian cherts, pelagic limestones, sandstones, and serpentines. Sedimentary rocks mostly represent the sediments that accumulated in the magmatic arc or collision-related basins of various sizes developed both on the metamorphic basement and the ophiolite nappes. The magmatic arc-related basins include Çankırı, Kırıkkale, Tuzgölü, Ulukışla, and Şarkışla, whereas the collision-related ones comprise Refahiye, Sivas, Yıldızeli, and Yozgat-Sorgun Basins. The formers formed during the Cretaceous and the latter during the Eocene. Both types of basins dominantly accumulated turbidites until the Oligocene when they were obliterated and turned to constitute the neotectonic cover of the Central Anatolian ova regime (Şengör and Yılmaz, 1981; Şengör et al., 1982; Seymen, 1983; Görür et al., 1995*a, b*, 1998; Poisson et al., 1996; Yalınız et al., 2000; Görür and Tüysüz, 2001; Whitney and Hamilton, 2004; Okay, 2008).

4.3. West Anatolian Extensional Neotectonic Province

The basement of this province is characterized by the Sakarya Zone and the Anatolide-Tauride Block which were amalgamated into a single land mosaic after the closure of the Neo-Tethys Ocean along the İzmir-Ankara Suture (Figures 2 and 3). The Sakarya Zone is characterized in its lower part by strongly deformed and locally metamorphosed Paleo-Tethyan active continental margin units, ranging in age from Permian to Triassic. These units form a stratigraphic basement for a sedimentary sequence, ranging in age from Lower Jurassic to Eocene. The Paleo-Tethyan basement rocks comprise metabasite-marble-fillat series with exotic eclogite and bluschist lenses, passing upward across a tectonic contact into Triassic clastic and basic volcanic rocks with abundant Carboniferous and Permian exotic blocks, including shallow-water carbonates, basalts, and radiolarian cherts. This basement is unconformably overlain by Lower to Middle Jurassic molasses sandstones and rift volcanics, grading upward into Upper Jurassic to Lower Cretaceous limestones and then into Upper Cretaceous to Eocene flysch with volcanic interbeds (Şengör et al., 1984; Okay et al., 1991, 1996). In the northern parts of the central and the eastern Pontides, the Cretaceous to Eocene units constitute the Neotethyan magmatic arc and the southern passive continental margin of the Black Sea, opening as a back-arc basin behind the magmatic arc (Yılmaz and Boztuğ, 1986; Okay et al., 1994, 2002, 2006; Görür, 1997; Görür et al., 1997). Eocene rocks pass upward in places into Oligocene-Neogene fluvio-lacustrine deposits.

The Anatolid-Tauride Block shows complex stratigraphic, structural, and metamorphic features. It has a thick sedimentary sequence sitting on a Pan-African crystalline basement above an angular unconformity. The sequence consists of Palaeozoic continental to inner shelf clastic and carbonate rocks in the lower part and Triassic to Upper Cretaceous carbonates in the upper part. The block seems to have stayed as a carbonate platform until the closure of the Neo-Tethys Ocean between the Cretaceous and

Palaeocene. During the elimination of the ocean, the Anatolide-Tauride Block was subjected to strong deformation, ophiolite obduction, thrusting, and regional metamorphism. The major metamorphic zone of the block is the Menderes Massif, a Barrovian-type metamorphic belt. It has a pre-Cambrian core of micaschists, gneiss, granulite, and eclogite intruded by metagranites. This crystalline basement is succeeded by metasedimentary cover rocks of Palaeozoic to Lower Tertiary age. The lower part of the cover sequence consists mainly of quartzite, phyllite, and marbles of the Permo-Carboniferous age, passing upward into Triassic to Cretaceous carbonates, mainly marbles. Above the marbles are red pelagic recrystallized limestones overlain by a slightly metamorphosed flysch sequence with serpentine blocks. This flysch sequence is tectonically overlain by various nappes of the Anatolide-Tauride Terrains, i.e. Lycian Nappes and Bornova Flysch (Özgül, 1984; Şengör et al., 1984; Okay, 1984, 2008; Okay et al., 1996). Neogene rocks rest on top of the pre-Neogene units above an angular unconformity and constitute fluvio-lacustrine sediments with calc-alkaline volcanics deposited mainly in grabens (Şengör et al., 1985).

4.4. North Anatolian Neotectonic Province

The basement of the North Anatolian Province consists of three different terranes, namely Strandja, İstanbul, and Sakarya Zones (Figures 2 and 3). Pre-Neogene stratigraphy of the Sakarya Zone is already given above. The pre-Neogene stratigraphy of the Strandja and the İstanbul Zones is as follows: The Strandja Zone starts at the base with Permian metamorphic rocks intruded by granitoids. The metamorphic rocks are overlain with an angular unconformity by a metasedimentary sequence of the Triassic to Jurassic age; Triassic rocks comprise continental to shallow-marine clastic and carbonate rocks, passing upward across an angular unconformity into clastic sediments of Jurassic age. The metasedimentary sequence is succeeded tectonically by melange or un-conformably by Cenomanian conglomerates and neritic limestones followed by Senonian arc-related magmatic rocks (Moore et al., 1980; Chatalov, 1988; Okay et al., 2001; Sunal et al., 2006; Okay, 2008). In the Thrace, this sequence is overlain by the infill of the Thrace Basin. The infill ranges in age from Middle Eocene to Pliocene and is dominated by a shallowing upward and dominantly clastic succession. The Middle Eocene to Lower Oligocene sediments are represented in the deeper part of the basin by tuffaceous turbidites and on the margins by continental to shallow-marine clastics, volcanoclastics and carbonates. Post Lower Oligocene sediments are mainly brackish to terrestrial in nature. The pre-Oligocene rocks of the infill of the Thrace Basin accumulated in the arc-related basinal setting above the northward subducting Intra-Pontide Ocean, whereas post-Oligocene rocks developed in a dextral strike-slip shear zone, constituting the widest part of the North Anatolian Shear Zone extending between the East Anatolia and the Aegean (Görür et al., 1984; Görür and Okay, 1996; Şengör et al., 2005; Siyako and Huvaz, 2007; Görür and Elbek, 2013).

The İstanbul Zone is represented by an Ordovician to Quaternary thick sedimentary sequence, sitting with an angular unconformity on top of a Late Pre-Cambrian crystalline basement. The crystalline basement is characterized by gneiss, amphibolite, metavolcanics, metaophiolite, and granitoids. The sedimentary sequence on the basement shows marked stratigraphic differences along the length of the zone. In its western part, Ordovician rocks comprise continental clastics of arkosic nature, passing upward into Silurian quartzites and overlying shales. The shales are succeeded by Devonian reefal limestones, grading up into interbedded shales and cherty limestones of the same age. On top of them are Carboniferous radiolarian cherts and siliciclastic turbidites. The turbidites are unconformably overlain by Triassic rocks. Triassic rocks consist at the base of red sandstones with basaltic volcanic interbeds, passing upward into shallow- to deep-marine limestones and siliciclastic turbidites. The Triassic series are succeeded across an angular unconformity by Upper Cretaceous-Palaeocene clastic, carbonate, and andesitic volcanic rocks. In the European side of İstanbul, Palaeozoic rocks are unconformably overlain by Eocene and Neogene sediments. Eocene sediments comprise reefal limestones and marls, passing upward across an angular unconformity into the Neogene sediments represented mainly by fluvio-lacustrine clastic with tuffaceous interlayers. In the eastern part of the İstanbul Zone, around Zonguldak, the sedimentary sequence displays different stratigraphic development for certain periods. For instance here,

the Devonian neritic carbonates pass upward into deltaic clastic rocks of the Carboniferous with coal seams. These sediments are unconformably overlain dominantly by continental red clastics of the Permian age succeded with a transitional contact by Triassic lacustrine marl, clays, mudstone, and limestone. On contrary to the western part, the Jurassic is present here and is represented by Middle and Upper Jurassic rocks, grading upward into Cretaceous neritic carbonates. Middle Jurassic rocks are coal-bearing deltaic clastics at the base, grading upward into deep-water siliciclastic turbidites and then back into the deltaic sequence again. Upper Jurassic rocks are mostly characterized by thick neritic carbonates, extending in age up to Aptian. These shallow-water carbonates are succeeded by a sequence of Aptian to Eocene age, representing the passive continental margin sediments of the Western Black Sea Basin. The sequence consists predominantly of volcanogenic coarse clastic rocks, shales, and carbonates with a deepening upward character. The volcanoclastic rocks are mostly turbidites with huge exotic blocks. The neotectonic Miocene sedimentary cover of the eastern part of the İstanbul Terrain comprises dominantly fluvio-lacustrine sediments and overlies the Eocene rocks with an erosional contact (Okay et al., 1994; Görür, 1997; Ustaömer et al., 2005; Okay, 2008; Hippolyte et al., 2016; Tüysüz, 2022).

4.5. Neogene Stratigraphy of the Neotectonic Provinces

In the East Anatolian Contractional Neotectonic Province (Figure 2), the sediments characterizing the neotectonic episode accumulated in various basins, such as Muş, Ahlat-Adilcevaz, Karayazı-Tekman, Kağızman-Tuzluca, and Erzurum-Pasinler-Horasan basins. These basins are generally ramping, intermountain, and pull-apart in nature and contain sedimentary successions, ranging in age from Middle Miocene to the Pliocene age. Middle Miocene units are spatially limited and have a regressive sequence, starting with shallow marine sediments at the base and lagoonal facies at the top. They consist of clayey limestone, marl, sandstone, and siltstone in part with volcanic rocks, such as basalt, trachyte, andesite, and pyroclastic rocks. The Middle Miocene rocks pass upward across an unconformity into a continental Upper Miocene sequence that is characterized by sandstone, siltstone, and conglomerate in the lower part and clayey limestone, tuff, agglomerate, and lava in the upper part. The Pliocene rocks in the region are comprised of fluvio-lacustrine sandstone, siltstone, conglomerate, marl, and limestone associated with basalt, andesite, and trachy-andesite (Irrlitz, 1972; Şaroğlu and Güner, 1981; Güner, 1984; Şengör et al., 1985; Şaroğlu and Yılmaz, 1986).

In the Central Anatolian Ova Province (Figure 2), the Neogene sediments were deposited in two types of basins: Ova and strike-slip fault-related basins. Ovas are large, roughly equant extensional basins bounded by more than two oblique-throw faults (Şengör, 1980; Şengör et al., 1985). These basins contain widespread gypsiferous series deposited in fluvio-lake environments together with clastic and volcanic rocks. Strike-slip basins formed in association with the EAFZ, forming the eastern boundary of the province. These basins include Karlıova, Bingöl, and Lake Hazar (Hempton et al., 1983; Aksoy et al., 2007). The Adana Basin, which is associated with the western end of the EAFZ, is not a strike-slip basin. It formed as an incompatibility gap associated with displacements around the triple junction in the vicinity of Kahramanmaraş (Şengör et al., 1980, 1985). During the neotectonic episode, all the strike-slip basins accumulated Miocene to Pliocene sediments, comprising fluvio-lacustrine clastic and carbonate rocks with tuff, tuffite, agglomerate basalt and andesitic basalt (Yalçın and Görür, 1984; Okay, 2008).

Neotectonic cover rocks of the West Anatolian Extensional Neotectonic Province (Figure 2) are characterized by fluvio-lacustrine sediments and associated magmatic rocks of the Upper Oligocene to Quaternary age. Their Upper Oligocene to Lower Miocene part was deposited in large interconnected lake basins, covering almost the whole province, whereas the rest was confined to the graben systems. The most known graben structures are east-west oriented Gediz, Küçük Menderes, Büyük Menderes, and Kerme grabens. In their sediments rich borate, sodium sulphate, lignite, and clay are found. The associated magmatic rocks comprise both intrusive and extrusive rocks. Intrusive rocks are mostly characterized by granodiorites and monzonites, whereas extrusive rocks display a large variety of composition, including basaltic andesite, andesite, trachyandesite, latite, and dacite (Helvacı, 1995; Yılmaz, 1997; Görür et al., 1995*a, b*; Aldanmaz et al., 2000; Yılmaz et al., 2001).

The North Anatolian Neotectonic Province (Figure 2) is characterized by very weak active tectonism. Besides the Thrace Basin, considerable depositional areas in this province during the neotectonic period (Neogen) are absent. The Thrace Basin formed in the dextral North Anatolian Shear Zone and accumulated during this period mostly fluvio-lacustrine coal-bearing clastics and carbonates in part with tuffaceous material (Görür and Okay, 1996; Görür and Elbek, 2013). Along the southern boundary of the province, there are many sedimentary basins of various sizes formed in the NAFZ. These basins, from west to east, are Gelibolu, Yalova, Gölcük-Derince, Adapazarı, Düzce, Bolu, Çerkeş-Kurşunlu, Tosya, Kargı, Vezirköprü, Havza-Lâdik, Taşova-Erbaa, Niksar, Suşehri, Refahiye, and Erzincan basins. The basins developed in an autonomous boundary region between the North Anatolian, West Anatolian Extensional, and Central Anatolian Ova Neotectonic provinces, and therefore they cannot be considered to belong to any of these provinces. They developed as pull-apart, compressional ramp, transtensional, and fault-wedge basins and accumulated during the neotectonic phase of limnic and fluviatile sediments with volcanic interbeds. Limnic sediments are comprised of marls and limestones in part with interbedded fine clastics and volcanics. The volcanics are mostly calc-alkaline in nature and range in composition from basaltic andesite to rhyolite. Fluviatile sediments are composed of conglomerates, sandstones, and mudstones locally with tuffs and tuffites. All these continental sediments may contain vertebrate, ostracode, spores, and pollen fossils (Tatar, 1975, 1978; Seymen, 1975; Şengör and Yılmaz, 1981; Barka, 1985; Şengör et al., 1985; Görür et al., 1995*b*).

5. Geothermal Potential of the Neotectonic Provinces

In order to judge the geothermal potential of the neotectonic provinces of Türkiye, their palaeotectonic and neotectonic settings, litho-stratigraphy, geological structures, and heat flow must be taken into account. Besides the heat flow, all these features were already outlined in the preceding paragraphs. The heat sources of the provinces are discussed below on the basis of the temperature distribution map of Türkiye at depth of 1000 m prepared by Başel et al. (2013) according to the kriging geostatistical method (Figure 4).

5.1. East Anatolian Contractional Province

In the East Anatolian Contractional Province, temperature distribution at 1000 m below the surface ranges between 40°C and 80°C. In the southeastern

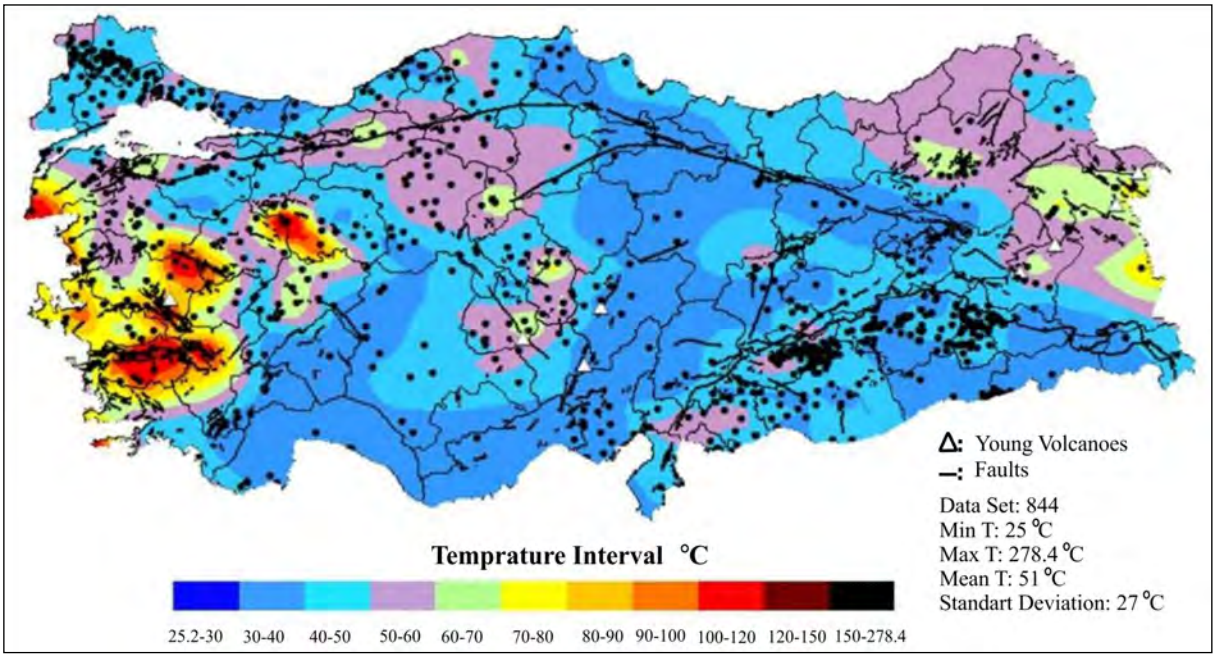

Figure 4- Temperature distribution map of Türkiye at 1000 m below the surface (after Başel et al., 2013).

part of the province, the temperature at the same depth is low and generally varies from 30°C to 50°C. Here, it only reaches 60°C around Gaziantep and Adıyaman, situated along the EAFZ (Figure 4). In the eastern part of the province, the temperature at the same depth is about 50°C to 60 °C but in the vicinities of Erzurum, Ağrı, Bitlis, and Van, it may rise up to 80°C. Geothermal fields are quite common in the province and are found in Ağrı-Diyadin, Bitlis-Nemrut, Van-Erciş, Diyarbakır-Çermik, Şanlıurfa-Karaali-Kabahaydar, Adıyaman-Çörmük-Besni, Gaziantep-Areban-Kartalköy, Batman-Çermik, Şırnak-Beytüşşebap-Besta, Batman-Taşlıdere, Mardin-Ulusu and Siirt-Billoris (Figure 5). Development of these geothermal fields was of course controlled by both the tectonism and the magmatism that prevailed in the province during the neotectonic period. During this period, the East Anatolian Contractional Province underwent N-S contraction and as a result of this E-W trending folds, thrusts, and continental ramp basins developed in the north and south of the region. The middle part of the province has been the site of strike-slip faults and associated basins. Related to these neotectonic activities, a widespread calc-alkaline volcanism also took place in the province until the historical times. The youngest volcanoes in the province are Süphan, Nemrut, Karaca, Tendürek, and Ağrı. Because of the coeval tectonism and magmatism, the geothermal potential of the province must be high. Especially, transtensional and pull-apart areas of the strike-slip faults may be good targets for geothermal explorations. Present-day hot water springs appear to be located in such places. Compressional structures in the province, such as the transpressional part of the strike-slip faults, ramp basins, and the Bitlis-Zagros Suture Zone must be handled carefully in terms of geothermal expeditions. However, in southeast Anatolia, joints, fractures, and folds formed parallel with the orientation of shortening of the province may be favorable places for geothermal resources. Of course, younger volcanoes are another attractive target for investors in geothermal energy. These recent volcanoes may hide very productive geothermal systems beneath their lavas and pyroclastics in the region. Abundant hot water springs around the Ağrı may be an indication of this (Figure 5) (Mutlu and Güleç, 1998; Bektaş et al., 2007; Ulusoy et al., 2008; Baba et al., 2010; Başel et al., 2013; Alacali, 2018; Çırmık, 2018; Bilim et al., 2018).

5.2. Central Anatolian Ova Neotectonic Province

Temperature variation in this region 1000 m below the surface is dominantly between 30°C and 50°C. Although around Çorum, Çankırı, Bolu, Ankara, and

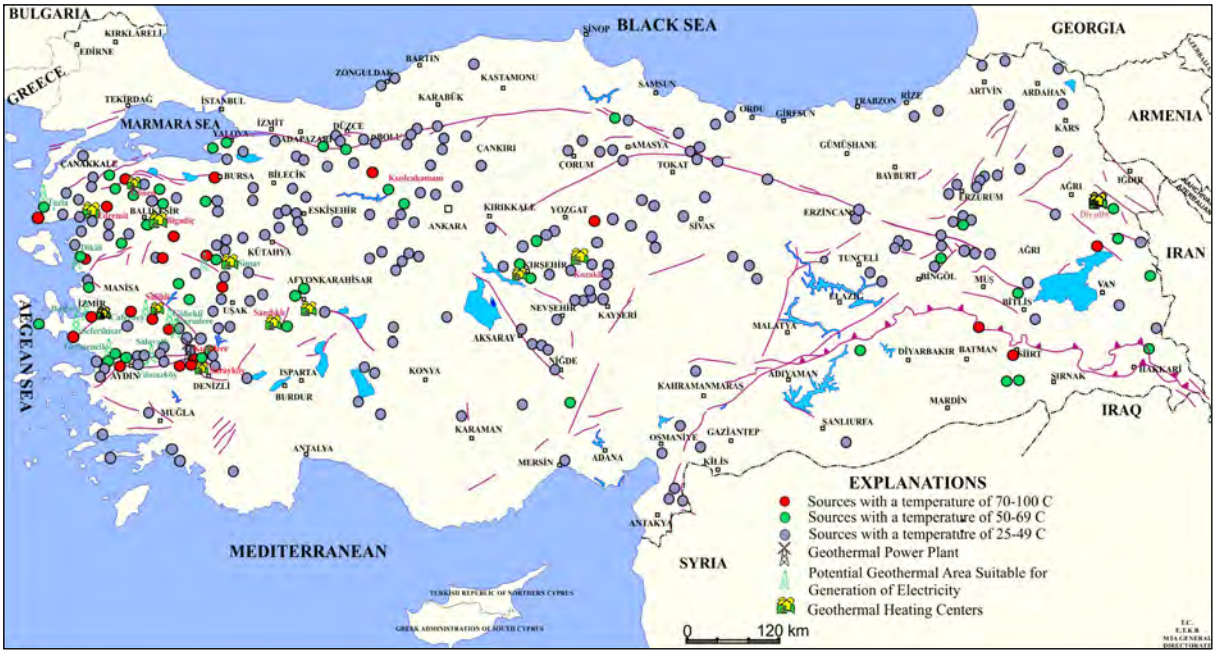

Figure 5- Distribution of geothermal springs in Türkiye (modified from MTA Geothermal Map, 2022).

Kırıkkale, near the NAFZ, it ranges from 50°C to 60°C (Figure 4). Comparable temperatures are also seen at this depth in the Cappadocia region in the south, around Nevşehir, Aksaray, and Niğde where most of the geothermal fields of the province are found. Some of these fields are Kırşehir-Terme, Nevşehir-Kozaklı, and Aksaray-Ziga (Figure 5). Although the geothermal fields may give an idea about the heat flow in this province, the temperature at depth of more than 1000 m is much higher in the Cappadocia. In the Sivrihisar-3 well drilled here by the 3S Kale Energy Company, 294ºC temperature was measured at 3800 m depth. This is the highest temperature measured at this level up to now in Türkiye. Like the Cappadocia, other parts of the Central Anatolian Ova Province seem to be hot at depth as indicated by the existence of many hot water springs and thermal fields in Niğde, Sivas, and the EAFZ, delimiting the province from the east. Along the EAFZ, thermal springs commonly occur in Bingöl, Tunceli, Kahramanmaraş, and Osmaniye (Figure 5). The reason for the elevated temperature in the interior of the Kırşehir Block must be related to its magmatic evolution. Magmatism was very active and common during both palaeo- and neotectonic evolution of this terrain. The neotectonic volcanics are observed in Afyon, Kırka, Konya, Nevşehir, Kayseri, Ankara, Isparta, Karaman, Ceyhan, Hasandağ, Acıgöl, and Erciyes. Actually, volcanoes such as Hasandağ and Erciyes continued their activities up to the historical times. These volcanic activities probably enhanced the geothermal potential of this province and perhaps created common geothermal systems in the region. Besides the volcanism, when the Anatolian Plate started its westward motion during the neotectonic episode, the Central Anatolian Ova Neotectonic Province was deformed and cut into slices by various strike-slip fault branches of the North Anatolian Fault Zone. These faults, of course, must have increased porosities and permeability in the province and thus facilitated the convective and conductive heat transfers to the upper levels. However, up to now, this region unfortunately has not been investigated as much as it deserves. There is a rumour going around that there are not enough fluids in this province at depth. Even so, if this region is much hotter than the rest of Türkiye, it may form attractive petro-thermal geothermal systems (hot rock/dry rock systems). These systems are human-made structures to exploit the earth's crust's heat that contains no fluids in place; therefore, most of their reservoir parameters can be controlled for optimum productivity. Testing and experiences in various countries have proved beyond a doubt that it is technically feasible to recover enough amounts of thermal energy from these systems. The techniques for constructing such artificial reservoir systems are still in the developing stage but surely they will become soon common knowledge worldwide (Mortensen, 1978; Duchane and Brown, 2002; Ateş et al., 2005; Brown, 2009; Başel et al., 2013; Kıyak et al., 2015; Bilim et al., 2017; Şener and Baba, 2019; Aydemir et al., 2019).

5.3. West Anatolian Extensional Neotectonic Province

In this province, crustal extension and magmatism have taken place coevally during the neotectonic episode. Owing to the N-S extension, the crust in western Anatolia is thinned by the formation of graben structures with various sizes and orientations. The grabens have created relatively narrow zones of lower lithospheric thinning and mantle upwelling, thus increasing the geothermal gradient in the region. As seen in Figure 4, this region is the hottest part of the country at least 1000 m below the surface. In large part of the region, the temperature at this depth varies from 50°C to 120°C and the temperatures approach the upper limit at Çanakkale (Ezine, Bayramiç, Ayvacık), Balıkesir (Ayvalık), İzmir (Dikili, Buca), Aydın, Muğla (Datça), Denizli (Babadağ, Pamukkale, Honaz, Merkezefendi), Manisa-Kütahya (Demirci, Selendi, Simav, Şaphane, Pazarlar) and Eskişehir (İnönü, Seyitgazi, Çifteler, Han). The temperature distribution suggests that thermal conditions within the grabens are favorable for geothermal energy production. Actually, western Anatolia is ranked first in terms of geothermal energy production in Türkiye (Figure 5). The cities with well-known geothermal fields are as follows: Çanakkale (Tuzla), Balıkesir (Bigadiç, Hisaralan, Gönen), İzmir (Seferihisar, Balçova, Dikili, Aliağa, Çeşme), Aydın (Germencik, Salavatlı, Yımazköy-İmamköy), Denizli (Kızıldere, Gölemezli, Karahayıt, Pamukkale), Manisa (Salihli-Caferbeyli, Salihli-Kurşunlu, Alaşehir-Kavaklıdere, Turgutlu-Urganlı, Saraycık, Kula) and Kütahya (Simav, Gediz-Abide). In most of these areas, thermal energy production is made from the basement rocks, although in a few of them, it is produced from the neotectonic cover.

Because of the high success rate, western Anatolia has attracted considerable attention and therefore most of the geothermal energy investments have been made in this region. This attraction has caused excessive and damaging exploitations in the region, resulting in drops in reservoir pressures and the occurrence of great production problems (Şimşek, 1985, 2003; Özgür, 2002; Tüfekçi et al., 2010; Başel et al., 2013; Korkmaz et al., 2014; Erkan, 2015; Pazvantoğlu et al., 2021; Serpen et al., 2022).

5.4. North Anatolian Neotectonic Province

Examination of Figure 4 shows that temperature in this province at 1000 m depth changes in most places between 30°C and 50°C above the normal geo-gradient. However, in certain places such as Edirne, Silivri-Çerkezköy, Yalova, Sakarya, Düzce, Bolu, Karabük, and Kastamonu, the temperature reaches 60°C. These places, except Edirne and Silivri-Çerkezköy, are located in and around the NAFZ, indicating that the fault zone probably transferred the heat from the interior of the Earth to this depth. Edirne and Silivri-Çerkezköy areas are located in the Thrace Basin where volcanism was active in Eocene to Neogene time, including the neotectonic episode. This region is also under the effect of strike-slip tectonic activity during this episode. The deep strike-slip faults in these areas, such as Kırklareli, Lüleburgaz, Babaeski, and Ganos, might have formed pathways for the heat at depth to come to the surface.

North Anatolian Neotectonic Province doesn't show much volcanism and active tectonism, other than weak east-west shortening. Therefore its geothermal potential seems low. However, the Thrace Basin and the NAFZ may have high geothermal potential. The NAFZ, which is a plate boundary structure with a lithospheric scale, may serve as channels for heat and geothermal fluids from hot deeper levels of the crust to reach shallow depths and form rich geothermal sources. As a matter of fact, there are many surface manifestations like hot springs along this fault zone, including Yalova, Adapazarı, Düzce, Bolu, Amasya, Tokat, Erzincan, and Bingöl (Figure 4). The well-known geothermal fields along the fault zone comprise of Çekirge (Bursa), Armutlu (Yalova), Termal (Yalova), Akyazı (Sakarya), Kaplıca (Bolu), Mudurnu-Babas (Bolu), Seben-Kesenözü (Bolu), Hamamözü (Amasya), Gözlek (Amasya), Reşadiye (Tokat) and Kurşun-Çavundur (Çankırı). All these geothermal fields have developed in association with the NAFZ and its branches. Their reservoir and cover rocks are dominantly developed in the palaeotectonic terrains of the basement as they are situated on the different neotectonic provinces along the fault zone.

Most of the basins, which developed along the NAFZ, have high geothermal gradients but particularly those formed in the trans-tensional and pull-apart portions of the fault zone are favorable in terms of geothermal energy. Geothermal investigations in the NAFZ may be difficult, because of extremely complicated geology. This fault zone is superimposed on the İzmir-Ankara-Erzincan and Intra-Pontide sutures that represent the final closure of the Neo-Tethys Ocean. During the closure, palaeotectonic terrains to the north of the ocean thrusted over onto the terrains in the south together with the accretionary melange formed during the subduction. Accretionary melange also exits on the Pontides to the north of the sutures as retrocharriages. Of course, these tectonic events made the substratum geology of the North Anatolian Fault Zone too complicated. Despite all the complications, superimposed suture and the North Anatolian Fault Zone are the most convenient places for geothermal investigations as they may play an important role with their deep roots in the crust in conveyance of heat from the interior of the Earth to the shallow areas. There is no doubt that careful studies will lead to discoveries of rich geothermal resources (Mamontov et al., 2005; Yapmış et al., 2005; Maden, 2012; Başel et al., 2013; Görür and Elbek, 2013; Pasvanoğlu and Çelik, 2019; Temizel et al., 2021).

6. Results

This paper gives an up-to-date overview of the geothermal potential of Türkiye on the basis of the neotectonic episode in Türkiye. This episode is characterized by fluvio-lacustrine sediments and associated magmatism with a relatively high geothermal background induced by the continental collision between the Arabian and Eurasian plates. The most known geothermal systems in this country occur as hydrothermal systems, including both vapour-and liquid-dominated geothermal fields. However, the high thermal anomalies in the Central

Anatolian Ova Neotectonic Province indicate that the largest geothermal potential of Türkiye is perhaps the hot-dry rock (HDR) or enhanced geothermal systems (EGS) of this province. These systems today have significant technical and economic challenges. If they are overwhelmed in near future, Türkiye's commercial utilization of this resource will be immense by any measure. Therefore, exploration activities should be directed from the West Anatolian Extensional Province to the Central Anatolian Ova and the East Anatolian Contractional Provinces where HDR/EGS and hidden hydrothermal systems with no surface thermal manifestations may be common.

References

Aksoy, E., İnceöz, M., Koçyiğit, A. 2007. Lake Hazar basin: A negative flower structure on the East Anatolian Fault System (EAFS), SE Turkey. Turkish Journal of Earth Science 16(3), 319–338.

Alacali, M. 2018. Hydrogeochemical investigation of geothermal springs in Erzurum, East Anatolia (Turkey). Environmental Earth Sciences 77(24), 1-13.

Aldanmaz, E., Pearce, J. A., Thirlwall, M. F., Mitchell, J. G. 2000. Petrogenetic evolution of late Cenozoic, post-collision volcanism in western Anatolia, Turkey. Journal of Volcanology and Geothermal Research 102(1-2), 67–95.

Ateş, A., Bilim, F., Büyüksaraç, A. 2005. Curie point depth investigation of central Anatolia, Turkey. Pure and Applied Geophysics 162(2), 357–371.

Aydemir, A., Bilim, F., Koşaroğlu, S., Büyüksaraç, A. 2019. Thermal structure of the Cappadocia region, Turkey: a review with geophysical methods. Mediterranean Geoscience Reviews 1(2), 243–254.

Baba, A., Yiğitbaş, E., Ertekin, C. 2010. Hydrogeochemistry of geothermal resources in the eastern part of Turkey: A Case study, Varto Region. International World Geothermal Congress 2010, International Geothermal Association.

Barka, A. 1985. Kuzey Anadolu Fay zonundaki bazı Neojen-Kuvaterner havzalarının jeolojisi ve tektonik evrimi. Ketin Sempozyumu Kitabı, Türkiye Jeoloji Kurumu, 209-227, Ankara.

Başel, E. D. K., Satman, A. Serpen, U. 2013. Türkiye'nin tahmini yeraltı sıcaklık haritaları. II. Ulusal Tesisat Kongresi, 17 Nisan 2013, İzmir, 37-44.

Bektaş, Ö., Ravat, D., Büyüksaraç, A., Bilim, F., Ateş, A. 2007. Regional geothermal characterization of East Anatolia from aeromagnetic, heat flow, and gravity data. Pure Applied Geophysics 164(5), 975–998.

Beyazpirinç, M., Akçay, A. E., Özkan, M. K., Sönmez, M. K., Dönmez, M. 2022. The new age data and pre-Paleogene stratigraphy of the Kırşehir Massif, Central Anatolia. Bulletin of The Mineral Research and Exploration 167, 1-23.

Bilim, F., Koşaroğlu, S., Aydemir, A., Büyüksaraç, A. 2017. Thermal investigation in the Cappadocia Region, Central Anatolia-Turkey, analyzing curie point depth, geothermal gradient, and heat-flow maps from the aeromagnetic data. Pure and Applied Geophysics 174(12), 4445–4458.

Bilim, F., Aydemir, A., Koşaroglu, S., Bektaş, O. 2018. Effects of the Karacadag Volcanic Complex on the thermal structure and geothermal potential of southeast Anatolia. Bulletin of Volcanology 80(6), 1-16.

Bozkurt, E. 2001. Neotectonics of Turkey – a synthesis. Geodinamica Acta 14(1-3), 3-30.

Brown, D. W. 2009. Hot dry rock geothermal energy: Important lessons from Fenton Hill. Proceedings of Thirty-Fourth Workshop on Geothermal Reservoir Engineering, Stanford University.

Chatalov, G. 1988. Recent developments in the geology of the Strandzha Zone in Bulgaria. Bulletin of the İstanbul Technical University of İstanbul 41, 433-465.

Çırmık, A. 2018. Examining the crustal structures of eastern Anatolia, using thermal gradient, heat flow, radiogenic heat production and seismic velocities (Vp and Vs) derived from curie point depth. Bollettino di Geofisica Teorica ed Applicata 59(2), 117–134.

Çiçek, A. 2020. The electric power production targeted unconventional geothermal systems (UGS), some conceptual designs, and their thermodynamics classification. Bulletin of The Mineral Research and Exploration 163(163), 211-228.

Duchane, D., Brown, D. 2002. Hot dry rock (HDR) geothermal energy research and development at Fenton Hill, New Mexico. Geo-Heat Centre Quarterly Bulletin 23, 13–19.

Erkan, K. 2015. Geothermal investigations in western Anatolia using equilibrium temperatures from shallow boreholes. Solid Earth 6(1), 103–113.

Görür, N. 1997. Cretaceous syn- to post-rift sedimentation on the southern continental margin of the Western Black Sea basin. Robinson, A. G. (Ed.). Regional and petroleum geology of the Black Sea and the surrounding region. AAPG Memoir no. 68, 227-240.

Görür, N., Elbek, Ş. 2013. Tectonic events responsible for shaping the Sea of Marmara and its surrounding region, Geodinamica Acta 26(1-2), 1-11.

Görür, N., Okay, A. I. 1996. A fore-arc origin for the Thrace Basin, NW Turkey. International Journal of Earth Science (Geol. Rundschau) 85, 662–668.

Görür, N., Tüysüz, O. 2001. Cretaceous to Miocene palaeogeographic evolution of Turkey: Implications for hydrocarbon potential. Journal of Petroleum Geology 24(2), 119–146.

Görür, N., Monod, O., Okay, A. I., Şengör, A. M. C., Tüysüz, O., Yiğitbaş, E., Sakınç, M., Akkök, R. 1997. Palaeogeographic and tectonic position of the Carboniferous rocks of the western Pontides (Turkey) in frame of the Variscan belt. Bulletin de la Société Géologique de France 168(2), 197-205.

Görür, N., Oktay, F. Y., Seymen, I. Şengör, A. M. C. 1984. Paleotectonic evolution of the Tuzgölü basin complex, Central Turkey: Sedimentary record of a Neo-Tethyan Closure. Geological Society of London Special Publication 17, 467–482.

Görür, N., Sakınç, M., Barka, A., Akkök, R. Ersoy, Ş. 1995*a*. Miocene to Pliocene palaeogeographic evolution of Turkey and its surroundings. Journal of Human Evolution 28(4), 309-324.

Görür, N., Şengör, A., Sakınç, M., Akkök, R., Yiğitbaş, E., Oktay, F. Y., Barka, A., Sarıca, N., Ecevitoğlu, B., Demirbağ, E., Ersoy, Ş., Algan, O., Güneysu, C., Aykol, A. 1995*b*. Rift formation in the Gökova region, southwest Anatolia: Implications for the opening of the Aegean Sea. Geological Magazine 132(6), 637-650.

Görür, N., Tüysüz, O., Şengör, A. M. C. 1998. Tectonic evolution of the Central Anatolian Basins. International Geology Review 40(9), 831-850.

Güner, Y. 1984. Nemrut Yanardağı' nın jeolojisi, jeomorfolojisi ve volkanizmasının evrimi. Jeomorfoloji Dergisi 12, 23-65.

Gürer, Ö. F., Kaymakçı, N., Çakır, Ş., Özburan, M. 2003. Neotectonics of the southeast Marmara region, NW Anatolia, Turkey. Journal of Asian Earth Sciences 21, 1041–1051.

Helvacı, C. 1995. Stratigraphy, mineralogy, and genesis of the Bigadiç borate deposits, Western Turkey. Economic Geology 90, 1237-1260.

Hempton, M. R., Dunne, L. A., Dewey, J. F. 1983. Sedimentation in an active strike-slip basin, southeastern Turkey. Journal of Geology 91, 401–412.

Hippolyte, J. C., Espurt, N., Kaymakçı, N., Sangu, E., Müller, C. 2016. Cross-sectional anatomy and geodynamic evolution of the Central Pontide orogenic belt (northern Turkey). International Journal of Earth Science (Geol Rundsch) 105, 81–106.

Irrlitz, W. 1972. Lithostratigraphische und tektonische Entwicklung des Neogens in Nordost-Anatolien. Schweizerbart and Borntraeger Science Publishers, 120.

Kıyak, A., Karavul, C., Gülen, L., Pekşen, E., Kılıç, A. R. 2015. Assessment of geothermal energy potential by geophysical methods: Nevşehir region, Central Anatolia. Journal of Volcanology and Geothermal Research 295, 55–64.

Korkmaz, E. D., Serpen, U., Satman, A. 2014. Geothermal boom in Turkey: Growth in identified capacities and potentials. Renewable Energy 68, 314–325.

Kwaya, M., Kurowska, E., Bata, T. 2019. Geothermal Exploration in Nigeria. Proceedings World Geothermal Congress, 25-29 April 2010 Bali, Indonesia.

Maden, N. 2012. Two-Dimensional geothermal modelling along the Central Pontides Magmatic Arc: Implications for the geodynamic evolution of Northern Turkey. Surveys in Geophysics 33, 275–292.

Mamontov, V. K., Yakovlev, A. G., Bayraktutan, S. M. 2005. Formation of the geothermal resources of the north-eastern part of Turkey. Proceedings World Geothermal Congress, 24-29 April 2005, Antalya, 24–29.

Miranda-Barbosa, E., Sigfússon, B., Carlsson, J., Tzimas, E. 2017. Advantages from combining CCS with geothermal energy. Energy Procedia 114, 6666–6676.

Moore, W. J., Mckee, E. H., Akıncı, Ö. 1980. Chemistry and chronology of plutonic rocks in the Pontide Mountains, northern Turkey. European Copper Deposits, 209–216.

Mortensen, J. 1978. Hot dry rock: a new geothermal energy source. Energy 3(5), 639-644.

MTA Geothermal Map. https://www.mta.gov.tr/en/arastirmalar/jeotermal-enerji-arastirmalari. September 1, 2022

Mutlu, H., Güleç, N. 1998. Hydrogeochemical outline of thermal waters and geothermometry applications in Anatolia (Turkey). Journal of Volcanology and Geothermal Research 85, 495–515.

Nwankwo, C. N., Ekine, A. S. 2009. Geothermal gradients in the Chad Basin, Nigeria from bottom hole temperature logs. International Journal of Physical Sciences 4, 777–783.

Okay, A. I. 1984. Distribution and characteristics of the northwest Turkish blueschists. The Geological Evolution of the Eastern Mediterranean. Geological Society Special Publication 17, 455-466.

Okay, A. I. 2008. Geology of Turkey: A Synopsis. Anschnitt 21, 19-42

Okay, A. I., Siyako, M., Bürkan, K. A. 1991. Geology and tectonic evolution of the Biga Peninsula. Special Issue on Tectonics. Bulletin of the Technical University of Istanbul 44, 191-255.

Okay, A. I., Şengör, A. M. C., Görür, N. 1994. Kinematic history of the opening of the Black Sea and its effect on the surrounding regions. Geology 22, 267-270.

Okay, A. I., Satır, M., Maluski, H., Siyako, M., Monie, P., Metzger, R., Akyüz S. 1996. Paleo- and Neo-Tethyan events in northwest Turkey: geological and geochronological constraints. Cambridge University Press, Cambridge, 420-441.

Okay, A. I., Satır, M., Tüysüz, O., Akyüz, S., Chen, F. 2001. The tectonics of the Strandja Massif: Late-Variscan and mid-Mesozoic deformation and metamorphism in the Northern Aegean. International Journal of Earth Sciences 90, 217–233.

Okay, A. I., Monod, O., Monié, P. 2002. Triassic blueschists and eclogites from northwest Turkey: Vestiges of the Palaeo- Tethyan subduction. Lithos 64, 155–178.

Okay, A. I., Tüysüz, O., Satır, M., Özkan-Altıner, S., Altıner, D., Sherlock, S., Eren, R. H. 2006. Cretaceous and Triassic subduction-accretion, HP/LT metamorphism and continental growth in the Central Pontides, Turkey. Geological Society of America Bulletin 118, 1247-1269.

Özgül, N. 1984. Stratigraphy and tectonic evolution of the Central Taurides. Tekelti, O., Göncüoglu, C. (Ed.). Geology of the Tauride belt. General Directorate for Mineral Research and Exploration (MTA) Ankara. Special Publication, 77–90.

Özgür, N. 2002. Geochemical signature of the Kızıldere Geothermal Field, Western Anatolia, Turkey. International Geology Review 44, 153–163.

Pasvanoğlu, S., Çelik, M. 2019. Hydrogeochemical characteristics and conceptual model of Çamlıdere low temperature geothermal prospect, northern Central Anatolia. Geothermics 79, 82–104.

Pazvantoğlu, E. B., Erkan, K., Şalk, M., Akkoyunlu, B. O., Tayanç, M. 2021. Surface heat flow in Western Anatolia (Türkiye) and implications to the thermal structure of the Gediz Graben. Turkish Journal of Earth Sciences 30(9), 991-1007.

Poisson, A., Guezou, J. C., Ozturk, A., Inan, S., Temiz, H., Gürsöy, H., Kavak, K. S., Özden, S. 1996. Tectonic setting and evolution of the Sivas Basin, Central Anatolia, Turkey. International Geology Review 38, 838-853.

Rybach, L. 2010. Status and prospects of geothermal energy. Proceedings World Geothermal Congress 2010 Indonesia 25-29 April 2010, Bali, 1-5.

Saemundsson, K., Axelsson G., Steingrímsson, B. 2009. Geothermal systems in a global perspective. Surface exploration for geothermal resources short course organized by UNU-GTP and LaGeo. United Nations Geothermal Training Programme, 1-14.

Serpen, U., Çobanoğlu, M., Korkmaz, E. D., Demirkıran, Z., Kılınç, G. 2022. Assessment of geothermal power potential in the Gediz Basin, Turkey. Geothermics 105(102495), 1-12.

Seymen, İ. 1975. Kelkit vadisi kesiminde Kuzey Anadolu Fay Zonu' nun tektonik özelliği. PhD Thesis, İTÜ, 198, İstanbul (unpublished).

Seymen, İ. 1983. Tectonic features of the Kaman Group in comparison with those of its neighbouring formations around Tamadağ (Kaman-Central Anatolian Crystalline Complex). Türkiye Jeoloji Kurumu Bülteni 26, 89-98.

Siyako, M., Huvaz, O. 2007. Eocene stratigraphic evolution of the Thrace Basin, Turkey. Sedimentary Geology 198, 75–91.

Stefansson, V. 2000. The renewability of geothermal energy. Proceeding World Geothermal Congress, Kyush-Tohoku, 883–888.

Sunal, G., Natal'in, B. A. Satır, M., Toraman, E. 2006. Paleozoic magmatic events in the Strandja Massif, NW Turkey. Geodinamica Acta 19(5), 283-300.

Şaroğlu, F., Güner, Y. 1981. Doğu Anadolu'nun jeomorfolojik gelişimine etki eden ögeler: jeomorfoloji, tektonik, volkanizma ilişkileri. Türkiye Jeoloji Kurultayı Bülteni 2(24), 119-130.

Şaroğlu, F., Yılmaz, Y. 1986. Doğu Anadolu' da neotektonik dönemdeki jeolojik evrim ve havza modelleri. Bulletin of the Mineral Research and Exploration 107, 73-94.

Şener, M. F., Baba, A. 2019. Geochemical and hydrogeochemical characteristics and evolution of Kozaklı geothermal fluids, Central Anatolia, Turkey. Geothermics 80, 69–77.

Şengör, A. M. C. 1979. The North Anatolian Transform Fault: Its age, offset, and tectonic significance. Journal of the Geological Society London 13, 268-282.

Şengör, A. M. C. 1980. Türkiye'nin neotektoniğinin esasları. TJK Konferans Serisi, 2, 40.

Şengör, A. M. C., Yılmaz, Y. 1981. Tethyan evolution of Turkey: A plate tectonic approach. Tectonophysics 75, 181-241.

Şengör, A. M. C., Yılmaz, Y., Ketin, İ. 1980. Remnants of a pre–Late Jurassic ocean in northern Turkey: Fragments of Permian-Triassic Paleo-Tethys? GSA Bulletin 91(10), 599–609.

Şengör, A. M. C., Yılmaz, Y., Ketin, İ. 1982. Remnants of a pre-Late Jurassic ocean in northern Turkey: Fragments of Permian-Triassic Paleo-Tethys: Reply. Geological Society of America Bulletin 93, 932–936.

Şengör, A. M. C., Satır, M., Akkök, R. 1984. Timing of tectonic events in the Menderes Massif, western Turkey: Implications for tectonic evolution and evidence for pan-African basement in Turkey. Tectonics 3(7), 693-707.

Şengör, A. M. C., Görür, N., Şaroğlu, F. 1985. Strike-slip faulting and related basin formation in zones of tectonic escape: Turkey as a case study. Biddle, K. T., Christie-Blick N. (Ed.). Strike-Slip Deformation, Basin Formation, and Sedimentation Society of Economic Paleontologists and Mineralogists Special Publication, Tulsa, 37, 227-264.

Şengör, A. M. C., Tüysüz, O., İmren, C., Sakinç, M., Eyidoğan, H., Görür, N., Le Pichon, X., Rangin, C. 2005. The North Anatolian Fault: A new look. Annual Review of Earth and Planetary Sciences 33, 37–112.

Şimşek, S. 1985. Present status and future developments of the Denizli- Kızıldere Geothermal Field of Turkey. International Symposium on Geothermal Energy, Hawaii, 203-210.

Şimşek, S. 2003. Present status and future development possibilities of Aydın- Denizli Geothermal Province. International Geothermal Conference, September 2003, Reykjavík, 11–16.

Tatar, Y. 1975. Tectonic structures along the North Anatolian fault zone, northeast of Refahiye (Erzincan). Tectonophysics 29, 401-409.

Tatar, Y. 1978. Kuzey Anadolu Fay Zonu'nun Erzincan-Refahiye arasındaki bölümü üzerinde tektonik incelemeler. Hacettepe Üniversitesi Yerbilimleri 4, 201–236.

Temizel, E. H., Gültekin, F., Ersoy, A. F., Gülbay, R. K. 2021. Multi-isotopic (O, H, C, S, Sr, B, Li) characterization of waters in a low-enthalpy geothermal system in Havza (Samsun), Türkiye. Geothermics 97, 1-14.

Tüfekçi, N., Süzen, M. L., Güleç, N. 2010. GIS based geothermal potential assessment: a case study from Western Anatolia, Turkey. Energy 35(1), 246-261.

Tüysüz, O. 2022. Geology of the Kurucaşile – Cide region, NW Türkiye. Bulletin of the Mineral Research and Exploration 167(167), 149 – 178.

Ulusoy, I., Labazuy, P., Aydar, E., Ersoy, O., Çubukçu, E. 2008. Structure of the Nemrut caldera (Eastern Anatolia, Turkey) and associated hydrothermal fluid circulation. Journal of Volcanology and Geothermal Research 174, 269–283.

Ustaömer, P. A., Mundil, R., Renne, P. R. 2005. U/Pb and Pb/Pb zircon ages for arc-related intrusions of the Bolu Massif (W Pontides, NW Turkey): Evidence for Late Precambrian (Cadomian) age. Terra Nova 17, 215–223.

Whitney, D. L. Hamilton, M. A. 2004. Timing of high-grade metamorphism in central Turkey and the assembly of Anatolia. Journal of the Geological Society 161, 823 – 828.

Yalçın, M. N., Görür, N. 1984. Sedimentological evolution of Adana Basin. Tekeli, O., Göncüoğlu, M. C. (Ed.). Proceedings of the International Symposium on the Geology of the Taurus Belt 26-29 September 1983, Ankara, 165-172.

Yalınız, M. K., Göncüoğlu, M. C., Özkan-Altıner, S. 2000. Formation and emplacement ages of the SSZ-

type Neotethyan ophiolites in Central Anatolia, Turkey: Palaeotectonic implications. Geological Journal 35, 53–68.

Yapmış, J., Güleç, N., Karahanoğlu, N. 2005. Geothermal fields along the North Anatolian Fault Zone (NAFZ): assessment of geothermal potential. Proceedings World Geothermal Congress, 24–29 April 2005, Antalya, 1-9.

Yılmaz, O., Boztuğ, D. 1986. Kastamonu granitoid belt of northern Turkey: First arc plutonism product related to the subduction of the paleo-Tethys. Geology 14(2), 179–183.

Yılmaz, Y. 1997. Geology of western Anatolia. Schindler, C., Pfisher M. (Ed.). Active Tectonics of Northwestern Anatolia–The Marmara Polyproject. vdf Hochschulverlag AG an der ETH, Zürich, 31-53.

Yılmaz, Y., Genç, Ş. C., Karacık, Z. Altunkaynak, E. 2001. Two contrasting magmatic associations of NW Anatolia and their tectonic significance. Journal of Geodynamics 31, 243-271.

Bull. Min. Res. Exp. (2023) 171: 123-142

Bulletin of the Mineral Research and Exploration

http://bulletin.mta.gov.tr

Geothermal gradient variation in the Büyük Menderes Graben: implications for geothermal potential of the graben, Western Anatolia, Türkiye

Adrian WIGGINS[a*] and İbrahim ÇEMEN[a]

[a]*University of Alabama, Department of Geological Sciences, Tuscaloosa, USA.*

Research Article

Keywords:
Extensional Terrane, Tectonics, 3D Model, Temperature Gradient Map, Leapfrog.

ABSTRACT

The Büyük Menderes Graben (BMG) is an E-W oriented active extensional geothermal basin within the Menderes Massif, a metamorphic core complex, in Western Anatolia, Turkey. 1500 (megawatts-energy) MWe of installed geothermal capacity for power production exist as of December 2019 in Western Anatolia, mostly generated in the BMG. While the BMG is a vastly producing geothermal resource, it is predicted that it has higher production potential. This study aims to a) quantitatively test the geothermal gradients in the Aydın-İncirliova-Osmanbükü Geothermal Field (IGF), and b) compare the IGF with a neighboring geothermal field. This study also aims to compare the IGF with a neighboring geothermal field. To complete this study, information from stratigraphic columns, bottom hole temperatures, and continuous temperature logs from 13 geothermal wells is utilized with Leapfrog Geothermal to create 3D models of the geology and subsurface temperature distribution. Then, isothermal contour maps of the field are created. The geologic modeling suggests that synextensional deposition has occurred within the graben. The temperature modeling suggests both that thermal breakthrough may have occurred in the field, and that the IGF has a higher geothermal gradient than the nearby Germencik Geothermal Field.

Received Date: 30.09.2022
Accepted Date: 05.05.2023

1. Introduction

The Büyük Menderes Graben (BMG) is an E-W oriented active extensional basin within the Menderes Massif, a metamorphic core complex, in Western Anatolia, Turkey. It is part of a graben system that includes the BMG and three smaller N-S oriented grabens, comprising nearly 2200 km^2 and extending about 140 km from the Aegean Sea in the west to the Denizli Graben (Figure 1) in the east (Özpolat et al., 2020). The three N-S oriented grabens are the Cine, Bozdoğan and Karacasu Grabens (Figure 1).

The BMG is a geothermal basin in the Western Anatolia Geothermal Province (Özgür and Çalışkan, 2013; Yamanlar et al., 2020). In total, 1500 (megawatts-energy) MWe of installed geothermal capacity for power production exist as of December 2019 in Western Anatolia, most of which is generated in the BMG (Yamanlar et al., 2020) from many geothermal power plants, from east to the west, Kızıldere, Pamukören, Salavatlı, Hüseyinciler, Yılmazköy and Germencik (Figure 2).

Faulds et al. (2010) proposed that the geothermal resources of the BMG are inherently linked to geodynamic and structural controls. For example, crustal-scale geoelectrical evidence suggests that extensional tectonics control the flow of geothermal

Citation Info: Wiggins, A., Çemen, İ. 2023. Geothermal gradient variation in the Büyük Menderes Graben: implications for geothermal potential of the graben. Bulletin of the Mineral Research and Exploration 171, 123-142. https://doi.org/10.19111/bulletinofmre.1293039

**Corresponding author: Adrian WIGGINS, aawiggins@crimson.ua.edu*

fluids utilizing both high and low-angle normal faults. Faulds et al. (2010) suggested that elevated heat flow results from fault termination splays, or horsetails, in the western section of the BMG. Alemdar (2015) suggested that asthenospheric material has risen beneath the eastern section of the BMG, which may be a regional source of heat (Figure 6). Yamanlar et al. (2020) noted that the geothermal gradient is variable throughout the BMG, with the highest gradient in the eastern section and the lowest in the middle of the graben (Figure 3). Tonkul et al. (2021) performed 3D reservoir temperature modeling of the Germencik Geothermal Field (GGF) in the western BMG, showing reservoir temperatures vary between 150-200°C. The reservoir temperatures for the middle of the graben have been reported to be between 169 °C–188 °C (Haklıdır and Şengün, 2020). However, the reason why the geothermal gradient differs so drastically throughout this region it not well understood.

This study will test the hypothesis that rising asthenospheric material and fault splays may contribute to the E-W geothermal gradient variability in the BMG. The models show the areas of high geothermal gradient, which indicate the areas with high geothermal potential. We will interpret the models based on geological and geophysical data to determine if there is a relationship between fault splays and geothermal gradient variability. The outcomes of this study will further our understanding of geothermal resource distribution in the BMG. This understanding can be applied to other active extensional terranes with major graben structures, such as the Basins and Range province in southwestern USA and will provide guidance for future geothermal energy investigation and development.

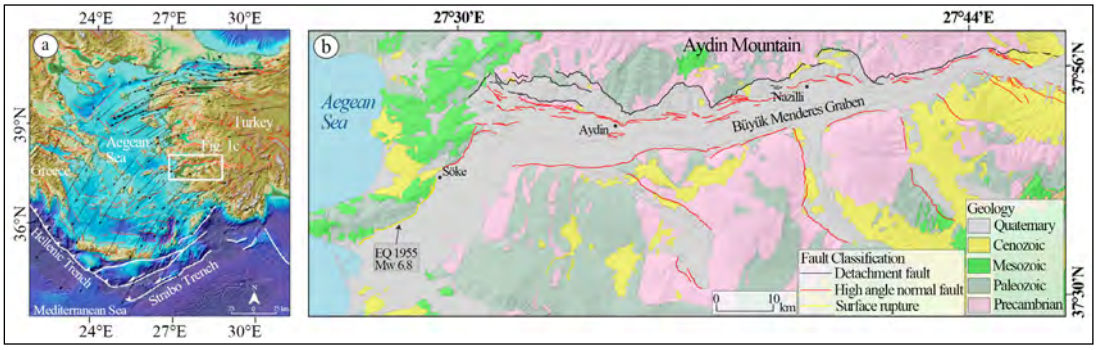

Figure 1- Western Anatolia maps showing the geology and relief of the BMG (Özpolat et al., 2020). a) Simplified active tectonic map of Western Anatolia and the Aegean Sea. b) Geological map of Aydın Mountain and the BMG.

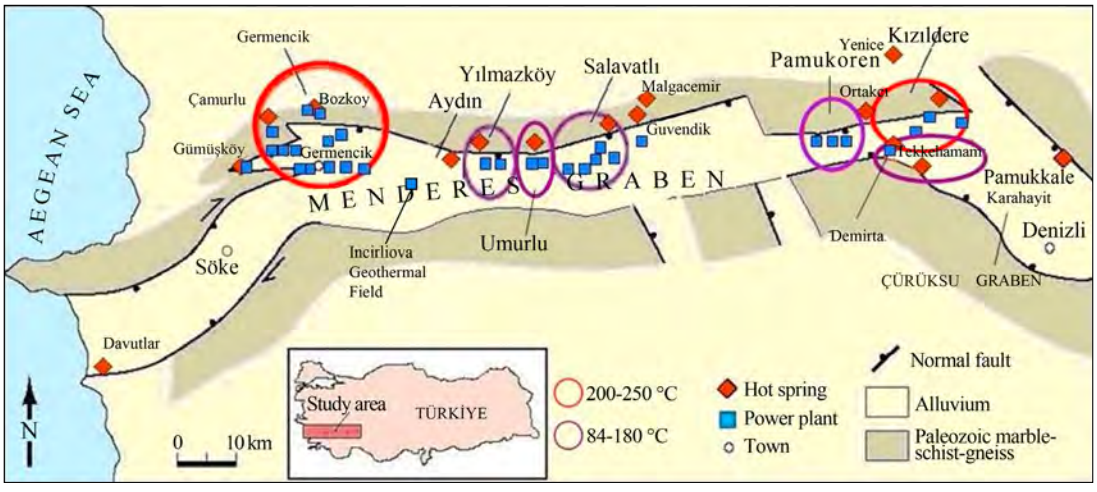

Figure 2- Map of power plants and hot springs in BMG (Modified from Faulds et al., 2010; Yamanlar et al., 2020). Temperatures indicated by circles represent the reservoir temperature range for each system.

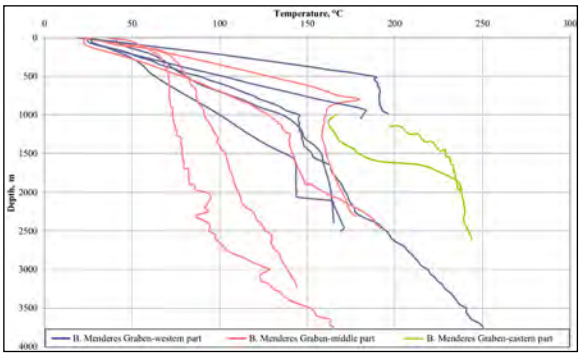

Figure 3- Geothermal gradients in the west, central, and eastern sections of the BMG (Yamanlar et al., 2020).

1.1. Statement of Problem

This study aims to use interpolation to model the 3D variation of geothermal gradient with respect to rock units present in the Incirliova Geothermal Field in the central section of the BMG and compare them to other models developed in different areas of the BMG.

The main objectives of this study are:

- To identify the regions of high temperature in the subsurface in the Incirliova Geothermal Field area within the BMG based on the interpretation of available well logs together with temperature logs;
- To develop a 3D model for the stratigraphy and temperature distribution of the Incirliova Geothermal Field;
- To develop isothermal contour maps at 50°C intervals for the Incirliova Geothermal Field area;
- To compare the 3D temperature model created using bottom hole temperatures with one that includes continuous temperature logs; and
- To compare the 3D temperature model of a centrally located Incirliova Geothermal Field to those in the western and the eastern parts of the BMG.

1.2. Methodology

We used well temperature measurements, well logs, and heat flow data with 3D modeling software to create spatial models of the BMG with respect to lithology and temperature. HD Energy Solutions acquired a variety of data for thirteen different geothermal wells from the Incirliova Geothermal Field (IGF) (Figure 4). Twelve of the wells included BHT information and were used for this study. Eleven of those wells

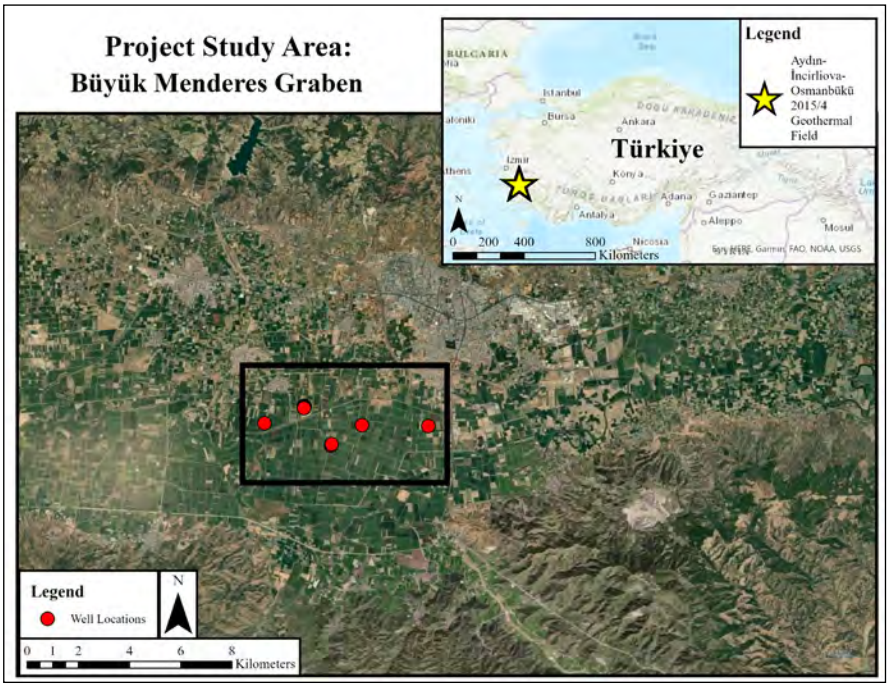

Figure 4- Location of study area and wells. The top right inset map shows the location of the BMG in Türkiye. The larger bottom map shows the generalized location of the IGF and thirteen wells used in this study. Some of the wells were drilled from the same platform, making their locations, provided in overlap on the map.

included stratigraphic columns. The twelve wells used in modeling are the following: Incirliova 1, Incirliova 2, Incirliova 3, Incirliova 4, Incirliova 5, Incirliova 6, Efeler-1, Batı Efeler-1, Incirliova Enjeksiyon-1, Incirliova Enjeksiyon-2, Incirliova Enjeksiyon-4, and Incirliova Enjeksiyon-5.

Seequent Leapfrog Geothermal software (Leapfrog) is used to develop the 3D models using the well data. The lithologic logs from the wells provided stratigraphic control for the geologic modeling. Temperature logs were used in addition to BHT to create a combined temperature model. These efforts estimated the basin geometry and stratigraphy within the IGF and the spatial temperature distribution in two different scenarios. The geometry, stratigraphy, and temperature distribution were then compared with other geothermal fields from the east and west sections of the BMG.

2. Main Text

2.1. Geologic Overview

2.1.1. Tectonic Evolution

The Western Anatolia Extended Terrane (WAET) is one of the best-developed examples of post-collisional extended terranes worldwide. It WAET, which includes BMG, is bounded by the North Anatolian Fault Zone to the north, by the Lycian nappes to the south and by the ENE-trending Southwest Anatolian Shear Zone (SWASZ) to the southeast.

Çemen et al. (2006) suggested that in the Cenozoic Era, Western Anatolia, Turkey experienced three consecutive stages of northward extension (Figure 5). Before the Cenozoic extension occurred, the Menderes massif formed from several events. First, the Pan African orogeny in Cambro-Ordovician time formed the core metamorphic rocks, then the Alpine orogeny from Mesozoic through Cenozoic time formed the overlying sequence of metamorphic rocks (Çemen et al., 2006). The first stage of the extension was initiated by orogenic collapse around 30 Ma in Late Oligocene time (Figure 5a and b). This extension initiated the SWASZ and the Gokova, Kale, and Tavas basins. During the second extension stage, beginning in the Early Miocene time, the Alaşehir and Büyük Menderes Grabens were formed (Figure 5c), likely due to the subduction roll-back of the Aegean subduction zone (Cemen et al., 2006). Geochronology using argon dating also suggests subduction roll-back has occurred in the WAET throughout the Miocene (Uzel et al., 2020). The third stage of the extension was initiated about 5 Ma ago in Late Miocene to the Early Pliocene time, when the westward escape of the Anatolian Plate started, and generated high angle oblique-slip normal faults in the graben (Figure 5d). Based on gravity modeling, Alemdar (2015) and Mahatsente et al. (2017) have suggested that the asthenospheric material has risen through the lithosphere up to the mantle-crust interface beneath the BMG at 29°E (Figure 5). Recent studies have suggested that the BMG evolved from a supra-detachment basin in the Miocene to a rift basin in the Pliocene and Quaternary using a rolling-hinge model for basin evolution (Sümer et al., 2020).

2.1.2. Stratigraphy

Three main rock groups in the BMG (Figure 7) are the Pre-Neogene basement rocks, Neogene sedimentary units, and Quaternary deposits (Sert, 2015). The basement rocks are high-grade metamorphic rocks such as marble, gneiss, and schist (Cemen et al., 2006). The sedimentary rock units include three successions that unconformably overly each other (Cohen et al., 1995; Bozkurt, 2000; Göğüş, 2004; Şen and Seyitoğlu, 2009): the Early-Middle Miocene Başçayır, the Late Miocene Aydın, and the Pliocene Huseyinciler formations (Sert, 2015; Merey, 2016). Unconformably overlying these sedimentary rock formations is the Quaternary Hamzali Formation (Kazancı et al., 2009).

Pre-Neogene Metamorphic Basement Rocks

The Pre-Neogene metamorphic basement rocks of the BMG (Figure 7) consist of metamorphic rocks of the Menderes Metamorphic Core Complex (MMCC). These rocks were exhumed due to extensional tectonics in the region (Seyitoğlu et al., 2002; Çemen et al., 2006; Gessner et al., 2013). It is suggested that the fractures in these metamorphic rocks provide the heat exchange necessary to achieve the high temperatures observed in the region (Faulds et al., 2010). Roche et al. (2019) suggested that some marble is karst, which provides pockets of geothermal fluids.

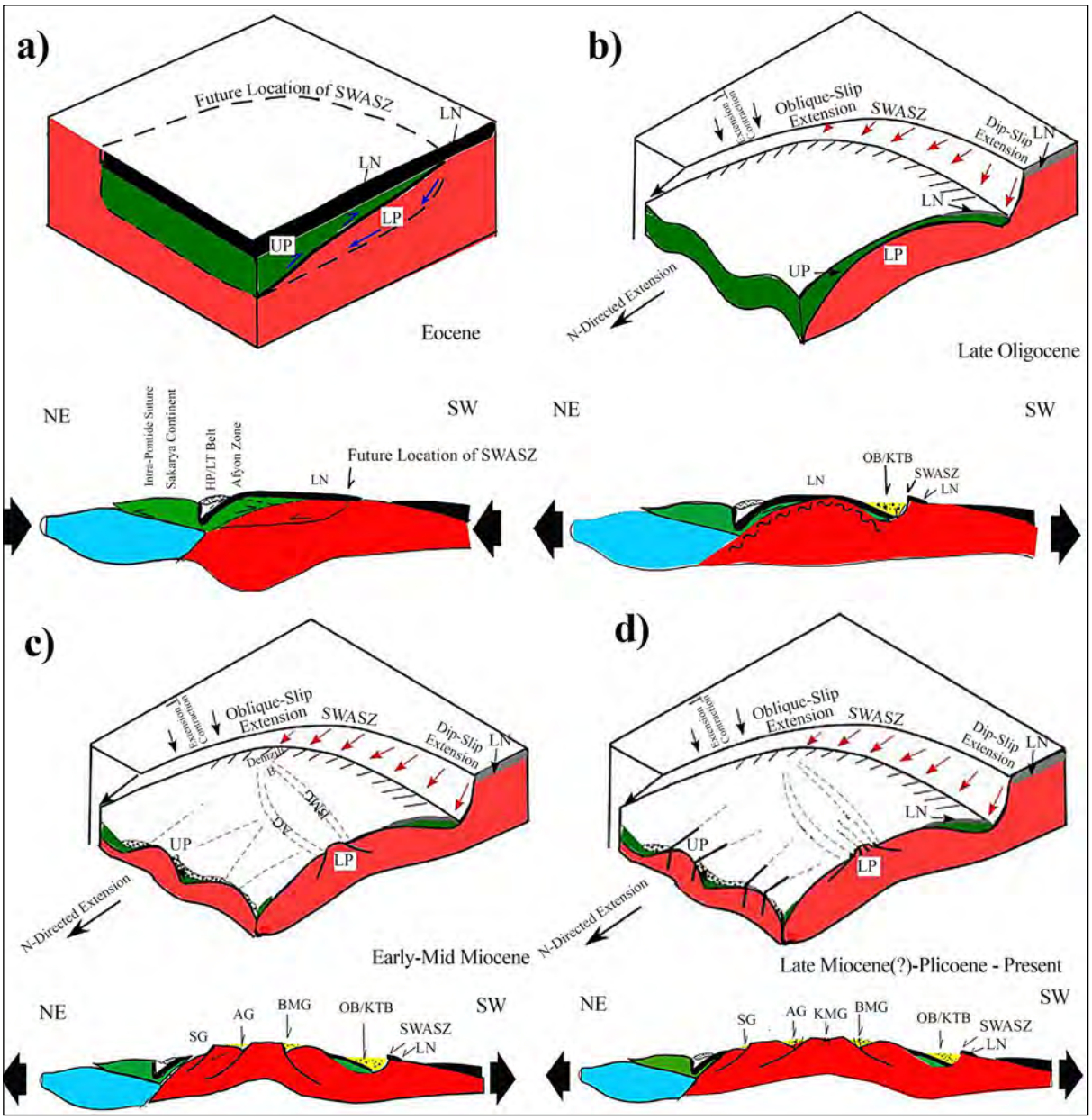

Figure 5- 3D cartoons and related schematic cross-sections (modified from Seyitoğlu et al., 2004; Sert, 2015) displaying the proposed three-stage extensional model of the Cenozoic evolution of Western Türkiye in a) Eocene, b) Late Oligocene, c) Early to Middle- Miocene and d) Late Miocene-Pliocene to present (not to scale). Abbreviations: AG: Alaşehir Graben; BMG: Büyük Menderes Graben; OB/KTB: Ören and Kale-Tavas basins; KMG: Kucuk Menderes Graben; LN: Lycian nappes; LP: lower plate; SG: Simav graben; SWASZ: Southwest Anatolian shear zone; UP: upper plate (from Çemen et al., 2006).

Başçayır Formation

The Başçayır Formation is the oldest syn-extensional sedimentary sequence (early-middle Miocene) in the BMG (Çifçi et al., 2011). There is an unconformable boundary between the Başçayır Formation and the metamorphic basement rocks. The base of the unit is conglomerate and overlain by a shale-dominated sequence that is laterally filled with alluvial fan deposits (Cohen et al., 1995).

Aydın Formation

The Aydın Formation (late Miocene) consists of a coarse-grained conglomerate with interbedded layers of sandstone, mudstone, and claystone (Bozkurt,

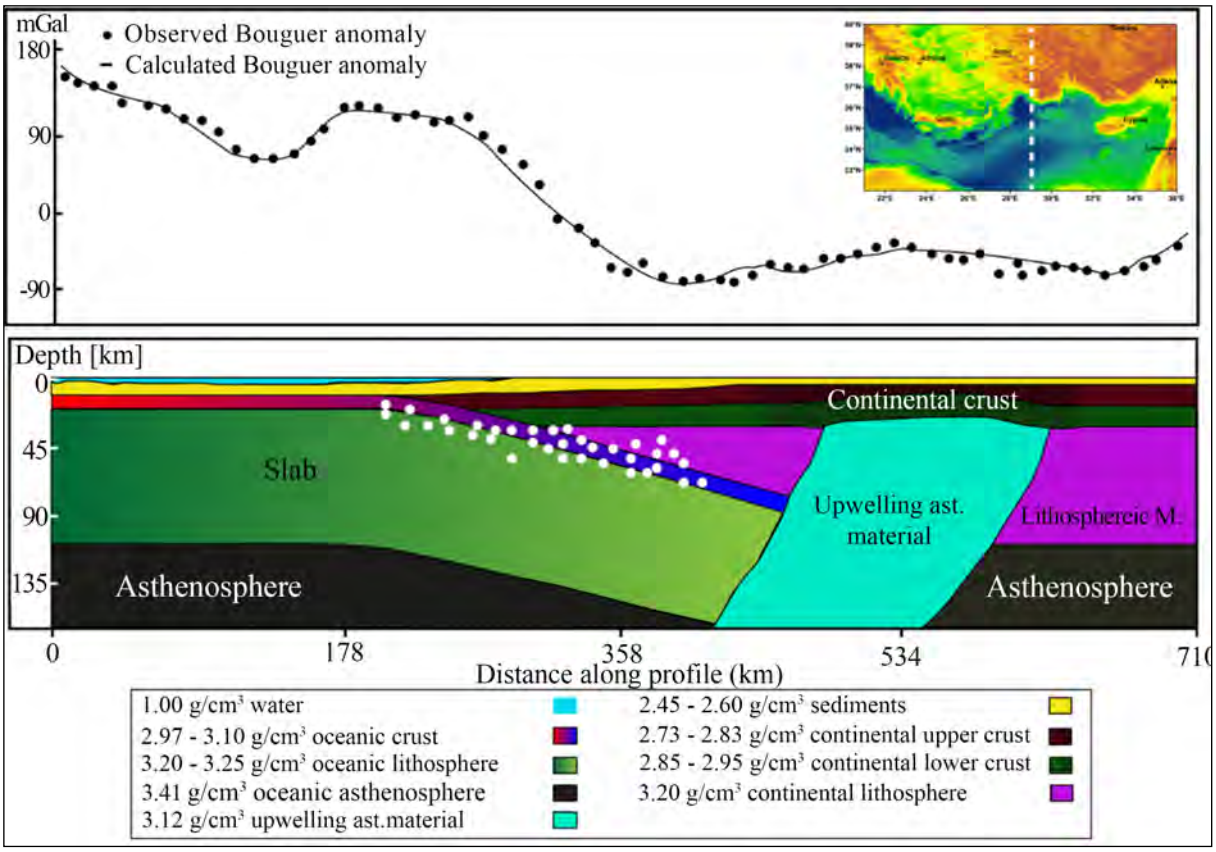

Figure 6- 2.5-D gravity model along a north-south transect at 29°E (Alemdar, 2015; Mahatsente et al., 2017). The upwelling asthenospheric material is underneath the BMG.

2000; Şen and Seyitoğlu, 2009). The clastic sediments in this formation were sourced from the Menderes Metamorphic Core Complex rocks and the rocks of the underlying Başçayır formation. The Aydın Formation was also deposited syn-extensionally (Sert, 2015). Sert, 2015, interpreted N-S oriented seismic reflection cross sections of the BMG and showed that the Aydın Formation is thicker in the center and gradually thinner towards the north and south edges. This is also evident in the cross section (Figure 10) published by Lovekin et al. 2019.

Hüseyinciler Formiation

The Huseyinciler Formation (Pliocene) consists of alluvial and fluvial clastic rocks, namely poorly-sorted conglomerates in a clay matrix with interbedded sandstone and mudstone (Yılmaz et al., 2000).

Quaternary Alluvium (Hamzalı Formation)

The Quaternary Hamzalı Formation consists of alluvial fan deposits and modern clastic sediments commonly found along the northern boundary of the BMG. The Büyük Menderes River carries the clastic sediments from east to west in the BMG. This succession is thicker in the east and mostly consists of mud and muddy sand (Kazancı et al., 2009; Çiftçi and Bozkurt, 2010).

2.1.3. Structural Geology

The BMG is the largest active graben in Western Anatolia. It has been proposed that the BMG formed by normal faulting along the main graben bounding fault, the Büyük Menderes Detachment, that is south-dipping and located along the northern side of the graben (Çemen et al., 2006; Şen and Seyitoğlu, 2009). The modern Büyük Menderes Detachment is low-angle, but kinematic evolution studies suggest it originally formed at a high angle (Merey, 2016). Continuous motion along the detachment is suggested to be responsible for the thicker syn-depositional sequences found in the center of the graben, which thin towards the north and south (Yılmaz et al., 2000;

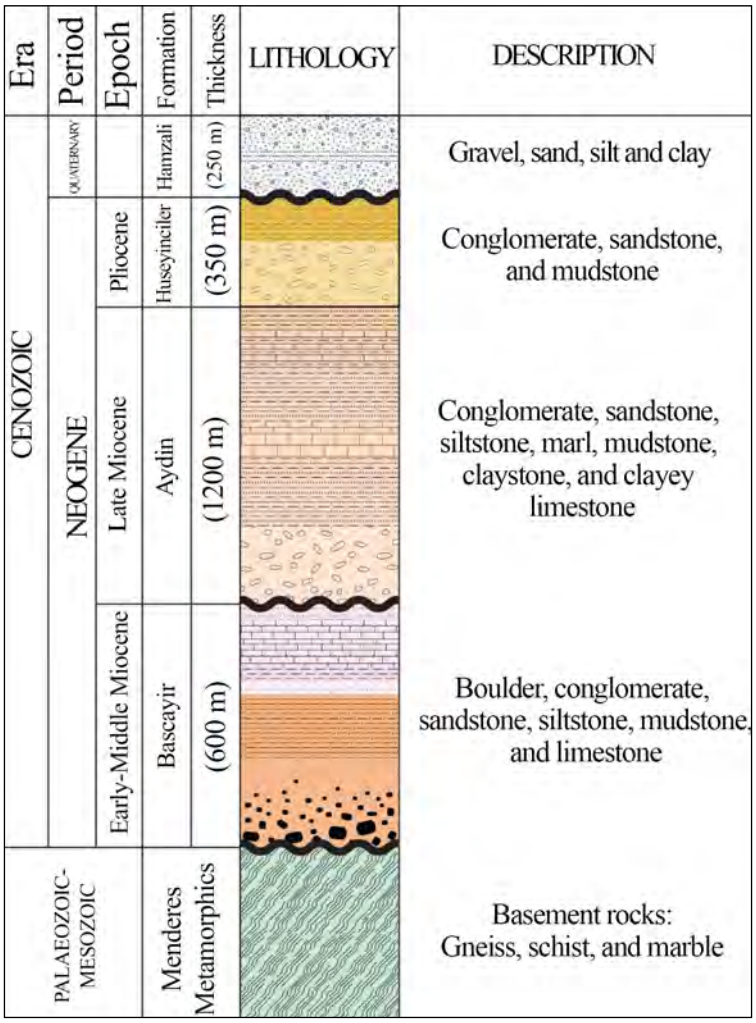

Figure 7- Generalized stratigraphy of the BMG (modified from Sert, 2015).

Seyitoğlu et al., 2004; Çemen et al., 2006; Sen and Seyitoğlu, 2009; Sert, 2015).

The low-angle graben detachment faults, initiated during the second stage of extension (Figure 5c), and high-angle normal faults, initiated during the third stage (Figure 5d), intersect at the interface between the Başçayır Formation and the basement rocks. It was previously thought that the BMG exhibited a rollover structure similar to that of the Alaşehir Graben north of the BMG (Seyitoğlu et al., 2004). Merey (2016) proposed new evidence suggesting that the BMG does not contain a rollover structure and was instead formed by active rifting. However, the origin of rifting remains to be not well understood.

Roche et al. (2019) performed a structural analysis of two geothermal fields in the BMG: the Germencik field in the west and the Salavatlı geothermal field in the east. Both of these geothermal fields are along the northern flank of the graben, near the main detachment fault. Faulds et al. (2009) analyzed the structure of the Germecik, Aydın, Yılmazköy, and the Kızıldere geothermal fields, and realized that they are found all along the northern detachment fault of the graben.

Faulds et al. (2010) suggested that within the Germencik geothermal field, horsetailing fault terminations exist in the basement rock (Figure 8), creating highly porous and permeable fractured rock that serves as reservoirs for geothermal fluids. The high surface areas of these reservoirs also allow high rates of heat transfer between the rock and the fluids. The faults then act as conduits for the fluids to return to the surface, where they may be utilized for geothermal energy production.

2.1.4. Heat Flow in the BMG

Roche et al. (2019) examined both a local-scale and basin-scale analysis of the geothermal activity in the BMG with respect to structural, lithological, and geodynamic controls. Based on oxygen, hydrogen, and helium isotopes studies of geothermal waters from the BMG, it has been suggested that the heat source of the BMG is not of magmatic origin (Roche et al., 2019). Instead, the source of heat in the BMG is shallow asthenospheric material at the interface with the crust. Geophysical surveys, including kinematic reconstruction and gravity surveys of the subsurface, also have suggested that there is a slab tear beneath the eastern portion of the BMG, which results in uplifting asthenosphere to the east (Figure 5) (Alemdar, 2015; Merey, 2016; Mahatsente et al., 2017).

2.1.5. Geothermal Fields in the BMG

Conventional geothermal systems require a source of high temperatures, reservoirs (permeable and porous lithology) with large quantities of hot fluids, a cap rock (impermeable lithology) above the reservoir, and a permeable pathway for fluid recharge (Roche et al., 2019). These conditions are all present in many areas in the BMG, which explains its geothermal potential and its numerous geothermal fields that are actively producing renewable clean energy. As of 2019, there were 27 operating geothermal fields in Western Anatolia, and 16 of those were in the BMG (Mertoğlu et al., 2019). Tonkul et al. (2021) conducted a case study of the Germencik Geothermal Field in the western BMG. They used numerical modeling to create a 3D distribution of the subsurface temperatures in the field (Figure 8). This study aims to similarly model a different geothermal field that corresponds to "Aydın-Incirliova Field" in Mertoğlu et al. (2019). This field will hereby be known as the Incirliova Geothermal Field (IGF).

2.1.6. Incirliova Geothermal Field

The IGF is ~7 km SE from the town of Incirliova, and ~7 km SW from the city of Aydın, and ~15 km SE from the Germencik Geothermal Field. The production, exploration and injection wells in this field are arranged in an overall E-W trend (Figure 4). The IGF is about halfway between the north and south margins of the BMG (Figures 1 and 9), which locates it in the western-central part of the graben, and far from the surface outcropping of either of the detachment faults of the BMG. The reservoir target of the drilling program was a fractured marble formation in the metamorphic basement (Lovekin et al., 2019). The IGF was developed by the company 3S Kale. A published seismic reflection profile of the field (Figure 10) shows that the northern faults dip southward and the southern faults dip northward (Lovekin et al., 2019), which is consistent with the interpretations of other reflection seismic profiles in the graben (Sert, 2015; Merey, 2016).

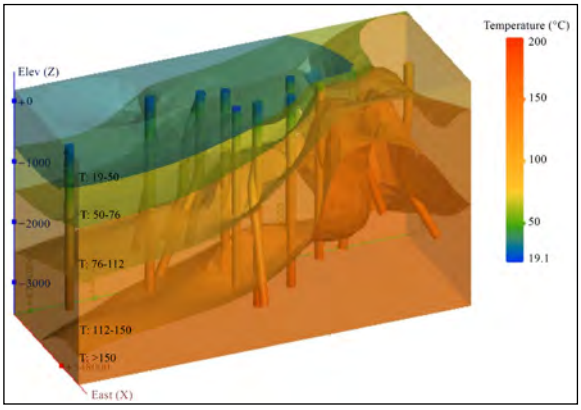

Figure 8- Numerical 3D temperature model of the Germencik Geothermal Field, facing SW (Tonkul et al., 2021).

2.2. Data

Data from thirteen geothermal wells drilled in Incirliova Geothermal Field were supplied by HD Energy Solutions for this study. Data provided with the wells included the name of well, date, name of the quadrangle, well coordinates at wellhead, coordinates at the total depth, depth in MD and TVD, the temperature at kelly bushing and at total depth (BHT), maximum discharge, and state of the well (production or injection). In addition, wireline logs (temperature and pressure), mud loss, and lithology logs were supplied for eleven wells. One of the wells, Osmanbükü-1 did not have BHT information. The dates provided with both the BHT and well log data span between 2015 and 2018, before the plant began operating in late 2018. This suggests that both data sets could be exploration data and that the BHT and temperature logs could be combined within one model. This is uncertain, however, and the BHTs could be production data instead.

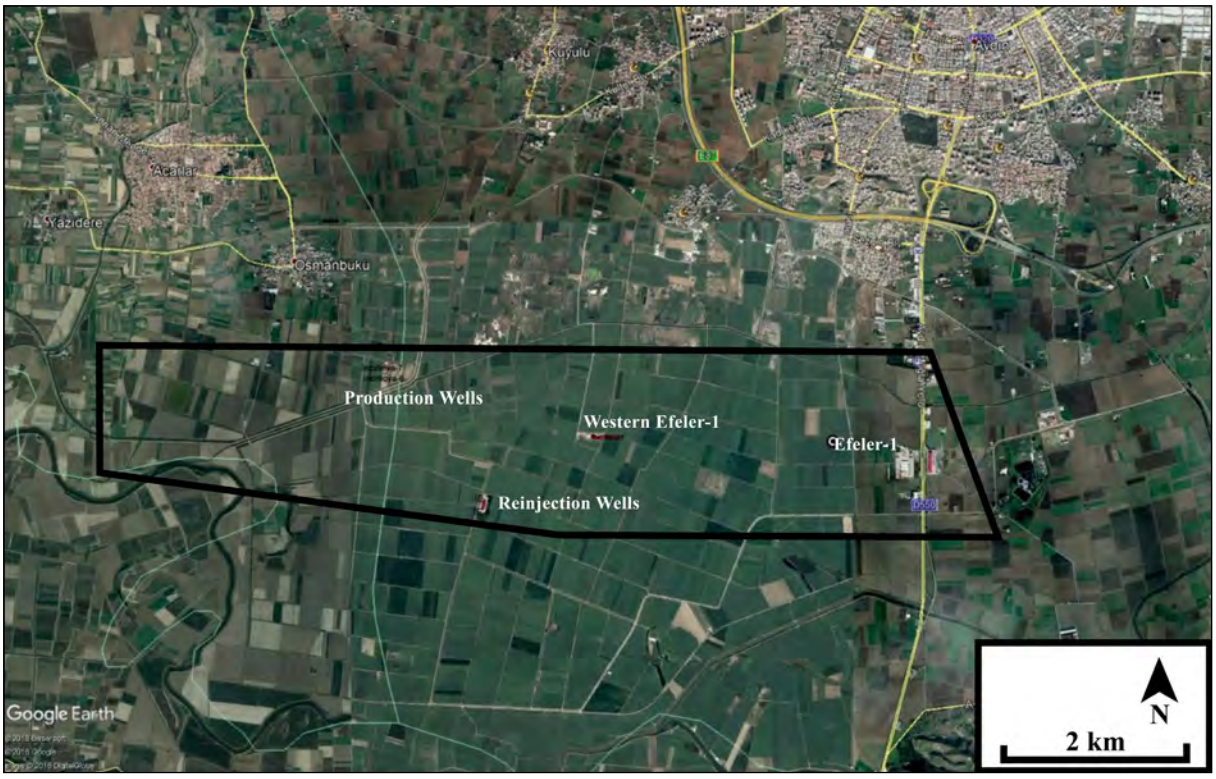

Figure 9- Location of the geothermal lease for the IGF (Modified from HD Energy Solutions).

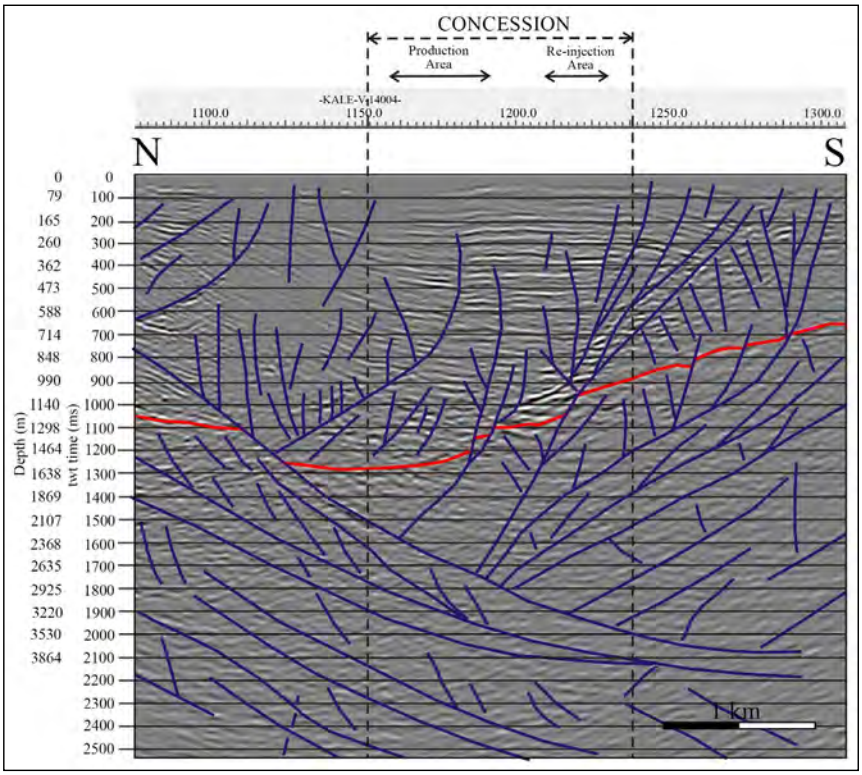

Figure 10- Seismic cross-section of the IGF, showing faults illustrated in the section. The red line represents the boundary between the Başçayır Formation and the basement metamorphics (Lovekin et al., 2019).

2.3. Modeling, Outputs, and Observations

The models generated for this study used Leapfrog Geothermal and ArcMap software. The wells were plotted in ArcMap to check their location. Once the locations of the wells were confirmed, the map was exported as a georeferenced image and imported into Leapfrog. The digital elevation model (DEM) data were constrained to a dataframe of the same size as the well location map and that was exported as raster images and imported into Leapfrog.

2.3.1. Well Deviation

The subsurface well data were prepared in file formats which were compatible with Leapfrog. This included converting XY coordinates of top and bottom of the well into spherical coordinates, so the 3D well deviation could be plotted in Leapfrog.

2.3.2. Temperature Data

The file formatting also included preparing the temperature data. To prepare the data for BHT interpolation, the average atmospheric surface temperature and the BHT were used. For each well, the average atmospheric temperature of the region, 18.2 °C, was assigned to the depth at 0 m, and the BHT was assigned as the temperature at total depth. The temperature logs were provided in graphical image format, so they first needed to be digitized into a numeric data set. To do so, the temperature logs were first upscaled to a higher resolution by tracing and redrawing in Adobe Illustrator. Then the online application Plot Digitizer was used to assign numeric values to the continuous data series for temperature.

2.3.3. Generating the Models

A workflow was derived to aid the completion of this study (Figure 11). Three models were prepared for the project once the files were loaded into Leapfrog. The geologic model was created first. It was constructed from youngest to oldest. This simultaneously preserves volume while honoring the boundaries of the model, the DEM, and the well data. Since no other independent geophysical data, such as 2D or 3D seismic lines, were available, the geologic models are not constrained by any additional information. The next two models were temperature models based on numeric modeling. The second model created was the BHT-driven temperature model. It was created using atmospheric surface temperature and BHT for each well, then interpolating the wells' temperatures in three dimensions. The third model used the five available continuous temperature logs and combined them with BHT data for any well without a temperature log. The interpolation method used to generate the numerical models was Radial Basis Function.

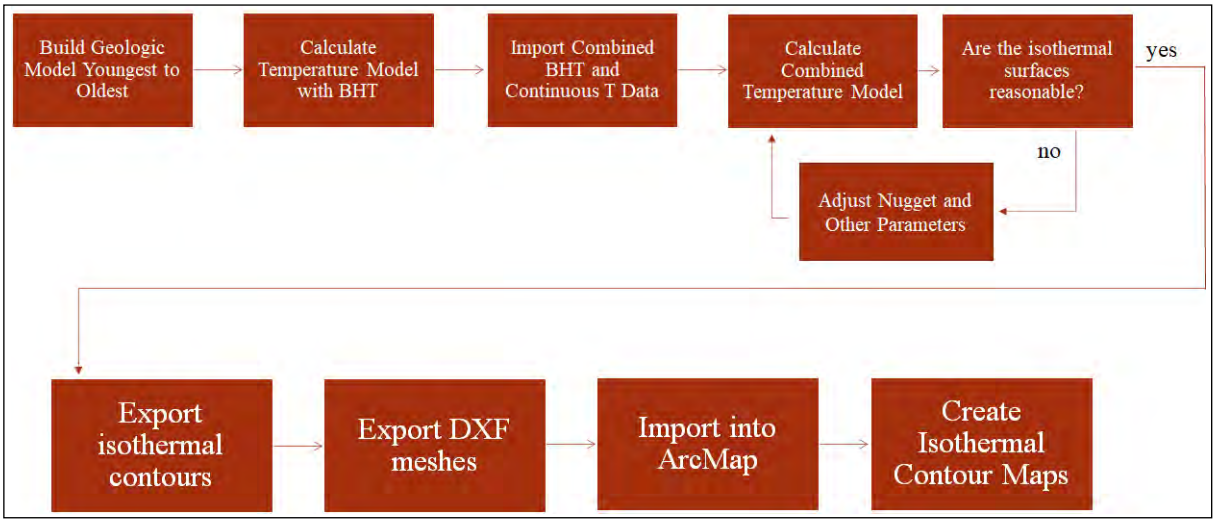

Figure 11- Modeling and contour map-making workflow.

2.3.4. Creating Isothermal Contour Maps

A combination of Leapfrog and ArcMap software was used to create the isothermal contour maps. Two main types of data were first exported from Leapfrog, then those files were used to construct the isothermal maps in ArcMap. First, the desired temperature model in Leapfrog was selected. Second, the "Isocontour" tab was selected and used to generate contour lines in shapefile format at 100 m intervals for the temperature isosurfaces in the model. Third, the same temperature isosurface was selected in Leapfrog and was used to export a mesh as a DXF file.

Fourth, a new project was started in ArcMap. The corresponding DXF file, and contour lines were imported for each isothermal contour map. The Spatial Analyst toolbox in ArcMap was used to create an elevation raster from the polyline mesh provided by the DXF file. The output raster was the subsurface elevation distribution at a given temperature. The raster was then assigned a reasonable color gradient to represent the depth distribution. Then, the isothermal contour lines were overlaid on the temperature and formatted as contour lines using the properties panel within the data layer in ArcMap. This is followed by a final map, created using Layout View in ArcMap. The process was repeated for each isothermal contour used in each temperature model.

2.4. Model Outputs and Observations

Each model of the Incirliova Geothermal Field (IGF) is bounded by a rectangular prism with the following dimensions: 7190 m in length, 2084 m in width, and 4320 m in depth. The unit used for the scale in each figure is in meters (m). All figures are true-to-scale.

2.4.1. Geologic Model

The observed lithologies of the wells were used as constraints to determine the geologic model. The wells are shown as 3D cylinders with the color-coded lithology according to the formation list in the figure (Figure 12). As stated in the stratigraphy section, the geologic model (Figure 12) includes the basement metamorphic rocks and the overlying

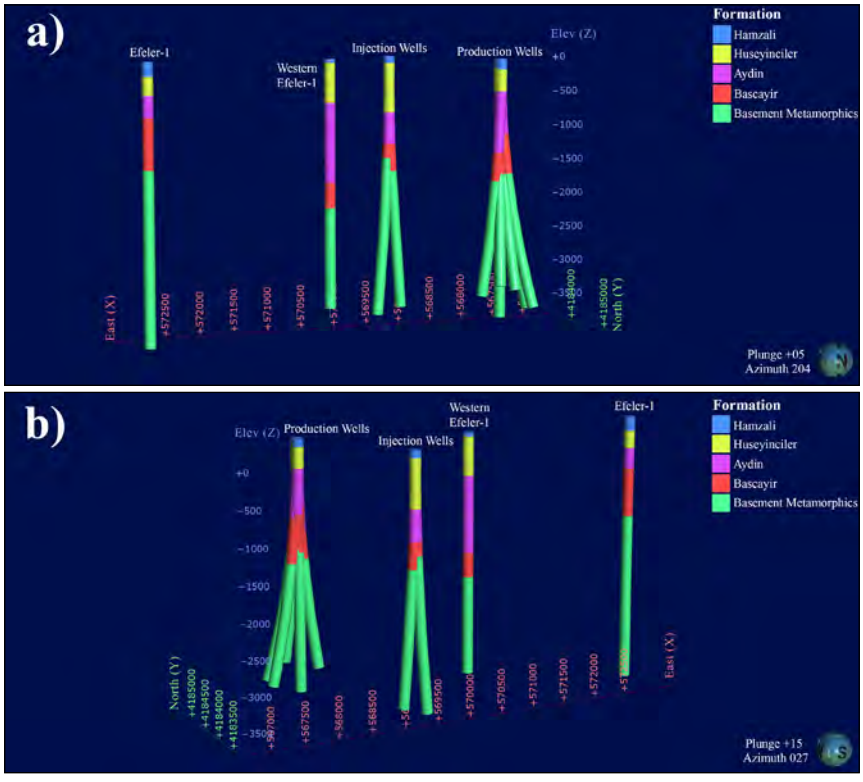

Figure 12- a) Lithology of the wells facing SW, Names of wells are included, b) Lithology of the wells facing SE.

four main Cenozoic sedimentary rocks succession. The formation names honor the names provided in the stratigraphic column (Figure 7). It follows the stratigraphy of basement metamorphic rocks, followed by early-middle Miocene rocks (Başçayır Formation) late Miocene rocks (Aydın Formation), Pliocene rocks (Hüseyinciler Formation), and Quaternary sediments (Hamzalı Formation).

The 3D model output shows that the sedimentary rock formations are not of equal or consistent thickness. The Başçayır Formation, in red, shows thickest sediments in the northeast section of the field (Figure 13). Meanwhile, the Başçayır Formation appears to pinch-out in the southwest section of the field (Figure 14). In general the sedimentary rock formations appear thickest towards the north, where their location roughly represents the midway point between the north and south flanks of the BMG.

2.4.2. Temperature Models

The results of temperature modeling include both the 3D models generated in Seequent Leapfrog and the isothermal contour maps as described in section 3.2.4.

3D Temperature Models

The first temperature model generated for the geothermal field used only BHT and atmospheric temperature for each well (Figure 15 and 16). The temperatures in each well were interpolated in 3D across the field's subsurface within the constraints of the model.

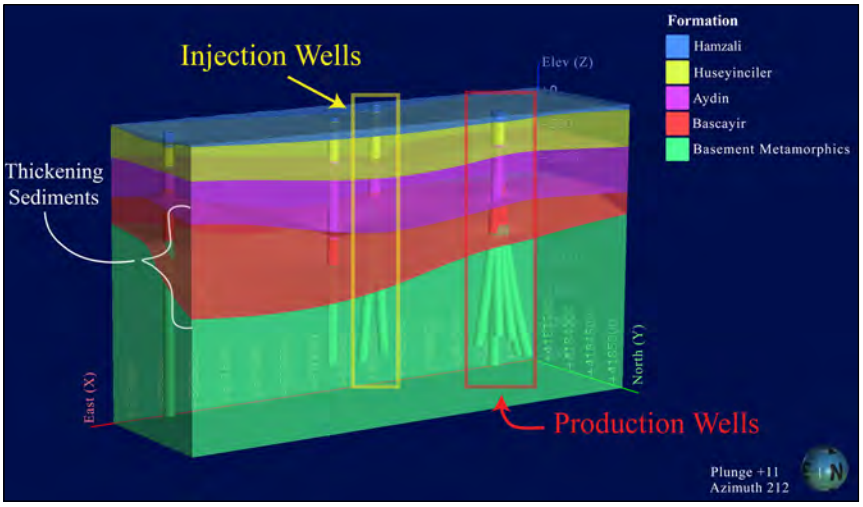

Figure 13- Overall 3D geologic model of the IGF, view is to the SW (azimuth 212°). The injection wells are outlined in yellow, and the production wells are outlined in red.

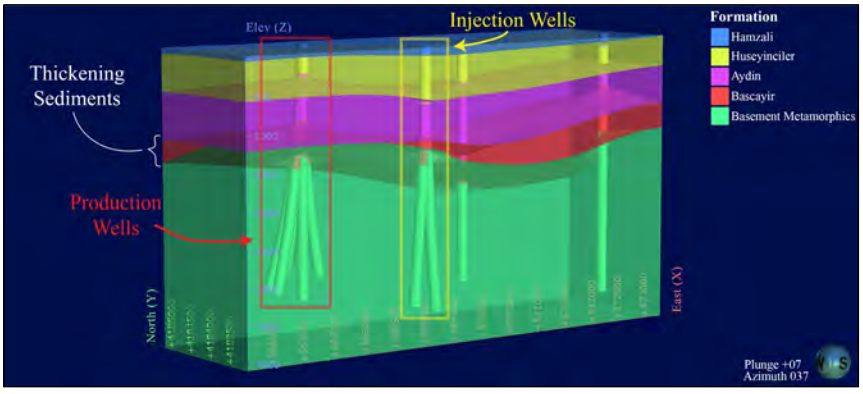

Figure 14- A 3D geologic model of the IGF, view is to the NE (azimuth 037°).

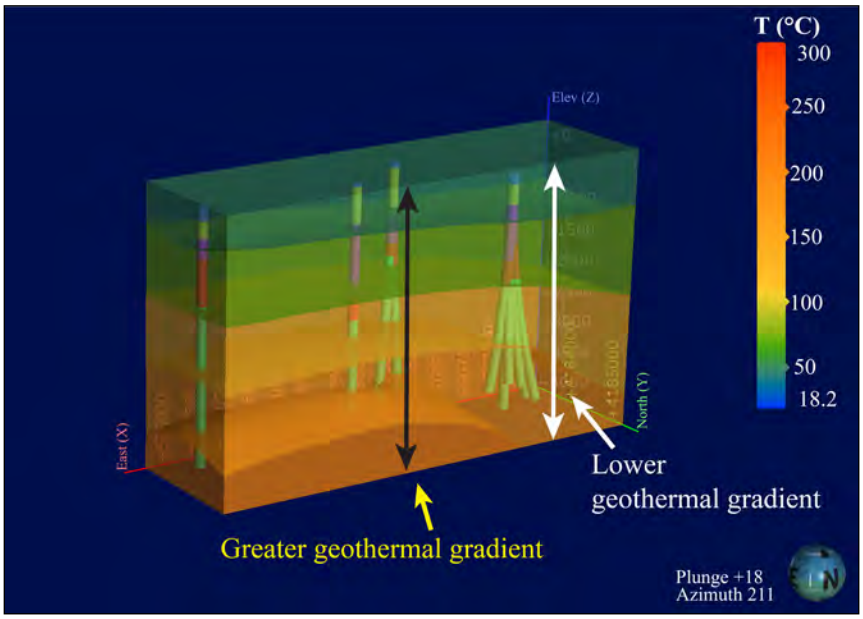

Figure 15- The 3D geothermal gradient based on BHT in the IGF, view to the SW (azimuth 211°). Isothermal contours at 50°C intervals are shown as surfaces of solid color.

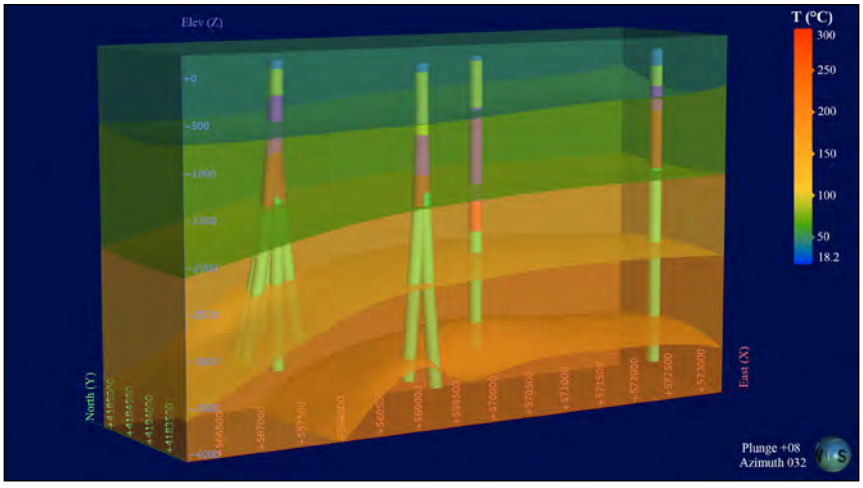

Figure 16 – BHT temperature model of the IGF, view is to the NE (azimuth 032°).

The second temperature model generated for the geothermal field combined all available continuous temperature logs with BHT data from the wells with no temperature logs. These temperatures were interpolated the same way as stated in the previous model.

2.4.3. Isothermal Contour Maps

The isothermal contour maps show the temperature isosurfaces from the 3D models as seen on a map view with contour lines. Each contour line is 100 m. Each map represents one temperature at 50°C intervals for each geothermal temperature model constructed in Leapfrog. Four maps were made for the BHT-driven model and five maps were made for the continuous temperature model (Figure 17). One example map from each set is shown for the 50°C contour (Figure 18 and 19).

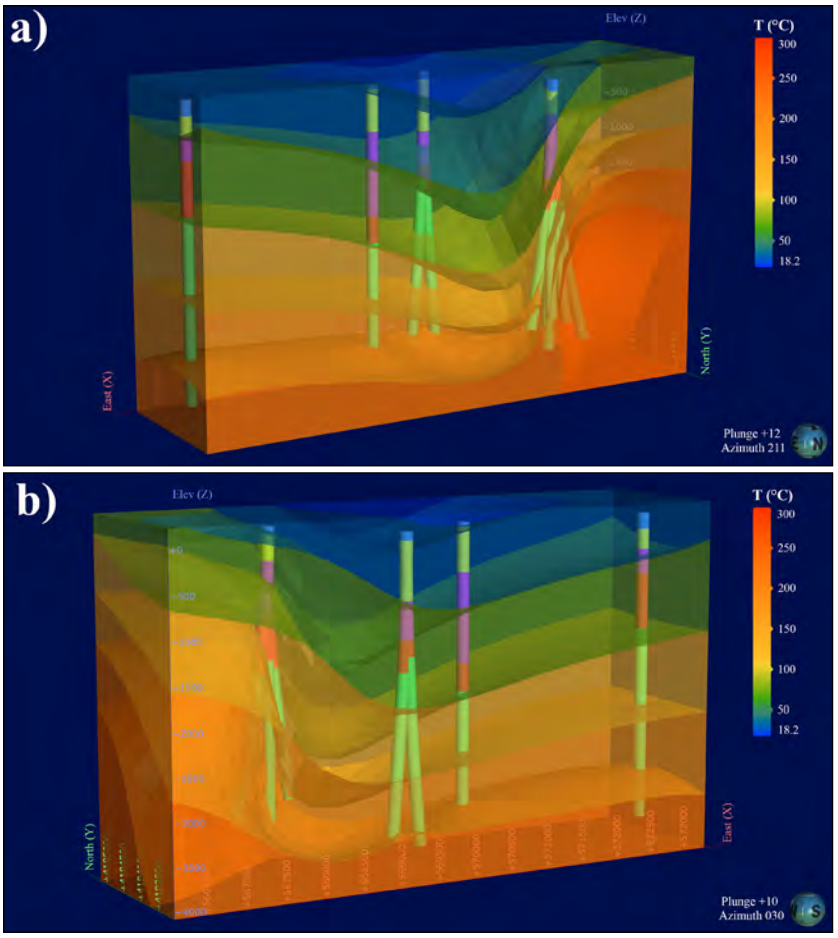

Figure 17- a) Temperature model combining BHT and continuous temperature data of IGF, view is to the SW (azimuth 211°), b) Temperature model combining BHT and continuous temperature data of IGF, view is to the NE (azimuth 030°).

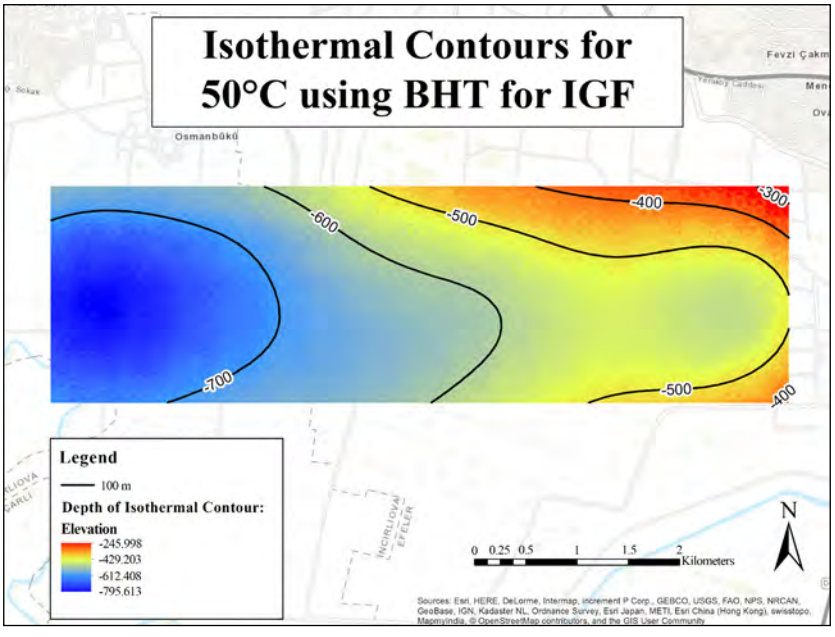

Figure 18- Example of isothermal contour map created for the IGF BHT model at 50°C.

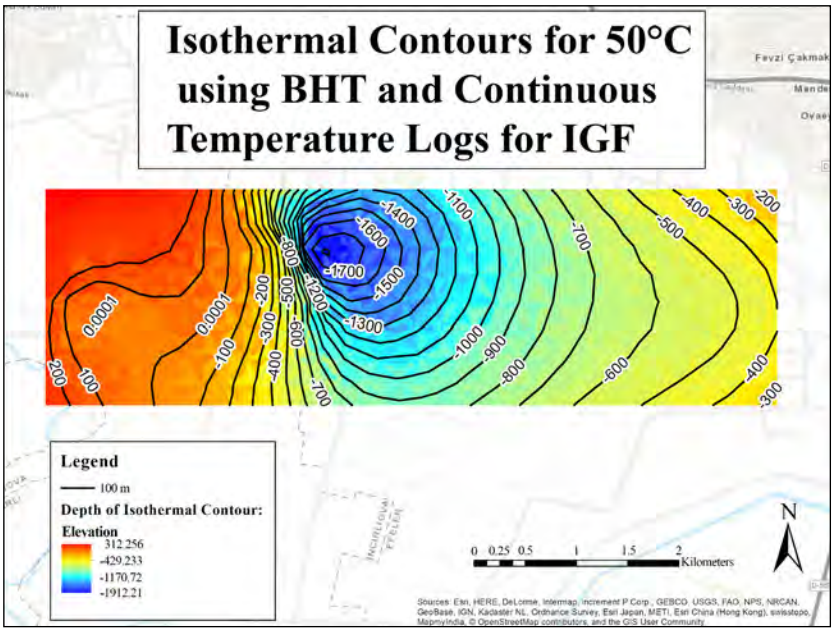

Figure 19- Example of isothermal contour map for isothermal contour map with continuous temperat ure logs.

3. Discussion

3.1 Discussion of Geologic Model

3.1.1. Implications for Geothermal Production

In the geologic model, the total depths of the wells penetrate the metamorphic basement rocks. This shows that the targeted reservoir formation in the IGF is the metamorphic basement. The basement rock most likely makes a better reservoir rock because it has high heat transfer capabilities. The top of the metamorphic basement likely contains erosional features and fractures which allow high surface area for heat transfer to geothermal fluids. Some of these fractures are observable as fault surfaces in the published cross-section from Lovekin et al. (2019) (Figure 10). Other important characteristics of the reservoir include the physical characteristics derived from its composition. Since the metamorphic basement reservoir contains marble, it is likely that some $CaCO_3$ has dissolved in the hot geothermal fluids and created voids in the subsurface. These features likely include interconnected spaces that can fill with geothermal fluids. The fractures, erosional features, and dissolution features all likely aid convective heat transfer by allowing higher permeability, porosity, and, subsequently, flow of geothermal fluids within and along the top of the basement.

3.1.2. Implications for Sedimentation and Tectonics

On the southern side of the geologic model, the Başçayır Formation appears to “pinch out” and the basement rocks and the late Miocene rocks form a contact (Figure 13 and 14). It is unlikely that the Başçayır Formation is absent due to its original position or sedimentation. Instead, the absence of the Başçayır Formation is possibly due to normal faulting along a north dipping fault. This is also apparent in the thicknesses of the Başçayır Formation reported in the well logs and as seen in lithologic model (Figures 13 and 14). Furthermore, compared to the production wells, the Başçayır-Aydın contact occurs at greater depth in the injection wells. The Başçayır Formation is much thinner in one of the injection wells, Incirliova Enjeksiyon-4, and this could be accounted for by both faulting and synextensional sedimentation. The synextensional sedimentation interpreted from the varying thicknesses of sedimentary rocks from this model is consistent with observations from rock outcrops and interpretations of structural data in the BMG from other studies (Sümer et al., 2020).

The model suggests that synextensional sedimentation occurred in this region. When compared to the published seismic profile of Lovekin et al. (2019), the IGF is just south of the intersection of the

BMG's north and south graben bounding faults. Even without including fault surfaces in the model, the geologic model shows thicker sedimentary sections north of the production wells (Figure 13).

Fault surfaces were not included in this model because structural fault data was unavailable. If available, types of data that could be used to model fault surfaces could be surface structural measurements or seismic reflection data. 3D seismic reflection data would be optimal to model and interpret the fault surfaces in the subsurface. Despite the lack of fault modeling, the geologic model is still valid because the individual faults seen in the published cross-section from Lovekin et al. (2019) do not have much displacement (Figure 10).

Active sedimentation in basins is known to suppress heat flow within the basins (Theissen and Rüpke, 2010). The effect of active sedimentation in the BMG most likely suppresses heat flow, but it might not be consistently suppressed throughout the basin. Since the most sedimentation occurs in the center of the graben, it is likely that heat flow is most suppressed in the center of the graben and the least suppressed at the north and south boundaries where the sediment is thinnest.

3.2. Discussion of Temperature Models and Isothermal Contour Maps

3.2.1. Isothermal Contour Maps

Figures 18 and 19 use a map view to show the spatial distribution of the isothermal contours that were created in Leapfrog. Each map shows an isocontour surface that represents a single temperature. These surfaces are called isothermal contours, and, for each model, every map displays a different temperature value that increases sequentially by 50°C. The elevation where that temperature occurs in subsurface is represented by a color gradient and elevation contour lines. In the color gradient, blue represents greater depth and red represents closer proximity to the surface.

The first set of isothermal contour maps show the distribution of temperature based on the BHT-driven model (Figure 18). These maps show greater geothermal gradients in the east and lower geothermal gradients in the west. The contours have a gentle slope to the west with a relative maximum in the eastern portion.

The second set of isothermal contour maps show the distribution of temperature based on the continuous temperature model (Figure 19). In general, these maps show greatest geothermal gradient in the west and lesser geothermal gradients in the eastern IGF. Due to modeling error, the very western portion of these maps may show unrealistic results of high temperatures close to the surface. The validity and handling of this discrepancy in results is further discussed in section 3.2.3. With respect to the maps, the error causes the color gradient for depth to be less helpful in interpreting subsurface temperatures for the 50, 100, and 150 °C isothermal contours in this map set. The isothermal contour lines are still accurate for the surfaces generated in the modeling. The slight rise in slope to the west may not be reasonable, but the steep slopes, as seen by many contour lines stacked on top of each other, show a steep uplift of temperature that is observed in the 3D models. This section is where the production wells are drilled, as observed in Figures 15 and 16.

3.2.2. Implications for Reservoir Management and Data Source

In the BHT temperature model, the greatest geothermal gradient is at the site of the injection wells, and the lowest geothermal gradient is at the site of the production wells (Figure 15). While this seems counter-intuitive, it could be explained based on the data source. If the BHT data used in this study was from a well-monitoring service sometime after production was initiated, then the geothermal system may have reached thermal equilibrium, which has resulted in the phenomenon known as "thermal breakthrough." This refers to a condition in the field that occurs after production begins. In this scenario, during sustained production, the subsurface temperatures of the reservoir at the production wells decrease over time until the system reaches equilibrium.

In the combined temperature model, the subsurface temperatures at the production wells are elevated, and significant 250°C temperature isosurfaces are visible (Figure 17). Compared to the BHT temperature model, the 200°C thermal isosurface in the combined model

occurs 2000 m closer to the surface. This difference in the depth suggests a thermal breakthrough has occurred in the reservoir. The elevated temperatures are shown for all the temperature isosurfaces in the western portion of the IGF. However, the temperatures in the east side of the IGF appears relatively consistent when the two models are compared. This may be due to the BHT data used to supplement the continuous temperature data. Overall, the elevated temperatures in the production region suggest that the continuous temperature data was from the exploration stage and predates any thermal breakthrough in the reservoir.

However, if the differences between the BHT and combined temperature models are not a result of geothermal production, then it could be explained by natural causes. Since the BMG is actively extending and known to be seismically active (Figure 1), then the changes in the reservoir temperature over time could be the result of changes in the fracture and fault connectivity in the subsurface. Earthquakes in the region could cause new fractures and faults that allow new recharge and circulation patterns to form in the reservoir. For example, if colder recharge fluids were no longer able to enter the reservoir due to sealing by a fault, then the reservoir temperature might increase. In another hypothetical situation, colder geothermal fluids may be allowed to access the reservoir through newly formed fracture pathways, subsequently resulting in lower temperature distribution for the reservoir.

3.2.3. Comparison with the Germencik Geothermal Field (GGF)

The IGF is ~15 km SE of the GGF. The numerical temperature models of the IGF (Figure 15 and 16) from this study are compared to those of the GGF (Figure 8). In all the models, depths of up to about 3000 m are used. The combined temperature model from this study, and the GGF show similar uplifts of isothermal contours on one side of the geothermal field. Some of the isothermal contours may seem unreasonable in both the IGF combined model and the GGF model. This is because they extend to the surface, showing temperatures of 50 to 100°C extending to the surface, which is unrealistic. The unrealistic elevations of the isothermal contours can also be seen in the western parts of the isothermal contour maps (Figure 19). Nevertheless, the IGF and GGF models both show similar shapes of relatively high temperatures upwelling at depth into similar shapes. The IGF model shows similar temperatures at same depth as the GGF model, however the IGF model shows a 250°C contour around 2 km depth that the GGF model does not include. This suggests that the IGF has a higher geothermal gradient than the GGF at a depth of 2 km. The GGF case study by Tonkul et al. (2021) used 3D interpolative numerical modeling in Leapfrog to validate their reservoir temperature calculations obtained by geothermometry. In the GGF, geothermometry has shown that the reservoir temperature is between 190°C and 232°C (Tonkul et al., 2021). The reservoir temperatures for the GGF obtained by geothermometer calculations are consistent with those obtained by numerical modeling. Since the IGF models presented in this study closely resemble those of the GGF, which is validated by reservoir temperatures calculated by geothermometry, then it stands to reason that the IGF interpolative temperature models are valid.

3.2.4 Geothermal Gradient Variability throughout the BMG

The variability of the geothermal gradient throughout the BMG cannot be fully explained by this study. This study, however, does provide more insight to the factors which cause the variability. Regions of the BMG that feature highly fractured basement rock likely provide localized areas of higher geothermal gradients. The western portion of the BMG appears consistent with the interpretation that highly fractured basement rock creates conditions appropriate for high geothermal gradients. However, the eastern portion of the graben was not able to be evaluated in this study because data were not available from geothermal fields in the eastern BMG. Therefore, this study does not adequately test the hypothesis suggesting that the origin of high geothermal gradients and high heat flow in eastern portion of the graben is due to rising asthenospheric material. This hypothesis remains untested.

The distribution of temperature in the BMG is likely controlled by the distribution of convective hydrothermal systems throughout the region. Convective hydrothermal systems require adequate

permeability for heat and fluid flow to occur. Structural geologic setting has been identified as the main control of permeability distribution in extensional settings (Faulds et al., 2010). The IGF is unique in the fact that it is the only commercial geothermal system occurring greater than ~5 km from the surface expression of the Büyük Menderes Detachment. One possible structural setting for the IGF could be an intersection at depth between the northwest-striking Çine Graben fault, the Büyük Menderes Detachment, and the southern detachment fault. This structural intersection could provide enough permeability to create a commercial convective geothermal system occurring in the center of the BMG.

4. Results

The geologic models show a simplified structure within the BMG due to the omission of fault surfaces. Despite this, the geologic model is valid without fault surfaces because the individual faults do not have much displacement. Pinch-outs are observed in early versions of the model, which may be data-driven due to wells drilled on either side of a hydraulically conductive fault. The pinch-outs also may be error-introduced artifacts of software functions such as interpolation. However, the thicknesses of geologic units observed in the model show thicker sediments toward the center of the BMG, which suggests that synextensional deposition occurred in the graben.

The two temperature models, one made from bottom hole temperature (BHT) measurements and the other made from both continuous temperature logs and BHT data, suggest that the geothermal reservoir has experienced a thermal breakthrough, where reservoir temperatures at the production wells have declined over time via sustained production.

The IGF, a west-central geothermal field within the BMG, has similar characteristics to the GGF, a western-located geothermal field in the BMG. The IGF appears to have a higher geothermal gradient, as evident in the higher temperature isothermal contour surfaces shown at similar depths. This is likely due to a different structural setting involving the NW-striking Çine Graben fault; however, this hypothesis remains to be tested.

4.1. Recommendations

The spatial variability of the geothermal gradient in the BMG could be further described if more isothermal contour maps and 3D models, such as those created in this study, were created for other geothermal fields in the BMG. To fully explain the variability, other information would be needed to support the case. This information could include the fracture structures of the basement and sedimentary rocks and the behavior of the asthenosphere-lithosphere interactions.

The geologic models created in this study may be improved by using seismic reflection data and structural measurements to evaluate and include the effects of faulting within the geologic model.

With fault information included, numeric flow simulations, such as TOUGH2, could be combined with the Leapfrog models to create reservoir heat and fluid flow simulations. Other physical modeling software could be used, too. The physical models would improve the understanding of the temperature and heat flow distribution because they would be able to include more physical parameters and solve for equilibrium states of the subsurface. This would provide a more realistic estimation of the subsurface interactions between rocks, fluids, energy, and structural geology. The conductive heat flow of the IGF could be solved analytically by combining thermal conductivity values of rocks in Western Anatolia (Balkan et al., 2017) with the geologic model calculated in this study. The thermal conductivity values reported were for common rock types of Western Anatolia in both saturated and dry conditions. For geothermal systems, the saturated condition is used.

Acknowledgement

We are pleased to thank Dr. Geoffrey Tick and Dr. Bo Zhang from the University of Alabama and to Dr. Rezene Mahatsente for their suggestions to this research. Thanks to Bastien Poux, formerly of Seequent, for making the Leapfrog Geothermal software available for the Çemen research group on an academic license. Thank you to HD Energy Solutions for supplying the data that made this research possible.

References

Alemdar, S. 2015. A model of the crust and upper mantle structure of the Hellenic and Cyprus subduction zones constrained by gravity and seismic data [M.S.]: The University of Alabama, 100 p., http://search.proquest.com/pqdtglobal/docview/1764970978/abstract/C59EED0D12424A60PQ/1 (accessed November 2020).

Balkan, E., Erkan, K., Şalk, M. 2017. Thermal conductivity of major rock types in western and central Anatolia regions, Turkey: Journal of Geophysics and Engineering, 14, 909–919.

Bozkurt, E. 2000. Timing of Extension on the Büyük Menderes Graben, Western Turkey, and Its Tectonic Implications: Geological Society, London, Special Publications, 173, 385–403.

Çemen, I., Catlos, E., Göğüş, O., Özerdem, C. 2006. Postcollisional Extensional Tectonics and Exhumation of the Menderes Massif in the Western Anatolia Extended Terrane, Turkey. In: Post-collisional Tectonics and Magmatism in the Eastern Mediterranean Region: Special Paper of the Geological Society of America, 409, 353–379.

Çiftçi, N. B., Bozkurt, E. 2010. Structural evolution of the Gediz Graben, SW Turkey: temporal and spatial variation of the graben basin: Basin Research, 22, 846–873.

Çifçi, G., Pamukçu, O., Çoruh, C., Çopur, S., Sözbilir, H. 2011. Shallow and Deep Structure of a Supradetachment Basin Based on Geological, Conventional Deep Seismic Reflection Sections and Gravity Data in the Buyuk Menderes Graben, Western Anatolia: Surveys in Geophysics, 32, 271–290.

Cohen, H. A., Dart, C. J., Akyüz, H. S., Barka, A. 1995. Syn-rift sedimentation and structural development of the Gediz and Büyük Menderes graben, western Turkey: Journal of the Geological Society, 152, 629–638.

Faulds, J., Bouchot, V., Moeck, I., Oğuz, K. 2009. Structural controls of geothermal systems in western Turkey: A preliminary report: Geotherm Resou Counc Trans, 33, 375–383.

Faulds, J., Coolbaugh, M., Bouchot, V., Moek, I., Oğuz, K. 2010. Characterizing Structural Controls of Geothermal Reservoirs in the Great Basin, USA, and Western Turkey: Developing Successful Exploration Strategies in Extended Terranes, in p., https://hal-brgm.archives-ouvertes.fr/hal-00495884 (accessed November 2020).

Gessner, K., Gallardo, L.A., Markwitz, V., Ring, U., Thomson, S. N. 2013. What caused the denudation of the Menderes Massif: Review of crustal evolution, lithosphere structure, and dynamic topography in southwest Turkey: Gondwana Research, 24, 243–274.

Göğüş, O. H. 2004. Geometry and Tectonic Significance of Buyuk Menderes Detachment, in the Bascayir Area, Buyuk Menderes Graben, Western Turkey:, https://shareok.org/handle/11244/8019 (accessed December 2020).

Haklıdır, F. S. T., Şengün, R. 2020. Hydrogeochemical similarities and differences between high temperature geothermal systems with similar geologic settings in the Büyük Menderes and Gediz Grabens of Turkey: Geothermics, 83.

Kazancı, N., Dündar, S., Alçiçek, M. C., Gürbüz, A. 2009. Quaternary deposits of the Büyük Menderes Graben in western Anatolia, Turkey: Implications for river capture and the longest Holocene estuary in the Aegean Sea: Marine Geology, 264, 165–176.

Lovekin, J., Görür, N., Şile, H. 2019. Case Study of the 3S Kale Incirliova Geothermal Project, Aydın Province, Turkey: 43, 6.

Mahatsente, R., Alemdar, S., Çemen, I. 2017. Effect of Slab-Tear on crustal structure in Southwestern Anatolia: Insight from Gravity Data Modelling: Geophysical Monograph Series.

Merey, O. 2016. Kinematic evolution of the Büyük Menderes Graben in western Turkey inferred from 2-D seismic interpretation and cross section restoration [M.S.]: The University of Alabama, 117 , http://search.proquest.com/pqdtglobal/docview/1877637004/abstract/EB02A76D8A4286PQ/1 (accessed November 2020).

Mertoğlu, O., Şimşek, Ş., Başarır, N., Paksoy, H. 2019. Geothermal Energy Use, Country Update for Turkey:

Özgür, N., Çalışkan, T. A. 2013. Active Geothermal Systems in the Menderes Massif, Western Anatolia, Turkey: Procedia Earth and Planetary Science, 7, 652–655.

Özpolat, E., Yıldırım, C., Görüm, T. 2020. The Quaternary landforms of the Büyük Menderes Graben System: the southern Menderes Massif, western Anatolia, Turkey: Journal of Maps, 16, 405–419.

Roche, V., Bouchot, V., Beccaletto, L., Jolivet, L., Guillou-Frottier, L., Tuduri, J., Bozkurt, E. 2019. Structural, lithological, and geodynamic controls on geothermal activity in the Menderes geothermal Province (Western Anatolia, Turkey): International Journal of Earth Sciences, 301.

Şen, S., Seyitoğlu, G. 2009. Magnetostratigraphy of early–middle Miocene deposits from east–west trending Alaşehir and Büyük Menderes grabens in western Turkey, and its tectonic implications.

Sert, S. 2015. Subsurface structural geology of the eastern part of the Büyük Menderes Graben, western Turkey. [electronic resource] : implications for structural evolution of the Büyük Menderes and Alasehir Grabens: [University of Alabama Libraries].

Seyitoğlu, G., Işık, V., Çemen, I. 2004. Complete Tertiary exhumation history of the Menderes Massif, western Turkey: an alternative working hypothesis: Terra Nova, v. 16, p. 358–364.

Sümer, Ö., Sözbilir, H., Uzel, B. 2020. Evolving from Supra-Detachment to Rift Basin in Rolling Hinge Model of the Büyük Menderes Graben: Türkiye Jeoloji Bülteni-Geological Bulletin of Turkey, 63.

Theissen, S., Rüpke, L. H. 2010. Feedbacks of sedimentation on crustal heat flow: New insights from the Vøring Basin, Norwegian Sea: Basin Research, 22, 976–990.

Tonkul, S., Baba, A., Demir, M. M., Regenspurg, S. 2021. Characterization of Sb scaling and fluids in saline geothermal power plants: A case study for Germencik Region (Büyük Menderes Graben, Turkey): Geothermics, 96, 102227.

Uzel, B., Kuiper, K., Sözbilir, H., Kaymakçı, N., Langereis, C. G., and Boehm, K. 2020. Miocene geochronology and stratigraphy of western Anatolia: Insights from new Ar/Ar dataset: LITHOS, 352–353.

Yamanlar, S., Korkmaz, E. D., Serpen, Ü. 2020. Assessment of geothermal power potential in Buyuk Menderes Basin, Turkey: Geothermics, 88.

Yılmaz, Y., Genç, Ş. C., Gürer, F., Bozcu, M., Yılmaz, K., Karacık, Z., Altunkaynak, Ş., Elmas, A. 2000. When Did the Western Anatolian Grabens Begin to Develop? Geological Society, London, Special Publications,173, 353–384.

Bulletin of the Mineral Research and Exploration

http://bulletin.mta.gov.tr

Impact of thermal water on environment: case study of Mila and Guelma region, Algeria

Rima KIFOUCHE[a], Foued BOUAICHA[a*] and Oualid BOUTERAA[a,b]

[a] *Laboratory of Geology and Environment (LGE), Université Constantine 1, Constantine 025000, Algeria*
[b] *Université Constantine 3, Algeria*

Research Article

Keywords:
Algeria, Guelma, Hydrothermal Effluents, Salinity, Stuyfzand Classification, Thermal Water.

ABSTRACT

A hydrochemical characterization of the waters of the study region (North-East Algeria) was carried out following samples taken at 36 thermal springs and their effluents during May 2022. The analysis of the waters allowed to establish the chemical facies and their classification according to the Stuyfzand's method and to deduce the aptitude of these waters for irrigation and the risks of salinity. The results revealed physico-chemical characteristics, relatively, variable. Q-mode cluster analysis was applied to the thermal water, generated four (4) groups clusters. Group1 represent a group of waters with low salinity dominated by Na-HCO_3; Stuyfzand's classification indicated that the waters are fresh-brackish with moderate to moderately high alkalinity. Taking into account the classification of Richards; we were able to identify the presence of the C3S1 class for the majority of the stations. The C3S1 class designates waters that can be used without any particular control for the irrigation of crops that are moderately tolerant to salts. These waters have average EC values of 3,616.3 µS/cm allowing their use in a less restrictive way for irrigation. Potential environmental effluents from the thermal spas could pollute both irrigation and drinking water, which represents a danger to the health of the region's inhabitants.

Received Date: 30.09.2022
Accepted Date: 18.04.2023

1. Introduction

In Algeria, more than 282 springs have been identified in the North, of which more than 50% are located in NE Algeria. The emergence temperature varies between 30°C and 96°C. The highest temperature is located in Guelma (Hammam Debagh). These resources would generally come from geothermal reservoirs of Mesozoic age of limestone and sandstone type. At depths between 1,500 and 2,500 m (Kedaid, 2006), their temperatures at depth can reach 120°C, and a relatively high geothermal gradient occurs in the north-east of Algeria (about 50°C) (Kedaid, 2006). The so-called high-energy geothermal resources are characterized by a temperature higher than 150°C and are mainly used for electricity production. The medium and low energy geothermal resources are characterized by a temperature between 30°C and 150°C and are intended for housing heating (60°C to 80°C), heating of greenhouses, fish farming, etc. The geothermal resources in Algeria are of low energy type.

The geothermal exploitation program in Algeria saw its beginnings with Ville (1852) and his research on rocks, waters, and mineral deposits in the provinces of Oran and Algiers. Bails (1888) followed with a notice on thermal and mineral springs in the department of Oran. Hanriot (1911) collaborated with Dr. Trolard on "The mineral waters of Algeria." Pouget and

Citation Info: Kifouche, R., Bouaichi, F., Bouteraa, O. 2023. Impact of thermal water on environment: case study of Mila and Guelma region, Algeria. Bulletin of the Mineral Research and Exploration 171,143-157. https://doi.org/10.19111/bulletinofmre.1285162

**Corresponding author: Foued BOUAICHA, fouedbouaicha@gmail.com*

Chouchak (1923, 1926) conducted a detailed study on the radioactivity of Algerian waters in the provinces of Oran, Algiers, and Constantine. Guigue (1940, 1947) published works on the main thermal springs of Algeria, focusing on geochemistry within the geological map of Algeria. Other notable contributions include the works of Cornet (1964), EURAFREP (1966) with the participation of Cormy and Demians d'Archimbaud (1970), Jacqmin, Facca (1966), Marinelli, and Tonani under the direction of SONATRACH. In 1974, Dr. B. Laissoub (1974) explored thermalism in Oranie, while in 1982, the Italian company ENEL collaborated with SONALGAZ to assess geothermal energy potential in the northern and eastern regions. The geothermal studies in the initial phase mostly focused on Algeria's northeast. The Center for Renewable Energies of Algeria (CDER) continued the geothermal work beginning in 1983, and the program was expanded to include the entire northern region of the country (Dib, 1985; Rezig, 1991; Bouchareb, 1994; 2012; Issaadi, 1992; Kedaid, 2006; Dib, 2008; Fekraoui, 2010; Saibi, 2009; Belhai et al., 2016; Belhai et al., 2017; Foued et al., 2017; Djemmal, 2018; Kouadra et al., 2018).

The exploitation of geothermal energy remains very limited in view of the existing geothermal potential. Balneology is the main use, except some cases in the south of the country. The physico-chemical characterization is very important to study the suitability of thermal waters for consumption and irrigation. In the thermal spas, thousands of visitors bathe, some people drink the thermal water without any pre-established restrictions during the therapeutic period. However, regarding the drinkability and physico-chemical quality of the water, the thermal waters of the study area according to the WHO guidelines (2006) are not safe for consumption because the samples are hard and the cations and anions exceed the WHO standards. The wastewater discharged from spas directly to environment may have a negative impact on land and groundwater. In this case, the health of the local inhabitants may be endangered.

By this time, no study has mentioned the subject of pollution by hydrothermal effluents. Due to this situation, we were compelled to initiate this study in order to evaluate the health condition of the streams subsequent to engaging in such activities, to understand the hydrochemistry of thermal waters in particular the management of these water resources in a sub-humid environment with semi-arid influences. The impact of these discharges on surface water was evaluated by taking water samples from the thermal spring itself, upstream and downstream of these discharges. Several approaches are used to assess the degree of water contamination in this study. Two of these studies are field survey and laboratory analysis done for the assessment of the degree of contamination.

2. Geological and Hydrogeological Settings

Our study region concerns the North-Eastern part of Algeria. It includes the wilayas of Mila and Guelma. The northern part of Algeria presents a very complex geological framework. The study area is located within the Tellian domain, which is a part of the Maghrebide chain. This chain spans over 2000 km, extending from Calabria (Italy) in the east to the Strait of Gibraltar in the west. It forms a segment of the Alpine peri-Mediterranean orogen, dating back to the Tertiary period, as described by Delga in 1969. The geological formations in this region are diverse, ranging in age from the Triassic to the Quaternary. These geological formations have undergone various tectonic phases, notably neotectonics, which have shaped the current geological structures and contributed to the presence of thermal springs. The Guelma Basin is qualified as a pull-apart basin created between two overlapping east-west dextral strike-slip faults. On the margins of this basin in pull-apart (Maouche et al., 2013), there is a series of N-S to NNW-SSE trending normal faults that intersect the subparallel shear faults (Delga, 1969; Meghraoui, 1988; Vila, 1980). The study area is a depression filled with Miocene (clays and gypsum marls) and the Quaternary (heterogeneous alluvium in the form of a terrace) deposits. These alluvial deposits, often very permeable and above all very thick, constitute an important source of water supplied by the infiltration of rainwater and by the lateral contributions of the Seybouse watershed. The infiltrations lead the surface waters to the deeper levels, which form the base of the watershed of a very important thermal reservoir in the study area and the neighboring areas (Bouaicha et al., 2019). The Mila basin lithostratigraphically reveals water

deposits with great hydraulic potential constituted essentially by the fissured and/or karstified carbonate formations of the Néritique Constantinois, formed by massive limestones of the Jurassic and limestones and marlstones of the Cretaceous, the pénitellienne series and the nappe de Djemila geological formation. The Constantine Neogene Basin is represented in the Mila area mainly by Neogene detrital and evaporitic deposits. The Triassic deposits injected along the tectonic faults or outcropping in the form of diapirs have a direct influence on the geochemical facies of warm waters (Figure 1).

The study area is defined by sub-humid climate with a semi-arid influence to the south, with variable precipitation in time and space. Guelma is characterized by an average annual precipitation of 675 mm/year. The annual temperature varies between 2.5°C (in January and February) and 34°C (in July and August). Hydrographically, the study area is characterized by a relatively dense hydrographic network composed essentially by Oued Seybouse and its main effluents Bouhamdane, Oued Chenior and Oued El Hammame. But Mila, the average annual precipitation of 600 mm and temperatures that are close to 40°C in summer and that fall below zero in winter. A significant hydrographic network characterizes the region, with Oued Rhumel merging with Oued Endja to create Oued El Kebir. Other notable watercourses include Oued Cotton, Oued Seguen, Oued Bouslah, and Oued Smendou, along with dams such as Hammam Grouz and Beni Haroun Dam. These dams have a combined capacity of 960 million m^3 and provide water supply to the neighboring cities, namely Constantine, Batna, Khenchela, Jijel, Mila, and Oum El Bouaghi.

3. Materials and Methods

3.1. Sampling and Analysis

The prospecting of grounds led us to choose 36 stations (Figure 2) distributed in a way to cover the

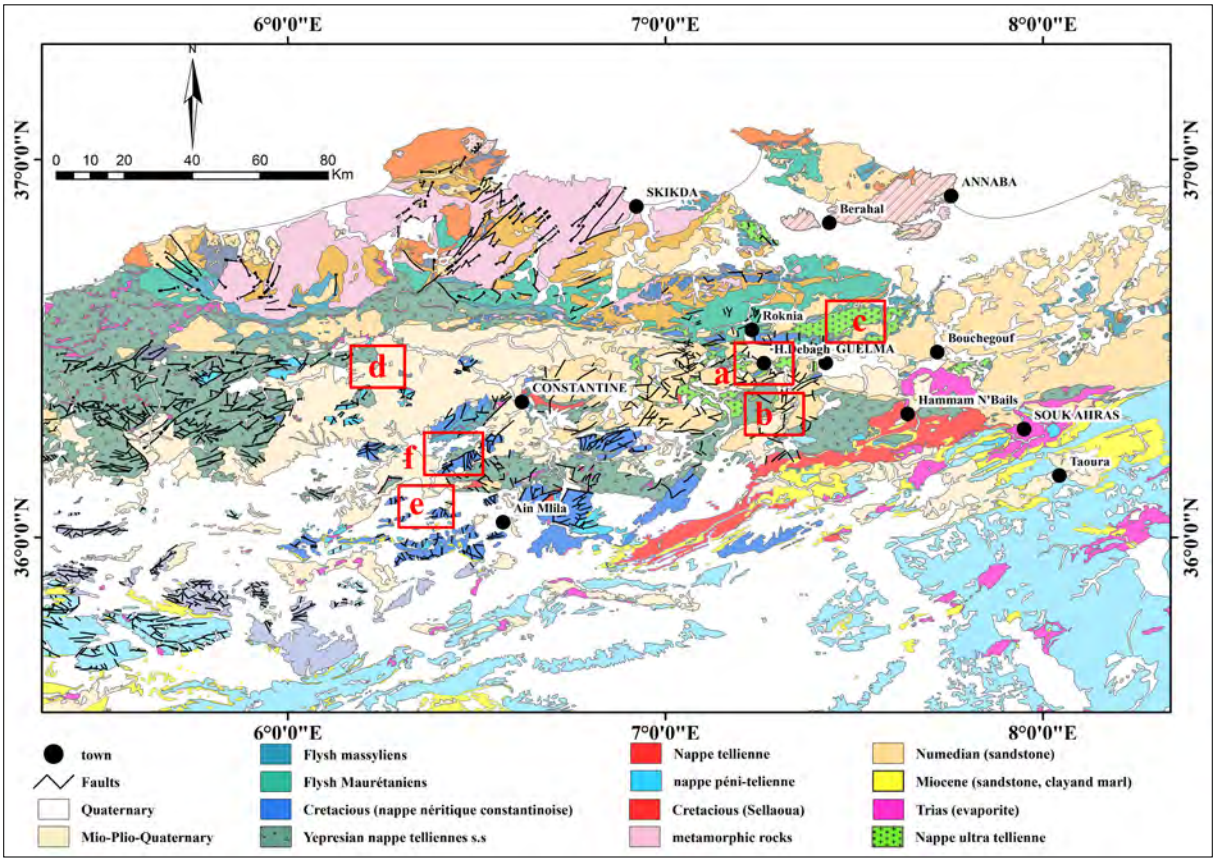

Figure 1- Geological maps of northeastern Algeria, with sampling sites; a) Chellelacomplexe, b) Guerfa, c) Ouled Ali, d) Beni Guechat, e) Teleghma, f) Hammam Grouz (Vila, 1978).

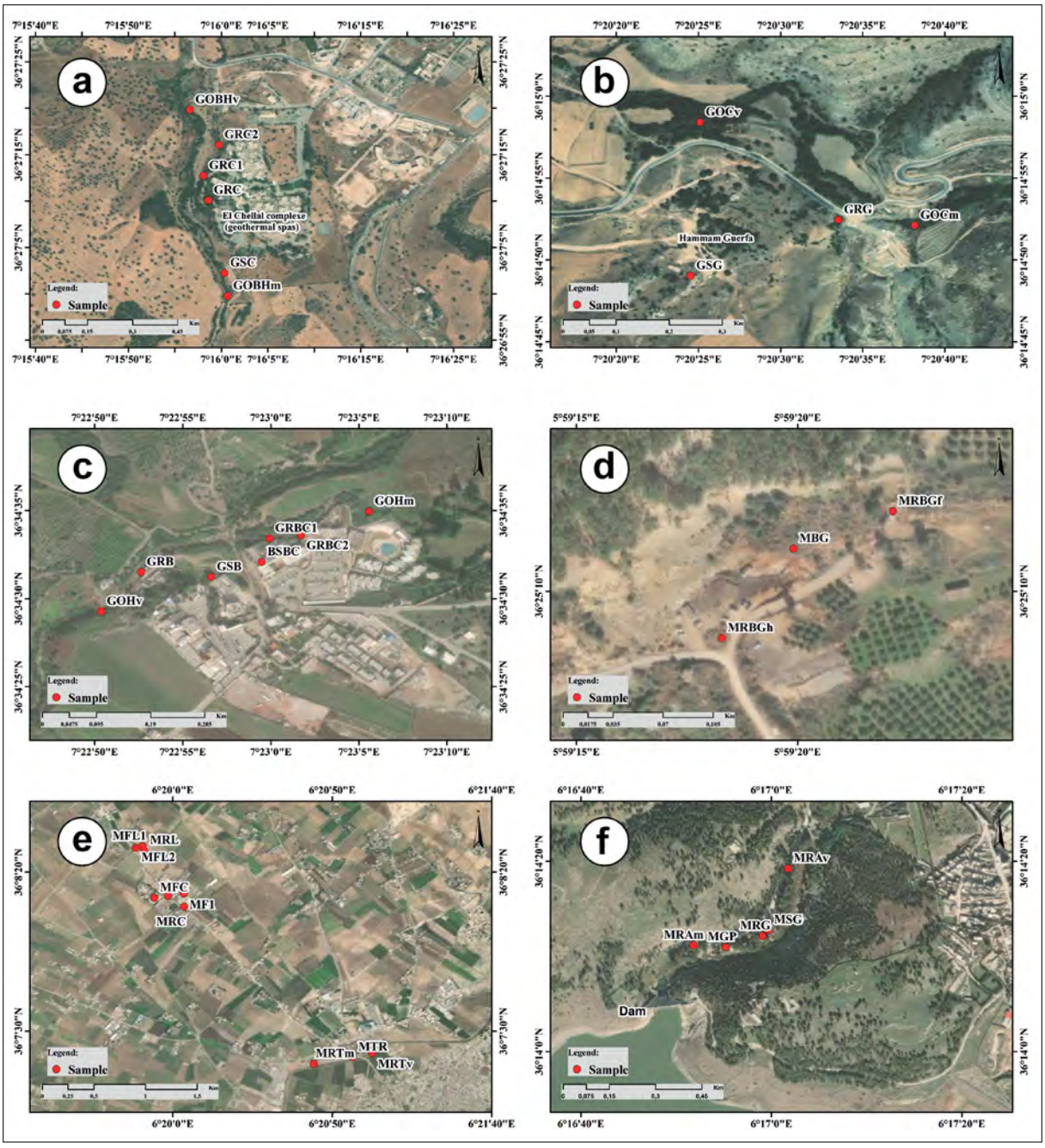

Figure 2- Map shows sampling sites; a) Chellela complexe, b) Guerfa, c) Ouled Ali, d) Beni Guechat, e) Teleghma, f) Hammam Grouz.

thermal areas characterized by a strong recrudescence of curists or tourists during the year (especially the period September - May). This generates important quantities of waste water (effluents of the hydrothermal stations or Hammam). These effluents are wasted without preliminary treatment.

The sampling was carried out during the month of May 2022. We have four types of water to analyze (thermal source, discharges of thermal complexes and upstream and downstream of wadis). It was carried out after rinsing the bottles with distilled water three times and placed in polyethylene bottles and stored in a cooler at a temperature of 4°C (APHA, 2005). Hydrogen potential (pH), electrical conductivity (EC), temperature (T°C), and dissolved oxygen (DO) were measured in situ using a multiparameter apparatus

type AZ 86031 Combo Water Meter-T°/pH/EC/DO (Taiwan). Thereafter the samples were transported to the laboratory for the analysis of chemical parameters such us: calcium (Ca^{2+}), magnesium (Mg^{2+}), sodium (Na^{+}), chloride (Cl^{-}), sulfate (SO_4^{2-}), carbonate (CO_3^{2}), bicarbonate (HCO_3^{-}), nitrate (NO_3^{-}), nitrite (NO_2^{-}), total hardness (TH) and biochemical oxygen demand for 5 days (BOD_5). Ca^{2+}, Mg^{2+} and TH are based on complexometric titration. There concentrations are measured by a standard solution of Ethylene-Diamine-Tetracetic-Acid (EDTA), which is a complexing agent. For CO_3^{2-} and HCO_3^{-} the volumetric method was also used but with the help of a 0.1N hydrochloric acid solution. Chlorides are determined by a titrated solution of silver nitrate in the presence of potassium chromate. Sulfates and nitrites were determined by a spectrophotometric method (spectrophotometer DR/2000) and Na^{+} by a flame photometer. The BOD_5 is measured with a BOD meter type BSB-Controller Modell 1020T, for 164ml of sample we add 3 capsules of NaOH, incubation for 5 days in the dark, the result is multiplied by the factor 10 in mg/l.

3.2. Statistical Analysis

3.2.1. Cluster Analysis

Hierarchical Cluster Analysis (HCA) is a strong classification tool based on dissimilarities between the objects desired for classification. This unsupervised statistical technique is largely used by scientists on hydrogeochemistry to classify water samples according to their similarity to each other (Alther, 1979; Williams, 1982; Farnham et al., 2000; Meng and Maynard, 2001; Alberto et al., 2001; Belkhiri et al., 2010; 2011; Foued et al., 2017; Bouaicha et al., 2019; Boutreraa, 2019 and Barkat et al., 2021). Q-mode HCA was used to distinct hydrochemical groups by classify water sample involving Ward's method (Ward, 1963) with Euclidean distance as a measure of similarity. All 15 hydrochemical parameters measured (pH, T°, EC, OD, DHT, Mg^{2+}, Ca^{2+}, Na^{+}, HCO_3^{-}, CO_3^{2-}, SO_4^{2-}, Cl^{-}, BOD_5, NO_3^{-} and NO_2^{-}) were utilized on the normalized data set to carry out the HCA.

3.2.2 Factor Analysis

As a multivariate analysis technique, factor analysis is used to reveal the latent structure of a data set of variables, which may explain observed variance in uncorrelated variables called factors (Brown, 1998). Factor analysis shows the common variance of variables and allows searching inter correlation among the variables. Factor analysis can be applied to any type of scientific data in order to establish a model of variation by reducing large sets of variables into factors allowing easy manipulation and interpretation. The extraction of latent factors can be done by several methods and the most commonly used is the principal components PC. The total number of PCs extracted and ranked in order of merit using this multivariate technique, denotes the total number alternative source of variation in the data. The first PC or factor present the highest Eigen value (Eigen vector sum) and explains essential variance of data set, whereas the last PC or factor contributes with least important variance. Factor loadings represent correlation coefficients between the variables and the factors, and terms high, moderate, and weak are used to factor loadings with absolute loading values: > 0.75, 0.75-0.50, and 0.50-0.30 respectively (Liu et al., 2003).

3.3. Hydrochemistry Process

The hydrochemical methods of characterization and classification of water used in this study are based primarily on the Piper diagram (Piper, 1944) and the Stuyfzand classification (Stuyfzand, 1989). The Piper diagram is used to represent the cationic, anionic and global facies. The Stuyfzand classification is used to determine the main type, type, sub-type and class of chemicals. Each of the four levels of subdivision contributes to the total code of the water sample. The main type is determined based on chloride. Water are classified as oligohaline (G), oligohaline-fresh (g), fresh (F), fresh-brackish (f), brackish (B), brackish-salt (b), salt (S) and Hypersaline (H). The type is determined by alkalinity index (HCO_3^{-} concentration). The classification of sub-types is determined by the prevailing cations and anions. The class is determined from the sum of Na^{+}, K^{+} and Mg^{2+} based on Stuyfzand's Equation (1) which calculates the Basic Exchange Index (BEI).

$$BEI = Na^{+} + K^{+} - 0.8768\ Cl^{-} \qquad \text{(Equation 1)}$$

3.4. Water Salinity

The qualitative parameters used, in addition to electrical conductivity (EC), to assess groundwater

Table 1- Evaluation equation of quantitative parameters.

Parameter	Equations
Na^+%	$Na^+\% = Na^+ + K^+ / (Na^+ + K^+ + Ca^{2+} + Mg^{2+}) * 100$ Equation 2
SAR	$SAR = Na^+ / \sqrt{(Ca^{2+} + Mg^{2+})/2}$ Equation 3
MAR	$MAR = Mg^{2+} / (Ca^{2+} + Mg^{2+})$ Equation 4
PI	$PI = Na^+ + \sqrt{HCO_3^-} / (Ca^{2+} + Mg^{2+} + Na^+) * 100$ Equation 5
RSC	$RSC = [(HCO_3^- + CO_3^{2-}) - (Ca^{2+} + Mg^{2+})]$ Equation 6

quality for irrigation purposes are outlined in Table 1. These are sodium percentage (Na^+ %), Sodium Adsorption Rate (SAR), Magnesium Adsorption Rate (MAR), Permeability Index (PI), and Residual Sodium Carbonate (RSC). The total soluble salt concentration determined by EC affects the choice of irrigation water. Plant growth can be negatively affected by high salinity. The Na^+% was evaluated by equation 2 (Raghaunth, 1989). The calculation of this percentage allows evaluating the potential degradation of the soil structure and the alteration of its properties (Eaton, 1950). An excess of sodium (Na^+ % > 80) can also cause toxicity in some plants. The SAR was determined by equation 3 (Wilcox, 1953). The MAR ratio (equation 4) highlights the importance of magnesium for the soil and the plant. It is considered an indispensable element when the MAR is less than 50. Otherwise, this chemical element becomes harmful (Raghaunth, 1989). The PI was calculated by equation 5 (Doneen, 1964). Three classes were obtained. The first two classes with a maximum of 75% deduce a good suitability of water for irrigation. The third class below 25% where the water is unsuitable for irrigation. The CSR highlights the abundance of carbonates and bicarbonates. In case it exceeds 1.5meq/l can harm the soil fertility.

4. Discussions

4.1. Hydrogeochemical Characteristics

The distribution of thermal springs in north-eastern Algeria is strongly influenced by the geological and hydrogeological characteristics of the region. In particular, this distribution coincides with the main structural features and reservoirs represented by the region's Jurassic and Cretaceous carbonate and Triassic formations.

The hydrochemical evaluation of the spring waters shows that the temperatures measured at the emergence are not representative of the real temperature of the reservoir. A possible cooling of the thermal waters may occur in several ways such as the movements of deeply-circulated hot waters, Joule-Thomson effect during degassing, heat exchange between water and surrounding rocks, and mixing with cold waters (Bouaicha, 2018). The conductivity of waters depends on the amount of ions. The values of conductivity are high in places. This is related to the easy solubility of evaporite-rich Triassic formations. For the main elements, calcium may have two main origins. They are dissolution of carbonates or gypsum. Magnesium comes from the dissolution of magnesium-rich carbonate rocks. Sodium is related to the rapid dissolution of evaporitic formations. For bicarbonates, they result from the dissolution of limestone rocks, which are the main geothermal reservoirs in the study area. Chlorides are generally related to the lithological nature of the different geological formations. So that evaporates remain the main source. In general, the waters rich in chlorides are rich in sodium as well. Sulfates are the predominant element in the thermal waters of the study area and may have different origins. They are geological (dissolution of gypsum), biological (degradation of organic matter) or anthropic (discharges from thermal baths or use of pesticides).

The summary of all the physico-chemical analyses are shown in Table 2. The analysis of the different physico-chemical parameters of the thermal waters showed a relative heterogeneity. The temperature varies between 16.6-65°C (effluent and thermal waters). Water is said to be thermal when its temperature at emergence exceeds the average annual air temperature (i.e. 4°C).

The temperatures of the thermal waters vary according to the geological conditions and the geographical situation. In Algeria, the hottest waters are those of Hammam Debagh with 96°C.

Table 2- Statistical Parameter values of the four principal water groups.

		T°	pH	EC	DO	TH	CO_3^{2-}	HCO_3^-	Ca^{2+}	Mg^{2+}	Na^+	Cl^-	SO_4^{2-}	NO_2^-	NO_3^-	DBO_5
Group 1	**Mean**	33.9	7.82	1165	4.1	8.8	18.3	237.9	72.14	58.99	98.9	156.2	200	0.022	0.7	10
	Min	16.6	7.28	578	0.3	3.36	0	183	44.09	13.87	14.26	21.3	118	0.007	0.1	5
	Max	40.6	7.95	1835	20.1	14.32	36.3	469.7	144.29	91.11	199.14	276.9	480	2.68	4.6	29
	SD	10.02	0.24	462.13	8.31	3.40	13.29	95.97	34.87	26.54	73.62	123.77	132.56	1.00	1.60	8.79
Group 2	**Mean**	38.80	7.48	1214	4.40	8.30	0.00	255.59	78.16	56.32	116.18	157.98	278.00	0.02	0.55	14.50
	Min	29.70	6.50	1020	0.60	5.68	0.00	164.70	40.08	22.47	5.33	14.20	80.00	0.00	0.20	5.00
	Max	65.00	8.00	2300	21.00	13.20	12.20	318.42	176.35	110.30	363.40	351.45	462.00	0.20	1.40	25.00
	SD	8.45	0.36	384.29	4.21	2.11	2.49	48.32	33.06	20.90	83.08	101.52	102.49	0.07	0.44	5.47
Group 3	**Mean**	51.05	7.06	2315	1.05	19.94	0	278.77	109.02	173.87	84.285	214.775	671.25	0.008	0.3	12.5
	Min	41	6.45	2310	0.8	17.08	0	230.58	49.7	172.6	44.51	177.5	652.5	0.005	0.3	10
	Max	61.1	7.67	2320	1.3	22.8	0	326.96	168.34	175.14	124.06	252.05	690	0.011	0.3	15
	SD	14.21	0.86	7.07	0.35	4.04	0.00	68.15	83.89	1.80	56.25	52.71	26.52	0.00	0.00	3.54
Group 4	**Mean**	42.3	6.9	22,700	3	38.4	0	644.16	673.34	56.79	1,906.47	3,271.325	840	0.036	1.2	19
	Min	38	6.19	22,500	2	35.2	0	606.34	641.28	37.63	1,753.33	3,237.6	710	0.022	1.2	5
	Max	55.6	7	24,000	7	41.6	0	710.04	705.41	75.96	1,971.71	3,305.05	920	0.049	1.4	20
	SD	9.18	0.44	814.45	2.65	3.20	0.00	52.48	32.07	19.17	112.10	33.72	105.99	0.01	0.12	8.39

* All values are in mg/l except pH, T (°C), EC (µS/cm) and TH (meq/l).

*EC (electrical conductivity), DO (dissolved oxygen), TH (total hardness), carbonate (CO_3^{2-}) and biochemical oxygen demand for 5 days (BOD_5).

In Mila region, the Beni Guechat spring stands out as the hottest, reaching 56.1°C (Figure 2d). On the other hand, the Ain Tinn spring exhibits the lowest temperature, measuring at 32°C. The classification of waters according to Verdeil (1982) is given as follows, hyperthermal waters (T > 45°C), orthothermal waters (37°C< T < 45°C), mesothermal waters (22°C < 37°C) and cold waters (T <22°C).

55% of the springs (11 out of 36) are classified as hyperthermal and 45% of them are classified as orthothermal (Issaâdi, 1992). pH values vary between 6.19 and 8. This indicates a slightly alkaline character. Generally, the values of EC are high ranging between 758-24,000 µS/cm. According to Issaâdi (1992), the thermomineral springs of Algeria are grouped into four based on the electrical conductivity (EC) values as follows: class 1 (EC < 2,000 µS/cm), class 2 (2,000 < EC < 7,500 µS/cm), class 3 (7,500 < EC < 15,000 µS/cm), class 4 (EC > 15,000 µS/cm).

78% of the sampled waters have conductivities lower than 2,000 µS/cm. These waters are weakly mineralized. They are linked to carbonate reservoirs. While 13% have conductivities ranging between 2,000-7,000 µS/cm. These are generally mesothermal waters. Finally, 8% of the waters have conductivities higher than 15,000 µS/cm. These waters are strongly mineralized and are affected by evaporate formations and hydrothermal effluents.

Concentrations of the major elements vary from one element to another. The order of abundance of anions in the majority of samples is as follows: Na^+> Ca^{2+}> Mg^{2+}; and the order of abundance of cations is: SO_4^{2-}> HCO_3^-> Cl^-. The maximum concentrations of Ca and Na are 705.41 and 1971.71 mg/l. However, they are higher than their standards of the WHO (2006) which is 100 and 200 mg/l, respectively. The source of Ca may be related to the dissolution of gypsum formations ($CaSO_4.2H_2O$) or the dissolution of carbonate formations ($CaCO_3$). The average concentrations of sodium in the waters is 302.42 mg/l. The presence of bicarbonates in the waters is due to the geological nature of the reservoir (neritic limestone). Therefore, the dissolution of carbonates releases Ca^{2+} and HCO_3^- when the waters are enriched in CO_2 after being in contact with the atmosphere and the average content is 298.71 mg/l. The concentrations of anions such as Cl^-, SO_4^{2-} range between 14.2-3305.05 mg/l and 80-920 mg/l, respectively. 30% of Cl^- (250 mg/l) and 62% of SO_4^{2-} (250 mg/l) exceed the desirable

limits (WHO 2006). The increase of SO_4^{2-} and Cl^- concentrations is the consequence of the dissolution of gypsum and halite minerals of the Triassic formations (diapirs area).

4.2. Cluster Analysis

The main ion concentrations were taken as normalized data. Hydrochemical groups were determined applying Q-mode clustering analysis (HCA), which is given as a dendrogram. HCA is performed by applying Ward's method of coupling with Euclidean distance for evaluating similarity of sample data. Four preliminary groups are chosen based on visual review of the dendrogram using pennon line (an imaginary horizontal line), each account for a hydrochemical facies.

- Group 1 represents a group of waters with low salinity (medium EC = 1,165 µS/cm) and surrender orders (mg/l) Na^+>Ca^{2+}> Mg^{2+} and HCO_3^-> SO_4^{2-}> Cl^- (Figure 3). The dominance of HCO_3^- and Na^+ (Figure 4**)** is closely tied to the aquifer's lithologic nature and also untreated effluents of hydrothermal complexes (Chellela, Bouchahrine and Teleghma) (Figure 2a, c and e).

- Group 2 is dominated by sulfate, bicarbonate and sodium. Chloride is also present with an important concentration (medium Cl^-=157.975 mg/l). This group has an electrical conductivity about 1,214 µS/cm and can be observed in south, west and north of Guelma (Chellala and Ouled Ali) (Figure 2a, c) and in southeast of Mila (Hammam Grouz and Teleghma) (Figure 2f, e). All the thermal sources come out along the lines of the fractures of the carbonate formations.

- The water type group 3 has an EC of 2,315 µS/cm and is dominated by sulfates and magnesium but also contains a significant concentration of chloride. This group characterizes the thermal spring of Guerfa. Guerfa thermal spring comes out through cracks in limestone massifs owing to fault or fold marked of presence of black marl and gray clays with occasionally reddish gypsum with conglomerates. During the last earthquake, the water gushed out with a red color (clay particles) for a few days, which indicates that the emergence is through an active zone on soft formations (gypsum to conglomerates).

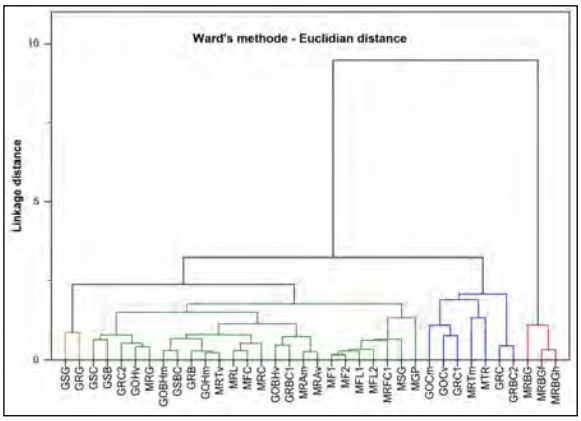

Figure 3- Dendrogram of cluster analysis.

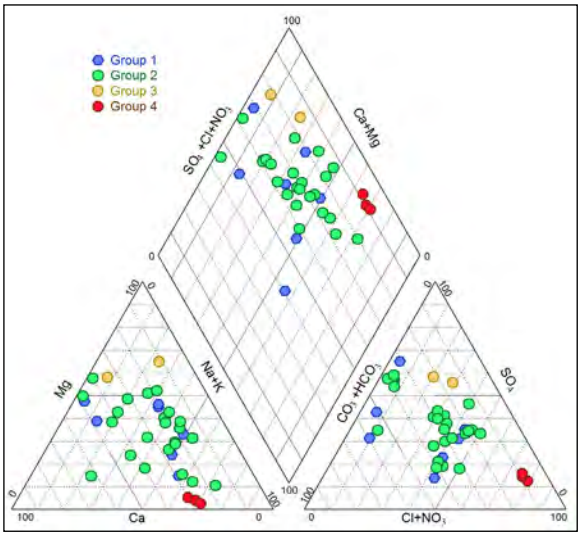

Figure 4- Piper diagram.

- The group 4 water type characterizes thermal source of Beni Guechat (Figure 2d) in the northern sector of Mila. Water of this group is very highly mineralized (22,700 µS/cm). Cl^-, Na^{2+} and SO_4^{2-} are the most dominant ions (Figure 4), which indicate that water spring facies is very strongly influenced by water-rock interaction by leaching of the evaporate formations. The high Na and Cl^- contents insinuate the dissolution of chloride salts. During hot weather, crystals of salts (NaCl) (Figure 5) precipitate around the emergence after evaporation of these waters.

4.3. Factor Analysis

Pertinence of the data for FA was monitored using Kaisere-Meyere-Olkin (KMO) and Cronbach's alpha tests. The value of KMO and Cronbach's alpha were

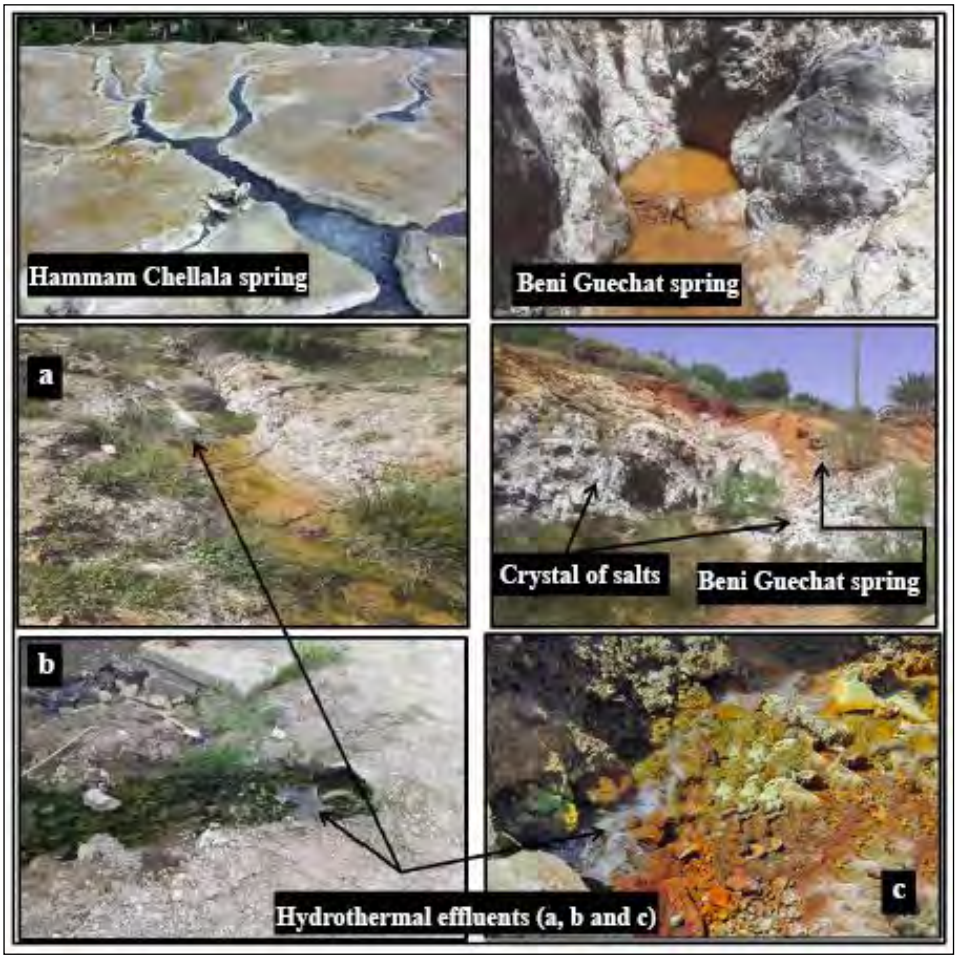

Figure 5- Hot springs and their effluents.

0.61 and 0.7 respectively. Therefore, these tests show that the sampling is appropriate for factor analysis. Based on the Kaiser criterion (Kaiser, 1960), four factors were extracted and rotated using the varimax normalization. These factors explain 76.91 % of the total variance (Table 3) is quite good and enough to explain sources of variation in the hydrochemistry. On the other hand, the communality, which is the portion of variance well explained by the factors for each variable, was > 0.5 for all variables. This indicates that all variables can be used for the FA.

Factor 1 explains about 45.26 % of the total variance, had high positive loadings for EC, TH, HCO_3, Ca^{2+}, Na^+, Cl^- and SO_4^{2-}. These loadings suggest that the observed pattern is likely a consequence of interactions between minerals and water.

Factor 2 accounts for 14.37% of the total variance and have high positive loadings for Mg^{2+} and moderately negative loading for BOD_5. These can be related to the anthropogenic activities.

Factor 3 represents about 10.58 % of the total variance. This shows high positive loadings for CO_3^{2-} and moderately absolute loading for DO, pH and T°. This indicates that the temperature has no influence on dissolution of carbonate minerals. The variables of NO_2^- and NO_3^- contribute strongly to the factor 4. This explains 6.69 % of the total variance and is probably related to anthropogenic activities such as sanitation activities and the agricultural practice.

4.4. Hydrochemical Classification

According to the chloride contents, 7 samples (19.44%) present a main type of oligohaline-fresh (low salinity; code g, Cl^- <0.141 meq/l), 5 samples present a fresh type, 2 samples present a brackish type, 3 samples brackish salty and the majority

Table 3- Scores of factor analysis of the physico-chemical parameters.

Parameter	F1	F2	F3	F4
T°	0.1862	0.5513	**-0.5565**	-0.2485
pH	-0.5015	-0.2236	**0.5969**	-0.0931
EC	**0.9828**	-0.0244	-0.1023	0.0181
DO	0.0206	0.0304	**0.6537**	-0.1118
TH	**0.9430**	0.2701	-0.1039	-0.0469
CO_3^{2-}	-0.0888	0.0113	**0.7788**	0.0244
HCO_3^-	**0.9046**	-0.1137	-0.1600	0.1060
Ca^{2+}	**0.9852**	0.0045	-0.0734	-0.0289
Mg^{2+}	0.0064	**0.8272**	-0.1052	-0.0601
Na^+	**0.9740**	-0.1161	-0.0640	0.0279
Cl^-	**0.9760**	-0.0542	-0.0872	0.0381
SO_4^{2-}	**0.8126**	0.3371	0.0207	-0.2183
NO_2^-	-0.1125	0.1003	-0.0350	**0.8316**
NO_3^-	0.1513	-0.3101	-0.0580	**0.7642**
BOD_5	0.0042	**-0.6552**	-0.0573	0.0093
Eigen value	6.7891	2.1563	1.5880	1.0041
Variance (%)	45.2606	14.3753	10.5866	6.6943
Cumulative variance (%)	45.2606	59.6359	70.2225	76.9168

presents (19 samples) 52.78% a main type of fresh brackish water of code f (Table 4). Based on the average chemical elements, the water subtypes are characterized by a dominance of Cl^-, SO_4^{2-} and Na^+. The concentrations of HCO_3^- of 16 samples range between 2-4 meq/l (44.44%), of 3 samples range between 8-16 meq/l and of 17 samples (47.22%) range between 4-8 meq/l. The alkalinity of all these samples are moderate to moderately high ranging between 2-16 meq/l (code 2, 3 and 4). This is originated from the dissolution of gypsum and/or limestone. According to the Stuyfzand classification, waters revealed a class in surplus of code (+) (high concentrations of K, Na and Mg), these concentrations are thought to originate from the processes of dissolution of the evaporates (Triassic undergrounds surrounding).

4.5. Suitability of Thermal Waters for Irrigation

The evaluation indices of the suitability of thermal waters in the study area for irrigation are reported in Table 5. The results of Na^+% showed that 7 sampling locations have excellent water quality, 13 sampling locations represent Good quality; 11 sampling locations represent Permissible quality and 5 sampling points report Doubtful quality (Figure 6).

The calculation of MAR shows that all the sampling locations have concentrations lower than 50 (i.e. acceptable class). Therefore, the water samples are classified as usable for irrigation.

The PI values show 3 classes, of which the majority 30 (83.33%) of the 36 water points have good water quality, the RSC values are low, not reaching 1.25 meq/l for all of the examined water samples.

EC reflect that the thermal waters of our study area, the majority (72.22%) have a permissible class, except for the region of Guerfa, Grouz and Oued Bouhamdane (Figure 2a, b and f) have a Doubtful quality. Additionally, Hammam Beni Guechat (Figure 2d) demonstrates unsuitable water quality due to its high salinity levels, which are likely to have a detrimental impact on the soil and plants.

Regarding the risk related to sodium, the waters are characterized by a SAR below 10 presenting a minimal risk of Na^+ accumulation. 3 samples present a high risk of alkalization. This shows that the waters may affect the permeability and cause infiltration problems.

Based on the US Salinity diagram (Figure 7) by Richards in 1954, we classified the thermal waters

Table 4- Stuyfzand classification.

	Classification level	Code	Number of samples	In %
Principal type	**[Cl^-] (meq/l)**			
Oligohaline	<0.141	G	-	-
Oligohaline-fresh	0.141 - 0.846	g	7	19.44
Fresh water	0.846 - 4.231	F	5	13.89
Brackish fresh water	4.231 - 8.462	f	19	52.78
Brackish water	8.462 - 28.206	B	2	5.56
Brackish salt	28.206 - 282.064	b	3	8.33
Saltwater	282.064 - 564.127	S	-	-
Hyperhaline	>564.127	H	-	-
Type	**[HCO_3^-] (meq/l)**			
Very low	<0.5	*	-	-
Low	0.5-1	0	-	-
Moderately low	1-2	1	-	-
Moderate	2-4	2	16	44.44
Moderately high	4-8	3	17	47.22
High	8-16	4	3	8.33
Very High	16-32	5	-	-
Rather extreme	32-64	6	-	-
Extreme	>64	7	-	-
Classes	**IEB= $Na^+ + K^+ - 0.8768 * Cl^-$**			
Deficit of ($Na^+ + K^+ + Mg^{2+}$)	< 0	-	12	33.33
Equilibrate of ($Na^+ + K^+ + Mg^{2+}$)	= 0	0	-	-
Surplus of ($Na^+ + K^+ + Mg^{2+}$)	> 0	+	24	66.67

in the study area based on salinity and SAR. Most of the waters (group 2 and majority of group 1) are of acceptable quality (C3-S1). However, some water points in Guerfa (group 3) (Figure 2b) and Oued Bouhamdane (Figure 2a) are classified as doubtful quality (C4S2). Beni Guechat (group 4) (Figure 2d) has unsuitable water quality. Overall, the waters have relatively low SAR, making them suitable for irrigating salt-tolerant crops on well-drained soils. Salinity levels need to be monitored.

Figure 6- Direct discharge of effluents heavily loaded with minerals and surfactants into the valley without pre-treatment.

The Wilcox (1955) diagram based on Na^+% and conductivity shows that most of the samples fall into the category of good to permissible water except for group 4 (unsuitable for irrigation) and group 3 (doubtful quality) (Figure 8). According Bremond and Vuichard (1973), water is difficult to use for irrigation as soon as it exceeds 1,500µS/cm. The level of irrigation water quality always depends on the soil type and the crops grown (Rodier, 2005).

5. Results

Physico-chemical parameters and hydrochemical techniques were used to describe the quality of the thermal waters used for irrigation in the study area. The study was based on 36 water samples (springs,

discharges and wadi). Q-mode cluster analysis was applied to the thermal water quality datasets and generated four groups of clusters (groups 1, 2, 3 and 4). Group 1 represents low salinity and Na^{+}-HCO_3^{-} partition orders. Group 2 is dominated by sulphate, bicarbonate and sodium. Chloride is also present in significant concentrations. Group 3 is dominated by sulphates and magnesium. However, they also contain significant concentrations of chloride. Group 4 is characterized by the thermal spring of Beni Guechat.

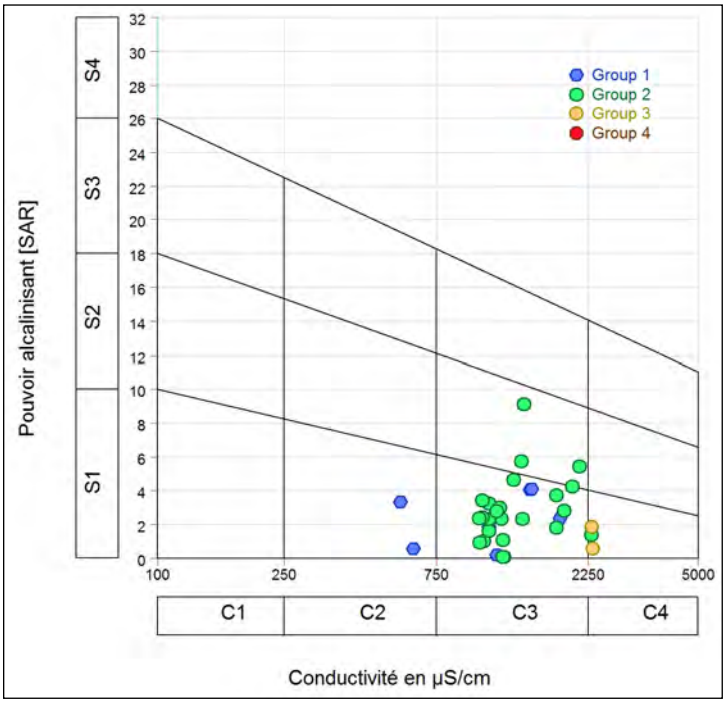

Figure 7- Classification of irrigation water using the Richards SAR method.

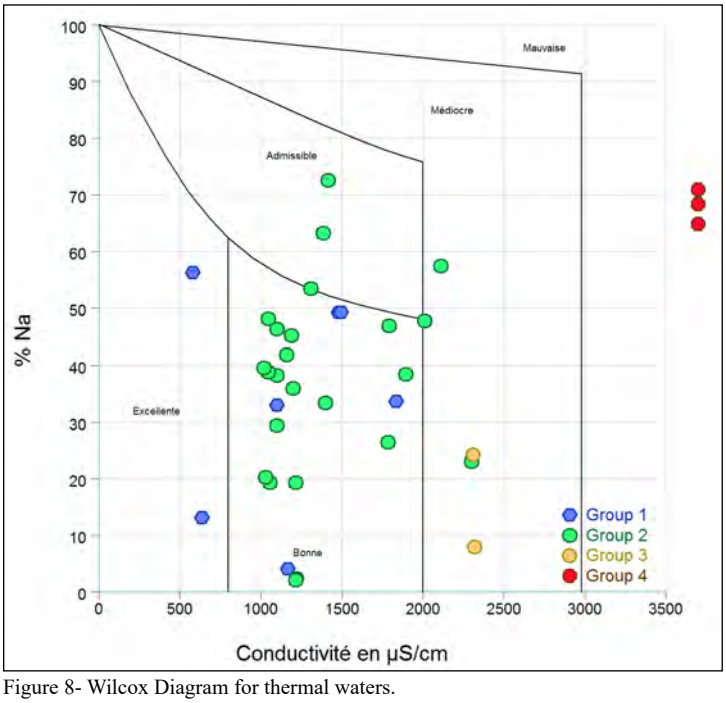

Figure 8- Wilcox Diagram for thermal waters.

Table 5- Suitability of thermal waters for irrigation according to the different classification indices.

Na^+ % (meq/l)	Class	Number of samples	In %
<20	Excellent	7	19.44
20-40	Good	13	36.11
40-60	Permissible	11	30.56
60-80	Doubtful	5	13.89
>80	Unsuitable	-	-
EC (Ds/m)			
<0.25	Excellent	-	-
0.25-0.75	Good	2	5.56
0.75-2	Permissible	26	72.22
2-3	Doubtful	5	13.89
>3	Unsuitable	3	8.33
SAR (meq/l)			
2-10.	Low	18	50.00
10-26	High	3	8.33
>26	Very High	-	
MAR (meq/l)			
<50	Permissible	36	100
>50	Unsuitable	-	-
PI (meq/l)			
>75	Very Good	3	8.33
25/75	Good	30	83.33
<25	Unsuitable	3	8.33
RSC (meq/l)			
<1.25	Good	36	100
1.25-2.5	Doubtful	-	-
>1.5	Unsuitable	-	-

The samples of this group are heavily mineralized. Cl^-, Na^+ and SO_4^{2-} are the most dominant ions.

The Stuyfzand classification revealed that the waters are moderately to moderately high alkaline, refreshing brackish. The fundamental interactions between the fluids and the clay minerals are reflected in these classes. The distribution of the physico-chemical characteristics showed that the Triassic formations are located near the high levels of RS, Cl^- and Na^+, either near the discharges or downstream of the wadis. The analysis of water quality indicators for irrigation use showed that, overall, the waters can be used without special treatment during the irrigation of crops with moderate salt tolerance on well-drained or well-permeable soils.

Hydrothermal effluents are highly charged waters and discharged into the environment without prior treatment. To better assess this impact, it would be necessary to monitor its evolution in time and space. The work requires more in-depth field studies and specific protocols. The planned next study will deal with trace metals (TMEs) and surfactants in order to monitor and predict the impact of effluents on surface and groundwater.

Acknowledgement

The authors would like to acknowledge the Special thanks to UNESCO (United Nations Educational, Scientific and Cultural Organization), IUGS (International Union of Geothermal Sciences) in the framework of the International Geoscience Program (IGCP 636). The authors thank also the DGRSDT (The Directorate General for Scientific Research and Technological Development, under the aegis of the Ministry of Higher Education and Scientific Research in Algeria). The authors would like to express their thanks to the anonymous reviewers of this manuscript, for their critical review and helpful discussions.

References

Alberto, W. D., del Pilar, DaMa., Valeria, AMa., Fabiana, P. S., Cecilia, H. A., de los Ángeles, BMa. 2001. Pattern Recognition Techniques for the Evaluation of Spatial and Temporal Variations in Water Quality. A Case Study: Suquýia River Basin (Córdoba–Argentina) Water Res., 35, 2881- 2894.

Alther, G. A. 1979. A simplified statistical sequence applied to routine water quality analysis: a case history. Ground Water 17:556–561.

APHA. 2005. Standard methods for the examination of water and wastewater, 19thed. American Public Health Association, Washington, DC, 1–467.

Bails, J. 1888. Les sources thermales et minérales du département d'Oran.

Barkat, A., Bouaicha, F., Bouteraa, O., Mester, T., Ata, B., Balla, D., Rahal, Z., Szabó, G. 2021. Assessment of Complex Terminal Groundwater Aquifer for Different Use of Oued Souf Valley (Algeria) Using Multivariate Statistical Methods, Geostatistical Modeling, and Water Quality Index. Water 13 (11), 1609.

Belkhiri, L., Boudoukha, A., Mouni, L., Baouz, T. 2010. Application of multivariate statistical

methods and inverse geochemical modeling for characterization of groundwater a case study: Ain Azel plain (Algeria) Geoderma, 159, 390-398.

Belkhiri, L., Boudoukha, A., Mouni, L., Baouz, T. 2011. Statistical categorization geochemical modeling of groundwater in Ain Azel plain (Algeria). J Afr Earth Sci 59, 140–148.

Belhai, M., Fujimitsu, Y., Bouchareb-Haouchine, F.Z., Haouchine, A., Nishijima, J. 2016. A hydrochemical study of the Hammam Righa geothermal waters in north-central Algeria. Acta Geochimica 35, 271–287.

Belhai, M., Fujimitsu, Y., Nishijima, J., Bersi., M. 2017. Hydrochemistry and gas geochemistry of the northeastern Algerian geothermal waters. Arabian Journal of Geosciences 10, 743.

Bouaicha, F. 2018. Le géothermalisme de la région de Guelma. Thèse de Doctorat en sciences, Université Constantine1, Algérie (in french).

Bouaicha, F., Hénia, D., Oualid, B., Nabil, M., Nabil, C., Kamel, B., Abdeslam, D. 2019. Geochemical assessment, mixing and environnemental impact of thermal waters in the Guelma geothermal system, Algeria. Acta Geochim.

Bouchareb-Haouchine, F. Z. 2012. Etude Hydrochimique des Sources Thermales de l'Algérie du Nord-Potentialités Géothermiques (Doctoral dissertation, These Doctorat en Sciences, USTHB, Algiers, 135.

Bouchareb-Haouchine, F. Z., Issaad, A., Bendhia, H. 1994. Estimation and interpretation of geothermal gradient in Northern Algeria. Bull. Surv. Geol. Algeria, 5, 69-74.

Boutreraa, O. 2019. Groundwater quality assessment using multivariate analysis, geostatistical modeling, and waterquality index (WQI): a case of study in the Boumerzoug-El Khroub valley of Northeast Algeria.

Bremond, R., Vuichard, R. 1973. Paramètres de la qualité des eaux. Ministère de la protection de la nature et de l'environnement. SPEPE, Paris, 179.

Brown, C. E. 1998. Applied multivariate statistics in geohydrology and related sciences. Springs, Berlin.

Cormy, G., Demians d'Archimbaud, J. 1970. Les possibilités géothermiques de l'Algérie. Geothermics 2, 110–116.

Cornet, A. 1964. Introduction à l'hydrogéologie Saharienne. SNED, Alger Algérie, 572.

Delga, D. 1969. Mise au point sur la structure Nord Est de la bamenu. Pub ser carte géol Algérie.NS. bull, 19, Alger.p89-131; Eaton FM, Soil Science. 69 (1950) 123-134.

Dib, H. 1985. Le thermalisme de l'Est algérien. Thèse de doctorat 3ème cycle, I.S.T. USTHB, Alger, Algérie, 315.

Dib, H. 2008. Guide pratique des sources thermales de l'Est algérien. Editions du Service Géologique national (Alger): 106.

Djemmal, S. 2018. Etude des sources thermominérales de la région de Sétif dans leur contexte structural (Est algérien). I.N.S.T.U, département de géologie. Université de Batna 2. Algérie.

Doneen, I. D. 1964. Notes on Water Quality in Agriculture. Published as a Water Science and Engineering, Paper 4001, Department of Water Sciences and Engineering, University of California, Davis.

Eaton, F.M. 1950. Significance of carbonates in irrigation waters. Soil Sci. 69: 123-133

EURAFREP. 1966. Appréciations sur les possibilités géothermiques de l'Algérie du Nord-Est.

ENEL. 1982. Etude de reconnaissance géothermique du constantinois oriental. Rapport général. Rapport interne. SONELGAZ, Algérie, 135p.

Facca, G. 1966. Appréciations sur les possibilités géothermiques de l'Algérie du Nord-Est.

Farnham, I. M., Stetzenbach, K. J., Sing, A. K., Johannesson, K. H. 2000. Deciphering groundwater flow systems in Oasis Valley, Nevada, using trace element chemistry, multivariate statistics, and geographical information system Mathematical Geol., 32, 943-968.

Fekraoui, A. 2010. Geothermal Activities in Algeria. Proceedings World Geothermal Congress.Bali, Indonesia, 25-29.

Foued, B., Hénia, D., Lazhar, B., Nabil, M., Nabil, C. 2017. Hydrogeochemistry and geothermometry of thermal springs from the Guelma region, Algeria. J Geol Soc India 90, 226–232.

Guigue, S. 1940. Les sources thermominérales de l'Algérie. Serv. Carte Géol. De l'Algérie. (Algerie. 3ème série, 5ème fasc).

Guigue, S. 1947. Les sources thermominérales de l'Algérie. Serv. Carte Géol. De l'Algérie. (Algerie. 3ème série, 9ème fasc).

Hanriot, M. 1911. Les eaux minérales de l'Algérie. H. Dunod. E. Pinat éditeurs. Paris.

Issaâdi, A. 1992. Le thermalisme dans son cadre géostructural. Apports à la connaissance de l'Algérie profonde et de ressource géothermales. Thèse doc. d'état. FSTGAT-USTHB. Alger. Algérie, 267.

Kaiser, H. F. 1960. The application of electronic computers to factor analysis. Educational and Psychological Measurement, 20, 141-151.

Kedaid, F. Z. 2006. Développement de la base de données géothermique de l'Algérie par un système d'information géographique. Revue des Energies Renouvelables, 9 N°4, 253 – 258.

Kouadra, R., Demdoum, A., Chabour, N., Benchikh, R. 2018. The use of hydrogeochemical analyses and multivariate statistics for the characterization of thermal springs in the Constantine area, Northeastern Algeria. Journal of Acta Geochim.

Laissoub, B. 1974. Etude des eaux minérales, thermales et thermominérales en Oranie. Le ministère de l'énergie, 2017. Programme des énergies renouvelables et de l'efficacité énergétique.

Liu, C. W., Lin, K. H., Kuo, Y. M. 2003. Application of factor analysis in the assessment of groundwater quality in a blackfoot disease area in Taiwan. Sci Total Environ 313, 77–89.

Maouche, S., Abtout, A., Merabet, N. E., Aïfa, T., Lamali, A., Bouyahiaoui, B., Bougchiche, S., Ayache, M. 2013. Tectonic and Hydrothermal Activities in Debagh, Guelma Basin (Algeria). Journal of Geological Research 2013, 1–13.

Meghraoui, M. 1988. Géologie des zones sismiques du Nord de l'Algérie. Paléosismologie, Tectonique Active et Synthèse sismotectonique, Paris Sud Orsay, France, Paris, 362.

Meng, S. X., Maynard, J. B. 2001. Use of statistical analysis to formulate conceptual models of geochemical behavior: water chemical data from the Botucatu aquifer in São Paulo state, Brazil Jour. Hydrol., 250, 78- 97.

Piper, A. M. 1944. A graphic procedure in the geochemical interpretation of water-analyses. Trans AGU 25, 914.

Pouget, I., Chouchak, D. 1923. Radioactivité des eaux minérales du département de Constantine.

Pouget, I., Chouchak, D. 1926. Radioactivit des eaux minérales du département d'Oran (Ibid., XIV, pp. 347-360).

Raghaunth, H. M. 1989. Groundwater Wiley Eastern Ltd New Delhi, 563.

Richards, L. A. 1954. Diagnosis and improvement of saline and alkali soils. Édit. US Department of Agriculture, Agricultural Handbook n° 60, Washington (USA), 160.

Rezig, M. 1991. Etude géothermique du Nord Est de l'Algérie. Université Montpellier II Sciences et Techniques du Languedoc (Montpellier).

Rodier, J. 2005. L'analyse de l'eau. Eaux naturelles, eaux résiduaires, eau de mer, 8e édition. (Ed)., Dunod, 1382.

Saibi, H. 2009. Geothermal resources in Algeria. Renewable and Sustainable Energy Reviews 13, 2544–2552.

Stuyfzand, P. J. 1989. A new hydrochemical classification of watertypes. IAHS Publ. 182, 89-98.

Vila, J. M. 1978. Carte structurale au 1/500 000 de la chaîne alpine d'Algérie orientale et des confins Algéro-Tunisiens. C.N.R.S & B.E.I.CI.P., France.

Vila, J. M. 1980. La chaine alpine d'Algérie orientale et des confins algérotunisiens. Thèse doctorat, univ de Pierre et Marie Curie, vol 2, Paris VI. France, 665.

Ville, M. 1852. Recherche sur les roches, les eaux et les gites minéraux des provinces d'oran et d'Alger.

Verdeil, P. 1982. Algerian thermalism in its geostructural setting. How hydrogeology has helped in the elucidation of Algeria's deep-seated structure. Journal of Hydrology 56, 107– 117.

Ward, Jr J.H. 1963. Hierarchical grouping to optimize an objective function Jour. Amer. Statis. Assoc., 58, 236-244.

Wilcox, L.V., US 1953. Geological Department Agriculture. Circ, 969, 19.

Wilcox, L.V. 1955. Classification and use of irrigation waters. U.S. Dept. Agric. Circular 969, Wash., U.S. Dept. Agric., DC, 19.

Williams, R. E. 1982. Statistical identification of hydraulic connections between the surface of a mountain and internal mineralized sources Groundwater, 20, 466-478.

WHO. 2006. Guidelines for drinking water quality: Recommendations, 1, 3. World Health organization, Geneva.

Bulletin of the Mineral Research and Exploration

http://bulletin.mta.gov.tr

Importance of reinjection in sustainability of geothermal resources and reinjection well locations in Türkiye

Nilgün DOĞDU[a*] and Oktay ÇELMEN[a]

[a] *General Directorate of Mineral Research and Exploration, Energy and Raw Materials Department, 06530, Ankara, Türkiye*

Research Article

Keywords:
Reinjection, Geothermal Resource, Sustainability, Reinjection Location.

ABSTRACT

Sustainability of geothermal energy is related with the type of geothermal resources (natural springs, well), usage situations (thermal, residential-greenhouse heating, energy, etc.), amount of use (optimal flow, appropriate pressure-temperature changes), conservation of resources, and is mostly achieved by reinjection of the geothermal fluid returning from usage. It is important to take measures to prevent adverse changes in temperature and pressure conditions in the reservoir to properly remove the fluid returning from use in geothermal areas from the environment and recharge the reservoir. Reinjection should be carried out under appropriate conditions for the protection of resources. In the operation of geothermal resources, reinjection/discharge conditions and obligations are also specified in the provisions of the Law No. 5686 and the implementing regulation. Various studies within the scope of exploration activities in geothermal fields, determining the production-reinjection areas and determination the location of the reinjection wells in conditions that will not adversely affect the production pressure-temperature conditions are of great importance for the sustainability of the geothermal reservoir.

Received Date: 17.10.2022
Accepted Date: 19.06.2023

1. Introduction

Ideal geothermal systems constitute four parameters, namely, (1) the heat source within the crust of a size and age that can form a geothermal system at an economical depth, (2) porous and permeable reservoir that are related with faults and fracture networks that have hydraulic channels for the transport of hot fluids in the reservoir zone, (3) the impermeable cap rock that keeps the heated fluid in the reservoir and maintain its heat, and (4) a suitable recharge area that naturally recharge the geothermal reservoir (Figure 1).

The heat source in a geothermal system is the heat originating from the mantle of the earth and this heat can be transported either conductively (radiation of heat) or convectively (with the movement of a substance, where it is carried by water). As a result of the solid crust (lithosphere) folding and fracturing along tectonic lines caused by movements of the earth's crust and magma differentiation in the upper mantle, the heat in the depths of the earth can reach shallow depths in the crust as a result of magmatic intrusions and volcanic activities. Lithological units formed by these folding and fractures forms reservoir zones within fractures. In that systems, water infiltrates the earth through faults and fractures, where it warms up in contact with magmatic intrusions and rises through faults or by the pressure force between descending cold water and rising hot water temperature. However,

Citation Info: Doğdu, N., Çelmen, O. 2023. Importance of reinjection in sustainability of geothermal resources and reinjection well location. Bulletin of the Mineral Research and Exploration 171, 159-175. https://doi.org/10.19111/bulletinofmre.1316785

**Corresponding author: Nilgün DOĞDU, nilgun.dogdu@mta.gov.tr*

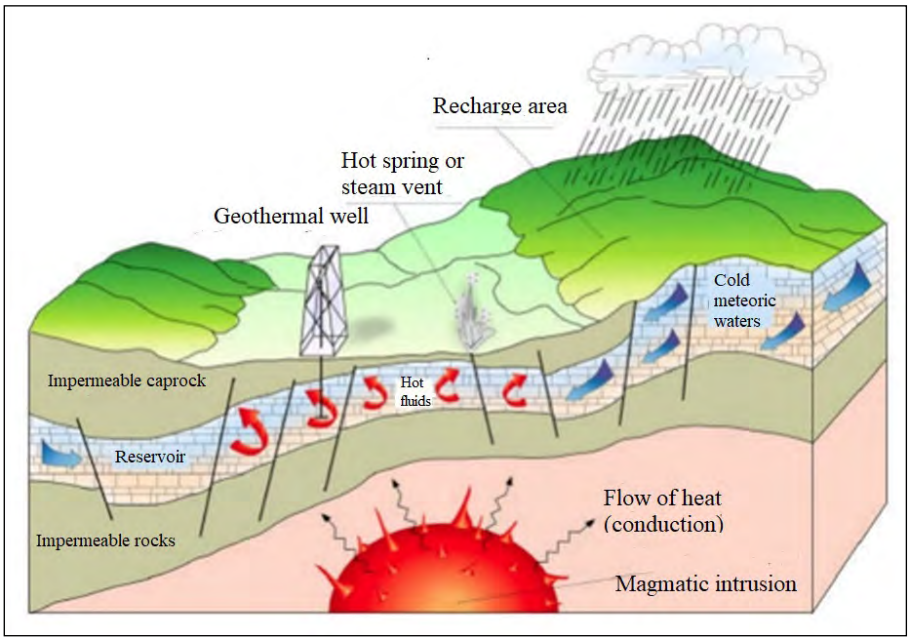

Figure 1- Schematic representation of a geothermal system (Barbier, 2002).

most of the time, in geothermal systems, the heat transport is not by the water circulation in contact with the magma, but also by the heat transfer from the mantle and crust to the earth. Meteoric waters infiltrate deep through fissures and fractures in the ground, and, after being heated in the above-mentioned heat anomaly areas, rise again towards the surface to economically shallow depths. The heated fluid carried upwards that can be stored in the crust economically at shallow depth in porous and permeable lithological units and/or zones. The geothermal reservoir must be connected to a recharge area over long distances so that it can be recharge continuously. In order for geothermal reservoir to remain protected without losing its energy, there must be an impermeable cover rock to prevent heat and fluid loss (Figure 2).

The concept of sustainability in geothermal systems covers the operation of the fluid obtained from the geothermal reservoir without changing its

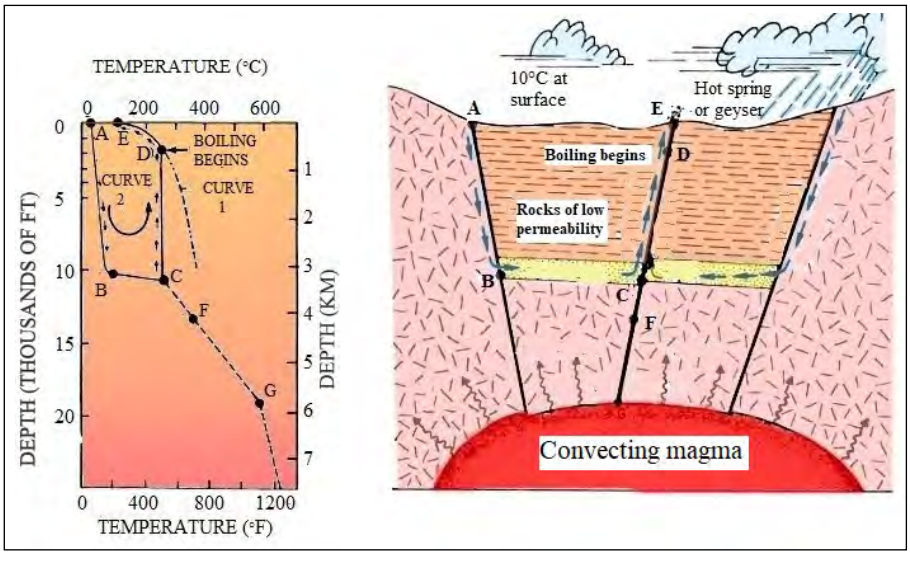

Figure 2- Conceptual model of a high-temperature geothermal system (White, 1973).

physical properties such as temperature, pressure and chemical structure negatively and, also, the protection of the geothermal resource from pollution effects. In order to ensure sustainability, geothermal fluids should be produced at optimum production rates and reinjected properly to ensure production-reinjection balance (Figure 3).

2. Reinjection in Geothermal Reservoirs

The first reinjection applications started in high-temperature, electricity-generating areas such as The Geysers, U.S.A. (1969), Otake, Japan (1972), Larderello, Italy (1974), Hatchobaru, Japan (1977), Kakkonda, Japan (1980) and Onuma, Japan (1981). Reinjection was primarily carried out to dispose of waste water from geothermal use. Later, reinjection became a "science" in the form of monitoring the reinjection process, and determining the reinjection strategy specific to each geothermal area due to its impact on the reservoir and the environmental (Kamila et al., 2021). Geothermal reinjection involves injecting energy-depleted fluid back into geothermal systems, providing an effective mode of waste-water disposal as well as supplementary fluid recharge (Axelsson, 2013). In heating and energy projects where geothermal water is used, reinjection of the water returning from use is necessary in order to keep high temperature and pressure conditions in balance and to prevent a decrease in flow rate.

In geothermal reservoirs where the liquid phase is dominant, the water temperature is lower than the evaporation temperature and stays in the liquid water phase. In terms of protection of the system and phase transition, it should be considered that a decrease in the amount of fluid has a risk of adversely affecting the reservoir pressure, and reinjection will have a positive effect in this case. However, in a high enthalpy geothermal reservoir used for electricity generation, a reservoir pressure decline can result to the reservoir temperature to be higher than the evaporation temperature that leads to more steam generation.

In two-phase geothermal reservoirs, there is a combination of liquid water and steam. High permeability and secondary porosity due to fractures, are important reservoir characteristics for this type of reservoir. The risk of pressure decline may affect

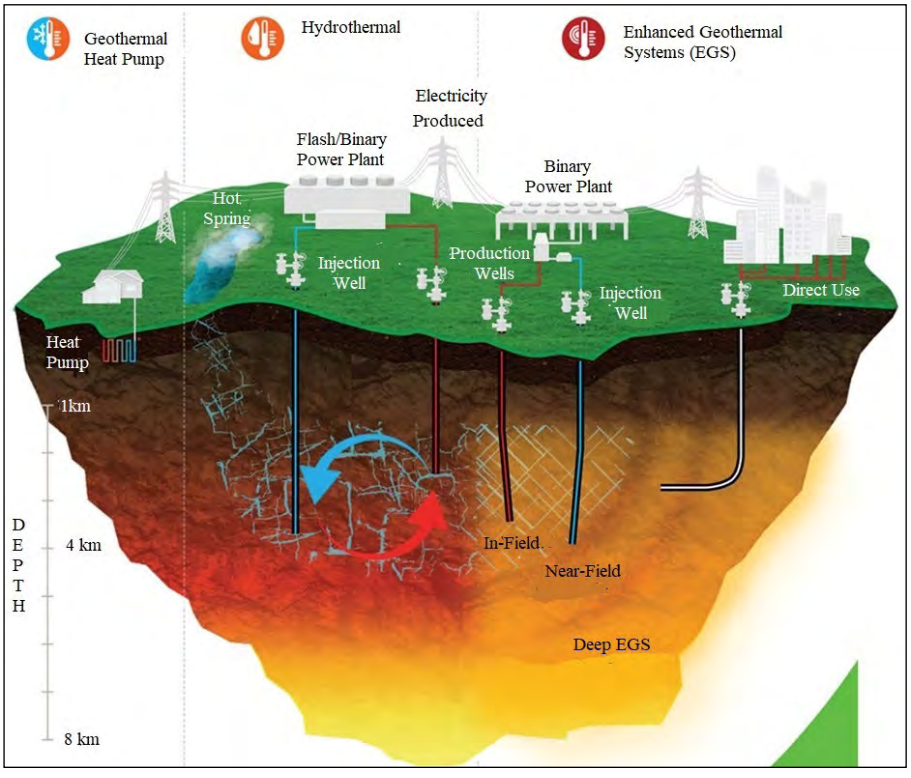

Figure 3- Operation conditions in different geothermal systems (Roberts, 2020).

reservoir very quickly. In such systems, as long as the production-reinjection balance is maintained, only short-term changes in pressure and temperature may be observed. In both relatively-low enthalpy areas with temperatures below 150°C and high enthalpy areas with temperatures above 150°C, the reinjection policy varies according to the purpose of use.

In geothermal reservoirs where steam phase is dominant, the fluid temperature is higher than the vapour pressure and the steam phase is dominant. In these reservoirs, it is important that the reinjection operation recharge the reservoir system continuously.

Below are the following reasons for conducting reinjection studies in geothermal fields are;

- Reduce pressure decline due to production and slow recharge,
- Prevent environmental pollution,
- Recover thermal energy after usage,
- Sustain energy in the reservoir to ensure the sustainability of the area, and
- Prevent subsidence and any surface movement on the surface due to mass extraction.

Reinjection also sustains pressure sustainability of the reservoir, reduce ground subsidence risk and be used to maintain significant surface thermal activity (Figure 4).

The amount of energy taken from the reservoir can be increased by recovering the mass and energy loss that occurs with production. Due to reservoir pressure decline, production from the geothermal wells may decrease. Since the liquid dominant phase controls reservoir pressure, protecting the amount of liquid phase will also protect the reservoir pressure.

In Türkiye, 90-100% reinjection of used thermal fluids is one of the indispensable reservoir management activities in curently operating geothermal power plants. In space heating (housing or greenhouse), approximately 70% of the used fluid is reinjected although sometimes geothermal fluid that used for direct heating may also used for thermal facilites and other integrated purposes.

If reinjection is not done properly in geothermal areas, the reservoir pressure may decrease and sometimes collapses may occur due to the decrease in the water level. On the other hand, geothermal

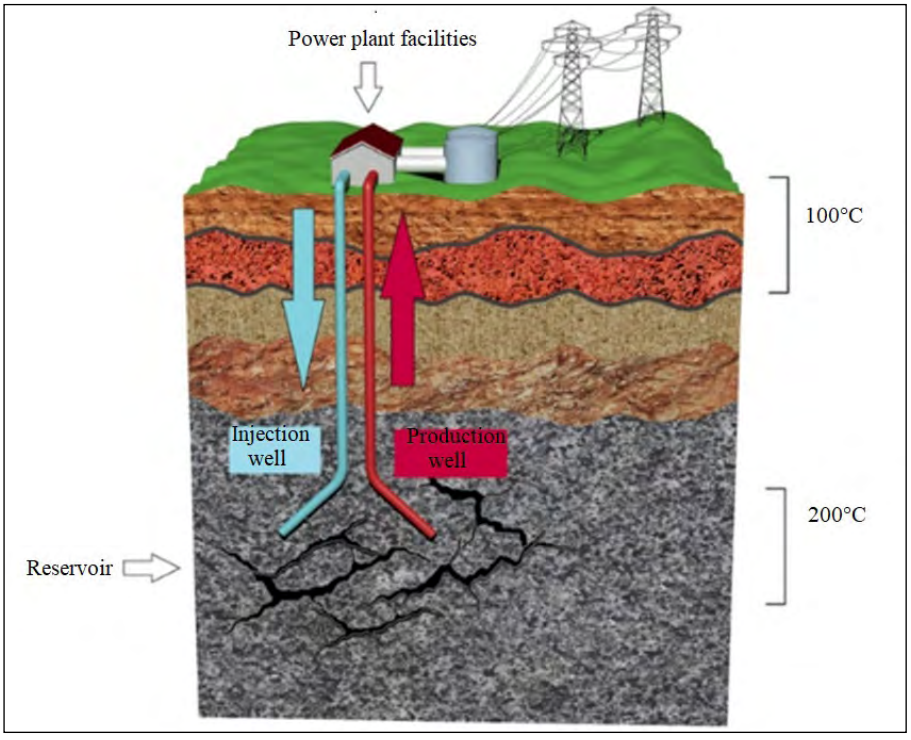

Figure 4- Scheme of deep geothermal system, production and injection wells (Vitaller et al., 2019).

resources that classified as renewable energy sources, cannot be renewed with the lack of reinjection and may be short-lived and run out. If reinjection is not performed under suitable conditions, it may cool and cause scaling, corrosion, etc. in the reservoir and also may adversely affect the surface waters.

The reinjection system, such as, distance to other wells (production/reinjection), amount of reinjected fluid, temperature, chemical properties, evaluation of short-term and long-term effects of thermal fluids, play an important role in the sustainable operation and development of the geothermal reservoir. The use of different and appropriate reinjection strategies in different geothermal areas requires examination and knowledge of all the technical characteristics of the geothermal area.

For this purpose, geothermal reservoir systems are classified for different purposes according to the active fluid (steam or liquid phase dominant) state in the reservoir, to form the model of the system according to its chemical composition.

Reinjection on the main fault zones of a fault-controlled geothermal system may cause negative results as the reinjected fluid would reach the production wells quickly (e.g.Nevşehir-Kozaklı geothermal field). When the previous surveys are examined in Turkey and the world, it is seen that reinjection strategies varies a lot. The process of reinjection varies in different geothermal fields: location of the recharge area, infield injection in the center of the production area, at the edge and outside of the production area, and either above, at the same level, or below the production zones. It is clear that reinjection can be done from different depths and locations in different reservoir systems in different areas, either by pumping or gravity. The important thing in all these applications is to ensure the sustainability of the field. The chemical properties of the produced fluid play an important role in designing the appropriate reinjection strategy for a geothermal field. To increase the performance of the reservoir, the geological structure of the area should be known in detail considering that the rapid routes from reinjection to reservoir, such as faults and fractures to avoid shallow circulation.

In the case of overproduction, reservoir collapse may occur due to pressure loss, water level decline and, consequently, the weight of the rocks/sediments above the reservoir may subside. Reinjection of the used fluid is a best practice for reservoir management that sustains reservoir pressure and prevent any reservoir collapse.

After the reinjection well is drilled, well tests (including injectivity, tracer, pressure fall-off and build-up, etc.) should be carried out to determine the optimal production-reinjection amount balance and prevent anomalous temperature and pressure declines in the reservoir. Chemical analyses should be performed on the water samples collected at least every 3 months in the reinjection wells and ~6 months in the production wells to better understand the parameters and conditions that will cause scaling and, corrosion problems. Chemical analyses also give some clues about whether sustainable production-reinjection process exist or not.

As it is known, both for the regulations of the Law No. 5686 and for the sustainable operation of the geothermal reservoirs, it is obligatory to reinject the used brine from operational activities, especially for space heating and electircity generation purposes. In such activities, reinjection at a suitable locations and conditions not only prevents long-term pressure and temperature drops in the reservoir, but also ensures that the geothermal brine not to harm environment physicochemically. In addition to this, due to geological characteristics or geometric shape of the licensed geothermal area, reinjection activity may not be carried out without causing temperature and pressure declines in the reservoir. In such cases, sometimes, the geothermal fluid can be operated without recharging the reservoir and/or reinjection may occur in the opposite direction out of the system. In this case, it is necessary to ensure the long-term sustainability of the reservoir by not using large-volume pumps, limiting mass extractionof thermal fluid to balance natural recharge of the geothermal system. If surveys shows that reinjection is technically impossible to perform, then, licensed owner should apply for MTA over Governorship to get permission for other possibilites and reservoir management policy under the Law No: 5686.

In the above cases, the used geothermal brine is reinjected underground to the appropriate formation

without significantly affecting the environment especially surface waters and near-surface aquifers while maintaining the pressure recharge process that is critical for the sustainability of the geothermal resource. It should be noted that disposing used geothermal fluid underground should be applied only in technically imperative situations. The main objective in geothermal reservoir management is to reinject the used geothermal fluid into the appropriate formation at a suitable distance (so that the injected brine gets heated up by the hot rocks as it travels back into the reservoir) to ensure the resource long-term sustainability. Mineral scaling due to the inherent chemical properties of the geothermal fluid is one of the most important problems encountered in the operation of geothermal fields. In cases where no precautions are taken, scaling affects the well production, production-reinjection line and other surface facilities, including the power plants, and the chemical properties of the produced fluid that will be reinjcted back. Of course, precautions must be taken to prevent mineral scaling.

In some cases, the first thing that comes to mind for reinjection strategy is to reinject geothermal fluid to some unused geothermal production wells. However, such application may cause cooling of the geothermal reservoir and production wells. Another thought is to recharge the thermal fluids by drilling a deeper well in the same area. Another application is to carry out this operation by drilling a little further away from that field (Atılgan, 1994). In recharging the geothermal fluid to the reservoir by reinjection wells, vertical and lateral wells should be chosen at a distance that will not adversely affect the wells or the reservoir by means of temperature and pressure.

2.1. Legal Regulations

Many regulations have been made in the Geothermal Resources and Natural Mineral Waters Law and Implementation Regulation No. 5686 for the reinjection and discharge-disposal of the produced thermal fluid after the use of geothermal resources. First of all, it is stated in the 3rd Article-Definitions section of the Law and in the 4th Article-Definitions section of the Implementation Regulation that "Reinjection: After the produced geothermal fluids used by artificial methods, all or the remaining part is sent back to the geological formations where they were produced".

In Article 14 of the Law: Regarding discharge in case the reinjection conditions cannot be met, there is a provision that "(4) The licensee may discharge the surplus fluid after usage, taking into consideration the environmental limits. If the contents of fluid does not enable the discharge of the fluid according to environmental limits, the licensee is required to reinject it. However, if General Directorate of Mineral Research and Exploration (MTA) confirms that reinjection is not possible due to the physical and chemical characteristics of the formation, the discharge shall be done by taking measures to prevent environmental pollution" provisions are included.

Article 23 of the Implementation Regulation: Protection of resource reservoirs section; " (2) Measures to protect the reservoir in the resource protection zone area survey; According to the reservoir parameters determined as a result of the production tests carried out before the source is put into operation, the total production amount that can be taken from and on the basis of the well, the amount of the fluid returning from use and the suitable locations for the underground reinjection of this fluid and the number of wells with appropriate capacity, It includes necessary practices to ensure sustainable production in case of detection of compounds that will cause partial or complete blockage of zones and production wells" provisions are included.

Article 24 of the Implementation Regulation: In the discharge and reinjection section, it contains provisions on reinjection application conditions, environmental legislation and its physical and chemical effects. (1) The license holder has done the chemical analysis of the fluid returned from use, by an accredited laboratory. If the chemical composition of the fluid exceeds the environmental limits, it is first purified by appropriate methods and reduced to the limits of the relevant environmental legislation. Then, the appropriate receiving environment is determined. The fluid returning from use is duly discharged to the determined receiving environment. Chemical analysis of the fluid obtained after treatment is performed every three months and it is checked whether it exceeds the environmental limits. (2) The license holder is obliged to reinject if the content of the fluid returning from use is not suitable for discharge according to the environmental limits specified in the environmental

legislation. If there is an existing well that has been dug in the area determined for reinjection and meets the reinjection conditions, it is evaluated. It is determined by making a preliminary assessment whether the fluid will have negative effects on the reservoir where it will be reinjected. If there is no adverse effect, reinjection can be done. If there is a negative effect, reinjection is performed after this effect is eliminated. Observations are continued as long as reinjection is made. In case of negative effects of reinjection on the reservoir and production values, the reinjection process is stopped and a search is made for a new location. (3) If the studies carried out give the result that reinjection is not possible, this situation is forwarded to MTA by the Administration together with all the information and documents, and it is examined, and if necessary, an on-site inspection is carried out by MTA, at the expense of the license holder. If MTA approves that reinjection cannot be performed in the operation license area due to the physical and chemical characteristics of the formation, the discharge is carried out by taking measures to prevent environmental pollution. (4) Reinjection and injection conditions may not be required in detached spa and natural mineral water enterprises outside the integrated geothermal resource usage area. In such cases, the fluid can be duly discharged to the appropriate receiving environment, by taking the opinion of the relevant ministry in terms of environmental legislation.

Articles 25 and 26 of the Implementation Regulation contain provisions regarding the integrated and optimum usage conditions of the geothermal fluid. "25-(4) Except for geothermal fluids suitable for energy generation and heating applications, the fluid is primarily used for health and thermal tourism purposes in areas where other fluids are present. For this purpose, after the exploration, research and development studies related to the fluid, the evaluation regarding whether it is suitable for use for health and thermal tourism purposes is made by the relevant Administration according to its physical, chemical or indication characteristics. In these areas, the part of the geothermal fluid subject to energy production and heating applications, at the temperature and flow rate in the range allowed by the reinjection conditions after these uses, is integrated for health and thermal tourism purposes. In areas where there is geothermal fluid suitable for energy and heating, the use of this fluid for health and thermal tourism purposes is allowed in cases where there is no demand or demand for energy and heating purposes or there is no potential for use." "26-(4) (Changed: OG (Official Gazette))-24/9/2013-28775) Real or legal persons, who have a geothermal fluid operation license suitable for integrated use, must first use the geothermal fluid in greenhouse and organic agriculture heating at the temperature and flow rate allowed by the reinjection conditions. In case the license holder does not establish a greenhouse himself, it is rented to third parties with the approval of the administration, primarily to the existing greenhouses. The administration is required to ensure that the matters specified in this paragraph are provided in the operation projects. The lower and upper limits of the rental price are determined by the administration. While determining the rental price, the prices determined in the nearest cultural and tourism protection and development regions are taken into account".

2.2. The Selection of the Reinjection Area and the Well Locations

Considering all the characteristics of the geothermal area and the reinjection under appropriate conditions ensure the sustainability of the geothermal resources. In particular, geological data (stratigraphy, lithology, tectonism, hydrogeology), borehole data (litostratigraphy, definitions, changed temperature in depth), geophysical data, well logs, flow rates, hydrogeochemical datas (temperatures of springs and wells, chemical compositions) are very important in addresing this issue. The additional factors affecting the selection of the reinjection well locations may be the foresight of the temperature changes of geothermal fluid that reach to the production zone.

2.2.1. Using Groundwater Flow Maps for Determining Reinjection Well Locations

By interpreting the geology, stratigraphic units, tectonic structures (fault, graben), well datas, hydrogeological characteristics of the geological units, the reservoir, cap rock and tectonic structure parameters, the flow conditions the reinjection area possible reinjection areas are determined. In this case, the determination of the flowstream paths, fracture network and hydrochemical parameters between the recharge and discharge zones in the area

plays an important role in the determination of the reinjection zone. We can use groundwater flow maps and tracer tests to determine the circulation time, direction and movement of water from the recharge zone to the discharge zone in the geothermal field (Figure 5). Hydrogeologic mapping requires the geology, hydrogeology (hydrologic, topographic, well data), geomorphology and hydrogeochemistry of groundwater as they affect the occurrence, flow and quality of groundwater (Figures 6 and 7).

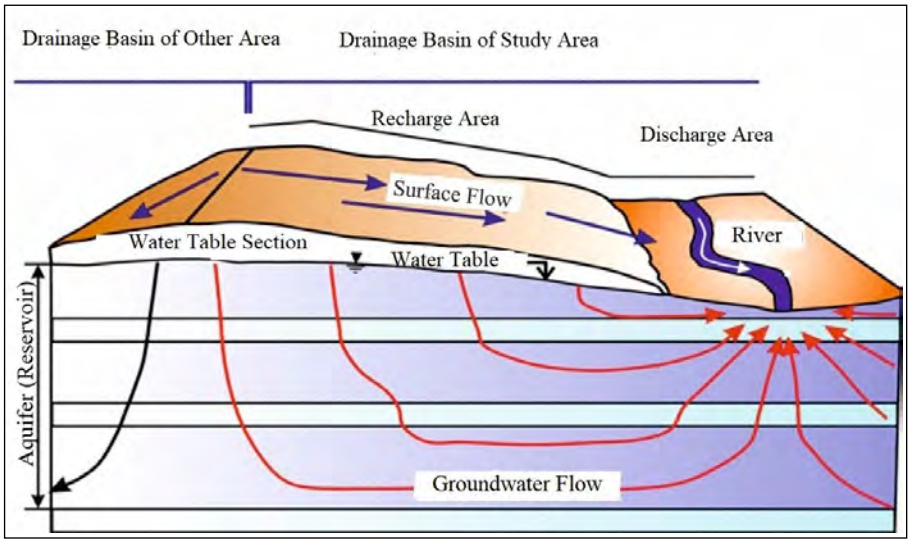

Figure 5- Groundwater drainage basin and flow paths (Tezcan, 2000).

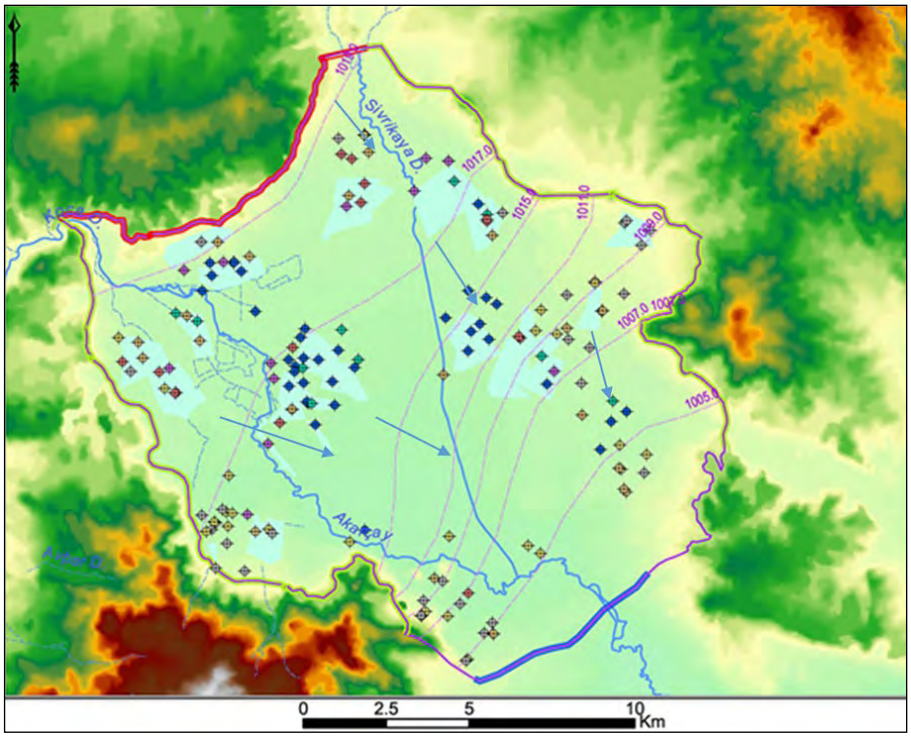

Figure 6- Groundwater flow, flow paths hydrogeological map of Afyon Plain (Doğdu, 2004).

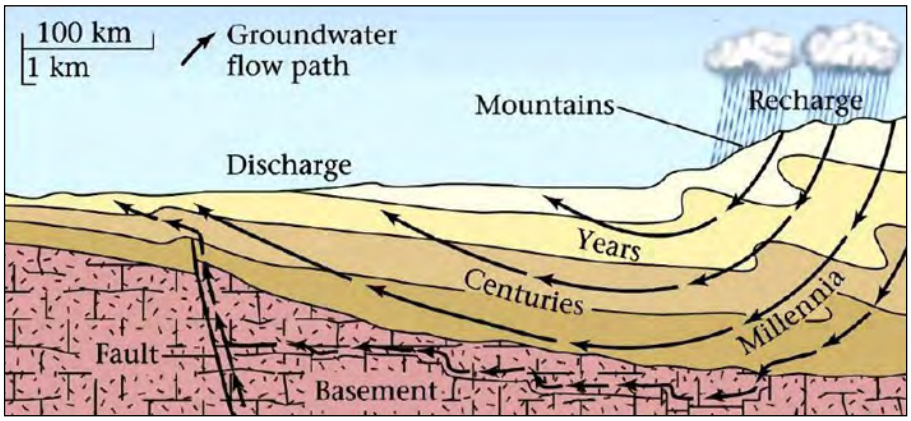

Figure 7- Groundwater flow paths (Şirin, 2019).

2.2.2. Using Tracer Tests for Determining Reinjection Well Locations

Tracer tests are widely used in hydrological and hydrogeological studies such as the determination of groundwater flow rate and direction and source of pollutants in groundwater. In some cases, the exact evaluation of the geothermal field to determine the circulation of production-reinjection system balance is tracer tests.

Tracer testing has become a highly important tool in geothermal research, development and resource management. Its purpose is mainly threefold: (1) general hydrological studies of subsurface flow, (2) reinjection research and management and (3) flow rate measurements in pipelines carrying two-phase geothermal fluids. Their role has, in fact, been more significant in reinjection studies. This ihis is because tracer tests provide information on the nature and properties of connections, or flow-paths, between reinjection and production boreholes. Additionally, it controls the possibility and rate of cooling of the production wells during prolonged re-injection of colder fluid. Enabling such cooling predictions is actually what distinguishes tracer tests in geothermal applications (studies and management) from tracer tests in groundwater hydrology and related disciplines (Axelsson, 2013).

Another important role that tracer testing plays is in geothermal research and management, in particular, concerning heat-transfer efficiency in reinjection operations and EGS development. Advances have been made in the introduction of new tracers, which both add to the multiplicity of available high-sensitivity tracers as well as being increasingly more temperature tolerant. However, the geothermal industry needs to follow advances in other disciplines and adopt those which are useful. In particular, advances in modelling of tracer return data, which has been limited so far, especially modelling of reactive tracer data, which can yield information on flow-channel surface areas in addition to their volumes (Axelsson, 2013).

2.2.3. Using Stable Isotopes for Determining Reinjection Well Locations

In geothermal fields, one of the most important criteria in the determination of the reinjection locations is to identify the recharge zone of the geothermal reservoir in the region. This determination is very important in terms of re-heating the reinjected hot water in the medium- to long-term circulation so that the reinjected fluid is heated by the reservoir rocks before it reaches the production area.

One of the methods used to find the recharge zone is to determine the recharge elevation If the recharge altitude is determined, the geology of the region and the hydrochemical properties of the water can be evaluated together, and the recharge area can be easily found with other geological and hydrogeolocial data.

Stable isotopes are used to determine the recharge elevation of geothermal water (Figure 8). As it is known, the main stable isotopes used in hydrology are the isotopes of oxygen and hydrogen in the structure of water. The ^{1}H-hydrogen isotope with mass number 1 of the element hydrogen has the highest

abundance in nature with 99.985%. The heavy isotope ^{2}H-deuterium, which has a mass number of 2, is less common. The stable isotopes of oxygen and hydrogen are generally used in geothermal waters to enlighten the circulation of water, reveal the extent of water-rock interaction and determine the recharge altitude of the geothermal resource.

Oxygen-18 and deuterium isotopes of precipitation can be used to determine the recharge area of the hot water resources of the regions from precipitation (Mazor, 1991). As the isotopic ratio of atmospheric water vapor rises above sea level, it becomes poorer in heavy isotopes. At the same time, there is a decrease in isotope content with altitude. Although it varies regionally, the $\delta^{18}O$ isotope value of the precipitation water may decrease between 0.15-0.5 per thousand despite every 100 metres of elevation increase. Based on this information, if the oxygen-18 isotope content of any water is known, it is possible to determine the recharge elevation of that water (Figure 8).

To determine the recharge altitude of a geothermal reservoir, first of all, the oxygen-18 and/or deuterium content of the precipitation in the region must be known. However, this data is notknown or has not been measured in some areas. In this case, the oxygen-18 data of cold water sources, which are formed as a result of short-term infiltration of precipitation, can also be used as analog. Thus, the elevation and stable isotope value of cold water, which is formed as a result of short-term infiltration of precipitation, is compared with the elevation and stable isotope value of hot waters.

Three cold water springs were used by Çelmen (2008) to determine the recharge altitude of some hot water springs (BT-1, BT-2, BT-3, BT-5) located in the Ankara-Beypazarı region. The water samples used in the study were BS-3 from Ilıcakpınar spring, BS-4 from Dikmen spring and BS-5 from Tahirler brackish water spring. In the study, the hot water sources of the Beypazarı region is found to have a recharge altitude

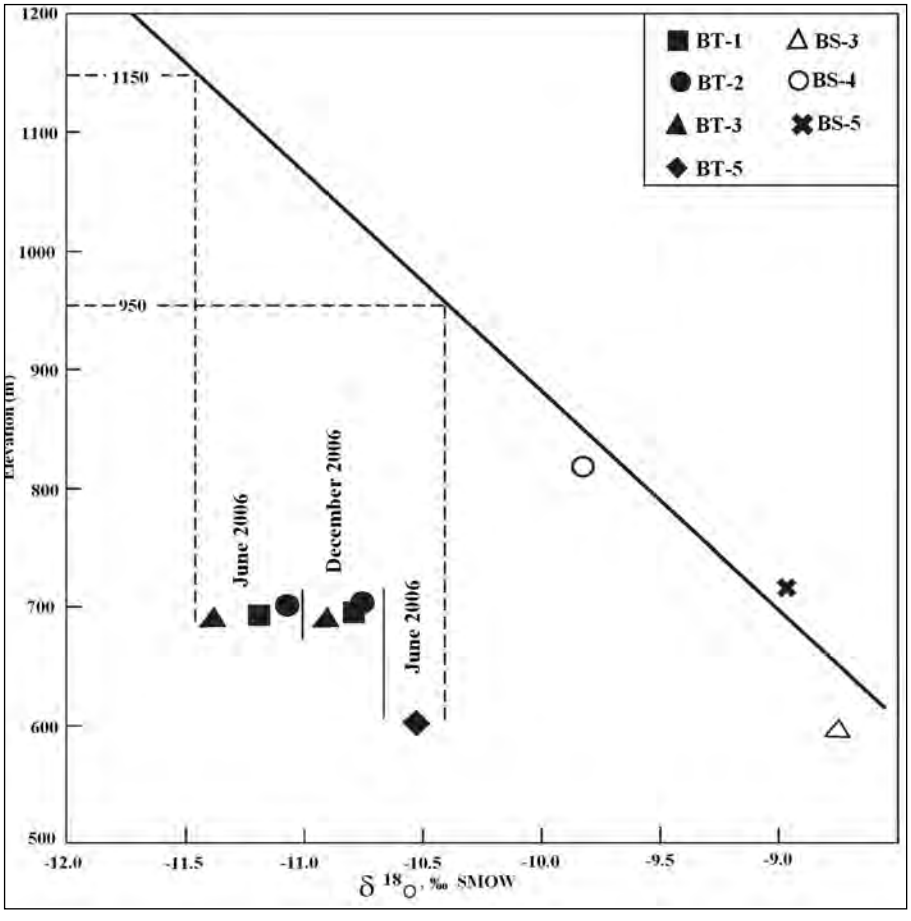

Figure 8- Oxygen-18 ($\delta^{18}O$) versus elevation diagram of the waters in the Beypazarı region (Çelmen, 2008).

of 950-1150 meters. After determining the recharge elevation of the geothermal resource in the study area, the recharge area of the geothermal resource can be found by evaluating the hydrochemical characteristics of the water, the hydrogeological cycle in the region and also the tectonic and geological structures of the region.

After the determination of the recharge area, a suitable reinjection location should be selected where the geothermal fluid can be reheated as it reaches the reservoir again in the medium- to long-term time periods. If the reinjected geothermal fluid reaches the production wells in a very short time, it will cause a decline in temperature in the reservoir. There are examples of this negative situation that seen in some geothermal fields.

2.3. Reinjection Wells and Locations Determined By MTA Studies

Geothermal energy research studies in Türkiye were initiated by the MTA in 1962. Distrubition of geothermal resources in Türkiye that prepared by MTA shown in Figure 9. With these studies, many geothermal fields with different temperatures were discovered and tendered for investment in accordance with the provisions of the Geothermal Resources and Natural Mineral Waters Law No. 5686 and its Implementation Regulation. Reinjection trials and applications continue in many geothermal fields where geothermal energy is used for electricity generation, greenhouse heating and residential heating by municipalities and a lot of companies.

2.3.1. Denizli-Kızıldere Geothermal Field

The geothermal exploration surveys in Denizli-Kızıldere geothermal field were initiated by MTA in 1968 with the geological, geophysical, geochemical, drilling and testing studies in the area; this geothermal field is currently in operation for energy production. With the studies carried out by MTA, 10 production and 9 reinjection wells were drilled.

The operating license area was purchased by Zorlu Energy through a tender from the Prime Ministry Privatization Administration, and a total of 89 wells were drilled for geothermal energy production in the licensed area. The fluid obtained from these drillings is used in Kızıldere I Geothermal Power Plant (GPP) with an installed power of 17.5 MWe, Kızıldere-II GPP with an installed power of 80 MWe and Kızıldere GPP-III with an installed power of 165 MWe (Figure 10).

All produced geothermal fluids are reinjected back into the reservoir with the reinjection system located at the edge of the production area.

2.3.2. Kütahya-Simav-Eynal-Çitgöl-Nasa Geothermal Field

In the Simav-Eynal-Çitgöl-Naşa geothermal field, drilling works have been carried out by the General Directorate of MTA and the Municipality since 1985 and the geothermal fluid obtained from the drillings is used for residential heating, greenhouse heating and thermal purposes. There are 40 production and 2 reinjection wells in the area. The production

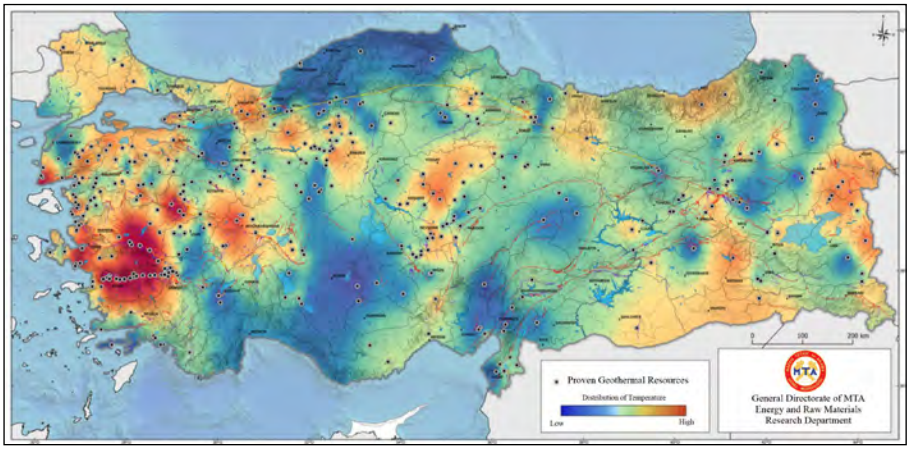

Figure 9- Distrubition of geothermal resources in Türkiye.

Figure 10- Kızıldere-3 Geothermal Power Plant by Zorlu Enerji Inc. in Denizli-Kızıldere geothermal field.

temperatures of the wells vary between approximately 45°C -136°C and the reinjected temperatures vary between 60°C-75°C (Doğdu et al., 2019). In Simav district, geothermal energy is used for 13.400 Re (residential equivalence) and also 265 decares of greenhouse heating as well as for thermal purposes. In the Simav-Eynal geothermal field Y-1 well is used for reinjection purposes. The geothermal wells in Çitgöl area are used for heating of 1,200 Re houses, and also for 130 decares of greenhouse heating as well as for thermal purposes. It has been determined that the wells in Naşa are used for thermal purposes in the spa facilities. It was observed that the geothermal fluid was reinjected into the existing Y-1 well during the periods of geothermal use in the winter months, but this was not sufficient for the sustainability of the geothermal reservoir. In this context, the reinjection area was determined as a result of the multidisciplinary evaluation of the geological, geophysical and other data of the MTA, and then for the purpose for the reinjection of water returned from Simav and Eynal residential and greenhouse heating uses, the reinjection well EJR-1 was drilled in 2022 by MTA (Figure 11) (Doğdu et al., 2022). But according to the observations and geothermal usage of the geothermal field, it has seen that at least 2-3 reinjection wells are needed for the long-term sustainability of geothermal resource in that region (Figure 11) (Doğdu et al., 2022).

2.3.3. Nevşehir-Kozaklı Geothermal Field

Nevşehir-Kozaklı geothermal field is considered as a medium enthalpy geothermal system based on available data and interpretations. In this geothermal area, drilling works have been carried out by the General Directorate of MTA and the Municipality since 1965. The geothermal fluid obtained from the drillings is used for residential heating, greenhouse heating and thermal purposes in the Nevşehir-Kozakli geothermal area. In the area, 2.294 residential heating, 67.000 m^2 greenhouse heating and 28 thermal facilities are used for thermal purposes. There are 25 production and 1 reinjection wells in the field (Figure 12). The production temperatures of the wells vary between approximately 36°C-92°C and the reinjected temperatures vary between 50°C-55°C. Thermal fluid is distributed by NEVJET AŞ to subscribers for residential heating and thermal use from the collection/distribution tank with a capacity of 1,500 tones, and fluid sent back to the reinjection well from the reinjection tank with a capacity of 500 tones. With surveys of MTA, 2 reinjection well locations have been determined by MTA in Nevşehir-Kozaklı geothermal area. Upon this survey, 1 reinjection well has drilled by authorities and currently used for reinjection purposes. According to long time surveys in Nevşehir – Kozaklı geothermal fields, it is suggested by MTA that, in order to ensure the sustainability of the geothermal field, the geothermal wells that are constantly used in the field should not be operated at full capacity before getting full production-reinjection balance of the reservoir. In terms of integrated use, distribution and used thermal water should be utilised for thermal purposes after residential heating and greenhouse heating applications. Finally, to ensure the sustainability of the geothermal field, reinjection of used brine should not be done at temperatures below 55°C-60°C.

In the Nevşehir-Kozaklı geothermal field, two sinkholes (Kozaklı-1 and Kozaklı-2) with a diameter of 90 x 70 meters and 22.3 x 21 meters were formed in 2007 and 2019 (Figure 13). It is thought that this situation is due to the inability to implement a suitable reinjection strategy and the lack of optimum production from geothermal wells. In addition to the existing wells, requested new wells will generate more thermal fluid from the geothermal reservoir and it would be

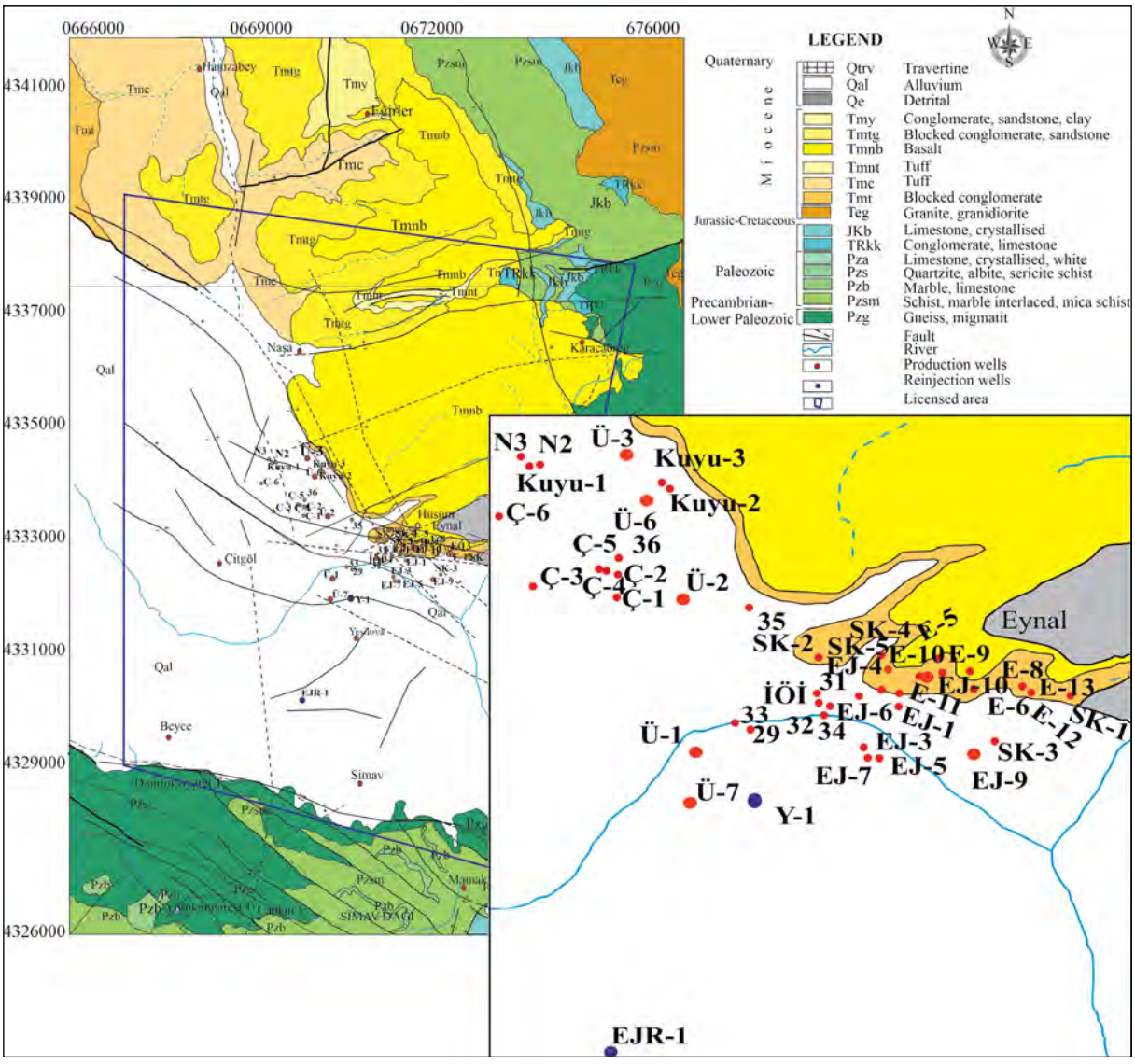

Figure 11- Kütahya-Simav-Eynal-Çitgöl-Naşa Geothermal Field (Doğdu et.al., 2022).

appropriate to ensure more controlled use of all wells, including conducting another round of interference testing to ensure the sustainability of the geothermal field. It would be appropriate to drill a new reinjection well in the reinjection area determined by the MTA. However, it would also be a good strategy to monitor existing reinjection and production wells for at least two periods to ensure that the reinjection volume does not adversely affect the geothermal reservoir.

It is clear that production-reinjection balance is very critical in some areaa to ensure the sustainability of the geothermal reservoir. If this geothermal balance is provided with good production-reinjection policy, new sinkholes that result from sudden water level changes due to the mass withdrawal from the production wells may be prevented.

2.3.4. Afyon-Sandıklı Geothermal Field

In the Sandıklı geothermal field, as a result of geophysical, geological studies and hydrogeological evaluations carried out within the framework of consultancy works carried out by MTA, a reinjection area was determined and a reinjection well (AFS-188) was drilled. In current time, Afyon-Sandıklı geothermal resource operation licensed area is used by SANJET Inc. According to the conversations with the authorities, 19,200 Re houses (equivalent to 33.000

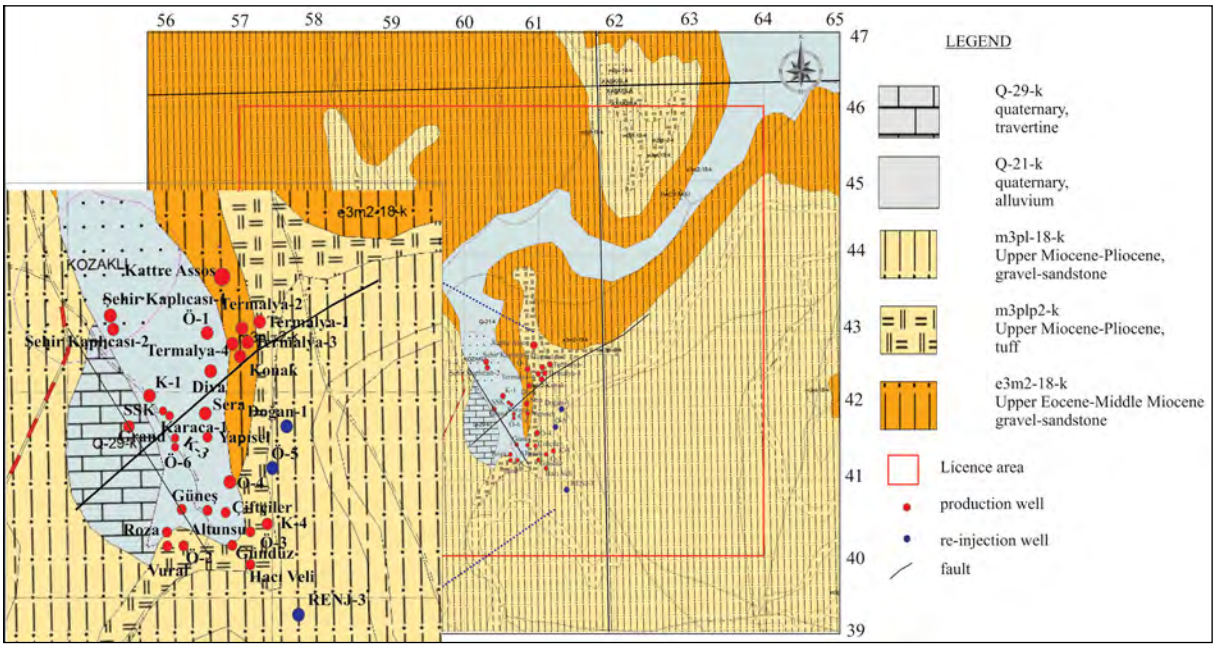

Figure 12- Nevşehir-Kozaklı Geothermal Field (Doğdu et al., 2018).

Figure 13- a) Kozaklı-1 sinkhole (2007) and b) Kozaklı-2 sinkhole (2019).

houses) and 24 greenhouses (1.500.000 m^2) were heated by geıthermal energy and 1.200 m^3-1.500 m^3 of geothermal fluid at a temperature of about 70°C-75°C in the current situation came to the heat center storage. It was learned that 1.200-1.500 m3 of geothermal fluid was reinjected at temperature approximately 40°C-45°C. According to the well information received from Afyon Special Provincial Administration, there are 33 production and 4 reinjection wells in the Afyon-Sandıklı geothermal resource operation licensed area.

The geothermal fluid in the field is used for both thermal tourism and space heating purposes. Geothermal operations should carried out by a plan as a result of the production and interference tests and reinject the fluid after heating purposes under suitable conditions to make sure the sustainability of the source. The effect of reinjection on the geothermal system should be monitored with the well tests and also should taking into account the measures and activites mentioned in the Geothermal Resources and Natural Mineral Waters Law No. 5686 and the Implementation Regulations.

In addition, as stated in the technical opinions given by MTA in previous Resource Conservation Area reports, no new wells should be drilled especially in the corridor extending from Hüdai thermal springs to İnpınarı location to ensure sustainability in the field, (Tamgaç et al., 2012). Also, that MTA study suggests that new production wells should be drilled at the north of Tozkoparan Tepe, Şaban well location, Savurmaz Harmanları, Gülbahçe location line, and south of the Sipsin Damları, Koruçayırı location, and Cinsigüzel locality line. It is strongly recommend to

monitoring geothermal field with production wells according to reinjection strategy in the field to ensure sustainability of the geothermal field.

2.3.5. Afyon-Merkez-Ömer-Gecek Geothermal Field

Afyon Merkez-Ömer-Gecek geothermal field is operated by AFJET Inc. for electricity generation, residential heating, greenhouse heating and other thermal purposes. This geothermal field is operated with a production-reinjection system.

In the Ömer-Gecek geothmeral area, AFJET Inc. used some closely spaced reinjection wells near production wells as observed by the MTA. A new reinjection area was determined by the MTA that would not affect the production wells according to a request of the Afyon Governship in 2016. To determine the new reinjection area, previous geological, geophysical and hydrogeological studies should be evaluated.

2.3.6. Afyon-Çobanlar Geothermal Field

There are six wells registered under the Çobanlar Municipality in the Afyon-Çobanlar geothermal area. In this area, geothermal wells are used for greenhouse heating and thermal tourism purposes. It was learned from the greenhouse authorities that the geothermal fluid used for heating the greenhouse, after being transported approximately 3.5 km, has an inlet temperature of 57°C-58°C and an outlet temperature of 32°C-35°C.

According to request of Afyon Government in 2016, a new renjection area was determined by MTA considering the location of reservoir, production wells and groundwater flow direction, etc.

2.3.7. Elazığ-Cipköy Geothermal Field

According to the request of the Elazığ Municipality in 2020, on-site investigations were carried out in the Elazığ-Cipköy geothermal area by MTA. Considering the studies carried out in the previous years, a new geothermal reinjection area was determined to ensure the sustainability and integrity of the reservoir. Also, the MTA suggested to produce geothermal fluids to use in optimum flow rates and to reinject after usage in greenhouse heating.

By evaluating all the geological, geophysical, hydrogeological and isotopic studies carried out, it is suggested that, the possible recharge elevation of the geothermal reservoir could be between 1300 meters - 1500 meters. At this elevation, the possible recharge of the system may be from marble-limestone units lithologically that located north-northwest of the geothermal area. Thus, it was suggested to consider drilling new geothermal reinjection wells from licence border (currently) to the Poyraz and Pelteköy locations.

3. Conclusions

Reinjection plays a crucial role in maximizing the efficiency and sustainability of geothermal energy production. From this point of view, ensuring the sustainability of geothermal resources depends on the protection of these resources to sustain production-reinjection balance policy.

Firstly, reinjection helps maintain reservoir pressure, ensuring a long-term and sustainable energy resource. Geothermal reservoirs are naturally pressurized and the extraction of fluids for energy production can lead to a decline in pressure over time. This can result in a reduced efficiency of energy extraction or even the complete depletion of the reservoir. However by reinjecting the used thermal fluids in the right conditions and locations, the pressure is maintained, allowing for continuous and reliable geothermal energy production.

Geothermal fluids may contain economical valuable minerals and dissolved substances that can be extracted and utilized for various industrial and agricultural purposes that may be not economical in todays technology. By reinjecting the fluids, these valuable resources can be preserved and potentially extracted in the future as technology advances.

Reinjection also helps to mitigate environmental impacts. Geothermal fluids often contains heavy metals and dissolved gases that can have negative impacts for the nature. If these fluids are not properly managed and disposed of, they can pose a risk to ecosystems and groundwater quality. However, by reinjecting the thermal fluids into the reservoir, the potential for contamination is minimized, and get ensure the protection of surrounding ecosystems and water sources.

In details, reinjection locations determinations should be surveyed with geological data (stratigraphy, lithology, tectonism, hydrogeology), borehole data (litostratigraphy, definitions, changed temperature in depth), geophysical data, well logs, flow rates, hydrogeochemical data (temperatures of springs and wells, chemical compositions) and also with flow maps, tracer tests and stable isotope studies. These datas should be examined together to ensure the recharge area of the geothermal system, to get rid of possible negative effects of reinjection such as scaling problems in the wells or cooling geothermal reservoir by short circulating of reinjected thermal fluid.

In some cases, because of the geographical shape of the licenced area (ununiformed or small sized), reinjection locations determinations may be difficult even impossible to determine. In this situation reinjection or discharge policy of the used thermal fluid should be evaluated by General Directorate of Mineral Research and Exploration under the Geothermal Law.

Finally, although the determination of a reinjection well in a geothermal system is very important for sustainable energy production, continuous monitoring of the production and reinjection balance is very crucial. With this monitoring and continous surveys, possible changes in the reservoir parameters (pressure, temperature, hydrochemical etc.) and also in the production and reinjection wells should be carried out to get long term green energy sustainability.

Acknowledgements

In this study, studies was utilized within the scope of geothermal energy survey and drilling studies and also geothermal resource protection zone area surveys implemented by the Energy Raw Material Research and Exploration Department of the General Directorate of Mineral Research and Exploration (MTA). The authors thank the technical and administrative personnel working in these projects, as well as the Denizli Governorship, Kütahya Governorship, Simav Municipality, Nevşehir Governorship, Kozaklı Municipality, Afyon Governorship, Elazığ Governorship and Elazığ Municipality officials for their contributions.

References

Atılgan, M. 1994. Jeotermal Kaynaklarda Re-enjeksiyonun Önemi. Jeotermal Uygulamalar Sempozyumu, 27-30 Eylül 1994, Pamukkale Üniversitesi, Denizli, Turkey, 56-60.

Axelsson, G. 2013. Tracer tests in geothermal resource management. In EPJ Web of Conferences (Vol. 50).

Barbier, E.2002. Geothermal energy technology and current status: An overview. Renewable and Sustainable Energy Reviews. 6(1–2):3-65.

Çelmen, O. 2008. Hydrogeochemical and isotopic investigation of the thermal and mineralized springs between Sivrihisar and Beypazarı region (in Turkish). Ankara University. Graduate School of Natural and Applied Sciences. Ph.D. Thesis, 239, Ankara, Turkey.

Doğdu, N. 2004. Determination of Hydraulic Properties of Afyon Plain by Indicator Geostatistics and Inverted Modeling Techniques. Hacettepe University. Graduate School of Natural and Applied Sciences. Ph.D. Thesis, 66, Ankara, Turkey.

Doğdu, N., Orakcı, A., Atmaca, İ., Akar, M., Duran, Y. 2018. Kozaklı (Nevşehir) 2007/18 numaralı işletme ruhsatına ilişkin Kaynak Koruma Alanı Etüt Raporu, General Directorate of Mineral Research and Exploration. Report No: 13746. 122, Ankara, Turkey (unpublished).

Doğdu, N. Aydoğdu, Ö. Akar, A. Şahan, M. Akar, M. Duran, Y. Bilgiç, Ö. 2019. Simav-Eynal-Çitgöl-Naşa (Kütahya) 105 numaralı işletme ruhsatına ilişkin kaynak koruma alanı etüt raporu. General Directorate of Mineral Research and Exploration. Report No: 13813, 244, Ankara, Turkey (unpublished).

Doğdu, N., Şahan. M., Tamgaç, Ö. F., Öztel, İ., Akar, A., Güven, A., Toy, E., Atmaca, İ. 2022. Kütahya İl Özel İdaresi adına tescilli 105 nolu jeotermal kaynak işletme ruhsat sahası Ü-1, Ü-2, Ü-3, Ü-6 jeotermal araştırma sondajları kuyu bitirme raporu. General Directorate of Mineral Research and Exploration. Report No: 14076. 122, Ankara, Turkey (unpublished).

Kamila, Z., Kaya, E., Zarrouk, S.J. 2021. Reinjection in geothermal fields: An updated worldwide review 2020. Geothermics. Volume 89.

Mazor, E. 1991. Applied Chemical and Isotopic Groundwater Hydrology. Open University Press, Suffolk, 274.

Roberts, D. 2020. Geothermal energy is poised for a big breakout, www.vox.com.

Şirin, Ö. 2019. Yeraltısuyu akışı, yeraltısuyu boşalımı ve Darcy Kanunu, https://docplayer.biz.tr.

Tamgaç, Ö.F., Doğdu, N., İncegil, F., Ünal H., Akar, M 2012. Sandıklı (Afyonkarahisar) jeotermal alanına ait kaynak koruma alanları etüt raporu. General Directorate of Mineral Research and Exploration. Report No: 11526, 74, Ankara, Turkey (unpublished).

Tezcan, L. 2000. Groundwater Models. Lecture Notes. Hacettepe University, Geological Engineering Department. Ankara, Turkey (unpublished).

Vitaller, A. V., Angst, U., Elsener, B. 2019. Corrosion Behaviour of L80 Steel Grade in Geothermal Power Plants in Switzerland, Metals - Open Access Metallurgy Journal 9 (3), 331.

White, D. E. 1973. Characteristics of Geothermal Resources. in P. Kruger and C. Otte, eds., “Geothermal Energy: Resources, Production, Stimulation” (Stanford University Press, Stanford, 69 - 94.

Bulletin of the Mineral Research and Exploration

http://bulletin.mta.gov.tr

Geothermal power corridor-connecting the Middle East Countries

Dornadula CHANDRASEKHARAM[a*]

[a] *İzmir Institute of Technology, İzmir, Türkiye.*

Research Article

Keywords:
Geothermal Energy, Food-Water-Energy Security, Sustainable Development, EGS.

ABSTRACT

The Middle East economy and life depend on imports, be it food, water, or energy, despite each country in the region having enormous energy resources to exploit and reduce dependency on countries outside the region and develop a socioeconomic model of regional cooperation and synergy. An estimated 371 TWh of electricity available from geothermal energy resources can be utilized by these countries to support basic needs and be free from food-energy-water imports by sharing their energy resources. The total amount of CO_2 emissions from these countries is currently 945 x 10^6 kg, so these countries can further earn about 92 million euros from carbon savings, by using geothermal energy along this corridor. This amount can be utilized for augmenting the energy supply from geothermal sources. In this work, the available geothermal resources are evaluated, and suggestions are made how this energy can be best utilized for peaceful existence and cooperation in the region.

Received Date: 30.04.2023
Accepted Date: 20.06.2023

1. Introduction

This communication is aimed at countries that have scarce water resources and hence depend heavily on imported food and/or desalinated water using enormous amounts of high CO_2 emitting fossil energy sources, even though they have huge untapped geothermal energy resources and countries that have plenty of green energy potential and water but still depend on imported energy due to poor infrastructure to develop the green energy resources. Although the regions discussed in this paper have other sources of energy such as solar photovoltaics (PV) and Wind, these sources can not provide base load electricity and their efficiencies are about 20%. The energy densities of these two sources are very low and the reliability is also low (Shanmugam, 2023). Hence these sources are not included for review in this paper. Here we consider Saudi Arabia as a glaring example of the first group of countries and Türkiye which belongs to the second group. Between these two groups, fall other countries that lie between Türkiye and Saudi Arabia. We will focus on geothermal energy that is available in these countries and analyze how sharing this energy, like transboundary aquifers, will help them.

In today's world, transboundary rivers, aquifers, and oil fields are common, which supply water or oil to different countries. Transboundary aquifers, viz. Guarani Aquifer, spread over Argentina, Brazil, Paraguay, and Uruguay, in Europe and GCC countries (Kuwait, Saudi Arabia, Oman) share common formations producing hydrocarbons as well as aquifers (Chandrasekharam et al., 2016*a*). Similarly, electricity is also shared through a grid system within a country or across the countries; for example, nuclear

Citation Info: Chandrasekharam, D. 2023. Geothermal Power Corridor-connecting the Middle East Countries. Bulletin of the Mineral Research and Exploration 171, 177-184. https://doi.org/10.19111/bulletinofmre.1317427

**Corresponding author: Dornadula CHANDRASEKHARAM, dchandra50@gmail.com*

power, thermal and hydropower are shared in Europe (https://ec.europa.eu/eurostat/statistics). Sharing through a grid within the country is very common since most of the thermal power plants are located near the coal source while hydropower is within a suitable water drainage system. So, it is possible to share geothermal power using interregional grid systems for sustainable development of the regions and to collectively contribute to the climate change control goal. Geothermal power transmission using grids and mini-grid within countries is common. It is possible to use a transboundary transmission system to supply geothermal power across the countries.

The focus here is to evaluate the geothermal energy potential of the Red Sea, Saudi Arabia, Jordan and Türkiye and suggest ways to involve all the Middle East countries to provide carbon free food-energy-water (FEW) and support their United Nations (UN) Sustainable Development Goals through a common geothermal power corridor (GPC).

2. Methodology and Status of Potential

2.1. Methodology

The radioactive heat production of the granites has been calculated using the procedure of Rybach (1976). Electricity generation from such granites is calculated using the procedure adopted by Somerville et al. (1994) for hot dry rock project in Cooper Basin, Australia.

2.2. Power from The Red Sea Ridge Flanks

According to a recent study (Chandrasekhar and Chandrasekharam, 2023), the Red Sea together with the high radiogenic granites and Harrats (volcanic fields) of the western Arabian Shield have very high geothermal energy potential.

This region can generate 49 x 10^{11} kWh of electricity while the annual electricity consumption of Saudi Arabia is only 2.89 x 10^{11} kWh. This region together with the granites and Harrats of Syria, eastern and central volcanic provinces and the western geothermal province of Türkiye can form a transboundary geothermal power grid (Figure 1**)**, which is termed here, the Geothermal Power Corridor (GPC). The heat flow value of the eastern flank of the Red Sea ridge, along its 2000 km length from the Gulf of Aden to the Gulf of Aqaba, varies from 96 to 205 mW/m^2 (Girdler, 1970; Girdler and Evans, 1977). This is a locus of geothermal zones, with supercritical temperature (378 °C) encountered at a depth of 2 to 3 km. This is due to the presence of the 1200 °C isotherm (melting temperature of basalts) at a depth of 10 to 12 km, which is indicated by the presence of hot brine pools at shallow depth in the axial valley (Degens and Ross, 1969) and the presence of shallow sheet-dike intrusions along 20° Parallel on the eastern side of the ridge axis (Cochran et al., 1986; Follmann et al., 2021; Chandrasekhar and Chandrasekharam, 2023). 3D THM (Thermo-Hydro-Mechanical model using COMSOL V6) modelling of a supercritical geothermal zone below an active volcanic terrain (with single loop EGS configuration: shown in Figure 2) indicates that temperatures of 275 °C can be obtained at the production wellhead that can generate 53 MWe (Chandrasekharam et al., 2023).

Two hundred off-shore geothermal platforms, between the transform faults (with 10 km spacing between the wells), over 2000 km long, western flank of the Red Sea ridge tapping this supercritical heat should generate, according to the above model, 10600 MWe. This is equivalent to 84 billion kWh per year. When oil rigs can operate off-shore, much smaller geothermal platforms can operate as well. The number of geothermal wells over the eastern flanks can be increased subsequently once the power production system is established. After all, there is a constant supply of heat to tap along the spreading ridge.

2.3. Power from Western Arabian Shield Margin

The hydrothermal sources at Jizan and Al Lith, the Harrats (volcanic fields) and the high radiogenic granites are the main geothermal sources along the western Arabian Shield margin. The Ocean ridge slice, with its dike swarms and ophiolites, in association with acid differentiates thrusted over, the thin continental margin at Jizan and Al Lith, with high heat flow (100 mW/m^2) and geothermal gradient (90 °C/km) (Figure 3 and 4), form the main loci of hydrothermal reservoirs, with a capacity to generate 1.2 x 10^9 kWh and 134 x 10^6 kWh respectively (Chandrasekharam et al., 2014; 2015; 2016*a*; 2016*b*).

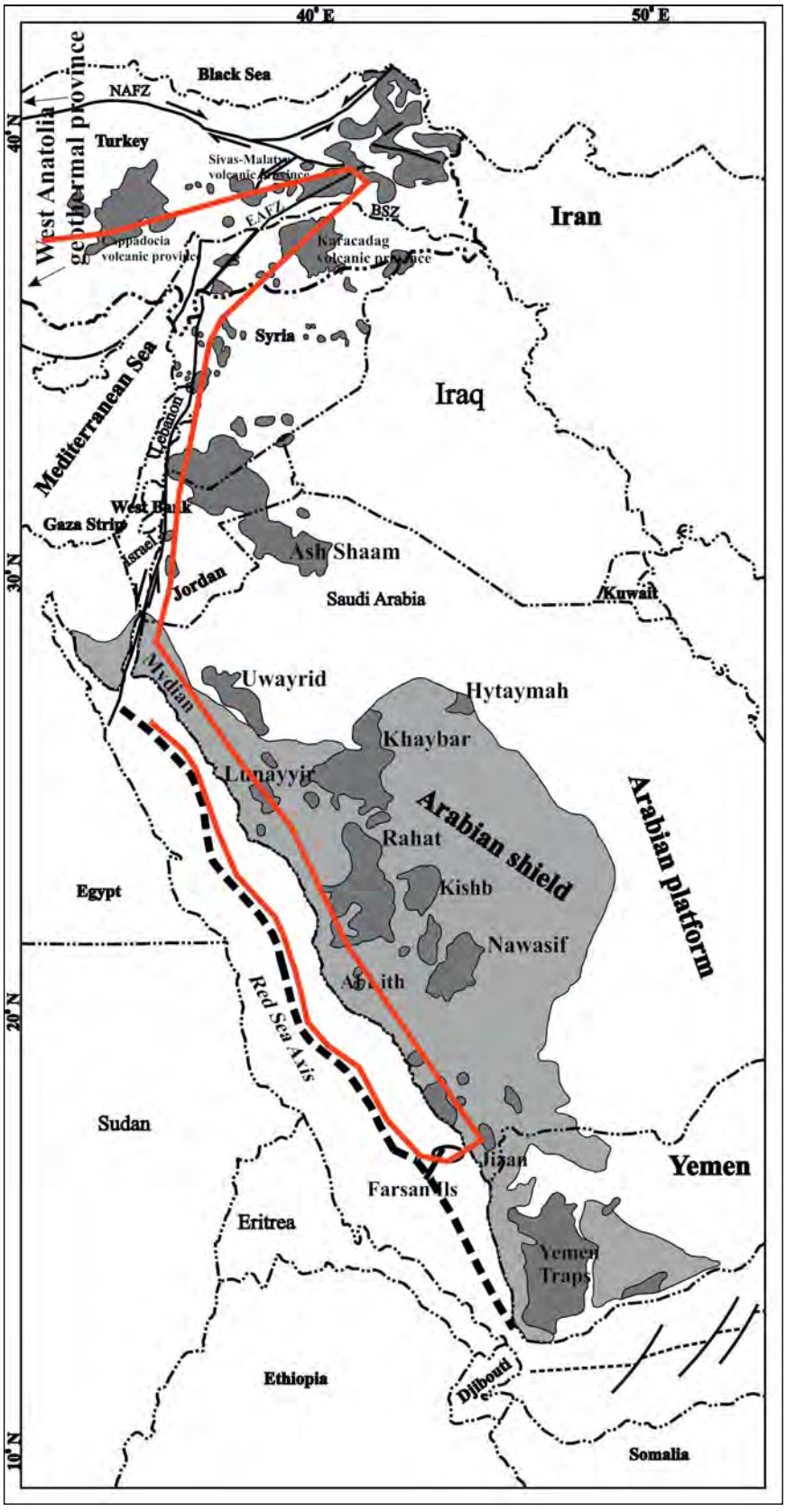

Figure 1- The red line indicates the Geothermal Resources Corridor connecting geothermal provinces of the Red Sea ridge, Western Arabian Shield, Jordan and Türkiye.

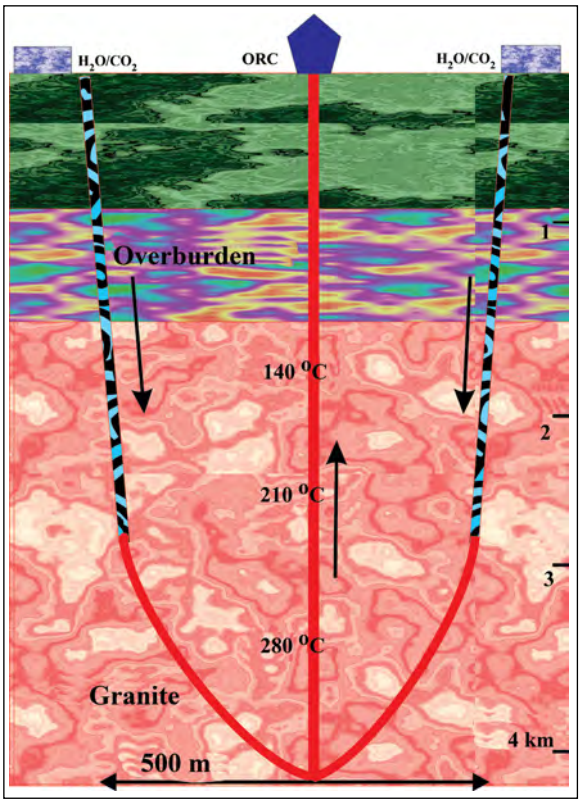

Figure 2- Schematic Closed loop Enhanced Geothermal System model used for THM modeling using COMSOL V6 described in the Section 2.6.

2.4. Power from High Radiogenic Granites of The Shield

The granites, with a cumulative outcrop area of 162000 km^2, spread over the western Arabian Shield, are very fertile rocks with radiogenic heat generating capacity of 5 to 134 $\mu W/m^3$ with high heat flow values (50 to 1382 mW/m^2) (Chandrasekharam et al., 2015). The Mydian granites, located in the NW part of the Shield (Figure 4) are the most fertile rocks with the highest heat generation capacity of 134 $\mu W/m^3$. Now that technology (closed loop EGS technology) to tap this energy is mature, all these high radiogenic granites (162000 km^2) along the western margin of Saudi Arabia can be utilized for power generation. Assuming about 2% of the heat energy is recovered for power generation from the entire volume of high radiogenic granites (1m thick), the amount of power that can be generated is around 256 x 10^9 kWh. Assuming daily per-capita electricity consumption of 2000 kWh, these granites alone can support 128 x 10^6 people (Chandrasekharam et al., 2015). Thus, as discussed above, the minimum energy that can be tapped from the Red Sea ridge flanks, hydrothermal sources in Jizan and Al Lith and the high radiogenic granites is about 340 TWh.

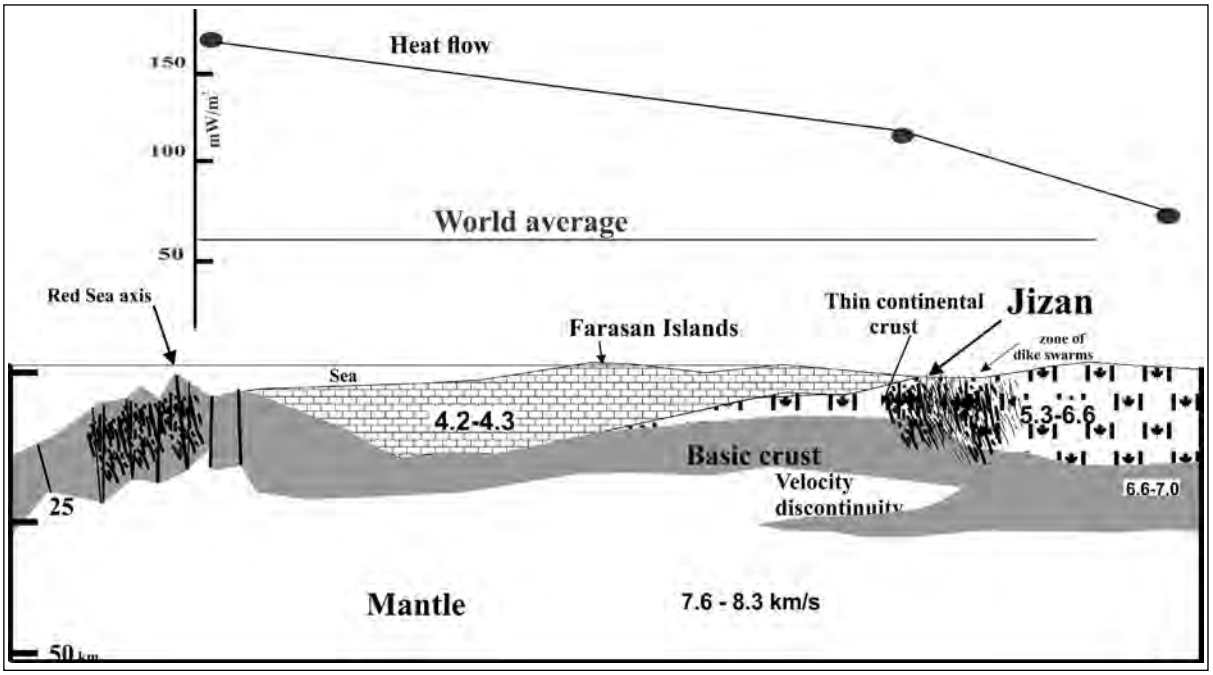

Figure 3- Heat flow and subsurface structure below Jizan, Western Saudi Arabia.

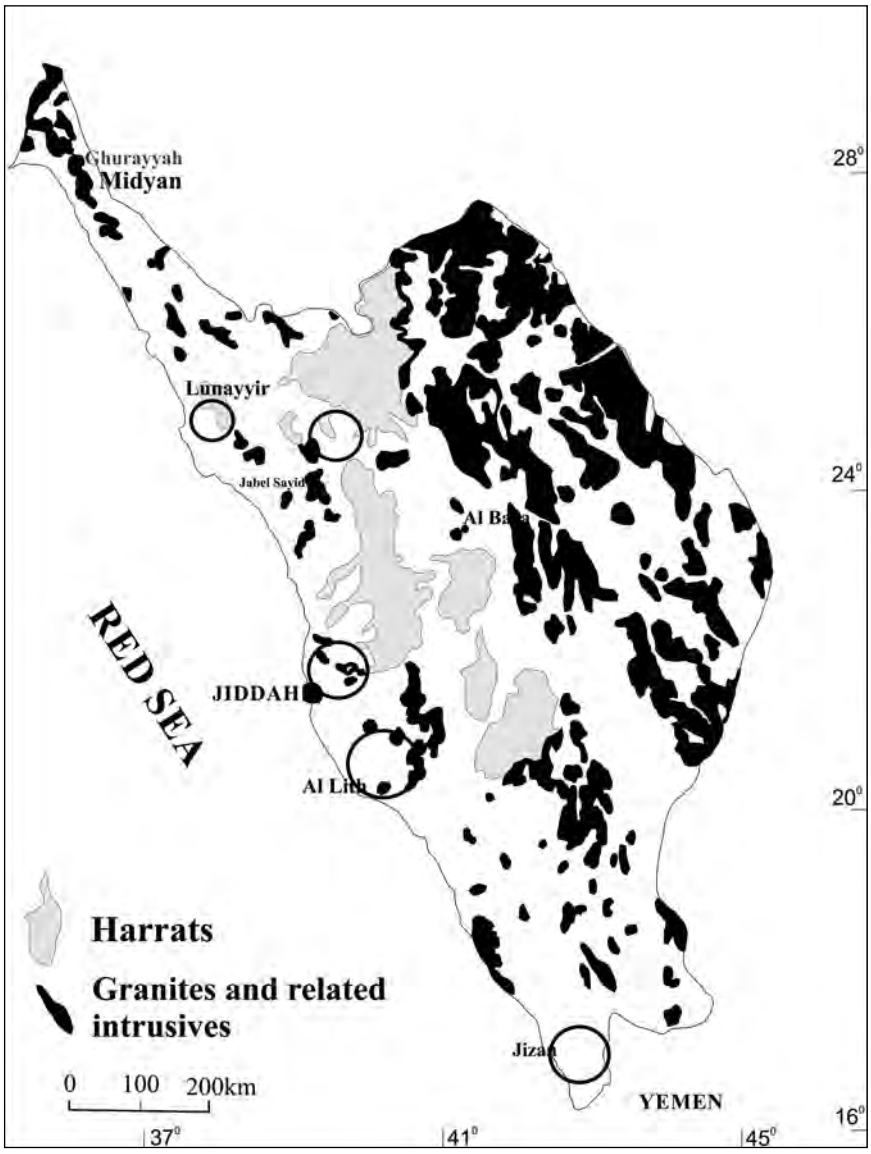

Figure 4- Western Saudi Arabian Shield showing the Harrats and high radiogenic granites.

2.5. Curie Isotherm of Red Sea and Western Arabian Shield

The curie depth isotherm is very shallow ~10 km over the ridge flanks, as anticipated, and below the Farasan islands, Jizan and Al Lith hydrothermal provinces. All along the coastal region, extending from Al Lith to Mydian, the Curie isotherm depth is below 30 km (Aboud et al., 2016). The Curie isotherm supports a shallow high-temperature regime over the entire eastern Red Sea margin and the western Shield region, including the Harrats.

2.6. Power from Türkiye Geothermal Provinces

Türkiye has hydrothermal as well as EGS sources. Currently, the hydrothermal sources in western Anatolia are generating 1680 MWe (Baba and Chandrasekharam, 2022). The high radiogenic granites spread over the entire country, with an outcrop area of 6910 km^2, recorded radioactive heat generation varying from 7 to 20 $\mu W/m^3$ and heat flow value > 100 mW/m^2 (Chandrasekharam et al., 2022). As an example, the power that can be generated from 3 such granites from Kestanbol, Hamit and Eskisehir regions is 716 x 10^6 kWh (Chandrasekharam and

Baba, 2021; Tolga et al., 2022; Chandrasekharam et al., 2022; Chandrasekharam, 2022). Thus 2% of the power (assuming that this is the minimum that can be extractable) that can be generated from the 6910 km^2 high radiogenic granites is of the order of 10900 x 10^6 kWh. Besides these granites, Türkiye has super-hot EGS provinces in Central and Eastern Anatolian regions where the critical temperature geothermal regime lies at a shallow depth (3 km) and magma chambers at a 5 km depth. COMSOL V6 three-dimensional thermo-hydro-mechanical (THM) model on one such supercritical province in Central Anatolia indicate that, adopting a closed loop extraction method (Figure 2), the temperature that can be obtained is around 275 °C from a production well, with an injection volume of water of 500 L/s (Chandrasekharam et al., 2023). This well-head temperature is very similar to some of the hydrothermal systems that are currently generating 53 MWe (Di Pippo, 2012; Miravallis, Costa Rica). About 15 such closed-loop supercritical EGS sites from the central and eastern Anatolia regions can supply a minimum of 750 MWe (~6 x 10^9 kWh).

2.7. Curie Isotherm of Türkiye

Among the countries that fall under the GPC, Türkiye occupies a unique place with its high thermal regime represented by a shallow Curie Isotherm at 6 to 20 km due to the presence of subduction zones, thin and fragmented continental crust, shallow Moho depth, presence of magma chambers at crustal levels and high heat flow from the mantle as well as from the high radiogenic granites discussed above. This region is the only continental segment where such a high thermal configuration is present. The geothermal potential of this country has not been exploited to the fullest extent (Chandrasekharam et al., 2023).

2.8. Jordan

Although geologically Jordan is the northward extension of the western Arabian shield, with its high radiogenic granites and harrats, there is no significant research carried out on the geothermal resources of this country (Figure 1). However, the regional Curie Isotherm lies at 5 km SE of Harrat Ash-Shaam. A critical temperature thermal regime is envisaged at about 3 km depth in this region. Based on THM modeling (using COMSOL V6) results obtained over a stratovolcano in Türkiye (Chandrasekharam et al., 2023), it is reasonable to assume minimum extractable power of about 150 MWe (~2 x 10^9 kWh, three wells with loop-technology).

3. Discussion and Conclusions

The geothermal energy available along the GPC (371 TWh) is a conservative estimation. This can be increased in future with new developments in drilling and heat extraction technologies. There are high heat flow sites (125 to 472 mW/m^2) in Jordan along 31°-30' N parallel, along the Wadi Zerqa fault zone. These unexplored sites may add an additional quantity of energy to the GPC in future. This energy (371 TWh) can be shared by the countries discussed here, depending on sustainable development and disaster mitigation programmes. Geothermal energy sources, irrespective of the natural hazards, will be able to provide an undisrupted supply of power with > 90% efficiency and for 95% of the year. The best way to utilize this energy is to get fresh water to support domestic and agricultural sectors. On an average, 5 kWh of electrical energy is required to get 1000 L of freshwater using desalination technology. GPC can generate about 75 x 10^{12} L of freshwater that can support about 5.87 billion people (current total population of Saudi Arabia, Jordan and Türkiye is 131 million) with a per-capita water consumption of 35 L/day (this is the global average per-capita consumption). The food-energy-water (FEW) benefits derived from this corridor can be utilized by other countries along this corridor that have poor FEW security.

Geothermal energy, with a very low carbon footprint, can benefit all the countries along this GPC with large carbon savings. The total amount of CO_2 emissions from Saudi Arabia (524 x 10^6 kg), Jordan (24 x 10^6 kg) and Türkiye (397 x 10^6 kg) are 945 x 10^6 kg. The amount that can be earned from carbon savings is about 92 million euros (carbon credit value: 97 euros /1000 kg, https://carboncredits.com/carbon-prices-today/26 Feb 2023). This amount can be utilized for augmenting the energy supply from the sources discussed above and can be utilized for making this corridor a green society with inclusive growth with self sufficiency in food and water. Once this GPC is fully established, it can integrate the entire landmass along this corridor into a green zone, a zone free from carbon emissions.

Acknowledgement

Publication of this work is supported by TUBITAK (Project No:120C079). The author thanks the reviewers for their constructive comments and suggestions.

References

Aboud, E., Alotaibi, A. M., Saud, R. 2016. Relationship between Curie isotherm surface and Moho discontinuity in the Arabian shield, Saudi Arabia. Journal of Asian Earth Sciences 128, 42–53.

Baba, A., Chandrasekharam, D. 2022. Geothermal Resources for sustainable development. Case study: Turkey. International Journal of Energy Research. 1-18.

Chandrasekharam, D. 2022. Enhanced geothermal systems (EGS) for UNSustainable development goals. Discover Energy.

Chandrasekharam, D., Baba, A. 2021. High heat generating granites of Kestanbol: Future Enhanced Geothermal System (EGS) province in Western Anatolia, in "Geothermal Energy for sustainable development" Eds. Chandrasekharam and A. Baba, Turkish Journal of Earth Sciences, 30, 1032-1044.

Chandarasekharam, D., Lashin, A., Al Arifi, N. 2014. The potential contribution of geothermal energy to electricity supply in Saudi Arabia. International. Journal of Sustainable Energy.

Chandrasekharam, D., Lashin, A., Al Arifi, N., Al Bassam, A., El Alfy, M., Ranjith, P. G., Varun, C., Singh, H. K. 2015. The potential of high heat generating granites as EGS source to generate power and reduce CO_2 emissions, western Arabian shield, Saudi Arabia. Journal of African Earth Sciences, 112, 213-233.

Chandrasekharam, D, Lashin, A., Al Arifi, N., Al Bassam, A., Varun, C. 2016*a*. Desalination of seawater using geothermal energy to meet future fresh water demand of Saudi Arabia. Water Resources Management.

Chandrasekharam, A., Lashin, N. Al Arifi, A. Al Bassam. 2016*b*. Red Sea Geothermal Provinces. CRC Press, 220 p.

Chandrasekharam, D., Baba, A., Ayzit, A., Singh, H. K. 2022. Geothermal potential of Kaymaz and Sivrihisar granites, Eskisehir region, western Anatolia. Renewable Energy, 196, 870-882.

Chandrasekharam, D., Mrityunjay, S., Baba, A. 2023. Sahinkalesi massif, a resurgent dome and super-hot EGS province: Hasandag stratovolcanic province, Central Anatolia (Renewable Energy-under review).

Chandrasekhar, V., Chandrasekharam, D. 2023. Red Sea geothermal belt: Potential clean energy source to power NEOM and nearby countries Chapter 9 in (Ed) N. Rasul and I. Stewart. Rifting and Sediments in the Red Sea and Arabian Gulf regions, CRC Press, UK, 356p.

Cochran, J.R., Martinez, F., Steckler, M.S., Hobart, M. A. 1986. Conrad Deep: a new northern Red Sea deep. Origin and implications for continental rifting. Earth Planet Sci Lett 78: 18-32.

Degens, E.T., Ross. D. A. 1969. Hot brines and recent heavy metal deposits in the Red Sea. A geochemical and geophysical account. Berlin: Springer-Verlag, 609 p.

Di Pippo, R. 2012. Geothermal power plants, 3rd edn. Elsevier, New York, pp 463–474.

Follmann, J., van der Zwan, F.M., Preine, J., Hübscher, C., Bousquet, R., Augustin, N. 2021. Gabbro discovery in Discovery Deep: First plutonic rock samples from the Red Sea Rift axis. Frontiers Earth Sci 9.

Girdler, R.W. 1970. A review of Red Sea heat flow. Phil Trans Roy Soc London 267: 191-203.

Girdler, R.W., Evans T. R. 1977. Red Sea heat flow. Geophys J R Astr Soc 51: 245-251.

Rybach, L. 1976. Radioactive Heat Production: A Physical Property Determined by the Chemistry. In: RGI. Strens (Editor), The Physical and Chemistry of Minerals and Rocks. Wiley-Interscience Publication, New York, USA, pp. 245-276.

Shanmugam, G. 2023. Fossil Fuels, Climate Change, and the Vital Role of CO_2 Plays in Thriving People and Plants on Planet Earth. Bulletin of the Mineral Research and Exploration.

Somerville, M., Wyborn, D., Chopra, P., Rahman, S., Don Estrella, Theo Van der Meulen, 1994. Hot Dry Rock Feasibility Study. Energy Research and Development Corporation, unpublished report. 214 p.

Tolga, A., Chandrasekharam, D., Baba, A. 2022. Salihli Granitoid, Menderes Massif, Western Anatolia: A Sustainable Clean Energy Source for Mitigating CO_2 Emissions. In: Gökçekuş, H., Kassem, Y. (eds) Climate Change, Natural Resources

and Sustainable Environmental Management. NRSEM 2021. Environmental Earth Sciences. Springer, Cham.

https://carboncredits.com/carbon-prices-today/26 Feb 2023.

https://ec.europa.eu/eurostat/statistics-explained/index.php?title=Main_Page (3 March 2023).

Bulletin of the Mineral Research and Exploration

http://bulletin.mta.gov.tr

A brief overview on geothermal scaling

Tuğba ISIK[a], Alper BABA[b], Dornadula CHANDRASEKHARAM[b,c] and Mustafa M. DEMİR[d*]

[a]*General Directorate of Mineral Research and Exploration, Department of Mineral Analysis and Technologies, Ankara, Türkiye*
[b]*İzmir Institute of Technology, Department of International Water Resources, İzmir, Türkiye*
[c]*Indian Institute of Technology, Department of Earth Sciences, Bombay, India*
[d]*İzmir Institute of Technology, Department of Material Science and Engineering, İzmir, Türkiye*

Review Article

Keywords:
Antiscalants, Deposit, Geothermal Energy, Precipitation, Scaling.

ABSTRACT

Hot spring waters are rich in terms of minerals. Since there are dramatic changes in thermodynamic parameters in geothermal power plants, such as a decrease in temperature and pressure, severe precipitation occurs throughout the system components in an uncontrolled manner. There are three main chemistries in deposits: carbonates (mainly calcium carbonates), silicates (metal silicates), and sulphides (antimony sulphide-stibnite). Energy harvesting is remarkably reduced out of the insulating nature of the deposit. Various actions need to be taken to mitigate this undesirable issue of scaling in geothermal systems. Geothermal systems are in fact quite complex, and the composition of brine and, accordingly, the chemistry of the deposit are not identical. Therefore, each system should be studied individually, and a tailor-made remedy should be developed. In this overview, the types of deposits in terms of chemistry and the actions (pH modification or antiscalant dosing) that should be taken to reduce scaling are mentioned, and potential chemistries of antiscalants are given.

Received Date: 10.08.2022
Accepted Date: 03.01.2023

1. Geothermal Energy and Scaling

The energy demand of countries has been remarkably increasing in recent years due to the high rate of population growth and industrial activities. Fossil fuels are major sources of this global demand, but the increasing awareness about the environmentally hazardous effects of these sources put the usage of clean and renewable energy sources forward, such as geothermal energy, solar energy, wind energy, and hydro energy (Owusu and Asumadu-Sarkodie, 2016). According to the latest Intergovernmental Panel on Climate Change report, it has been decided to limit the global average surface temperature increase to 1.5°C by 2030, which means the utilisation of renewable sources should be promoted (Leitzell and Caud, 2021). In comparison with the other renewable alternatives, geothermal energy is a cost-effective, technically proven, reliable, clean, and safe one, and it has been operated in various fields and applications for many decades (Brophy, 1997; Çiçek, 2020). Geothermal systems can deliver hot water into the buildings, which enables a free water heating possibility during power generation. Besides, geothermal energy has the smallest footprint among other major energy sources due to the innovations in technology.

The repeated opening and closing of Paleozoic and Mesozoic oceans dominate the geological and tectonic evolution of Türkiye, which is one of the most seismically active regions in the world (Dewey and Şengör, 1979). It is located within the Alpine-Himalayan orogenic belt at the geological margin between the African-Arabian and Eurasian plates.

Citation Info: Isık, T., Baba, A., Chandrasekharam, D., Demir, M. M. 2023. A brief overview on geothermal scaling. Bulletin of the Mineral Research and Exploration 171, 185-203. https://doi.org/10.19111/bulletinofmre.1228900

**Corresponding author: Mustafa M. DEMİR, mdemir@iyte.edu.tr*

The young volcanic activities, hydrothermally altered areas, and block faulting bring forth a wide range of hot springs in Türkiye; there are a total of nearly 1000 hot water springs in the country (Mineral Research and Exploration Institute (MTA), 1980; Mutlu and Güleç, 1998; Öngen and Ergüler, 2021). The geothermal fields in Türkiye can be grouped into four regions: western Anatolia, the North Anatolian fault zone, eastern Anatolia, and central Anatolia (Baba and Ármannsson, 2006). Türkiye's electricity generation capacity and the total installed direct heat use reached 1663 MWe and 5113 MWt, respectively, in 2022 (Şener et al., 2022). With these values, Türkiye ranked 4th in energy production and 2nd indirect use worldwide (Baba and Chandrasekharam, 2022). Considering Anatolia's Curie depth and heat flux, the probable thickness of the batholith can be regarded as 10 km. For example, the total granitoid area of Western Anatolia is 4221 km^2, and at least 2% of these granitoid can provide approximately 810^7 MWh of electricity by enhanced deep geothermal systems (Chandrasekharam and Baba, 2022). This high thermal regime gave rise to a large number of hydrothermal provinces throughout Türkiye. Moreover, the hydrogeochemical properties of the resources in Anatolia, which are so rich in geothermal resources, are quite different from each other. Moreover, each geothermal field shows different chemical composition from the others due to the complex lithology, tectonics, volcanic activities, and the structure of surrounding rocks. The majority of thermal waters in Türkiye are Na^+ - Ca^{2+} - HCO_3^- type, but on the coasts of western Anatolia, Na^+ - Cl^- type is also observed. The Argavlı and Sazlıköy springs are characterized as low-temperature springs, and Ca^{2+}, Mg^{2+} and HCO_3^- ions are dominated. On the other hand, the Gümüşköy region contains high-temperature wells with Na^+, K^+, Cl^-, and HCO_3^- predominant ions (Baba and Sözbilir, 2012).

Although its numerous advantages, such as energy harvesting and heating houses, geothermal energy has a serious obstacle. Because geothermal brine is composed of a mixture of minerals and gases, the high-temperature brine may cause operational limitations in geothermal systems called scaling and eventually corrosion (Figure 1) (Doğan et al., 2014). Scaling may result in plugging the wells and lines, and power plants face curtailment of production. In addition, the existence of scale on the wall of pipelines reduces both the steam or brine flow and effective heat transfer, which reduces the efficiency of geothermal plants and causes financial losses (Baba and Ármannsson, 2006). There are many studies to prevent the scaling problem in geothermal systems and treatment either with acids or organic antiscalants. However, acid treatment is a tedious process and requires more attention because the dosage and placement of the dosage in the system are highly critical; that high level of dosing may result in serious corrosion. On the other hand, increasing the solubility of ions/stability of colloids that are precursors of deposit by using antiscalants is a promising approach to minimize the scaling problem (Demir et al., 2014).

2. Scaling and Formation Mechanism

From the chemical point of view, scaling is nothing but the precipitation of compounds from aqueous solutions. Precipitates (deposits) are formed when certain cations and anions are combined and produce an insoluble ionic solid. Solubility guidelines give an essential impression about deposit formation (Petrucci et al., 2011). Petrucci et al. (2011) summarize the

Figure 1- a) Scaling examples from some geothermal fields (Doğan et al., 2014), scale formation in b) Tuzla geothermal field and c) antimony sulfide (stibnite) scaling examples from geothermal fields obtained from Kübilay geothermal power plant.

solubility rules for common ionic solids as follows: i) Group 1 cation and NH_4^+ form soluble salts, ii) the salts of nitrates, acetates, and perchlorates are soluble, iii) silver, lead, and mercury (I) salts are insoluble, iv) chlorides, bromides, and iodides are soluble, v) carbonates, phosphates, sulfides, oxides, and hydroxides are insoluble with some exceptions, and vi) sulfates are soluble apart from calcium, strontium barium. According to this guideline, the potential precipitation reactions could be predicted, and required precautions could be taken. All carbonates and silicates, which are, the main chemistry of geothermal scaling, insoluble in aqueous systems (Petrucci et al., 2011).

Precipitation of scales on the surface of heat exchanger tubes is a well-known problem called as fouling (Bott, 1995). Fouling decreases the thermal conductivity and overall heat transfer coefficient, which reduces the performance of heat exchangers due to the pressure drop in the fluid flow rate (Tubular Exchanger Manufacturers Association, 1952). This fouling layer increases in thickness with time until the heat exchanger loses its performance, whereby shutting down the system becomes a must. Geothermal fluids comprise several soluble species and dissolved gases with various concentrations. During the operation of geothermal systems, any change in the thermodynamics of the system, such as pressure and temperature thermodynamic change, may result in scaling or corrosion. The composition of geothermal fluids varies from site to site that there are various types of scale compositions due to the varied elemental constituents, and their composition depends on many parameters such as temperature and pressure of the fluid and water-rock interactions (Karabelas et al., 2002). Calcium carbonate and calcium silicate are the major constituents in geothermal fluids, while calcium sulphate, calcium carbonate, barium sulphate, calcium oxalate, strontium sulphate, and colloidal iron oxides are seen in some sites (Zhang et al., 2011). Generally, brines with a low and moderate temperature (<150 °C) end up the formation of calcium carbonate whilst high-temperature ones with high Total Dissolved Liquid (TDS) content yield siliceous scales (Owen and Michels, 1984; Corsi, 1986; Zhang et al., 2011). The term scaling generally refers to the formation and precipitation of inverse solubility salts when the salt exceeds its equilibrium solubility. The basic concept of scale formation is based on the solidification of an ionic substance that the change in Gibbs free energy transfers the substrate from a supersaturated state to an equilibrium state (Karabelas et al., 2002). For nucleation and growth, the driving force is needed that in geothermal systems, the change in temperature and pH is the most notable parameters. Figure 2 demonstrates a representative deposit developed in various geothermal fields.

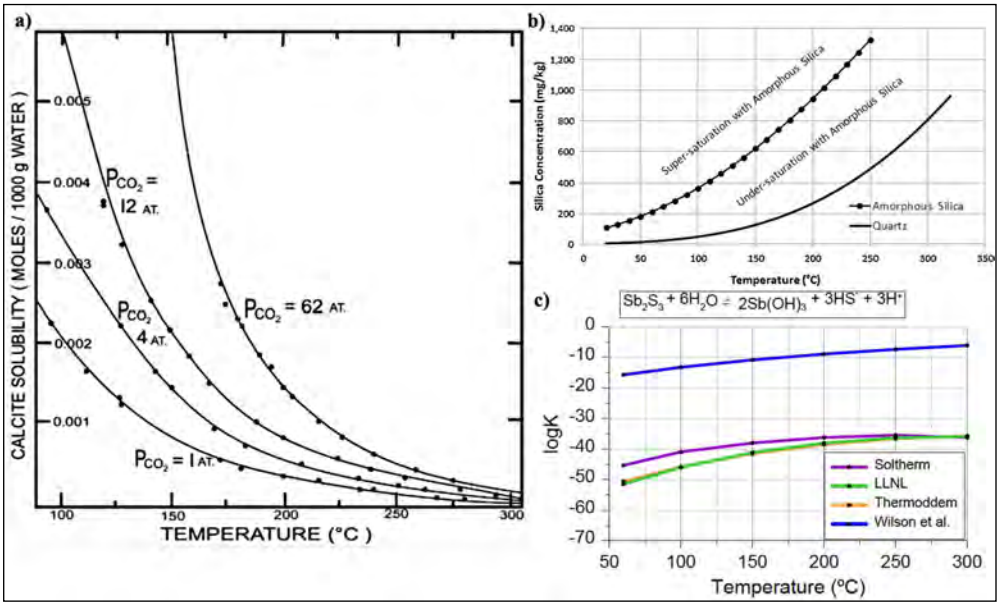

Figure 2- Effect of temperature on; a) calcite ($CaCO_3$), b) silica and c) stibnite solubility (Zarrouk and Purnanto, 2014; Buscarlet et al., 2016; Deendarlianto and Itoi, 2021).

The parameters pH, temperature, and pressure are the crucial ones that affect scaling in geothermal fluids. A high pH increases the concentration of carbonate ions and therefore induces scaling, whilst silica dissolution shows a different trend by changing pH (Kaypakoğlu et al., 2012). Calcite solubility increases as temperature decreases (Figure 2a) (Zarrouk and Purnanto, 2014; Deendarlianto and Itoi, 2021). Similar to the solubility of CO_2, increasing pressure improves the solubility of calcite. Silica, on the other hand, shows opposite behaviour against temperature (Figure 2b). Increasing temperature increase the solubility of silica and silica-containing deposits, for example, metal silica. Figure 2c demonstrates the dissolution of stibnite under the temperature effect. There is an increase in solubility as the temperature increases (Buscarlet et al., 2016).

2.1. $CaCO_3$

Calcite ($CaCO_3$) is the most abundant mineral in geothermal waters. There are different forms of calcite, such as aragonite and vaterite. However, since vaterite is not stable, it turns into calcite. Therefore, calcium carbonate precipitates mostly in calcite and aragonite forms. The factors affecting calcite scaling in geothermal waters are temperature, pH, and partial pressure of CO_2. As geothermal waters rise from the depths, their temperature and pressure decrease. CO_2 dissolved in the geothermal water due to the high pressure in the depths tends to escape from the geothermal water due to the decrease in pressure. At this time, the pH rises, and calcite scaling begins. This point where calcite scaling starts is called the flashing point or boiling point. Calcite scaling can be explained by Equation 1.

$$Ca^{2+}(aq)+2HCO_3\text{-}(aq) \leftrightarrow CaCO_3(s)+CO_2\uparrow(g)+H_2O)(l) \quad (1)$$

Calcite solubility is inversely proportional to temperature. In other words, calcite solubility decreases as the temperature increases. Therefore, in geothermal power plants, calcite scaling should not be expected in regions where cooling starts, such as heat exchangers, transmission lines, and reinjection wells. Calcite scaling is more common in production wells where the temperature is higher. In geothermal power plants calcite scaling can be controlled if the pressure of the geothermal fluid is kept above the partial pressure of the CO_2. On the other hand, using chemical inhibitors is another method to prevent calcite scaling.

Calcite scaling has been studied by different researchers around the world. Arnorsson (1989) studied calcite scaling theoretically and observed a decrease in the partial pressure of CO_2 due to boiling. This supported the supersaturation state and scaling of calcite. Akhmedov (2009) developed a kinetic model to calculate the calcium carbonate formation rate in his study. Ryley (1980) studied the relationship between wellhead pressure and mass discharge based on reservoir lithology and friction losses in a geothermal well. Barelli et al. (1982) focused on a two-phase flow model to understand the effect of heat exchange with height, non-condensable gases (NCGs), and salts in geothermal wells. A mathematical model for the estimation of calcite formation rates and analysis of the effect of calcite formation on flow rate were investigated by Satman et al. (1999). Patzay et al. (2003) simulated the flashing depth, temperature/pressure, and partial pressure profiles of non-condensable gases with the help of computer software. Wangen et al. (2016) considered the reduction problem in porosity due to scaling in the radius of the geothermal well with an analytical estimation. Siega et al. (2005) conducted a study on chemical inhibitors that prevent scale formation in the Mahanagdong geothermal field. Rangel et al. (2019) studied a chemical inhibitor in the Ribeira Grande geothermal field and concluded that this inhibitor was effective for 25 years in preventing calcite scaling. Lee et al. (2015) studied the effectiveness of two types of chemical inhibitors in the Chingshui geothermal field, whose production has decreased due to calcium carbonate scaling. Ramos-Candelaria et al. (2000) studied an inhibitor to prevent calcite scaling in the Mindanao geothermal field, which causes a production loss of 0.6 Mw per month. Calcium carbonate crystallization can be seen in many piping systems, and it is a common problem in low and medium-temperature geothermal systems. The crystallization occurs through three stages: supersaturation, nucleation, and crystal growth. The first stage, supersaturation, is the driving force of the crystallization process and directly affects the nucleation rate (Sousa and Bertran, 2014). The nucleation stage depends on the supersaturation level of the solution, but the diffusion of atoms and ions on the surface of nuclei governs the

crystal growth. There are mainly three polymorphs of calcium carbonate, which are called calcite, vaterite, and aragonite (Rafferty, 1999; Karabelas et al., 2002). Whilst high-concentration gradients favour the calcite crystallization, high temperature promotes aragonite crystallization (Ueckert et al., 2020). Among the other polymorphs, calcite is the thermodynamically most stable form at any temperature but least soluble in water (Putranto et al., 2018). Aragonite and calcite have similar structures, and carbonate ions are formed in a staggered arrangement relative to each other with the inter-planar structure that electrostatic repulsion can be reduced. Vaterite is the less dense form of calcium carbonate polymorphs, and carbonate ions are eclipsed relative to each other. However, the transitions between these forms are possible under specific conditions, e.g., the required temperature is 0 – 30 °C from vaterite to calcite and 60 - 80 °C from aragonite calcite (Boulos et al., 2014). The magnesium ion favours the precipitation of aragonite rather than calcite, and inhibits the nucleation and growth stages of calcite (Nancollas, 1982).

In geothermal systems, reinjection of brine into subsurface formations results in calcium carbonate scale formation. The formation mechanism occurs that the presence of CO_2 release during the flashing of vapour phase results in a pH increase in the geothermal systems, and supersaturation conditions deposit the $CaCO_3$ solid (Rafferty, 1999; Karabelas et al., 2002). Calcite is one of the most abundant minerals in drilled geothermal systems and hydrothermally altered rocks, and aragonite has also been reported in some fields. However, vaterite formation has not been identified in geothermal systems (Arnorsson, 1989).

2.2. Silica

Silica is considered one of the essential elements due to its abundance in the earth's crust and its important role in a variety of different processes (Petkowski et al., 2020). Silica scaling is a problem that can occur in medium and high enthalpy geothermal fields. In hydrothermal fields, silica occurs in different forms at different depths. These are generally in the form of amorphous silica, chalcedony, cristobalite, and quartz. Quartz is the most stable form of silica with the lowest solubility among these forms. The solubility of amorphous silica in geothermal waters decreases with temperature and creates a scale problem in regions where steam separation and cooling occur. Therefore, transmission lines, heat exchangers, reinjection wells, and in some cases, production wells in geothermal power plants are the riskiest equipment in terms of amorphous silica scaling (Utami, 2000; Gunnarsson and Arnórsson, 2005; Mundhenk et al., 2013; Demir et al., 2014; Baba et al., 2015; Pambudi et al., 2015).

Silica scaling is more complex than other types of scaling and has not been fully understood until now. For example, unlike calcite scaling, silica scaling is controlled by the polymerization kinetics of silicic acid [$Si(OH)_4$] (Ellis and Mahon, 1977). This silica polymerization is expressed by Equations 2 and 3.

$$2\cdot Si(OH)_4 \rightarrow (OH)_3SiOSi(OH)_3 + H_2O \quad (2)$$

$$Fe^{3+} H_2O + Si(OH)_4 \rightarrow Fe(OH)_3 \cdot SiO_2 + 3H^+ \quad (3)$$

These reactions define the first step of silica polymerization. In some geothermal fields, amorphous silica is found together with Al and Fe to form metal silicates (Gallup, 1993). Fe-O-Si bonds seen in Equation 3 are one of these metal silicates. Another metal silicate group is the Al-O-Si group. Al and Fe concentrations in geothermal waters lead to amorphous silica scale. Although Al concentrations in geothermal waters rarely exceed 5 mg/kg, the contribution of this value to scale formation is 10% by weight (Al_2O_3-SiO_2) (Ichikuni, 1983; Gallup, 1997; Yokoyama et al., 2002; Ueda et al., 2003; Ikeda and Ueda, 2017).

Silica scaling is the most challenging scale problem to remove and is complex to other scale types. This is because the silica scale is inert to many chemicals and resistant to mechanical cleaning. There are different studies on silica scaling in the literature (Gallup, 2002; Brown, 2011; Tobler and Benning, 2013; Andhika et al., 2015). Kristmannsdóttir mentioned that silica scaling caused a general problem in reinjection wells in 1989. On the other hand, significant silica (SiO_2) scaling in heat exchangers of binary geothermal power stations has been encountered in; Rotokawa and Ngawha, New Zealand (Wilson et al., 2007), Blundell, Utah (Gallup, 2011), two fields in the Imperial Valley, California (Gallup, 2011) and most likely many other plants around the world. One of the main contributors is that

binary plants generally operate at lower geothermal fluid reinjection temperatures than flash plants (Zarrouk and Moon, 2014) with a correspondingly higher silica saturation index. Investigating the efficiency of pH modification and the use of organic inhibitors have been the solution methods for reducing and preventing silica scaling (Gallup, 2002; Gallup and Barcelon, 2005; Baba et al., 2015).

For silica dissolution, aqueous hydrofluoric acid (HF) solutions have been studied for many years for wet chemical etching. F^-, HF, and HF_2^- species in solution attack the glass and adsorbed on surface siloxane, vicinal silanol and silanol groups, respectively (Demadis et al., 2012*b*). Thus, chemical cleaning by means of HF treatment, either in the form of pure HF or in situ creation by combining HCl and ammonium bifluoride (ABF) is accepted as silica scale dissolution method for decades (Mccartney et al., 2017). In an aqueous solution, HF acts as a weak acid, and there is an equilibrium between H^+ and F^- ions. Then, F^- attacks undissociated HF to form bifluoride anion (HF_2^-), which is responsible for the attack of the silica matrix and etches the silica surface (Wong et al., 2009) Whilst HF is effective for the dissolution of silicate scaling, it is not as effective in dissolving metal silicates. Note that, F^- forms precipitation with Ca^{2+} and Mg^{2+}. Therefore, HF is a toxic chemical once it touches the human skin, it penetrates to the skin and causes the destruction of the deep tissue layer (Schwerin and Hatcher, 2022).

Amorphous silicate formation is based on the condensation polymerization of the silicic acid in acidic or basic environments (Figure 3) (Nassif and Livage, 2011). In most of the geothermal systems, dissolved CO_2 is found in $CO_{2(aq)}$ and HCO_3^- forms. Dissolved CO_2 is available in the geothermal hot water reserves. The temperature of geothermal fluid decreases while it moves through the well to the surface, and CO_2 is released into the vapor phase due to the pressure decrease. When the CO_2 amount in the geothermal fluid decreases, the water loses its acidity, the solubility of silicate decreases, and the fluid becomes over-saturated. When the steam flushes, the temperature of the brine drops and becomes even more saturated. In that case, the silica content, which is already unstable, becomes even more unstable (Demadis, 2010).

After the removal of CO_2 from the system, the pH of the system rises, and the major ions in geothermal fluid (such as Fe^{2+}, Mg^{2+}, Ca^{2+}) precipitate in the hydroxide form. Moreover, increased pH and the presence of Fe^{2+}, $Fe^{3+}$and Al^{3+} ions stimulate the silica polymerization simultaneously, and metal hydroxides interact with silica polymers to form metal silicate compounds, which are very hard to dissolve. These compounds are comprised of various oligomeric structures in amorphous form and have similarities with colloidal silica (Gallup et al., 2003). During polymerization, there is a need for a balance between

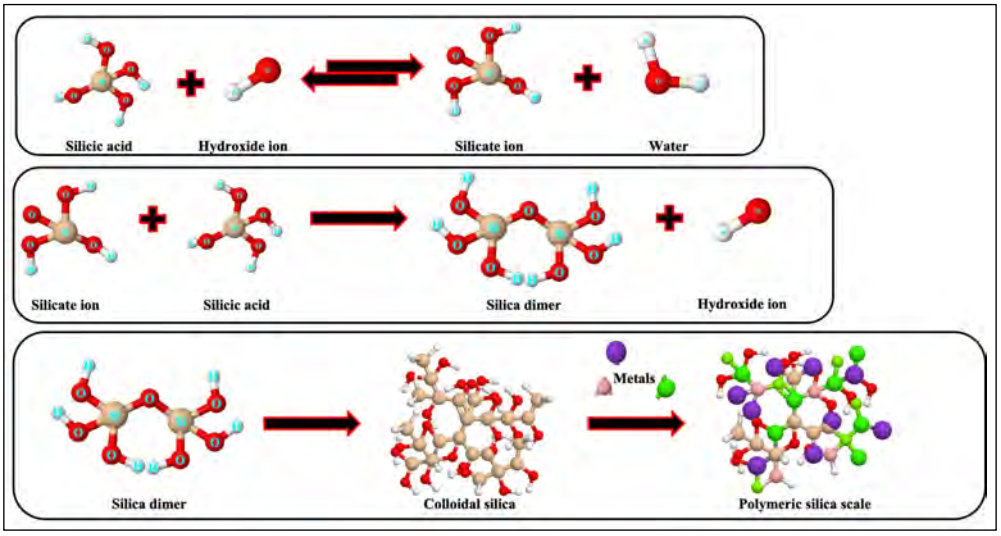

Figure 3- Polymerization reaction of ortho silicic acid (red: oxygen, white: hydrogen, nude: silicon, purple and green: metal ions).

unionized and ionized silica species. At high pH, the formation possibility of metal silicates increases because ionization of silicic acid is favoured, and silica polymerization slows down (Gill, 1993; Demadis and Mavredaki, 2005). Metal silicates can form in metal-rich geothermal brines, and commonly presented metal ions are aluminum (Al), magnesium (Mg), and iron (Fe). Metal silicates have much lower solubility than bare silica and have complications during the cleaning processes (Gallup, 2011).

Metal silicate scaling is probably the most difficult scale in geothermal systems because silica is found abundantly in all geothermal fluids, and its concentration increases with temperature. The formation of scale has economic sevre consequences such as increased costs for pumping, cleaning, and maintenance, loss or abandoning and reinjection of system due to clogging (Karabelas et al., 2002). Furthermore, the deposit formation reduces the inner width of the pipes and prevents heat transfer and the efficiency of production drops (Topçu et al., 2019*a*).

Thus, there is an increased need to understand the scaling and mitigate this problem. Generally, the elimination of silica deposition before it is formed is one of the frequently used methods (Demadis, 2005). However, silica polymerization has not been completely understood yet because every geothermal fluid has unique characteristics due to different environmental conditions such as salinity, temperature, and water-rock interactions. On the other hand, the removal of silica scaling by using acid treatment is another point of research. Water-rock interactions have been conducted by several researchers, and the chemical composition of geothermal brines is determined by their origin, the lithology of interacted rocks, and the temperature of the system (Gören et al., 2021).

2.3. Stibnite (Antimony Trisulphide)

Antimony-rich sulphide deposits have been observed in several geothermal plants, and their formation mechanism has drawn attention in the last years due to the dissimilarities from those carbonates and silicates. Antimony is found in sulfide derivatives such as stibnite and sulfosalts and forms stable interactions with sulphur. There are two oxidation states of antimony, which are trisulphide (Sb^{3+}) and pentasulphide (Sb^{5+}). Stibnite (Sb_2S_3), also known as antimony trisulphide, is a mineral with an orthorhombic crystal lattice. It has been observed in various power plants, and also it is the main component of hydrothermal systems. Stibnite dissolution occurs in water as hydroxide forms and hydrogen sulphide formation increases during the storage of stibnite. Equation 4 shows the dissolution of stibnite in water.

$$Sb_2S_3 + 6\ H_2O \rightarrow 2\ Sb(OH)_3 + 3H_2S \quad (4)$$

In geothermal reservoirs, in which H_2S is already present, stibnite can form sulfosalts of antimony after dissolution (Equation 5). At this stage, $H_2Sb_2S_4$ is a significant problem when H_2S concentration is high, or the system temperature is relatively low (Kevin, 2013; Haklıdır and Balaban, 2019).

$$Sb_2S_3 + H_2S \rightarrow H_2Sb_2S_4 \quad (5)$$

However, stibnite causes corrosion in geothermal systems and its mitigation is vital for the efficient running of the system (Ellis and Mahon, 1977). Stibnite precipitation can be controlled by pH and temperature. Because in condensers and heat exchangers, pH and temperature play an essential role such that the deposition of sulphur-based scales has been observed in these parts of the system. Although antimony is found in low concentrations in brine, stibnite formation is a major problem at low temperatures and pH. Wilson et al. (2007) reported that stibnite forms in the heat-exchanger units of New Zealand binary geothermal power stations, Rotokawa and Ngawha, and has developed into an ongoing problem. They determined the conditions to produce stibnite scaling and quantified the rate of deposition in each system. Also, they determined the Sb routes through geothermal fluids. Reyes et al. (2003) and Raymond et al. (2005) claimed that Sb is found not only in brine fraction but also may be transported in the vapour phase. A similar problem has been reported in an exploration well in Italy and in a pipe fragment in a Berlin station (Cappetti et al., 1995; Raymond et al., 2005). In Türkiye, stibnite scaling is a growing problem in many geothermal plants and is observed in the Germencik Geothermal Field (GGF) of the Büyük Menderes Graben (BMG) system. Tonkul et al. examined the stibnite scaling on the preheater of GGF and determined the optimum reinjection temperature as 95 °C to prevent the

stibnite scaling (Tonkul et al., 2021). Avoiding of low pH and temperature, caustic dosing, chemical inhibition by antiscalants, chemical removal and mechanical removal such as high-pressure water blasting are possible methods to mitigate stibnite scaling (Kevin, 2013) Figure 2b shows the stibnite scaling from geothermal fields obtained from Kübilay geothermal power plant. Moreover, hot caustic soda (NaOH) circulation has been used in New Zealand and is considered as the most effective method for the dissolution of stibnite deposits in heat exchangers (Brown, 2011). Inanli and Atilla also utilised hot NaOH and found it successful to remove magnesium – iron silicates (İnanli and Atilla, 2011).

Karaburun et al. (2022) and Çiftçi et al. (2020) studied the solubility of stibnite in the presence of potential antiscalants containing various functional groups such as acrylic acid, sulphonic acid, and phosphonic acid under both in the lab (reflux and autoclave) and in the field. Both testing pointed out that sulphonic acid containing antiscalants were found to be the most effective ones in mitigation of the sulphide-rich deposits.

3. Sources supplying materials for scaling

Geothermal waters generally contain large amount of dissolved minerals and gases. These minerals and gases precipitate when the geothermal waters move from hot environment to cooler environment and get deposited in almost ll the appliances that carry the fluids. Types of scaling depend on the geothermal reservoir composition. The types of reservoir rocks widely depending on the geographic location of the geothermal systems. There are three main reservoir rocks that are commonly encountered. There are sedimentary rocks such as sandstones, volcanic rocks such as basalts and andesites and plutonic rocks like granites.

Silica is the most common dissolved mineral in high temperature geothermal systems (250 °C) occurring in countries like Iceland and New Zealand. The dissolved silica is usually in amorphous form. When the geotheral fluid cool, the steam separates thereby making the liquid supersaturated in silica, resulting in precipitation (Mahon, 1966; Gunnlaugsson et al., 2014). The reservoir rocks are volcanic, like basalt and andecite.

Iron siliate sacling occurs commonly in geothermal waters where the reservoir rocks are ultramafic rocks like peridotite, dunite and pyroxenite where Mg-Fe silicte minerals dominate in these rocks. These geothermal systems are found in Indonesia and New Zealand (Gunnlaugsson et al., 2014). They are commonly associated with iron sulphide scales.

Sulphide scaling is common in geothermal systems rich in H_2S gas, that are commonly associated with active volcanic regions (like Iceland) or in geothermal systems where the reservoir rocks are rich in sulphide minerals like galena (PbS), covellite (CuS), chalcopyrite ($CuFeS_2$), stibnite (SbS_2). These minerals are common in geothermal systems in Iceland, Italy, Indonesia and Türkiye (Ármannsson and Hardardóttir, 2010; Gunnlaugsson et al., 2014; Tonkul et al., 2021).

Calcite scaling is very common, especially when the reservoir rocks are of limestone or dolomite such a those found in Italy (Montanari et al., 1994) and Türkiye and volcanic rocks such as those found in Iceland and New Zealand (Simmons and Christenson, 1994; Gunnlaugsson et al., 2014).

4. Methods to Prevent Scaling

For several years, the methods to control geothermal scaling have been investigated. pH modification and utilisation of scaling inhibitors are common remedies for the prevention of scaling in geothermal systems.

4.1. pH Modification

As a fruitful approach, pH modification has been used to reduce the scaling in geothermal power plants. Manipulation of the chemical composition of geothermal fluids can be performed by modifying the pH of the system. pH modification can be applied either by increasing pH to increase the solubility of the deposits (Lichti and Brown, 2013).

The addition of hydrochloric acid (HCl) into the geothermal fluids is a common strategy, and even a subtle decrease in pH below a certain value, at which the formation of carbonate scaling becomes impossible, results in the prevention of scaling. Hoyer et al. (1991) controlled the ferric silicate scaling at the Salton Sea by brine acidification. A small amount of HCl is injected into the brine to lower the pH by up to 0.3 units and this little pH change inhibits the ferric silicate

formation (Hoyer et al., 1991). The optimisation of acid dosage and choosing the acid injection point are two significant parameters. However, the main drawbacks of this approach using inorganic acid are the cost of consumed acid during the pH modification, corrosion and as well as health issues. Because most geothermal liquids have extremely large buffer capacity, even for a small decrease, a large amount of acid is required (Topçu et al., 2019*b*). There is a need for an alternative approach to prevent scaling and remediate the scaling problems in geothermal systems. For the mitigation of amorphous silica and metal silicates, pH modification with concentrated sulphuric acid (H_2SO_4) has been used in Mak-Ban (Bulalo, Philippines) geothermal field (Gallup, 2011). Similarly, concentrated H_2SO_4 is injected into the brine in Hatchobaru, Japan, and at pH 5-6, the silica scaling rate was reduced significantly (Kiyota and Uchiyama, 2011). Moreover, H_2SO_4 application contributes to the reduction of hazardous hydrogen sulphide emission from geothermal power stations that produced hydrogen sulphide gas was converted to H_2SO_4 by the help of a sulphur oxidising bacteria *Thiobacillus thioparus* (Hirowatari, 1996). Corrosion is a serious issue, particularly in the elbow part of the pipeline, when such inorganic acids are dosed in the system.

Since CO_2 removal triggers the formation of stibnite-based deposits, the application of organic acid R-COOH is a wise approach for pH modification. The smallest organic acid with one carbon atom and structure is similar to CO_2 in formic acid and is environmentally benign. Formic acid (H-COOH), the smallest organic acid with a single carbon atom, has been used to minimize silicate scaling in Tuzla regions successfully. The brine has pH of 7.2 and is reduced to 6.2 by the injection of CO_2 (Topçu et al., 2019*b*). It is the simplest organic acid with a similar chemical structure of CO_2 that removal of CO_2 from the system causes an increase in pH and results in silicate formation. This simple organic acid is able to inhibit the colloidal silica formation and enhances the dissolution of already formed scales. Baba et al. (2015) studied the required dosage and optimum conditions for formic acid treatment and reported that 55 ppm formic acid is a required concentration for the minimization of silicate scaling. However, formic acid offers a short-term solution to the scaling problems.

The use of gas having geological origin and acidic characteristics might be a possible solution to reduce the meta-silicate scaling in geothermal systems. Carbonic acid (H_2CO_3) has moderate acidity and a simple chemical structure. Carbonic acid dissociates into CO_2 which changes the solubility of brine and it comes from the magmatic processes or decomposition of organic matter in sedimentary rocks (Hibara et al., 1990; Topçu et al., 2019*b*).

Formic acid shows the most similar chemical structure to CO_2 and the acidity of the geothermal fluid can be modified via formic acid to bring back the optimum conditions and enhance silica dissolution. In Tuzla Geothermal Power Plant (TGPP), formic acid has been adopted to minimize the amorphous silica and metal silicate deposition. The optimum condition for formic acid dosage was determined as 55 ppm and the stand time is retarded from 1 to 6 months (Baba et al., 2015). Moreover, CO_2 injection is another approach to prevent metal silicate scaling. Topçu et al. (2019) injected CO_2 gas into to the TGPP with various flow rates, and the results emphasized that 20.6 m^3/s CO_2 injections showed a better performance than 55 ppm formic acid injection, and less corrosion is observed in CO_2 gas injection (Topçu et al., 2019*b*). In this way, a sustainable route can be achieved in geothermal systems by capturing the released CO_2 from the system and injecting it through the wells. As a new perspective to the pH modification and antiscalant application in geothermal systems, there is a patent application for the usage of CO_2 as an antiscalant (Baba et al., 2020).

4.2. Dosing of Antiscalants

Antiscalant utilisation is the most promising and eco-friendly method to struggle with the scaling problems, and there is a wide variety of inhibitor chemicals in the market according to the encountered problems. They are commercial products and have been used to ruin the crystal structure of scale minerals. Their application is carried out to prevent the calcite, silica, stibnite, and other possible scale formations, and inhibitors are picked up according to the reservoir temperatures of geothermal wells.

Various polymeric macromolecules have been used as antiscalants in geothermal systems, and commercially, there is a wide range of antiscalants in the market (Çiftçi et al., 2020). However, the vital

point is to test and choose the proper antiscalant for the field according to the physical conditions (pH, temperature, pressure, etc.) and chemical composition of the field. Performing the tests to choose the potential commercial antiscalants in the field conditions is a tedious and costly process. Therefore, the synthesis of geothermal deposits artificially in the laboratory under desired conditions (either with reflux or autoclave type pressurized reactor) is a more practical and economical way to perform the tests for antiscalant performances. Çelik et al. (2017) employed a reflux and autoclave reactor system to synthesize artificial metal silicate deposits in the laboratory (Figures 4a and 4b).

The reflux includes a round-bottom flask heated to 90 ℃ under atmospheric conditions. On the other hand, the autoclave reactor is comprised of a closed container, liquid and gas inlets, a magnetic mixing monitor, and temperature – pH probes. Hot silicone oil circulates throughout the closed container and heats the device up to 250 ℃ and the magnetic mixing motor stirs the reaction solution up to 3000 rpm (Çelik et al., 2017). By this way, the conditions of a real geothermal well can be mimicked under laboratory conditions without using large amounts of chemicals during the optimisation of antiscalant parameters.

There are two main mechanisms for the mitigation of deposits. The first one is stabilization of colloidal particles occurring in the brine. Colloids are accepted as the precursor of the deposit, .e. initial solid particles precipitated in the system. Since they have a submicron diameter, they have the large surface area to volume ratio. A strong tendency exists for aggregation and agglomeration, eventually deposit formation. Against the aggregation process, dispersion agents are applied to the system to coat the colloid surface such that the surface energy of the particles is reduced and the undesirable aggregation is prevented. The second mechanism is chelation. A Coulombic interaction

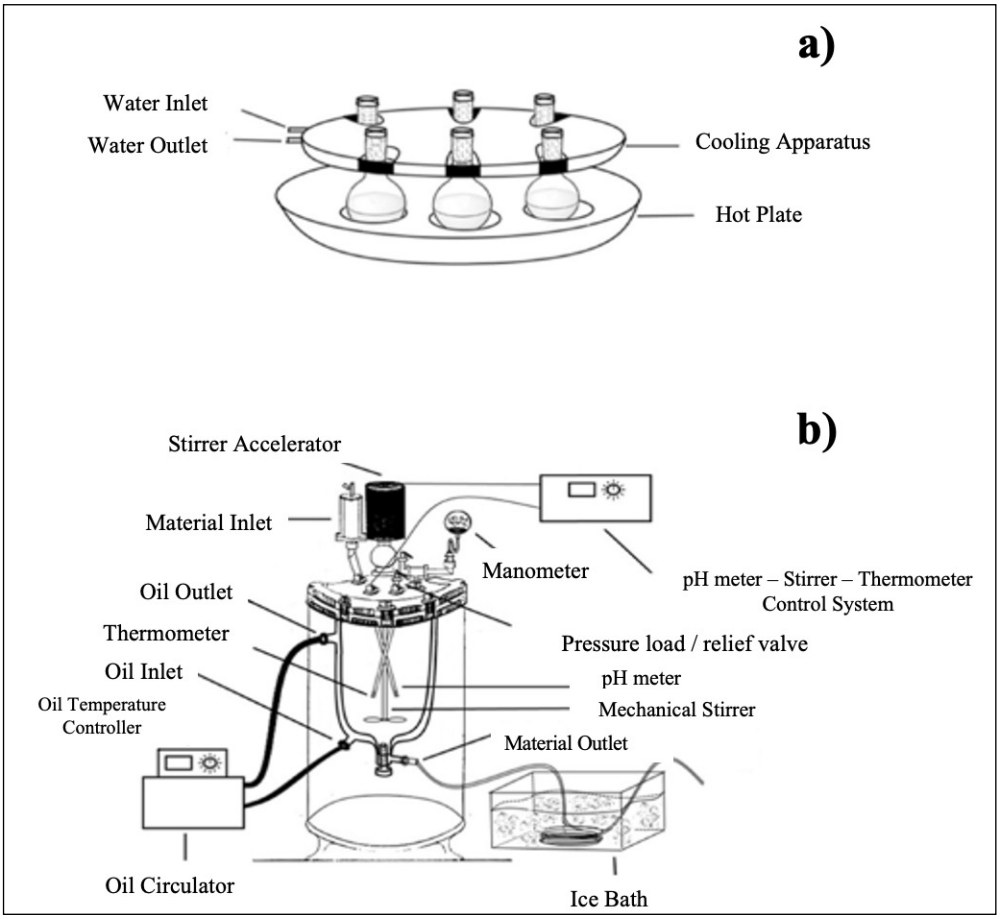

Figure 4- Schematic view of; a) reflux and b) autoclave reactor systems (Çelik et al., 2017).

takes place between electron-rich functional groups and a metal cations. This interaction prevents the metal to contribute the formation of a deposit. The cartoon demonstration given in Figure 5b shows interaction with one cation and one carboxylic acid group. However, there may be a higher number of cations for one negative central organic group. For comparison of both dispersion and chelation mechanisms, note that the colloids are large submicrometer structures containing more than thousands of atoms; on the other hand, chelation prevents one or several number of cation.

Figure 6 demonstrates the monomers of artificially synthesized antiscalants in an autoclave reactor system (Topçu et al., 2017). The antiscalants can work either by chelation or dispersion mechanism, and these monomers are able to work in both chelation and dispersion mechanisms.

Topçu et al. (2017) developed four different co-polymers by merging three different monomers with different combinations that have various chelating groups for metal cations. They synthesized homo and copolymers of acrylamide (AM), the sodium salt of vinyl sulfonic acid (VSA), and vinyl phosphonic acid (VPA) monomers via free radical polymerization and investigated their antiscaling performance against metal-silicate scaling was examined in an autoclave system to stimulate the real field conditions. The performance of synthesized antiscalants was evaluated by monitoring the ion concentration in the decantate solution after the removal of precipitates by centrifugation. They reported that VSA-rich copolymers showed the most promising antiscalant performance for Fe and Mg silicates. The solubility was improved to 225 ppm when 50 mL of 50 ppm antiscalant was employed at 137.6 °C and 3.2 bar for 45 min.

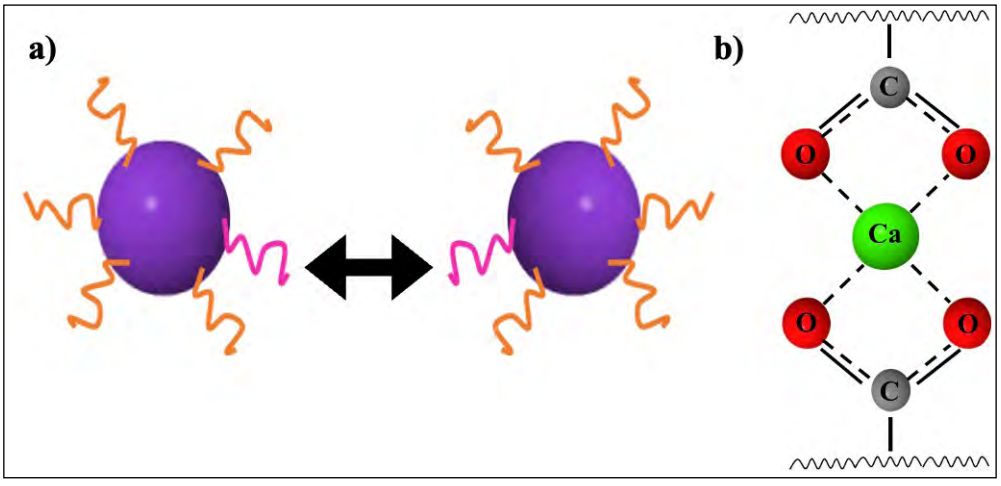

Figure 5- Main mechanisms of deposit formation; a) dispersion, steric stabilization of colloids against aggregation, b) chelation, chelation of Ca^{2+} with carboxylic acid group given as an example.

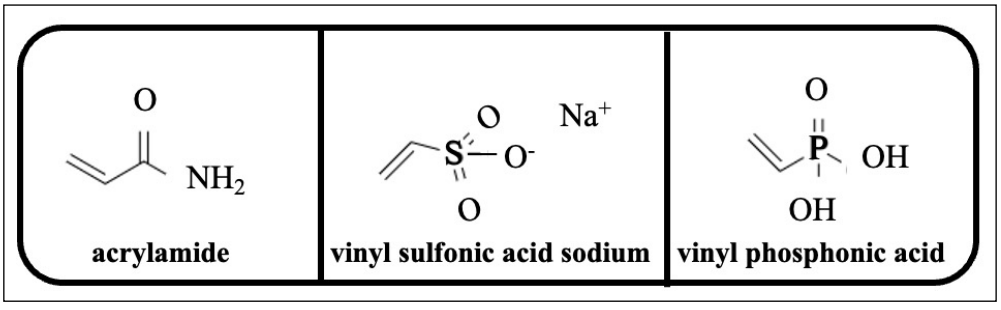

Figure 6- Molecular structure of monomers of artificially synthesized antiscalants (Topçu et al., 2017).

To get further understanding of the efficiency of metal-chelate agents without performing laboratory experiments, a complete information about the structural characteristics and selectivity performance of antiscalants may be provided by quantum mechanical calculations, and density functional theory (DFT) can be used to perform these first-principal calculations. Topçu et al. calculated the binding energies of antiscalant to the selected metal ions (Mg^{2+}, Ca^{2+}, and Fe^{2+}) and investigated the tendency of chelation performances (Topçu et al., 2019*b*). Using this approach, the chelating ability of molecules can be predicted before the tests, and the time and cost-efficient analysis can be performed (Figure 7).

Amine structural units have been proposed as potential silica inhibitors in the literature. Chauhan et al. (2014) synthesized a star-shaped polymer by using a polyacrylamide and polyacrylic acid modified bio-inspired algae core (Figure 8). The results of this study emphasized that experiments, which were carried out at a higher temperatures, have lower soluble silica levels and these star-shaped copolymers have nearly 95% inhibition performance at 55°C for 12 h of reaction time (Chauhan et al., 2014).

Chelating agents have been alternatively used for silica dissolution. (Fredd and Fogler, 1998) used ethylenediaminetetraacetic acid (EDTA) or nitrilotriacetic acid (NTA) to chelate or bind metals such as calcium. During the process, the chelating agent solvates the calcium ion and allows the calcite to be transported to the surface of the well or into the injection well. The rate of calcite dissolution by using chelating agents is lower than the utilisation of mineral acids which means the chelating agent moves through a longer path and dissolves more calcite along the way by entering all fractures (Rose et al., 2007).

The main idea of chelation is to entrap the sedimentary ions before their precipitation in the geothermal well and prevent their scale formation by stabilizing the silica colloids (Topçu et al., 2019*b*). Polymeric molecules have been used for the stabilization of colloidal silica particles either by van der Waals forces or hydrogen bonding. Preari et al. (2014) employed Polyethylene glycol (PEG), which has been used as non-ionic surfactant in the literature, and investigated the interaction between PEG and silica species at neutral conditions via hydrogen bonding. PEG is a typical dispersing agent this in fact, a surface active reagent. It adsorbs to

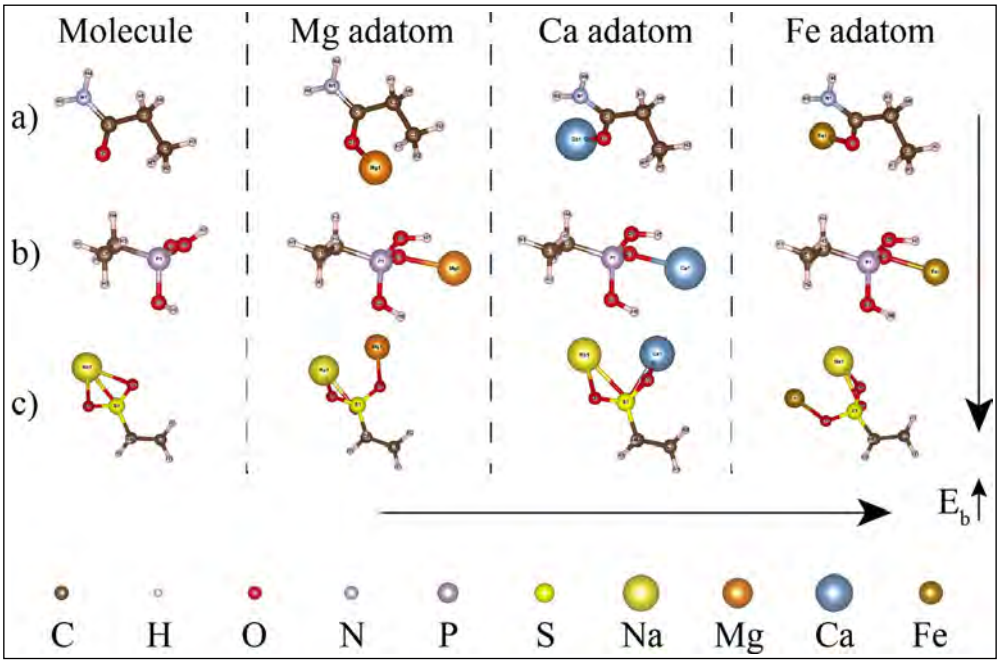

Figure 7- Schematic representation of the metal ions captured by antiscalant molecules; a) acrylamide, b) vinylphosphonic acid, and c) sodium salt of vinyl sulfonic acid (Topçu et al., 2019*b*).

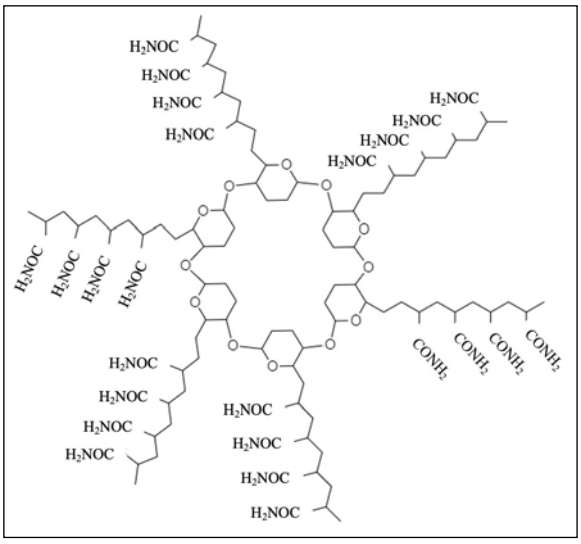

Figure 8- Structure of Algea core star shaped polyacrylamide dendrimer (Chauhan et al., 2014).

the surface of colloids and prevents aggregation and agglomeration of the individual silica particles (colloidal stabilization). The molecular weight of the dispersion agent is critical for the stabilization of the known size of the colloids. Note that smaller colloids need lighter molecular weight dispersing agents. Poly (vinyl alcohol) and poly (vinyl pyrolidone) are known examples of this group of agents.

Polymers with positively charged end-groups have been frequently preferred and compounds with protonated amines, amide moieties and phosphonium are promising candidates for silicate scale prevention applications (Demadis and Neofotistou, 2007; Spinde et al., 2011; Daniloytseva et al., 2011; Demadis et al., 2008; 2012*a, b, c*) Topçu et al. (2019*b*) employed polyethylene gloycol, polyvinyl alcohol, polyvinylsulfonic acid (PVSA), polyvinylphosphonic acid and polyacrylamide with various molecular weights as silica-targeted metal-silicate antiscalants. They provided evidence that orthosilicic acid polycondensation can be prevented by ether and alcohol moieties on polymer chains in the presence of various metal cations such as Fe^{2+}, Mg^{2+} and Ca^{2+}. Even these cations act as catalyst for polycondensation reaction, the silicate solubility is enhanced by using PEG and PVSA mixture not only in hot geothermal wells but also in cold industrial water systems. The dissolved silica concentration increased from 130 to 420 ppm when 100 ppm PEG and 25 ppm PVSA were employed as a mixture at 137.6 °C and 3.2 bar.

Dendrimers are another class of antiscalants that are repetitively branched globular molecules and some of them are effective silica inhibitors. Polyaminoamide (PAMAM) dendrimers have amine functional groups, and they are able to interact with negatively charged silica. Demadis et al. (2008) demonstrated the importance of ionic interactions over silica scaling and at high cationic charge densities, silica entrapment occurs due to the attack of $-NH_3^+$ groups (Neofotistou and Demadis, 2004; Demadis and Neofotistou, 2007). Different functional groups on PAMAM dendrimers have significant effects on silica scale prevention. Whilst -COOH groups were not efficient due to the repulsive forces between anionic silica and deprotonated COO^- groups, $-NH_2$ terminated dendrimers (Figure 9) have a remarkable effect on silica scaling (Neofotistou and Demadis, 2004). According to their results, 40 ppm $-NH_2$ terminated PAMAM increases silica concentration from 171 to 384 ppm. However, the dosage of these dendrimers is an important parameter, although they are promising solutions for silica scaling.

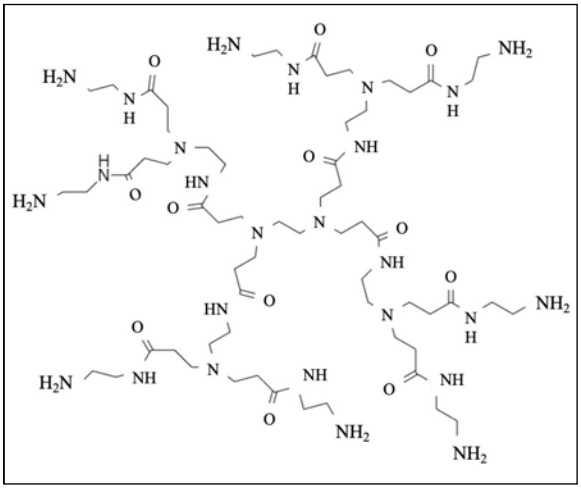

Figure 9- Chemical structure of $-NH_2$ terminated PAMAM (Neofotistou and Demadis, 2004).

During the application of antiscalants, white flocculant formation indicates the loss of inhibition performance of inhibitors in time because protonated $-NH_3^+$ groups entrap with anionic silica groups. Neofotistou and Demadis (2004) proposed the addition of an anionic polymer to prevent the flocculation effect of PAMAM-SiO_2 complex and Carboxymethylinulin (CMI) polymer was used

as an anionic polymer. Hereby, anionic groups of deprotonated -COO^- on CMI neutralizes the -NH_3^+ groups on PAMAM dendrimer and flocculation of -NH_2 and SiO_2 was prevented in the system. According to the results, a 40 ppm dosage of CMI is an adequate amount for inhibition performance. As an anionic polymer, polyepoxysuccinic acid (PESA) has been used by Zhang et al. (2011). to get rid of white flocculants, which were formed by the interaction between -NH_2 groups of adipic acid/ amine-terminated polyethers D230/ diethylenetriamine copolymer and silica particles. 20 ppm PESA neutralized the positive charges when 40 ppm copolymer was used. A copolymer of acrylic acid and hydroxypolyethoxy allyether was used by (Gill, 2011) to retard the silica polymerization and disperse the polymerized silica. Polyetyhelenemine has been also used as a scale inhibitor, and Demadis and Stathoulopoulou (2006) compared the efficiency of this -NH_2 terminated polymer with PAMALAM dendrimer. According to their results, both cationic polymers enhance the silica solubility, but high positive charge density results in inhibitor coprecipitation with anionic colloidal silica, whereas low charge densities render the inhibitor ineffective at lower dosages. 10 ppm PEI reaches 55% inhibitory efficiency at 24 hours, whilst 80 ppm PAMALAM dosage exhibits 60% inhibition.

5. Results

Scaling has been observed in all geothermal power plants to some extent, regardless of the chemistry of the deposit. The geothermal systems, particularly the ones electrical energy is harvested, are quite concentrated in terms of minerals. For instance, there are some distinct geothermal fields with highly corrosive fluids such as Tuzla (Çanakkale), Seferihisar (İzmir), Gülbahçe (İzmir) and Çeşme (İzmir). Total dissolved solid concentration usually exceeds 5.000 ppm which causes running and maintenance problems based on scaling and as well as corrosion (Baba, 2015). In addition to the high concentration of minerals, another issue that must be considered is the geothermal systems' dynamic nature. Power plants produce a large volume of brine so that the reservoir change over time, and new troubleshooting methods to the problems are required. Accordingly, the chemistry of the deposit is a subject to change. The formation of the deposition may not be entirely prevented; however, it can be minimized to an acceptable amount of time. Various potential chemistries have been mentioned in the text. Their performance varies depending on the temperature and salinity of the geothermal power plant of interest. A particular study must be performed for each field to find the best antiscalant or antiscalant composition for the increase of the performance of geothermal power plants. The performance of potential nominees commercial antiscalants can be tested by pressurized reactors readily employing field conditions. Moreover, computational tools can be used for the selection of the best functional group of antiscalant molecules.

Acknowledgements

DC thanks TUBİTAK (Project No: 120C079) for the support to participate in this work.

References

Akhmedov, G.Y. 2009. Kinetics of growth of calcium carbonate deposits in geothermal systems. Thermal Engineering 56, 909–913.

Andhika, M., Castaneda, M. C. H., Regenspurg, S. 2015. Characterization of silica precipitation at geothermal conditions, in: World Geothermal Congress.

Ármannsson, H., Hardardóttir, V. 2010. Geochemicqal patterns in saline high temperature geothermal systems. Water-Rock Interaction 133–136.

Arnorsson, S. 1989. Deposition of calcium carbonate minerals from geothermal waters- Theoretical considerations. Geothermics 18, 33–39.

Baba A. 2015. Application of geothermal energy and its environmental problems in Turkey. International Journal of Global Environmental Issues 14, 321–331.

Baba, A., Ármannsson, H. 2006. Environmental impact of the utilization of geothermal areas. Energy Sources, Part B: Economics, Planning and Policy 1, 267–278.

Baba, A., Chandrasekharam, D. 2022. Geothermal resources for sustainable development: A case study. International Journal of Energy Resources 46, 20501–20518.

Baba A., Sözbilir, H. 2012. Source of arsenic based on geological and hydrogeochemical properties of geothermal systems in Western Turkey. Chemical Geology 334, 364–377.

Baba, A., Demir, M. M., Koç, G. A., Tuğcu, C. 2015. Hydrogeological properties of hyper-saline geothermal brine and application of inhibiting siliceous scale via pH modification. Geothermics 53, 406–412.

Baba, A., Demir, M. M., Koç, G., Avcı, İ. 2020. Geothermal power plant system used as a line inhibitor to prevent the scaling of greenhouse gases emitted from the system. Patent number: WO2021145839A3.

Barelli, A., Corsi, R., del Pizzo, G., Scali, C. 1982. A two-phase flow model for geothermal wells in the presence of non-condensable gas. Geothermics 11, 175–191.

Bott, T. R. 1995. Fouling of Heat Exchangers. Elsevier Science, 524.

Boulos, R. A., Zhang, F., Tjandra, E. S., Martin, A. D., Spagnoli, D., Raston, C. L. 2014. Spinning up the polymorphs of calcium carbonate. Scientific Reports 4.

Brophy, P. 1997. Environmental advantages to the utilization of geothermal energy. Renewable Energy.

Brown, K. 2011. Antimony and arsenic sulfide scaling in geothermal binary plants. International Workshop on Mineral Scaling.

Buscarlet, E., Richardson, I., Addison, S., Moon, H., Quinao, J. 2016. Geochemical Modelling of Plant and Reservoir Processes at the Ngatamariki Geothermal Field. 38th New Zealand Geothermal Workshop.

Cappetti, G., D'Olimpio, P., Sabatelli, F., Tarquini, B. 1995. Inhibition of antimony sulphide scale by chemical additives: laboratory and field test results. World Geothermal Congress, Firenze.

Chandrasekharam, D., Baba, A. 2022. Carbon dioxide emissions mitigation strategy through enhanced geothermal systems: western Anatolia, Turkey. Environmental Earth Sciences 81.

Chauhan, K., Patiyal, P., Chauhan, G. S., Sharma, P. 2014. Star-shaped polymers of bio-inspired algae core and poly(acrylamide) and poly (acrylic acid) as arms in dissolution of silica/silicate. Water Resources 56, 225–233.

Corsi, R. 1986. Scaling and corrosion in geothermal equipment: Problems and preventive measures. Geothermics 15, 839–856.

Çelik, A., Topçu, G., Baba, A., Akdoğan, Y., Şentürk, U., Demir, M. M. 2017. Experimental modeling of silicate-based geothermal deposits. Geothermics 69, 65–73.

Çiçek, A. 2020. The electric power production targeted unconventional geothermal systems (UGS), some conceptual designs and their thermodynamics classification. Bulletin of the Mineral Research and Exploration 163, 211–228.

Çiftçi, C., Karaburun, E., Tonkul, S., Baba, A., Demir, M. M., Yeşilnacar, M. İ. 2020. Testing the performance of various polymeric antiscalants for mitigation of Sb-Rich precipitates mimicking stibnite-based geothermal deposits. Geofluids 2020.

Daniloytseva, E. N., Pal'shin, V. A., Likhoshway, Y. V., Annekov, V. V. 2011. Condensation of silicic acid in the presence of co (1-vinylimidazole–acrylic acid). Advance Science Letter 4.

Deendarlianto, K., Itoi, R. 2021. Numerical study of the effects of CO_2 gas in geothermal water on the fluid-flow characteristics in production wells. Engineering Applications of Computational Fluid Mechanics 15, 111–129.

Demadis, K. D. 2005. A structure/function study of polyaminoamide dendrimers as silica scale growth inhibitors. Journal of Chemical Technology and Biotechnology 80, 630–640.

Demadis, K. D. 2010. Recent developments in controlling silica and magnesium silicate foulants in industrial water systems. The Science and Technoloyg of Water Treatment, 179–203.

Demadis, K. D., Mavredaki, E. 2005. Green additives to enhance silica dissolution during water treatment. Environmental Chemistry Letters 3, 127–131.

Demadis, K. D., Stathoulopoulou, A. 2006. Solubility enhancement of silicate with polyamine/polyammonium cationic macromolecules: Relevance to silica-laden process waters. Industrial and Engineering Chemistry Research 45, 4436–4440.

Demadis, K. D., Neofotistou, E. 2007. Synergistic effects of combinations of cationic polyaminoamide dendrimers/anionic polyelectrolytes on amorphous silica formation: A bioinspired approach. Chemistry of Materials 19, 581–587.

Demadis, K. D., Ketsetzi, A., Pachis, K., Ramos, V. M. 2008. Inhibitory effects of multicomponent, phosphonate-grafted, zwitterionic chitosan biomacromolecules on silicic acid condensation. Biomacromolecules 9, 3288–3293.

Demadis, K. D., Ketsetzi, A., Sarigiannidou, E. M. 2012*a*. Catalytic effect of magnesium ions on silicic acid polycondensation and inhibition strategies

based on chelation. Industrial and Engineering Chemistry Research, 9032–9040.

Demadis, K. D., Somara, M., Mavredaki, E. 2012*b*. Additive-driven dissolution enhancement of colloidal silica. 3. fluorine-containing additives. Industrial and Engineering Chemistry Research 51, 2952–2962.

Demadis, K. D., Tsistraki, A., Popa, A., Ilia, G., Visa, A. 2012*c*. Promiscuous stabilisation behaviour of silicic acid by cationic macromolecules: The case of phosphonium-grafted dicationic ethylene oxide bolaamphiphiles. RSC Advances 2, 631–641.

Demir, M. M., Baba, A., Atilla, V., İnanli, M. 2014. Types of the scaling in hyper saline geothermal system in northwest Turkey. Geothermics 50, 1–9.

Dewey J. F., Şengör A. M. C. 1979. Aegean and surrounding regions: Complex multiplate and continuum tectonics in a convergent zone. GSA Bulletin 90, 84–92.

Doğan, I., Demir, M. M., Baba, A. 2014. Scaling problem of the geothermal system in Turkey. Baba, A., Bundschuh, J., Chandrasekharam, D.(Ed.). Geothermal Systems and Energy Resources: Turkey and Greece. Sustainable Energy Development 7, CRC Press.

Ellis, A. J., Mahon, W. A. J. 1977. Chemistry and geothermal systems. Academic Press.

Fredd, C. N., Fogler, H. S. 1998. The influence of chelating agents on the kinetics of calcite dissolution. Journal of Colloid Interface Science 204, 187–197.

Gallup, D. L. 1993. The use of reducing agents for control ferric silicate scale deposition. Geothermics 22, 39–48.

Gallup, D. L. 1997. Aluminum silicate scale formation and inhibition: Scale characterization and laboratory experiments. Geothermics 26, 4, 483–499.

Gallup, D. L. 2002. Investigations of organic inhibitors for silica scale control in geothermal brines. Geothermics 31, 415–430.

Gallup, D. L. 2011. Brine pH modification scale control technology. A review Mercury contamination in the oil and gas industry. GRC Transactions 35.

Gallup, D. L., Barcelon, E. 2005. Investigations of organic inhibitors for silica scale control from geothermal brines–II. Geothermics 34, 756–771.

Gallup, D. L., Sugiaman, F., Capuno, V., Manceau, A. 2003. Laboratory investigation of silica removal from geothermal brines to control silica scaling and produce usable silicates. Applied Geochemistry 18, 1597–1612.

Gill, J. S. 1993. Inhibition of silica-silicate deposit in industrial waters. Colloids and Surfaces A: Physicochemical and Engineering Aspects 74, 1, 101 – 106.

Gill, J. S. 2011. New Inhibitors for silica and calcium carbonate control in geothermal. International Workshop on Mineral Scaling.

Gören, A. Y., Topçu, G., Demir, M. M., Baba, A. 2021. Effect of high salinity and temperature on water–volcanic rock interaction. Environmental Earth Science 80.

Gunnarsson, I., Arnórsson, S. 2005. Impact of silica scaling on the efficiency of heat extraction from high-temperature geothermal fluids. Geothermics 34, 320–329.

Gunnlaugsson, E., Ármannsson, H., Thorhallsson, S., Steingrímsson, B. 2014. Problems in geothermaloperation_scaling and corrosion. Utilization of Low- and Medium-Enthalpy Geothermal Resources and Financial Aspects of Utilization, 1–18.

Haklıdır, F. S. T., Balaban, T. Ö. 2019. A review of mineral precipitation and effective scale inhibition methods at geothermal power plants in West Anatolia (Turkey). Geothermics 80, 103–118.

Hibara, Y., Tazaki, S., Kuragasaki, M. 1990. Advanced H_2S gas treatment system for geothermal power plant–"geothermal gas injection technology. Geothermal Science and Technology 2.

Hirowatari, K. 1996. Scale prevention method by brine acidification with biochemical reactors. Geothermics 25.

Hoyer, D., Kevin, K., Darrell, G. 1991. Salton Sea Unit 2-innovations and successes. Geothermal Resources Council - Transactions 15.

Ichikuni, M. 1983. Chemistry of silica formed from geothermal waters. Chikyukagaku 17, 137–141.

Ikeda, R., Ueda, A. 2017. Experimental field investigations of inhibitors for controlling silica scale in geothermal brine at the Sumikawa geothermal plant, Akita Prefecture, Japan. Geothermics 70, 305–313.

Inanli, M., Atilla, V. 2011. Metal silicate formation at Tuzla geothermal brine lines, in: Proceedings International Workshop on Mineral Scaling.

Karabelas, A. J, Andritsos, N., Koutsoukos, P. G. 2002. Scale formation in geothermal plants international summer school on direct application of geothermal energy scale formation in geothermal plants. International Summer School on Direct Application of Geothermal Energy.

Karaburun, E., Sözen, Y., Çiftçi, C., Sahin, H., Baba, A., Akbey, Ü., Yeşilnacar, M. İ., Erdim, E., Regenspurg, S., Demir, M. M. 2022. Experimental modeling of antimony sulfides-rich geothermal deposits and their solubility in the presence of polymeric antiscalants. Geothermics 104, 102452.

Kaypakoğlu, B., Sisman, M., Aksoy, N. 2012. Preventive methods for scaling and corrosion in geothermal fields. New Zealand Geothermal Workshop 2012 Proceedings.

Kevin, B. 2013. Mineral scaling in geothermal power production. Reykjavik, Iceland: United Nations University.

Kiyota, Y., Uchiyama, N. 2011. Silica scale prevention effects of brine pH modification at Hatchobaru power station, Japan. Proceedings International Workshop on Mineral Scaling.

Lee, B. H., Lin, C. K., Chuang, C. W., Liu, L., Lee, H., Liu, C. 2015. A test of calcium carbonate scale inhibition in Chingshui Geothermal Field, Taiwan. World Geothermal Congress.

Leitzell, K., Caud, N. 2021. Climate change widespread, rapid, and intensifying . Intergovernmental Panel on Climate Change.

Lichti, K. A., Brown, K. L. 2013. Prediction and Monitoring of Scaling and Corrosion in pH Adjusted Geothermal Brine Solutions. Corrosion.

Mahon, W. A. J. 1966. Silica in hot water discharged from drillholes at Wairakei, New Zealand. New Zealand Journal of Science 9, 135–144.

Mccartney, T. R., Gharaibeh, S., Shank, R. 2017. Improved methods for removal of silicate deposits. Heat Exchanger Fouling and Cleaning.

Mineral Research and Exploration Institute (MTA), 1980. Hot and mineral water inventory. Ankara.

Montanari, D., Minissale, A., Doveri, M., Gola, G., Trumpy, E., Santilano, A., Manzella, A. 1994. Geothermal resources within carbonate reservoirs in western Sicily (Italy): A review. Earth Science Reviews 169, 180–201.

Mundhenk, N., Huttenloch, P., Sanjuan, B., Kohl, T., Steger, H., Zorn, R. 2013. Corrosion and scaling as interrelated phenomena in an operating geothermal power plant. Corrosion Science 70, 17–28.

Mutlu, H., Güleç, N. 1998. Hydrogeochemical outline of thermal waters and geothermometry applications in Anatolia (Turkey). Journal of Volcanology and Geothermal Research 85, 495–515.

Nancollas, G. 1982. Formation of Scales of Calcium Carbonate Polymorphs: The Influence of Magnesium Ion and Inhibitors.

Nassif, N., Livage, J. 2011. From diatoms to silica-based biohybrids. Chemical Society Reviews 40, 849–859.

Neofotistou, E., Demadis, K. D. 2004. Silica scale inhibition by polyaminoamide STARBURST® dendrimers. Colloids and Surfaces A: Physicochemical and Engineering Aspects 242, 213–216.

Öngen, A. S., Ergüler, Z. A. 2021. The effect of urban heat island on groundwater located in shallow aquifers of Kütahya city center and shallow geothermal energy potential of the region, Turkey. Bulletin of the Mineral Research and Exploration 165, 217–234.

Owen, L. B., Michels, D. E. 1984. Geochemical engineering reference manual.

Owusu, P. A., Asumadu-Sarkodie, S. 2016. A review of renewable energy sources, sustainability issues and climate change mitigation. Cogent Engineering 3, 1.

Pambudi, N. A., Itoi, R., Yamashiro, R., Alam, B. Y. C. S., Tusara, L., Jalilinasrabady, S., Khasani, J. 2015. The behavior of silica in geothermal brine from Dieng geothermal power plant, Indonesia. Geothermics 54, 109–114.

Patzay, G., Karman, F. H., Pota, G. 2003. Preliminary investigations of scaling and corrosion in high enthalpy geothermal wells in Hungary. Geothermics 32, 627–638.

Petkowski, J. J., Bains, W., Seager, S. 2020. On the Potential of Silicon as a Building Block for Life. Life 10.

Petrucci, R. H., Herring, G. F., Madura, J. D., Bissonnette, C. 2011. General Chemistry: Principles and Modern Applications, 10th ed. Pearson Education.

Preari, M., Spinde, K., Lazic, J., Brunner, E., Demadis, K. D. 2014. Bioinspired Insights Into Silicic Acid Stabilization Mechanisms: The Dominant Role of Polyethylene Glycol-Induced Hydrogen Bonding. Journal of American Chemical Society 136.

Putranto, W. A., Umardhani, Y., Sulistyo, Yurianto, Bayuseno, A. P. 2018. Analysis of calcium carbonate polymorphs deposited in water piping system and the effect of tartaric acid additive. MATEC Web of Conferences.

Rafferty, K. 1999. Scaling in geothermal heat pump systems. Idaho Falls.

Ramos-Candelaria, M., Cabel, A. C., Buñing, B. C., Noriega, M. T. 2000. Calcite inhibition field trials at the Mindanao Geothermal Production Field (MGPF), Philippines. World Geothermal Congress.

Rangel, G., Pereira, V., Ponte, C., Thorhallsson, S. 2019. Reaming calcite deposits of well PV8 while discharging: A successful operation at Riberia Grande geothermal field, Sáo Miguel Island, Azores, European Geothermal Congress.

Raymond, J., Williams-Jones, A. E., Clark, J. R. 2005. Mineralization associated with scale and altered rock and pipe fragments from the Berlin geothermal field, El Salvador; implications for metal transport in natural systems. Journal of Volcanology and Geothermal Research 145, 81–96.

Reyes, A. G., Trompetter, W. J., Britten, K., Searle, J. 2003. Mineral deposits in the Rotokawa geothermal pipelines, New Zealand. Journal of Volcanology and Geothermal Research 119, 215–239.

Rose, P., Xu, T., Kovac, K., Mella, M., Pruess, K. 2007. Chemical stimulation in near-wellbore geothermal formations: Silica dissolution in the presence of calcite at high temperature and high pH. Thirty-Second Workshop on Geothermal Reservoir Engineering.

Ryley, D. 1980. The mass discharge of a geofluid from a geothermal reservoir—well system with flashing flow in the bore. Geothermics 9, 221–235.

Satman, A., Uğur, Z., Onur, M. 1999. The effect of calcite deposition on geothermal well inflow performance. Geothermics 28, 425–444.

Schwerin, D. L., Hatcher, J. D. 2022. Hydrofluoric Acid Burns. StatPearls Publishing.

Sener, F., Baba, A., Uzelli, T., Akkuş, İ., Mertoğlu, O. 2022. Geothermal Energy Strategy of Turkey.

Siega, F. L., Herras, E. B., Buñing, B. C. 2005. Calcite scale inhibition: The case of Mahanagdong wells in Leyte geothermal production field, Philippines. World Geothermal Congress.

Simmons, S. F., Christenson, B. W. 1994. Origins of calcite in a boiling geothermal system. American Journal of Science 294, 361–400.

Sousa, M. F., Bertran, C. A. 2014. New methodology based on staticlight scattering measurements for evaluation of inhibitors for in bulk crystallization. Journal of Colloid Interface Science 420, 57–64.

Spinde, K., Pachis, K., Antonakaki, I., Paasch, S., Brunner, E., Demadis, K. D. 2011. Influence of polyamines and related macromolecules on silicic acid polycondensation: Relevance to “soluble silicon pools”? Chemistry of Materials 23, 4676–4687.

Tobler, D. J., Benning, L. G. 2013. In situ and time resolved nucleation and growth of silica nanoparticles forming under simulated geothermal conditions. Geochim Cosmochim Acta 114, 156–168.

Tonkul, S., Baba, A., Demir, M. M., Regenspurg, S. 2021. Characterization of Sb scaling and fluids in saline geothermal power plants: A case study for Germencik Region (Büyük Menderes Graben, Turkey). Geothermics 96.

Topçu, G., Çelik, A., Baba, A., Demir, M. M. 2017. Design of polymeric antiscalants based on functional vinyl monomers for (Fe, Mg) silicates. Energy and Fuels 31.

Topçu, G., Çelik, A., Kandemir, A., Baba, A., Şahin, H., Demir, M. M. 2019*a*. Increasing solubility of metal silicates by mixed polymeric antiscalants. Geothermics 77, 106–114.

Topçu, G., Koç, G. A., Baba, A., Demir, M. M. 2019*b*. The injection of CO_2 to hypersaline geothermal brine: A case study for Tuzla region. Geothermics 80, 86–91.

Tubular Exchanger Manufacturers Association, 1952. Standard of Tubular Exchanger Manufacturers Association.

Ueckert, M., Wismeth, C., Baumann, T. 2020. Crystallization of calcium carbonate in a large-scale push–pull heat storage test in the Upper Jurassic carbonate aquifer. Geothermal Energy 8.

Ueda, A., Kato, H., Miyauchi, T., Kato, K. 2003. Investigation of pH control method to avoid silica scaling in the Sumikawa geothermal field. Journal of the Geothermal Research Society of Japan 25, 163–177.

Utami, P. 2000. Characteristics of the Kamojang geothermal reservoir (West Java) as revealed by its hydrothermal alteration mineralogy. World Geothermal Congress.

Wangen, M., Sagen, J., Bjørnstad, T., Johansen, H., Souche, A. J. R. 2016. Models for calcium carbonate precipitation in the near-well zone by degassing

of CO_2. The Open Petroleum Engineering Journal 9, 178–194.

Wilson, N., Webster-Brown, J., Brown, K. 2007. Controls on stibnite precipitation at two New Zealand geothermal power stations. Geothermics 36, 330–347.

Wong, L., Suratwala, T., Feit, M. D., Miller, P. E., Steele, R. 2009. The effect of HF/NH_4F etching on the morphology of surface fractures on fused silica. Journal of Non-Crystalline Solids 355, 797–810.

Yokoyama, T., Ueda, A., Kato, K., Mogi, K., Matsuo, S. 2002. A study of the alumina–silica gel adsorbent for the removal of silicic acid from geothermal water: increase in adsorption capacity of the adsorbent due to formation of amorphous aluminosilicate by adsorption of silicic acid. Journal of Colloid and Interface Science 252, 1–5.

Zarrouk, S. J., Purnanto, M. H. 2014. Geothermal steam-water separators: Design overview. Geothermics 53, 236–254.

Zarrouk, S. J., Moon, H. 2014. Efficiency of geothermal power plants: A worldwide review. Geothermics 51, 142–153.

Zhang, B. R., Chen, Y. N., Li, F. T. 2011. Inhibitory effects of poly (adipic acid/amine-terminated polyether D230/diethylenetriamine) on colloidal silica formation. Colloids and Surfaces A: Physicochemical and Engineering Aspects 385, 11–19.